U.PORTO

DOUTORAMENTO
CIÊNCIAS BIOMÉDICAS

New three-dimensional intestinal tissue engineering model as a multifunctional platform for drug and nanoparticle absorption studies

Maria Helena Macedo

D

2021

U.PORTO

Maria Helena Macedo: New three-dimensional intestinal tissue engineering model as a multifunctional platform for drug and nanoparticle absorption studies

D.ICBAS **2021**

New three-dimensional intestinal tissue engineering model as a multifunctional platform for drug and nanoparticle absorption studies

Maria Helena Macedo

INSTITUTO DE CIÊNCIAS BIOMÉDICAS ABEL SALAZAR

Maria Helena Rodrigues Macedo

NEW THREE-DIMENSIONAL INTESTINAL TISSUE ENGINEERING MODEL AS A MULTIFUNCTIONAL PLATFORM FOR DRUG AND NANOPARTICLE ABSORPTION STUDIES

Tese de Candidatura ao grau de Doutor em Ciências Biomédicas submetida ao Instituto de Ciências Biomédicas Abel Salazar da Universidade do Porto

Orientador
Doutor Bruno Filipe Carmelino Cardoso Sarmento
Categoria – Investigador Principal & Professor Associado Convidado Afiliação – i3S - Instituto de Investigação e Inovação em Saúde, INEB - Instituto de Engenharia Biomédica, Universidade do Porto & IUCS - Instituto Universitário de Ciências da Saúde

Co-orientadora
Doutora Cristina Carvalho Barrias
Categoria – Investigadora Principal
Afiliação – i3S - Instituto de Investigação e Inovação em Saúde, INEB - Instituto de Engenharia Biomédica, Universidade do Porto & ICBAS – Instituto de Ciências Biomédicas Abel Salazar

Co-orientadora
Doutora Elena Martínez
Categoria – Investigadora Principal
Afiliação – IBEC – Institute for Bioengineering of Catalonia, CIBER-BBN – Consorcio Centro de Investigación en Red de Bioingeniería, Biomateriales y Nanomedicina & Electronics and Biomedical Engineering Department, Universitat de Barcelona

DECLARAÇÃO DE HONRA

Eu, Maria Helena Rodrigues Macedo, declaro que a presente tese é de minha autoria e não foi utilizada previamente noutro curso ou unidade curricular, desta ou de outra instituição. As referências a outros autores (afirmações, ideias, pensamentos) respeitam escrupulosamente as regras da atribuição, e encontram-se devidamente indicadas no texto e nas referências bibliográficas, de acordo com as normas de referenciação. Tenho consciência de que a prática de plágio e auto-plágio constitui um ilícito académico.

Porto, 27 de Setembro de 2021

Maria Helena Rodrigues Macedo

Aos meus pais, ao meu irmão e ao meu namorado, as pessoas mais importantes da minha vida.

The work presented in this thesis was developed at:

Nanomedicines & Translational Drug Delivery Group
i3S - Instituto de Investigação e Inovação em Saúde
INEB - Instituto de Engenharia Biomédica
Universidade do Porto, Porto, Portugal
Rua Alfredo Allen, 208
4200-135 Porto, Portugal
www.i3s.up.pt | www.ineb.up.pt

And

Biomimetic Systems for Cell Engineering Group
IBEC – Institute for Bioengineering of Catalonia
Baldiri Reixac, 10-12
08028 Barcelona, Espanha
www.ibecbarcelona.eu

FINANCIAL SUPPORT

Maria Helena Macedo was supported by a national PhD grant (SFRH/BD/131587/2017) from Fundação para a Ciência e Tecnologia (FCT). This work was financed by the project NORTE-01-0145-FEDER-000012, supported by Norte Portugal Regional Operational Programme (NORTE 2020), under the PORTUGAL 2020 Partnership Agreement, through the Europe and Regional Development Fund (ERDF), by FEDER - Fundo Europeu de Desenvolvimento Regional funds through the COMPETE 2020 - Operacional Programme for Competitiveness and Internationalisation (POCI), Portugal 2020, and by Portuguese funds through FCT/Ministério da Ciência, Tecnologia e Ensino Superior in the framework of the project "Institute for Research and Innovation in Health Sciences" (UID/BIM/04293/2019), and also Partnership Agreement PT2020 UID/QUI/50006/2013 -POCI/01/0145/FED ER/007265. This work was also supported by IBEC, COST and by Instituto Ciências Biomédicas de Abel Salazar (ICBAS).

PUBLICATIONS

Ao abrigo do disposto do n.º 2, alínea a) do artigo 31º do Decreto-Lei n.º 115/2013 de 7 de Agosto, fazem parte integrante desta tese de doutoramento os seguintes trabalhos já publicados ou submetidos para publicação:

- **Macedo M.H.**, Torras N., García-Díaz M., Barrias C.C., Sarmento B., Martínez E., 2021, The shape of our gut: dissecting the importance of the villi architecture in a 3D bioprinted *in vitro* intestinal model, *in preparation*.

- **Macedo M.H.**, Barros A.S., Martínez E., Barrias C.C., Sarmento B., All layers matter: Innovative three-dimensional epithelium-stroma-endothelium intestinal model for reliable permeability outcomes, *submitted*.

- **Macedo M.H.**, Baião A., Pinto S., Barros A.S., Almeida H., Almeida A., das Neves J., Sarmento B., 2021, Mucus-producing 3D cell culture models, *submitted*.

- **Macedo M.H.**, Martínez H., Barrias C., Sarmento B., Development of an improved 3D *in vitro* intestinal model to perform permeability studies of paracellular compounds, Frontiers in Bioengineering and Biotechnology, 8(524018).

- Almeida A.*, Azevedo C.*, **Macedo M.H.*** & Sarmento B., 2020, 3D intestinal models towards a more realistic permeability screening, in *Nanotechnology for Oral Drug Delivery* (389-417), Academic Press. (*equal contribution)

- Lin K., Zhang D., **Macedo M.H.**, Cui W., Sarmento B., Shen G., 2018, Advanced Collagen-Based Biomaterials for Regenerative Biomedicine, Advanced Functional Materials, 29(3):1804943.

- **Macedo M.H.**, Araújo F., Martínez E., Barrias C.C., Sarmento B., 2018, iPSC-Derived Enterocyte-like Cells for Drug Absorption and Metabolism Studies, Trends in Molecular Medicine, 24(8): 696-708.

ACKOWLEDGMENTS

Doing a PhD is an adventure! As in any adventure, it has a beautiful, magical side, but also parts that frighten you. Doing a PhD is facing fears every day. Facing the unknown, facing failure and disappointment. At the same time, it makes you learn and grow. It teaches you how to be resilient, how to evolve, how to reach out to others and how to become a better person day by day. And as if it wasn’t already hard enough to do a PhD under normal circumstances, a pandemic came along to make sure this experience would be truly unforgettable. Although there were times of sadness and, sometimes, despair during these four years, there was also much joy and happiness, unforgettable moments, people and experiences.
As I said, a PhD is an adventure. And as in any adventure, you cannot make it alone. Fortunately, along this ride I have had amazing people by my side, supporting me and making it worthwhile. To these people, I would like to give a special thank you:

To my supervisor, professor Bruno Sarmento, for welcoming me in his research group. Thank you for believing in me and for all the support throughout this journey. For showing me that a PhD is not everything in life but, and at the same time, pushing me forward to achieve my goals. Thank you for all the patience, the advices and all the emails that were never left unanswered. Thank you for all the opportunities you provided me, for never cutting my wings and for encouraging me to fly higher. Thank you for all the good moments, all the jokes, all the talks. I will never forget everything you did for me and I’ll be forever grateful.

To my co-supervisor, professor Cristina Barrias, for always helping me when I was in need. Thank you for all the support during the PhD, for helping me solve problems, always coming up with ideas and solutions. Thank you for always find some of your time when I needed and always receiving me with a smile. Also, a special thanks to Sílvia Bidarra and Ana Luísa from the research group, with whom I shared the cell culture room so many times. Thank you for making me feel welcomed in the institute from the first day I met you, for all the good times shared and for all the help and thoughts you have given me.

To my co-supervisor, professor Elena Martínez, for welcoming me in her group in Barcelona in a way that made me feel home. Thank you for the opportunity of being part of the group for some months and learn valuable things. Thank you for being always so nice and understanding. Thank you to all the research team with whom I shared beautiful moments together, especially to Núria Torras and María García-Diaz, who thaught me so much during my stay and helped me whenever I needed.

To Catarina Gonçalves and Maria José Oliveira, thank you for being my PhD advisors. Thank you for all the patience, for all the good advices, for all your kind and motivating words.

To all the present and former group members of the Nanomedicines and Translational Drug Delivery Group. Thank you for all the moments shared, for the help, for the conversations, for the lunches and dinners, for the funny group activities. Although all of you have a place in my heart, there are three people from whose friendship I am especially and forever grateful.

To Andreia Almeida, thank you for your incredible friendship. When I met you, I felt like I had known you for a long time and I realized that we were similar in so many ways. At the same time, we were different and that allowed us to learn and grow with each other. Thank you for all the special moments we shared together, the good times in the lab and all the trips! In the lab we also shared bad moments and I think that united us even more. Thank you for always being there for me.

To Cláudia Azevedo, thank you for your incredible friendship. Thank you for being such an easygoing person, to be relaxed and to always look on the bright side of life, making people around you feel safe. Thank you for putting up with my matinal bad mood, I know I was not an easy person in the morning. Thank you for all the beautiful moments we shared in the lab, I'll truly miss them. And thank you for the trips and adventures we lived together.

To Flávia Sousa, thank you for your incredible friendship. Thank you for all your advice and for being a model of perseverance. Your way of living, pursuing what makes you happy and not giving up on anything, is an example. Thank you for all your help and support. Thank you for helping me with the statistical analysis of my first original paper, although I know you probably don't remember it anymore, it meant a lot to me.

Together with these three beautiful girls, we form an amazing quartet, the "fantastic four". Thank you to all of you for letting me be part of your lives, I have no doubt that you were responsible for the best moments of this PhD.

To Isabel Aced and Anna De Gea, my roommates in Barcelona. When I went to Barcelona in the middle of the third wave of the Covid-19 pandemic, I was prepared to have the loneliest time of my life. Fortunately, I found two wonderful people. Thank you for all the *jueves felices* and for all the good moments shared in our home. To Anna,

thank you for showing me Collserola and giving me the Calçotada experience. To Isa, thank you for all the brunches, for all the plans we made on weekends, for always spending time with me discovering Barcelona, although you already knew it. Thank you for all the talks, I have learnt so much from you, and my stay in Barcelona has changed me as a person. Some of those changes were thanks to you.
I'll be expecting you both in Portugal.

To all of my friends and family who were part of this journey:

Às minhas amigas de curso Margarida Araújo, Beatriz Cardoso, Diana Martins, Joana Pires e Helena Sousa. Obrigada pela vossa amizade, mesmo depois de terminarmos o curso. Obrigada por todos os jantares que partilhamos nestes 4 anos.

Aos meus amigos de liceu. Obrigada por todos os momentos passados, todos os cafés partilhados, todas as festas, todos os jantares, todos os piqueniques, todos os passeios. A vossa amizade ao longo destes anos foi muito importante para mim. Um especial agradecimento à Rosa Oliveira, que partilhou comigo os primeiros anos do doutoramento. Obrigada por todas as viagens para o i3S, animando as minhas manhãs. Obrigada por todas as conversas e desabafos e obrigada por me teres visitado em Barcelona.

Aos pais e irmãos do meu namorado, Adelaide, Laurindo e Paulinho, obrigada por me terem acolhido na vossa família e me fazerem sentir bem-recebida. Obrigada por todos os momentos partilhados, por toda a preocupação e por todo o apoio ao longo destes anos. Ao Paulinho, obrigada por me perguntares sempre como estava a correr o doutoramento e tentares realmente perceber o meu trabalho.

Aos meus avós, Rosa e Júlio, obrigada por me receberem sempre com um sorriso. Obrigada por me mostrarem que não é preciso muito para ser feliz. Aos meus avós que já partiram, Maria e Raul, obrigada por tudo o que me ensinaram. Obrigada por agora serem os meus anjos da guarda e olharem por mim.

Aos meus pais, Rosália e Alexandre, e ao meu irmão, Mário, as pessoas que fizeram de mim quem eu sou hoje. A vocês devo tudo o que conquistei. Obrigada por sempre me apoiarem, por acreditarem e me fazerem sentir especial e capaz. Aos meus pais, obrigada por todo os sacrifícios que fizeram para me darem sempre o melhor. Obrigada por me educarem e me transmitirem os valores mais importantes. Ao meu irmão, obrigada por me fazer ver o mundo com outros olhos. Por ter despertado em mim o gosto pela arte e pela descoberta. A todos vós, obrigada pelo vosso amor incondicional. O meu amor por vós é incondicional também. Obrigada por serem a melhor família que eu algum dia poderia pedir. Enquanto estiverem presentes na minha vida, tudo estará bem e nunca me sentirei desamparada. A vossa felicidade é a minha felicidade.

Ao amor da minha vida, Hugo, pela nossa bonita história. Obrigada por todo o apoio, compreensão e companheirismo ao longo destes anos. Obrigada por teres entrado na minha vida há mais de 10 anos, enquanto éramos umas crianças que não sabiam nada da vida e por nunca mais me teres largado. Obrigada por te teres tornado o meu melhor amigo. Obrigada por teres crescido comigo, por me teres feito mudar para melhor, por me tornares uma pessoa mais paciente e tolerante. Obrigada por todos os momentos lindos que já vivemos e por todos os que ainda temos por viver. Obrigada por me fazeres rir e alegrares a minha vida todos os dias. Obrigada por quereres continuar a partilhar a tua vida comigo, que seja para sempre. Obrigada pelo teu amor. Enquanto estiveres comigo sei que serei feliz.

TABLE OF CONTENTS

ABSTRACT

The drug development field is in constant growth. In a fast-paced world, where new diseases continually emerge and existing ones do not cease to evolve, the need for reliable treatments that can tackle these conditions is unquestionable.

Oral delivery is the preferred route for drug administration as it is non-invasive, allowing convenience and flexibility for the patients, which helps to maintain their compliance. Upon oral administration, drugs are mainly absorbed in the small intestine. Absorption after oral administration is crucial when the drug is intended to act systemically, outside the gastrointestinal tract (GI), otherwise it is unable to reach the site of action. Besides understanding drug absorption, it is also important to study other drug pharmacokinetic characteristics. Considering this, ADME (absorption, distribution, metabolism and excretion) studies are performed in a pre-clinical phase of drug development. In the case of absorption, intestinal *in vitro* cell-based models are used in a first stage since they are simple to obtain, can allow high throughput studies and may help diminishing costs by saving time and reducing animal experimentation.

The small intestine is a complex organ, composed by different layers and types of cells, and presents a distinctive architecture. Unfortunately, *in vitro* models currently used to predict drug absorption fail to recapitulate key features of the *in vivo* small intestine. The "gold-standard" of intestinal *in vitro* models is the Caco-2 model, developed in the 1980's. It consists on a single layer of Caco-2 cells, that become enterocyte-like cells, forming a polarized monolayer and displaying some features of intestinal enterocytes after 21 days in culture in semipermeable membranes of Transwell® inserts. Nevertheless, this model represents only one cell type – the enterocytes, and one single layer – the epithelium, of the human small intestine. Although some improvements have been made in order to make it a more relevant model, such as the addition of HT29-MTX cells that produce mucus and mimic the intestinal goblet cells, it still lacks the three-dimensional (3D) features of the human small intestine. Besides the epithelium, the intestinal mucosa is composed by the lamina propria, which not only impacts the epithelial behavior, but can also play a role on the absorption process itself. Different cells compose the intestinal lamina propria, that also contains blood and lymphatic vessels, providing the last barrier compounds need to cross to reach systemic circulation. In terms of architecture, the small intestine possesses several surface modifications, such as protuberances called villi and invaginations called crypts that harbor different types of cells and increase the surface area, allowing a more efficient absorption process.

Taking all the above-mentioned facts into consideration, the main goal of this thesis was to develop an innovative 3D *in vitro* intestinal model, composed by different intestinal layers - epithelium, lamina propria and microvascular endothelium, and cell types – epithelial, fibroblasts and endothelial cells. Such model should allow to represent more physiologically the human small intestine and obtain more reliable permeability predictions, helping to bridge the gap between *in vitro* and *in vivo* experiments. Although this is a more complex model composed by different cell layers, our aim was to maintain it as simple as possible, in order to be reproduced and used by others. At the same time, this study aimed at understating the impact of adding villus structures to the model.

First, a collagen type I layer with embedded human intestinal fibroblasts (HIF), to mimic the lamina propria, was optimized. Different parameters were tested to obtain a layer that could maintain its integrity for the entire time in culture without compromising fibroblasts viability. It became clear that different factors could affect collagen contraction by the fibroblasts, namely the final collagen concentration of the hydrogel as well the concentration of the collagen stock solution, the initial HIF seeding density, and the crosstalk with the epithelial and endothelial cells.

When the lamina propria layer was established with a collagen concentration of 6 mg/mL and a HIF initial seeding density of 1 x 10^5 cells/mL, the 3D model maintained its integrity for more than 14 days, allowing the formation of the epithelial layer on top (Caco-2 or co-culture of Caco-2 and HT29-MTX, mimicking enterocyte and goblet cells, respectively) and enabling to perform permeability studies with fluorescently labelled Dextran (4kDa), a paracellular marker. Two-dimensional (2D) models composed by Caco-2 or co-culture of Caco-2 and HT29-MTX were used as controls. The transepithelial electrical resistance (TEER) of the 3D models decreased, being more akin to *in vivo* values and the permeability assay revealed significantly higher absorption in the 3D models compared to the 2D analogues used as control.

Nevertheless, since the main aim was to establish a model that could be sustained for 21 days in culture to allow for complete cellular differentiation, as well as to test permeability of both paracellular and transcellular compounds, a further optimization was performed by decreasing the fibroblast initial seeding density to 0.5 x 10^5 cells/mL. This decrease in cellular density allowed the models to maintain their integrity for 21 days, without compromising HIF viability. Epithelial cells were added and the models, with and without an endothelial layer underneath the lamina propria, were fully characterized in terms of intestinal markers, drug transporters, expression of tight junctions (TJs) and MUC2 and most importantly, drug permeability, as compared to the standard 2D co-culture analogs. Both configurations of the 3D models revealed a better expression of drug transporters in general and specifically in P-glycoprotein (P-gp) and multidrug

resistance-associated protein 2 (MRP2), which can have an impact in efflux of several compounds. The TEER of the 3D models was lower and more similar to the reported *in vivo* values, which, in its turn, may impact paracellular transport. Regarding the permeability outcomes, the values that most resembled reported literature results obtained with animal models were achieved with the 3D model without the endothelial layer. The addition of an endothelium decreased the permeability, what could be expected since it provides an additional layer that is likely to partially hinder absorption.
Lastly, the incorporation of villi in the model was studied to understand the impact of these microstructures in cell behavior, differentiation and permeability. A stereolithography-based 3D bioprinting method and a hydrogel with a network of gelatin methacryloil (GelMA) and poly(ethylene glycol) diacrylate (PEGDA) laden with HIF were used to obtain the microstructures. A flat hydrogel was used as control and Caco-2 and HT29-MTX cells were seeded on top of both configurations. Epithelial cells were shown to completely cover the villus-like structures, forming a uniform cell layer. TEER values in the villi shaped hydrogel were lower than in the flat scaffold, confirming the impact of the intestinal architecture. Differences were also observed regarding drug transporters, with lower genetic expression of peptide transporter 1 (PEPT1) and organic cationic transporter 1 (OCT1) and lower P-gp activity in the microstructured model. In terms of permeability, the model resembling the intestinal architecture globally showed increased absorption of compounds compared to the flat model. Nevertheless, values of permeability were lower than the ones obtained with the previously mentioned 3D collagen model without the endothelium.

Overall, the 3D model composed by the collagen layer with HIF embedded mimicking the intestinal lamina propria and epithelial cells on top was the one that best predicted the outcomes of intestinal permeability. This was the simplest 3D model, fulfilling our main goal of developing a complex and reliable model in the simplest possible manner, enabling its widespread use. We believe that this model can help to bridge the gap between *in vitro* and *in vivo* studies, reducing the need for animal experimentation in pre-clinical drug developmental stages, thus complying with the 3Rs policy. The addition of the endothelial layer, as well as the incorporation of villi structures, were also important, as proofs of concept, to understand their impact on cell behavior and in the drug absorption process.

RESUMO

O desenvolvimento farmacêutico é uma área que está em constante crescimento. Num mundo acelerado, onde novas doenças estão continuamente a surgir e as já existentes não param de evoluir, a necessidade de tratamentos fidedignos que possam enfrentar estas enfermidades é inquestionável.

A via oral é a via preferencial para administração de fármacos porque é não-invasiva, permitindo conveniência e flexibilidade para o paciente e ajudando a manter o seu compromisso com a farmacologia prescrita. Após administração oral, os compostos são maioritariamente absorvidos no intestino delgado. Esta absorção é fundamental quando o fármaco necessita de atuar fora do trato gastrointestinal, caso contrário não consegue chegar ao local de ação. Além de perceber a absorção, é importante estudar outras características farmacocinéticas do fármaco. Tendo isto em conta, estudos de ADME (absorção, distribuição, metabolismo e excreção) são realizados numa fase pré-clínica do desenvolvimento farmacêutico. No caso da absorção, modelos intestinais *in vitro* são usados numa primeira fase por serem fáceis de obter, permitirem uma análise *high throughput* e permitirem reduzir custos, ao pouparem tempo e reduzirem a necessidade de experimentação animal.

O intestino delgado é um órgão complexo, composto por diferentes camadas e tipos celulares e apresenta uma arquitetura característica. Infelizmente, os modelos *in vitro* usados atualmente não conseguem recapitular a maior parte das características do intestino. O *"gold-standard"* dos modelos intestinais *in vitro* é o modelo Caco-2 que foi desenvolvido nos anos 80 e que consiste numa camada de células Caco-2 que, após atingirem confluência, se diferenciam células similares a enterócitos intestinais, formando uma camada celular polarizada e exibindo algumas características dos enterócitos após 21 dias em cultura em membranas semipermeáveis dos *inserts* Transwell®. No entanto, este modelo representa apenas um tipo celular – os enterócitos, e uma camada – o epitélio, do intestino humano. Apesar de já terem sido feitas melhorias a este modelo para tentar torna-lo mais relevante, como a incorporação de células HT29-MTX que produzem muco e mimetizam as células *goblet* presentes no intestino, continuam a faltar as características tridimensionais (3D) do intestino humano. Para além do epitélio, a mucosa intestinal é composta pela lamina própria, que tem um impacto tanto no comportamento das células epiteliais como no próprio processo de absorção. Diferentes tipos celulares compõem a lamina própria intestinal e vasos sanguíneos e linfáticos também estão presentes, constituindo a última barreira que os compostos necessitam de ultrapassar para alcançar a circulação sistémica. Em termos de arquitetura, o intestino possui várias modificações superficiais, como protuberâncias

chamadas vilosidades e invaginações chamadas criptas que contém diferentes tipos celulares e fazem aumentar a área do intestino, permitindo um processo de absorção mais eficiente.

Tendo em consideração tudo o que foi mencionado anteriormente, o objetivo principal desta tese foi desenvolver um novo modelo intestinal 3D *in vitro*, composto por diferentes camadas – epitélio, lamina própria e endotélio – e tipos celulares – células epiteliais, fibroblastos e células endoteliais – para representar mais fielmente o intestino humano e obter resultados mais fiáveis em termos de permeabilidade, ajudando a preencher a lacuna entre as experiências *in vitro* e *in vivo*. Apesar de este ser um modelo mais complexo, composto por diferentes camadas, o nosso objetivo era mante-lo o mais simples possível, de forma a poder ser reproduzido e usado por outros investigadores. Ao mesmo tempo, este estudo pretendeu estudar o impacto causado pela presença de vilosidades no modelo.

Em primeiro lugar, uma camada de colagénio tipo I com fibroblastos intestinais humanos embebidos, para mimetizar a lamina própria, foi otimizado. Diferentes parâmetros foram testados para obter uma camada que mantivesse a sua integridade durante todo o tempo de cultura, sem comprometer a viabilidade das células. Durante este processo de otimização, tornou-se claro que diferentes fatores poderiam afetar a contração do colagénio pelos fibroblastos, nomeadamente a concentração final de colagénio no hidrogel, a concentração da solução stock de colagénio, a densidade inicial de fibroblastos e o *crosstalk* com as células epiteliais e endoteliais. Quando esta camada foi estabelecida com uma concentração de colagénio de 6 mg/mL e uma concentração inicial de fibroblastos de 1 x 10^5 células/mL, o modelo manteve a sua integridade por mais de 14 dias, permitindo a formação da camada epitelial em cima (Caco-2 ou co-cultura de Caco-2 e HT29-MTX), possibilitando a realização de ensaios de permeabilidade usando o marcador paracelular dextrano com isotiocianato de fluoresceína (FITC-Dextran) 4kDa. Modelos bidimensionais (2D) compostos por Caco-2 ou co-cultura de Caco-2 e HT29-MTX foram usados como controlos. A resistência transepitelial (TEER) dos modelos 3D foi menor, sendo mais similar aos valores reportados *in vivo* e os ensaios de permeabilidade revelaram uma permeabilidade significativamente superior nos modelos 3D.

No entanto, visto que o objetivo principal era desenvolver um modelo que pudesse estar 21 dias em cultura para permitir uma diferenciação completa das células, assim como testar a permeabilidade tanto de compostos paracelulares como transcelulares, uma otimização adicional foi realizada, diminuindo o número inicial de fibroblastos para 0.5 x 10^5 células/mL, o que permitiu manter a integridade do modelo por 21 dias sem comprometer a viabilidade das células. As células epiteliais foram adicionadas e os

modelos, com ou sem células barreira endotelial por baixo da lamina própria, foram caracterizados em termos de marcadores intestinais, transportadores, expressão de *tight junctions (TJs)* e MUC2 e, mais importante, permeabilidade, e foram comparados com o modelo de co-cultura 2D. Ambas as configurações dos modelos 3D revelaram uma expressão de transportadores mais realista no geral e, especificamente, na *P-glycoprotein* (P-gp) e na *multidrug resistance-associated protein* (MRP2), que podem ter um impacto no efluxo de vários compostos. O TEER dos modelos 3D foi menor e mais similar aos valores reportados *in vivo* o que, por seu lado, pode ter um impacto no transporte paracelular. Quanto aos resultados de permeabilidade, os valores mais fiáveis foram obtidos para o modelo 3D sem a camada endotelial. A incorporação da camada endotelial diminuiu a permeabilidade, o que, de alguma maneira, era esperado visto que uma camada adicional está presente, constituindo mais uma barreira à permeabilidade.

Por último, a incorporação das vilosidades no modelo foi estudada para perceber qual seria o impacto destas microestruturas no comportamento e diferenciação celular e na permeabilidade. Um método de impressão 3D baseado em estereolitografia e num hidrogel composto por uma rede de gelatina metacrilada (GelMA) e poli(etilenoglicol) diacrilato (PEGDA) com fibroblastos embebidos foi usado para obter o *scaffold* com as vilosidades. Um hidrogel plano foi usado como controlo e células Caco-2 e HT29-MTX foram semeadas em cima de ambos os modelos. As células epiteliais foram capazes de cobrir as vilosidades, formando uma camada celular uniforme. Os valores de TEER no modelo com as vilosidades foram inferiores ao modelo plano, revelando o impacto da arquitetura intestinal. Também foram observadas diferenças nos transportadores, com uma expressão genética inferior do *peptide transporter 1* (PEPT1) e do *organic cationic transporter* 1 (OCT1) e uma atividade menor da P-gp no modelo microestruturado. Em termos de permeabilidade, o modelo com arquitetura intestinal mostrou uma permeabilidade globalmente superior. No entanto, os valores de permeabilidade obtidos foram inferiores aos obtidos com o modelo de colagénio sem a camada endotelial, referido anteriormente.

No geral, o modelo 3D composto pela camada de colagénio com fibroblastos embebidos, mimetizando a lamina própria, e as células epiteliais em cima, foi o que permitiu prever, com mais fiabilidade, os resultados de permeabilidade intestinal. Este era o modelo 3D mais simples, cumprindo o objetivo principal de desenvolver um modelo complexo e fiável da maneira mais simplista possível, permitindo o seu uso generalizado. Cremos que este modelo pode ajudar a preencher a lacuna entre as experiências *in vitro* e *in vivo*, reduzindo a necessidade da experimentação animal nas fases pré-clínicas do desenvolvimento farmacêutico. A adição da camada endotelial,

assim como a incorporação das vilosidades foi importante, como provas de conceito, para perceber o impacto destas alterações no comportamento das células em particular e do modelo como um todo.

LIST OF FIGURES

Cldn3, Cldn4, Cldn7, Cldn8, Cldn12 and Cldn15 in the duodenum, jejunum, duodenum, ileum and colon are summarized. (A) Bar height represents the expression level. (B) The colors represent the same claudins as in panel A. Colored dots and lines correspond to localization at tight junctions and basolateral membranes, respectively. Reprinted from [76] with permission from Elsevier.

Figure 1.6 - Diagram of major drug transporters proteins expressed at the intestinal epithelia including intestinal uptake (yellow) and efflux (light blue) transporters. Multidrug resistance protein (MDR1, P-glycoprotein), multidrug resistance associated protein (MRP), breast cancer resistance protein (BCRP), monocarboxylate transporter protein (MCT), peptide transporter protein (PEPT), organic anion transporting polypeptide (OATP), organic cation transporter (OCT), carnitine/organic cation transporter (OCTN), and plasma membrane monoamine transporter (PMAT). Reprinted from [94] with permission from Elsevier.

Figure 1.7 - (A) Schematic representation of the triple-culture 3D model. (B) Hematoxylin and eosin (H&E)-stained paraffin section showing myofibroblasts sustaining epithelial Caco-2 and HT29-MTX cells over them. (C) **Fibronectin** expression in a paraffin section of the triple-culture 3D model. Fibronectin was labeled with Alexa-Fluor® 488 (green) and nucleus with DAPI. Reprinted from [159] with permission from Elsevier.

Figure 3.1 - First attempt with embedded HIF in the collagen hydrogels to determine the optimal concentration of HIF. Different HIF seeding densities (A – 1 x 10^5; B – 2 x 10^5; C - 10 x 10^5 and D – 20 x 10^5 cells/mL) were embedded in the disks with a collagen concentration of 5 mg/mL. A control without cells was used confirm if contraction was related to the presence of fibroblasts.

Figure 3.2 - Metabolic activity of the HIF inside the collagen hydrogels with different initial seeding densities (A – 1 x 10^5; B – 2 x 10^5; C – 10 x 10^5 and D – 20 x 10^5 cells/mL) at different timepoints (1, 7, 14 and 21 days). Results are the average of triplicates and bars represent the standard error of the mean (SEM). Statistical differences $p < 0.05$ are denoted by (*), $p < 0.01$ are denoted by (**), $p < 0.001$ are denoted by (***) and $p < 0.0001$ are denoted by (****).

Figure 3.3 – **Vimentin** and **fibronectin** deposition by human intestinal fibroblasts in collagen hydrogels in condition A (1 x 10^5 cells/mL) after 21 days in culture. Picture

depicts a maximal projection of the several stacks of the gel. Fibronectin and vimentin were labelled with Alexa-Fluor 488 and with Alexa-Fluor 594, respectively. The nuclei were counterstained with DAPI.

Figure 3.4 - Second attempt with HIF embedded in the collagen hydrogels to determine the optimal concentration of collagen. Different collagen concentrations (E - 5; F – 6 and G – 7 mg/mL) were used with HIF embedded in an initial seeding density of 1 x 10^5 cells/mL. The behavior of the disks was assessed during 21 days.

Figure 3.5 - Metabolic activity of the HIF (initial seeding density of 1 x 10^5 cells/mL) inside the collagen hydrogels with different concentrations (E – 5; F - 6 and G – 7 mg/mL) at different timepoints (1, 7, 14 and 21 days). Results are the average of triplicates and bars represent the standard error of the mean (SEM). Statistical differences were calculated using 2-way ANOVA multiple comparisons to compare between cellular viability in each condition for each timepoint ($p<0.05$ are denoted by * and $p<0.01$ are denoted by **).

Figure 3.6 - Third attempt with HIF embedded in the collagen hydrogels to determine the optimal concentration of collagen. Different collagen concentrations (H - 5; I - 6 and J – 7 mg/mL) were used with HIF embedded in an initial seeding density of 0.5 x 10^5 cells/mL. The behavior of the disks was assessed during 21 days.

Figure 3.7 - Metabolic activity of the HIF (initial seeding density of 0.5 x 10^5 cells/mL) inside the collagen hydrogels with different concentrations (H – 5; I - 6 and J – 7 mg/mL) at different timepoints (1, 7, 14 and 21 days). Results are the average of triplicates and bars represent the standard error of the mean (SEM). Statistical differences were calculated using 2-way ANOVA multiple comparisons to compare between cellular viability in each condition for each timepoint ($p<0.05$ are denoted by *, $p<0.01$ are denoted by ** and $p<0.0001$ are denoted by ****).

Figure 3.8 - Fourth attempt with HIF embedded in the collagen hydrogels to determine the optimal concentration of FBS in medium to prevent contraction. Different percentages of FBS in cell culture medium (K – 0; L - 2; M – 5 and N – 10%) were used in hydrogels with a collagen concentration of 7 mg/mL and a HIF initial seeding density of 0.5 x 10^5 cells/mL. (The pictures for condition N are the same as for condition J). The behavior of the disks was assessed during 21 days.

Figure 3.9 - Metabolic activity of the HIF (initial seeding density of 0.5 x 10^5 cells/mL) inside the collagen hydrogels with a collagen concentration of 7 mg/mL and different percentages of FBS in cell culture medium (K - 0; L – 2; M – 5 and N – 10%) at different timepoints (1, 7, 14 and 21 days). Statistical differences were calculated using 2-way ANOVA multiple comparisons to compare between cellular viability in each condition for each timepoint ($p<0.01$ are denoted by ** and $p<0.0001$ are denoted by ****).

Figure 3.10 - **Vimentin** and **fibronectin** deposition by human intestinal fibroblasts in collagen hydrogels in condition M (5% FBS) after 21 days in culture. Fibronectin and vimentin were labelled with Alexa-Fluor 488 and with Alexa-Fluor 594, respectively. The nuclei were counterstained with DAPI.

Figure 3.11 - Third attempt of the collagen hydrogels with fibroblasts embedded and Caco-2 cells on top to determine the optimal concentration of collagen to prevent contraction. Different concentrations of collagen (S – 5; T - 6 and N – 7 mg/mL) were used and the HIF initial seeding density was maintained at 5 x 10^5 cells/mL. The behavior of the disks was assessed at 14 and 21 days.

Figure 3.12 - **Vimentin** and **fibronectin** deposition by human intestinal fibroblasts in collagen hydrogels in condition T (collagen concentration 6 mg/mL) after 14 and 21 days in culture. Picture depicts a maximal projection of the several stacks of the gel. Fibronectin and vimentin were labelled with Alexa-Fluor 488 and with Alexa-Fluor 594, respectively. The nuclei were counterstained with DAPI.

Figure 3.13 - Metabolic activity of the HIF (initial seeding density of 1 x 10^5 cells/mL) inside the collagen hydrogels with a collagen concentration of 6 mg/mL at different timepoints (1, 7, 14 and 21 days). Results are the average of triplicates and bars represent the standard error of the mean (SEM).

Figure 3.14 - **Vimentin** and **fibronectin** deposition by human intestinal fibroblasts in hydrogels with a collagen concentration of 6 mg/mL and a HIF initial seeding density of 1 x 10^5 cells/mL after 21 days in culture. Picture depicts a maximal projection of the several stacks of the gel. Fibronectin and vimentin were labelled with Alexa-Fluor 488 and with Alexa-Fluor 594, respectively. The nuclei were counterstained with DAPI.

Figure 4.6 - Assessment and comparison of the tight junctions' protein **ZO-1** and the mucin **MUC2** in the different models at different timepoints. ZO-1 was labelled with Alexa-Fluor 488 and MUC2 was labelled with Alexa Fluor 594. The nuclei were counterstained with DAPI.

Figure 4.7 - Comparison between 2D and 3D models regarding TEER values and permeability. (a) TEER values of the models over time. Comparison of the cumulative transport of FITC-Dextran across the (b) 2D models after 14 vs. 21 days in culture and (c) 3D models after 14 days in culture vs. 2D models after 21 days in culture. Comparison of P_{app} values of (d) 2D models after 14 vs. 21 days in culture and (e) 3D models after 14 days in culture vs. 2D models after 21 days in culture. Results are the average of triplicates (except for permeability of 3D Caco-2, which n=2) and bars represent the standard error of the mean (SEM). Statistical differences were calculated using 2-way ANOVA and Unpaired t-test ($p<0.05$ are denoted by *, $p<0.01$ are denoted by ** and $p<0.0001$ are denoted by ****).

Figure 5.1 - General overview of the procedure followed to obtain the 3D complete model.

Figure 5.2 – Human intestinal fibroblasts (HIF) (a) metabolic activity along the time in culture and (b) expression of **fibronectin** and **vimentin** after 21 days, when cells are seeded inside the collagen disks. The nuclei were counterstained with DAPI. Results for (a) are the average of triplicates, and bars represent the standard error of the mean (SEM). Statistical differences were calculated using 2-way ANOVA multiple comparisons to compare between different initial seeding densities of HIF in different days ($p<0.05$ is denoted by *).

Figure 5.3 – ALP activity levels in the different configurations of the models in different timepoints (7, 14 and 21 days) during the time in culture. Results are the average of triplicates, and bars represent the standard error of the mean (SEM). Statistical differences were calculated using 2-way ANOVA multiple comparisons to compare the levels of ALP in the different configurations for each timepoint ($p<0.05$ is denoted by * and $p<0.01$ is denoted by **).

Figure 5.4 – Normalized genetic expression of different intestinal markers between (a) 2D Caco-2 and 2D Co-culture models and (b) 2D Co-culture, 3D Co-culture and 3D

Complete models at 14 and 21 days. Results are the average of triplicates, and bars represent the upper and lower limits. Statistical differences were calculated using the log transformed data with 2-way ANOVA multiple comparisons in relation to (a) 2D Caco-2 21 days and (b) 3D Co-culture 21 days, used as references ($p<0.01$ is denoted by **, $p<0.001$ is denoted by $ and $p<0.0001$ are denoted by #).

Figure 5.5 - Normalized genetic expression of different intestinal transporters between (a) 2D Caco-2 and 2D Co-culture models and (b) 2D Co-culture, 3D Co-culture and 3D Complete models at 14 and 21 days. Results are the average of triplicates, and bars represent the upper and lower limits. Statistical differences were calculated using the log transformed data with 2-way ANOVA multiple comparisons in relation to (a) 2D Caco-2 21 days and (b) 2D Co-culture 21 days, used as reference ($p<0.05$ are denoted by *, $p<0.01$ is denoted by **, $p<0.001$ is denoted by $ and $p<0.0001$ are denoted by #).

Figure 5.6 – Comparison of protein expression of (a) **E-cadherin** and **P-gp**, (b) **Claudin-1** and **MPR2** and (c) **ZO-1** and **MUC2** between the 2D Co-culture, 3D Co-culture and 3D Complete models at 14 and 21 days. The nuclei were counterstained with DAPI.

Figure 5.7 - TEER values of the 2D Co-culture, 3D Co-culture and 3D Complete models during the 21 days in culture. Results are the average of nine replicates, and bars represent the standard deviation (SD).

Figure 5.8 – P_{app} ($x10^{-6}$ cm/s) values of Rhodamine 123 in the 2D Co-culture, 3D Co-culture and 3D Complete models at 14 and 21 days in the (a) apical to basolateral and (b) basolateral to apical directions and (c) ratio of the bidirectional transport. Results are the average of triplicates, and bars represent the standard error of the mean (SEM). Statistical differences were calculated using 2-way ANOVA multiple comparisons to compare P_{app} between each configuration at different time points and to compare between the same configuration at each timepoint ($p<0.05$ are denoted by *, $p<0.01$ are denoted by **, $p<0.001$ are denoted by *** and $p<0.0001$ are denoted by ****).

Figure 5.9 - P_{app} ($x10^{-6}$ cm/s) values of (a) Colchicine, (b) Atenolol and (c) Metoprolol in the 2D Co-culture, 3D Co-culture and 3D Complete models at 14 and 21 days. Results are the average of triplicates, and bars represent the standard error of the mean (SEM). Statistical differences were calculated using 2-way ANOVA multiple comparisons to compare P_{app} between each configuration at different time points and to compare

between the same configuration at each timepoint (p<0.05 are denoted by *, p<0.01 are denoted by **, p<0.001 are denoted by *** and p<0.0001 are denoted by ****).

Figure 6.1 - General overview of the procedure followed to obtain the bioprinted models.

Figure 6.2 – Live and Dead assay performed on the HIF embedded on the scaffolds with two different initial seeding densities. (a) Percentage of live cells and (b) maximum intensity projection of the hydrogels showing the live and dead fibroblasts.

Figure 6.3 – **Fibronectin**, **vimentin**, **alpha-SMA** and **collagen type IV** deposition by HIF in hydrogels with two different initial seeding densities after 21 days in culture. Pictures depict a maximum intensity projection. Vimentin and alpha-SMA were labelled with Alexa-Fluor 488, collagen type IV was labelled with Alexa-Fluor 594 and fibronectin was labelled with Alexa-Fluor 568. The nucleus was counterstained with DAPI and f-actin was stained with Phalloidin Rhodamine.

Figure 6.4 – Visualization of epithelial layer formation of top of the scaffolds. (a) Top view of the epithelial cells on top of flat and villus scaffolds at different timepoints (1, 7, 14 and 21 days) and monolayer visualization by staining of **nuclei** and **f-actin** in transversal cuts of (b) flat and (c) villus scaffolds after 21 days in culture. (d) TEER values along the 21 days in culture, where results are the average 18 samples and bars represent the standard error of the mean (SEM). Statistical difference p<0.0001 are denoted by ****.

Figure 6.5 – Activity and expression of intestinal markers. (a) ALP activity levels in flat and villus configurations of the models at different timepoints (7, 14 and 21 days) during the time in culture and (b) genetic expression of ISX, SI and VIL1 after 21 days in culture. For (a) results are the average of triplicates, bars represent the standard error of the mean (SEM) and statistical differences were calculated using 2-way ANOVA multiple comparisons to compare the levels of ALP in the different configurations for each timepoint (p<0.01 is denoted by **). For (b) results are the average of triplicates, bars represent upper and lower limits and statistical differences were calculated using the log transformed data with 2-way ANOVA multiple comparisons to compare expression of each gene between configurations.

Figure 6.6 - Normalized genetic expression of different intestinal transporters between the 2D and 3D Co-cultures and the bioprinted models (flat and villi) after 21 days in culture. Results are the average of triplicates, and bars represent the upper and lower limits. Statistical differences were calculated using the log transformed data with 2-way ANOVA multiple comparisons ($p<0.05$ is denoted by *, $p<0.01$ is denoted by **, $p<0.001$ is denoted by *** and $p<0.0001$ are denoted by ****). (^{a}) Data taken from the previous chapter.

Figure 6.7 - Comparison of protein expression of (a, b) **E-cadherin** and **fibronectin**, (c, d) **ß-catenin** and (e, f) **claudin-1** and **vimentin** in (a, c, e) flat and (b, d, f) villi configuration after 21 days in culture. E-cadherin, Claudin-1 and ß-catenin were labelled with Alexa-Fluor 488 and fibronectin and vimentin were labelled with Alexa-Fluor 594. The nuclei were counterstained with DAPI and (a, b) pictures depicts a maximal projection of the several stacks of the cut, where f-actin was counterstained with rhodamine phalloidin.

Figure 6.8 - P_{app} ($x10^{-6}$ cm/s) values of Rho 123 in the flat and villi models after 21 days in the (a) apical to basolateral and (b) basolateral to apical directions and (c) ratio of the bidirectional transport. Results are the average of triplicates, and bars represent the standard error of the mean (SEM). Statistical differences were calculated using 2-way ANOVA multiple comparisons to compare P_{app} between each configuration ($p<0.05$ are denoted by * and $p<0.001$ are denoted by ***).

Figure 6.9 - P_{app} ($x10^{-6}$ cm/s) values and percentage of permeated amount of (a, b) metoprolol, (c, d) atenolol and (e, f) colchicine in the flat and villus bioprinted models after 21 days. Results are the average of quadruplicates, and bars represent the standard error of the mean (SEM). Statistical differences were calculated using 2-way ANOVA multiple comparisons to compare P_{app} between each configuration and to compare percentage of permeated amount between each timepoint ($p<0.01$ is denoted by **, $p<0.001$ is denoted by *** and $p<0.0001$ are denoted by ****).

Figure A.1 - Example of a zymography obtained using the medium samples of day 21- It is possible to see the appearance of MMP9 and MMP2 bands right underneath Pro-MMP9 and Pro-MMP2, respectively, but so tenuous that makes quantification impossible.

Figure A.2 – Visualization of the endothelial cell monolayer formation after 21 days on (a) histological transversal cuts with H&E staining of HPMEC cells seeded alone on the basolateral side of the insert, (b) histological transversal cuts with H&E staining of HPMEC cells seeded in combination with the epithelial cells and the collagen layer with fibroblast and (c) top view of endothelial cells on the basolateral side of the insert in the 3D complete model immunoassayed for **CD31**, which is an endothelial cell adhesion molecule. Nuclei were counterstained with DAPI.

Figure A.3 - Percentage of permeated amount of colchicine, atenolol and metoprolol in the different models after 14 and 21 days. Results are the average of triplicates, and bars represent the standard error of the mean (SEM). Statistical differences were calculated using 2-way ANOVA multiple comparisons to compare P_{app} between each configuration and to compare percentage of permeated amount between each timepoint ($p<0.01$ is denoted by **, $p<0.001$ is denoted by *** and $p<0.0001$ are denoted by ****).

LIST OF TABLES

ACRONYMS AND ABBREVIATIONS LIST

2D	Two-dimensional
3D	Three-dimensional
3Rs	Replacement, reduction and refinement
ABC	ATP binding cassette
ADME	Absorption, distribution, metabolism and excretion
AFM	Atomic force microscopy
AJ	Adherens junction
ALP	Alkaline phosphatase
AMP	Antimicrobial protein
ANOVA	Analysis of variance
ATCC	American type culture collection
ATP	Adenosine triphosphate
Au	Gold
BCRP	Breast cancer resistance protein
BM	Basement membrane
BMP	Bone morphogenic protein
BS	Blocking solution
BSA	Bovine serum albumin
CAR	Coxsackie and adenovirus receptor
CD	Cluster of differentiation
CNT	Carbon nanotube
CYP	Cytochrome
DAPI	4',6'-diamino-2-fenil-indol
DLP	Digital light processing
DM	Desmosomes
DMEM	Dulbecco’s modified Eagle’s medium
E&H	Hematoxylin and eosin
ECGS	Endothelial cell growth supplement
ECM	Extracellular matrix
ELISA	Enzyme linked immunosorbent assay
ENT	Equilibrative nucleoside transporter
EpCAM	Epithelial cell adhesion molecule
ESAM	Endothelial cell-selective adhesion molecule
ET	Endothelin
F_a	Fraction absorbed

FAE	Follicle-associated epithelium
FBS	Fetal bovine serum
FGS	Fibroblast growth supplement
FITC	Fluorescein isothiocyanate
FM	Fibroblasts medium
GALT	Gut-associated lymphoid tissue
GC	Germinal center
GelMA	Gelatin methacryloil
GIT	Gastrointestinal tract
GJ	Gap junctions
HBSS	Hanks balanced salt solution
H&E	Hematoxylin and eosin
HGF/SF[4]	Hepatocyte growth factor/scatter factor
Hh	Hedgehog
HIF	Human intestinal fibroblasts
hMEC	Human microvascular endothelial cells
HPLC	High performance liquid chromatography
HPMEC	Human pulmonary microvascular endothelial cells
HUGO	Human genome organization
HUVEC	Human umbilical vein endothelial cells
i3S	Institute for research and innovation in health
IBEC	Institute for bioengineering of Catalonia
ICC	Immunocytochemistry
IFN	Interferon
Ig	Immunoglobulin
IL	Interleukin
ILC2	Group 2 innate lymphoid cells
IR	Infrared
ISC	Intestinal stem cell
ISX	Intestine specific homeobox
JAM	Junctional adhesion molecules
KGF	Keratinocyte growth factor
L/D	Live/Dead
LGR5	Leucine-rich repeat-containing G-protein coupled receptor 5
LPS	Lipopolysaccharide
M	Microfold

MCT	Monocarboxylate transporter
MDCK	Madin-Darby canine kidney
MDR1	Multidrug resistance 1
MHC	Major histocompatibility complex
MMP	Metalloproteinases
MRP	Multidrug resistance-associate protein
MTX	Methotrexate
MUC2	Mucin 2
NEAA	Non-essential amino acids
OAT	Organic anion transporter
OATP	Organic anion transporting polypeptide
OCT	Optimal cutting temperature
OCT	Organic cation transporter
OCTN	Organic/carnitine cation transporter
ON	Overnight
P-gp	P-glycoprotein
P_{app}	Apparent permeability
PB	Phosphate buffer
PBS	Phosphate buffered saline
PBST	PBS with 0.05% Tween-20
Pd	Palladium
PDFG	Platelet derived growth factor
PDL	Programmed death-ligand
PDMS	Poly(dimethylsiloxane)
P_{eff}	Effective permeability
PEG	Poly(ethylene glycol)
PEGDA	Poly(ethylene glycol) diacrylate
PEPT	Peptide transporter
PET	Polyethylene terephthalate
PFA	Paraformaldehyde
PHT	Peptide/histidine transporter
PLGA	Poly lactic-co-glycolic acid
PMAT	Plasma membrane monoamine transporter
PMMA	Polymethylmethacrylate
pNPP	p-nitrophenyl phosphate
PP	Peyer’s patches

PSA	Pressure sensitive adhesives
PSC	Pluripotent stem cell
PWB	Primary working buffer
PXR	Pregnane X receptor
RFU	Relative fluorescence units
Rho 123	Rhodamine 123
RT	Room temperature
SD	Standard deviation
SDS	Sodium dodecyl sulfate
SEM	Scanning electron microscopy
SEM	Standard error deviation
SI	Sucrase isomaltase
SIS	Small intestine submucosa
SLA	Stereolithography
SLC	Solute carrier
SLCO	Solute carrier organic
SMA	Smooth muscle actin
SWB	Secondary working buffer
TEER	Transepithelial electrical resistance
TFF	Trefoil factors
TGF	Transforming growth factor
TIMP	Tissue inhibitor of metalloproteinases
TJ	Tight junction
TNF	Tumor necrosis factor
UFLC	Ultra-fast liquid chromatography
UV	Ultraviolet
Vil1	Villin 1
ZO	Zona occludens

CHAPTER 1 – Literature review

This chapter contains information based on the following papers and books chapters:

- **Macedo M.H.**, Baião A., Pinto S., Barros A.S., Almeida H., Almeida A., das Neves J., Sarmento B., 2021, Mucus-producing 3D cell culture models, *submitted*.

In this review paper, I was responsible for the conception of the manuscript and execution of the introduction, potential and limitations, conclusion and gastric and intestinal models' section. Ana Baião was responsible for ocular and endometrial models' section, Soraia Pinto was responsible for the buccal and half of the nasal models' section, Andreia Sofia Barros was responsible for half of the nasal and lung models' sections, Helena Almeida and José das Neves were responsible for the overview of mucus section and Andreia Almeida was responsible for half of the lung models' section. All authors were responsible for reviewing the manuscript and Bruno Sarmento was responsible for submitting it. This review was not previously included in other thesis and it is partially reproduced in this section.

- Almeida A.*, Azevedo C.*, **Macedo M.H.*** & Sarmento B., 2020, 3D intestinal models towards a more realistic permeability screening, in *Nanotechnology for Oral Drug Delivery* (389-417), Academic Press. (*equal contribution)

In this book chapter, I was responsible for the conception and execution of the multilayered models' section. Andreia Almeida was responsible for the organoids' section and Claudia Azevedo for the gut-on-a-chip's section. The rest of the book chapter was written and revised by all of us. Bruno Sarmento was responsible for reviewing and submitting the manuscript. This book chapter was previously included in the thesis of Cláudia Azevedo and it is partially reproduced in this section.

- **Macedo M.H.**, Araújo F., Martínez E., Barrias C.C., Sarmento B., 2018, iPSC-Derived Enterocyte-like Cells for Drug Absorption and Metabolism Studies, Trends in Molecular Medicine, 24(8): 696-708.

In this review paper, I was responsible for the conception, execution and revision of the manuscript. Francisca Araújo, Elena Martinez and Cristina Barrias revised the manuscript and Bruno Sarmento was responsible for reviewing and submitting the manuscript. This review was not previously included in other thesis and it is partially reproduced in this section.

1.1. The digestive system

The digestive system is composed by the mouth or oral cavity, pharynx or throat, esophagus, stomach, small intestine (with the liver, gallbladder and pancreas as major accessory glands), large intestine and anus. Its main function is to obtain essential nutrients from ingested food. In order to obtain such nutrients, the digestive system performs a myriad of functions, including ingestion, mastication, propulsion, mixing, secretion, digestion, absorption and elimination. Four layers are present in all tissues of the organs that compose the gastrointestinal (GI) tract, from the esophagus to the anus. The innermost layer is the mucosa, which is composed by three sub-layers: the mucous epithelium, the lamina propria and the muscularis mucosae. The submucosa is a layer of thick connective tissue, beneath the mucosa, that contains nerves, blood vessels and small glands. The muscularis, in its turn, is composed of an inner layer of circular smooth muscle and an outer layer of longitudinal smooth muscle. The last layer is the serosa or adventitia, a connective tissue layer [1]. After crossing the first portions of the digestive system, compounds reach the stomach, where an acidic environment is found, with a pH ranging from 1.5 to 3.5, and enzymes responsible for digesting food are present and absorption starts to occur [2]. After overpassing the stomach, the content goes to the small intestine, which is a major site for absorption [3].

1.2. The small intestine

Absorption mostly occur in the small intestine, the major site for the absorption of nutrients, water, electrolytes and xenobiotics [4].

In adults it is 6 meters long and composed by three different parts [1]. First, connecting from the stomach, is the duodenum, which has the liver and pancreas associated to it and is about 25 cm long. It is followed by the jejunum, which is about 2.5 meters long and ends with the ileum, that has a length of around 3.5 meters [1].

1.2.1. Duodenum

The duodenum has several modifications on its surface to increase the area and allow a more efficient digestion and absorption process. These modifications are protuberances called villi, which have 0.5-1.5 mm in length. Each villus is covered by a simple columnar epithelium, containing a blood capillary network and a lymphatic capillary called lacteal. The absorptive cells present on the villi have, in their turn, microvilli of around 1 μm long that further increase the surface area. The combined microvilli on the entire epithelial apical surface form the brush border [1]. The duodenum has a pivotal role in mixing the digestive juices that come from the liver and pancreas with food [5].

1.2.2. Jejunum and ileum

The jejunum and ileum are similar in structure to the duodenum, with the difference that a gradual decrease in the tube diameter, the thickness of the wall, the number of circular folds and the number of villi occurs with progression in length, and folds are completely absent in the terminal ileum. The duodenum and jejunum are the major sites for nutrient absorption, although there is some absorption also occurring in the ileum. Lymph nodules called Peyer's patches (PP) are numerous in the mucosa and submucosa of the ileum, being that in a young adult, the human small intestine harbors more than 200 PP [1, 5]. PPs are equipped with the luminal antigen sampling machinery and form germinal centers (GCs) in response to food-derived antigens and commensal microorganisms taken up by microfold (M) cells [6, 7].

1.2.3. Intestinal Epithelium

The intestinal epithelium is composed by a single cell layer constituted by polarized and specialized epithelial cells that renew every 3-5 days [8]. Cell proliferation, differentiation and apoptosis mechanisms occur in an orderly fashion along the crypt-villus axis [9]. Epithelial cells are produced in the crypts of Lieberkühn by intestinal stem cells (ISCs) that differentiate and migrate up the villi, covering it and eventually shedding [8, 10]. ISCs promote vigorous self-renewal of the intestinal epithelium, which allows the small intestine to maintain its integrity and function [5, 11, 12]. In this sense, the crypt is mainly a proliferative compartment composed by multipotent stem cells, whereas the villi are seen as a differentiated compartment, with different types of cells that come from the multiple crypts [13, 14].

1.2.3.1. Absorptive cells

The enterocytes are columnar and polarized cells that make about 80% of the epithelial population and are key players in the intestine, having a role in the digestive, metabolic and barrier functions. The fact that they present an apical brush border is relevant in the absorption process [15]. They also play a role in immunity, expressing receptors involved in the innate immune response, acting as non-professional antigen-presenting cells, and releasing cytokines and chemokines, thus being involved in the recruitment and activation of leukocytes and regulating local immune responses [8, 16].

1.2.3.2. Secretory cells

Goblet cells secrete protective mucins and trefoil factors (TFF), which protect the epithelium against stress, chemical damage and microbial infections from bacteria [12, 17]. Mucins, together with other components, form mucus, which acts as a protective layer, serving as a first barrier to the luminal content and having an impact in the absorption process. It is also crucial for the maintenance of intestinal homeostasis [18]. Mucus properties and functions vary along the GI tract, but this topic will be addressed in more detail later in the introduction.

Paneth cells have a function in innate immunity and are the only differentiated cells that reside at the crypts, together with the undifferentiated population of ISCs. They contain secretory granules that harbor lysozymes, antimicrobial proteins (AMPs) and defensins that support ISCs [19, 20]. The antimicrobial peptides secreted by these cells establish a chemical barrier that protects intestinal tissue against bacterial invasion [6].

Enteroendocrine cells are present in a smaller number but are a diverse population of cell types that secrete hormones that can regulate satiety, motility, absorption, tissue repair, angiogenesis and enterocyte differentiation and polarization, among others [21, 22]. They express chemoreceptors on the apical side, enabling the detection of luminal substances [6, 23].

1.2.3.3. Tuft cells

Tuft cells are chemosensory and are pivotal in the organism defense, mainly against helminths [24]. They make up a small fraction of intestinal epithelial cells, but are able to expand when the tissue is infected by these parasites. When infection occurs, tuft cells secrete large amounts of interleukin (IL)-25, which is a key cytokine for the clearance of the parasites and, at the same time, acts as indirect feedback for tuft cells to expand. These characteristics make tuft cells critical sentinels in the gut epithelium, promoting type 2 immunity by activating tissue-resident group 2 innate lymphoid cells (ILC2s), which, in their turn, secrete IL-13 to promote ISCs self-renewal and goblet and tuft cell differentiation [6, 25-27].

1.2.3.4. Microfold cells

Microfold (M) cells are located in the follicle-associated epithelium (FAE) and are responsible for particulate antigen uptake in gut-associated lymphoid tissues (GALT), playing a pivotal role in immune surveillance on the mucosal surface [6, 28]. They have a unique morphology, lacking microvilli on their apical plasmatic membrane, contrary to enterocytes, presenting instead short fold-like structures or “microfolds” [29]. Besides, their basal plasma membrane possesses a deep invagination and forms a large sac-like structure regarded as the “M-cell pocket”, which facilitates the delivery of luminal agents to mononuclear phagocytes, such as macrophages and dendritic cells. They are highly active in phagocytosis and transcytosis, taking up luminal bacteria and antigens and presenting them to the cells in the M-cell pocket to initiate the immune response [6, 29]. M-cells play a critical role in the maturation of PPs and are critical for the development of mucosal immunoglobulin (Ig)A responses [6].

1.2.4. Lamina propria

The lamina propria is a layer of connective tissue that contains structural collagens, glycoproteins, chondroitin sulphate proteoglycans, hyaluronic acid and ground substance, producing a matrix that supports the epithelium [5, 30]. The lamina propria is localized underneath the epithelium and is highly vascularized, in order to maximize the possibility of molecules to reach systemic circulation through the mesenteric vessels. The blood and lymph capillaries are situated next to the epithelial surface, especially in the villi. To promote the absorption of substances, the lamina propria is able to undulate and dynamically mix the contents [5, 12]. Different types of cells are present in the lamina propria, such as different phenotypes of fibroblasts (non-contractile fibroblasts, contractile myofibroblasts and the protomyofibroblasts intermediate phenotype), mesenchymal stem cells, smooth muscle cells (of the muscularis mucosae or associated with the lymphatic lacteals), pericytes of the capillaries (also termed mural cells or vascular smooth muscle cells), white blood cells and endothelial cells (Figure 1.1) [31, 32]. The non-white-blood-cells and nonendothelial mesenchymal elements of the intestinal lamina propria share identical marker molecules, origins and have coordinated biological functions [32]. The stromal cells of the intestinal lamina propria are part of the mucosal immune system, displaying receptors and surface markers such as major histocompatibility complex (MHC) class II costimulatory (Cluster of differentiation (CD) 80 and 86) and inhibitory (programmed death-ligand (PD-L) 1 and 2) molecules, which are used by professional immune cells. These cells can exert either an immunostimulatory or immunosuppressive influence, depending on the microenvironment during the interaction with the immune cells [32].

The intestinal lamina propria is the most plastic tissue in the body, where degradation and repair of the ECM must be tightly controlled [30].

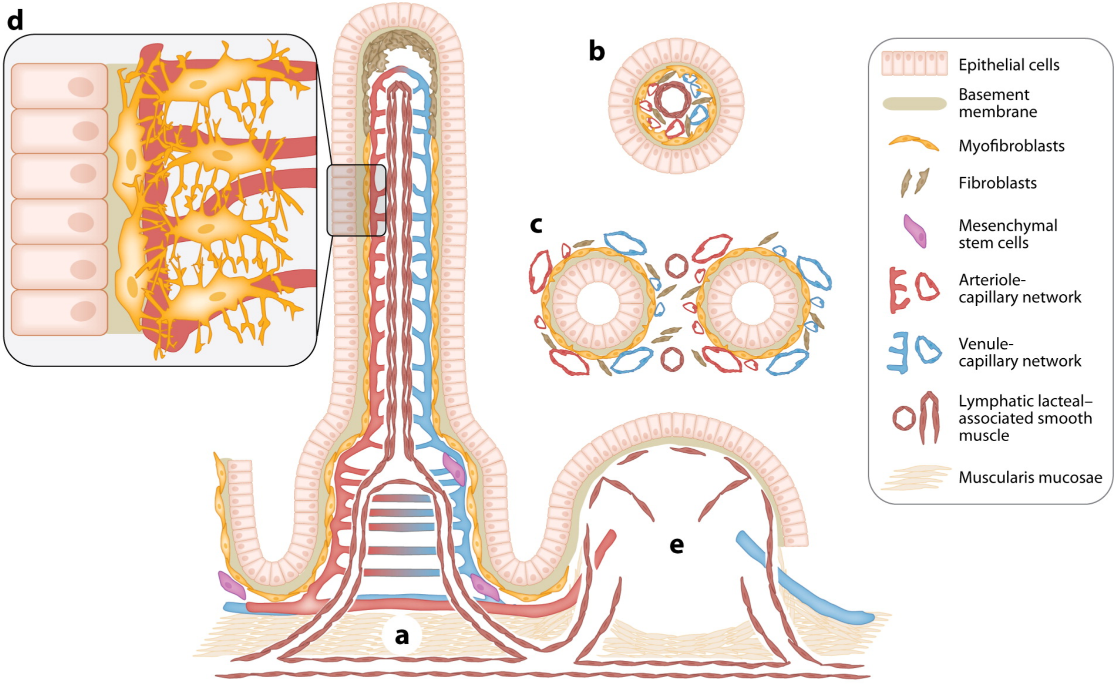

Powell DW, et al. 2011.
Annu. Rev. Physiol. 73:213–37

Figure 1.1 - The spatial relationships of the epithelium and mesenchymal elements of the small intestinal villus-crypt axis. (a) Longitudinal representation of the villus and crypt showing the epithelium and lamina propria containing subepithelial myofibroblasts and pericytes of the capillaries, mesenchymal stem cells, and smooth muscle associated with the lymphatic lacteal and the muscularis mucosae. Fibroblasts are shown, especially in the upper portion of the villus. (b) Cross sections through a villus show the lymphatic lacteal with associated smooth muscle. (c) A cross section through the crypts demonstrates the lymphatic pericytes. Panels b and c also show that the subepithelial myofibroblasts are essentially pericytes in subepithelial locations of the villus. (d) A higher-power depiction of the myofibroblasts and pericytes with cytoplasmic processes that surround and support the capillaries. (e) A Peyer's patch with its vascular, lymphatic, and stromal elements. Lymphocytes, macrophages, dendritic cells, and polymorphonuclear leukocytes are not shown. Reprinted from [31] with permission from Annual Reviews, Inc. (2011).

1.3. Epithelial-mesenchymal crosstalk

In the small intestine, as in most tissues, the intestinal epithelium is supported by a basement membrane (BM) that separates the epithelial cells from the lamina propria and the cells that inhabit it [33]. Nevertheless, although this separation exists, it is well established that the mesenchymal elements present in the lamina propria (fibroblasts, myofibroblasts, muscle cells, immune cells and microvascular endothelial cells) promote the epithelial-mesenchymal crosstalk (bidirectional instructive signals) [30, 34]. This crosstalk occurs during development and into adulthood, and shape the functions and architecture of the small intestine, being key to maintain cell functions, polarity, behavior and differentiation, and also contributing to the preservation of the stem cell niche and tissue homeostasis [35-38]. Crosstalk takes place because cells within a tissue interact with neighboring cells and the extracellular matrix (ECM) through biochemical and mechanical cues [38, 39]. The cellular context also plays a crucial role in the cell life cycle, in events like proliferation, migration and apoptosis [40].

Mesenchymal cells express important growth factors whose receptors can be found in the surface of epithelial cells, as the hepatocyte growth factor/scatter factor (HGF/SF[4]) and the keratinocyte growth factor (KGF), which regulate epithelial cell behavior. Besides, mesenchymal cells have an active participation in the formation of the BM and the expression and localization of some BM molecules, such as laminins, type IV collagen, nidogen and perlecan have been implicated in morphogenic events during developmental states or the proliferation and differentiation in the adult organ [36].

However, mesenchymal-epithelial crosstalk is not unidirectional and epithelial cells also provide signals to the stroma [41]. The hedgehog (Hh) signaling pathway plays a crucial role in epithelial-mesenchymal interactions during development. *In vivo* studies with transgenic mice have demonstrated that a reduction in production of Hh proteins by the epithelium leads to a depletion of stromal cells such as myofibroblasts, villus smooth muscle and muscularis mucosae cells, resulting in the expansion of the epithelial proliferative compartment [32, 42].

The myofibroblasts and muscularis mucosae cells, together with the epithelial cells, contribute to build the stem cell niche, both in normal tissue and during pathogenesis, through complex interactions involving different signaling pathways as Wnt, bone morphogenic protein (BMP) and Hh [32].

1.4. Intestinal absorption

The rate of transport across the small intestine is proportional to its surface area, which is vast due to the presence of mucosal folds, villi and microvilli, which makes it an organ well-adapted for absorption [5]. Nevertheless, there are barriers to the transport from the intestinal lumen to the blood. The mucosa produces secretions that contain mainly mucus, electrolytes and water and that have the function of lubricating and protecting the intestinal wall from the acidic digestive enzymes, but also pose a barrier to absorption [43]. Besides, the cell itself and the basement membrane also present a barrier. For a substance to be absorbed into the blood or lymph it has to cross the enterocytes, being transported across the luminal and basolateral membranes and, to be transported into the blood it needs to cross the membranes of the endothelial cells of the capillaries [5]. Some substances are absorbed into the blood capillaries, whether others are absorbed into the lacteal, being that size and lipid solubility are determining properties for this. Large molecules, particles and lipid-soluble substances are normally transported into the lymph, while small, water-soluble substances go to the blood. However, in each villus there is a broad network of capillaries but only one lacteal, which makes the surface area available for transport in to the blood much larger. Furthermore, blood flow is much greater than lymph flow [5].

1.4.1. Mucus

Mucus is a highly hydrated viscoelastic gel present at the epithelial surface of mucosae. It plays an important role in the protection against external insults of either physical, chemical or microbiological nature [44]. Mucus thickness in the small intestine is about few tens of micrometers, with discrete discontinuity sites being observed (e.g., at PPs), thus facilitating molecular exchanges between tissue and lumen, as well as immune surveillance by immune cells [45, 46].

Secretory mucins are the main building blocks of mucus. These glycoproteins undergo physical entanglement and establish non-covalent and covalent intra- and inter-molecular bonding responsible for the formation of a three-dimensional (3D) mesh structure [47]. Transmembrane mucins forming the glycocalyx serve as docking points between the latter and the underlying epithelium. Besides secretory mucins, other typical components of mucus include inorganic electrolytes (important in maintaining pH and iso-osmolarity), lipids, proteins (including immunoglobulins, enzymes, and antimicrobial peptides) and DNA, as well as cells and cellular debris, which collectively contribute to the viscoelastic properties of mucus [48, 49]. Small intestine mucus is rich in MUC2 and MUC6 (1-4% in total), playing an important role as a selective barrier that favors nutrient absorption while excluding toxins and pathogens [50-53].

1.4.1.1. Influence of mucus in intestinal absorption

Mucus can act as an important and selective barrier to absorption. Mucin concentration and overall organization are key factors dictating the average size of formed aqueous pores within the fiber mesh, thus establishing a cut-off threshold for how large molecules and supramolecular structures can be in order to be transported across mucus. Apart from steric hindrance, the physicochemical nature of mucin fibers allows the establishment of multiple low-affinity interactions with molecules or supra-molecular structures that fit the aqueous interstitial spaces [44]. These typically hydrophobic or electrostatic interactions are weak and reversible, but collectively strong enough to delay transport or even render immobilization within mucus. Such phenomena lead to constraints in distribution along the mucosal lumen [54]. On top of that, shedding/secretion dynamics of mucus contribute to mucosal clearance, thus setting a restricted time frame within which luminal-to-epithelial transport can occur [55, 56].

1.4.2. Intestinal transport mechanisms

The intestinal mucosa presents two main pathways to absorb nutrients and fluids. The paracellular path, where substances can pass through the tight junctions (TJs) of adjacent cells, through the intercellular spaces and the transcellular path, in which the substances must cross the apical cell border, enter the cell and then exit across the basolateral border.

1.4.2.1. Tight junctions and the paracellular pathway

The paracellular pathway is associated with the charge- and size-selective transport of materials through the space between the intestinal epithelial cells [57]. TJs are intercellular junctions that connect individual cells and are paramount in defining the characteristics of the paracellular barrier and its selectivity [43]. Throughout the GI tract, the specific characteristics of epithelial barriers present variability, according to each organ’s transport functions. The characteristics of the selectively permeable TJ barrier vary among different tissues and within different cell types composing a single tissue.

1.4.2.1.1. The importance of tight junctions

TJs function as a barrier, being capable of controlling the passage of ions, solutes, water and cells through the intercellular space, and act also as a fence, dividing the apical from the basolateral domain of the cell [58]. These characteristics are essential to prevent foreign substances and pathogens to invade the internal tissues and to facilitate the exchange of substances [59]. A disruption of the barrier leads to a loss of normal transport and inflammation [43]. The integrity of the barrier is often measured as the transepithelial electrical resistance (TEER) and the permeability to certain paracellular markers, such as mannitol and dextran. TEER correlates with the ability to separate ionic charge across the epithelia, which is reflected in a transepithelial electrical potential difference or the current that creates the potential, measured experimentally as the short circuit current. TJs are the most apical part of the apical junction complex, also composed by adherens junctions (AJs), that are involved in cell-cell adhesion and intracellular signaling. The apical junction complex, together with desmosomes (DMs) - involved in cell-cell adhesion, and gap junctions (GJs) - involved in intracellular communication, are fundamental to the maintenance of cellular polarity [43, 59, 60] (Figure 1.2).

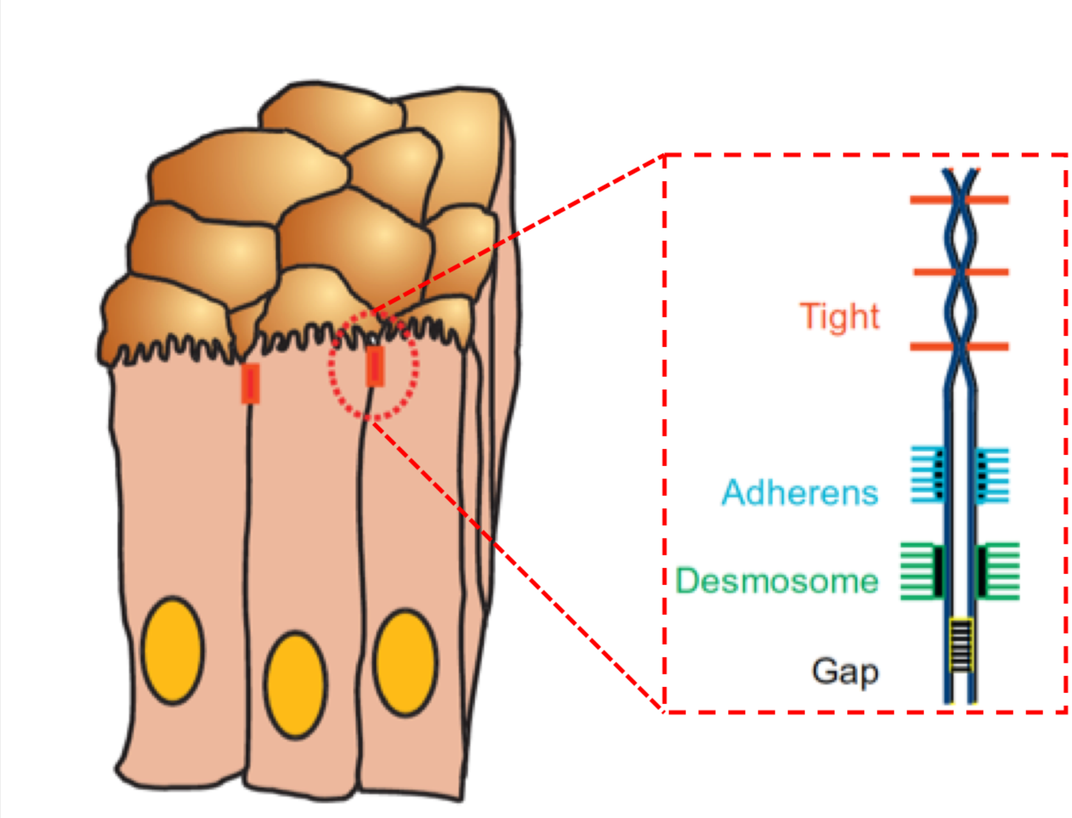

Figure 1.2 – Junction types within the apical junction complex between intestinal epithelial cells. Two columnar epithelial cells with apical brush border typical of the small intestine. A thick band of perijunctional actin and myosin filaments connected to the tight and adherens junctions are typical of intestinal epithelial cells. The "terminal bar" or apical junction complex when amplified reveals a series of intercellular contacts including the tight and adherens junctions, desmosomes, and gap junctions. Tight and adherens junctions are linked to the actin cytoskeleton and desmosomes to intermediate filaments. Reprinted from [42] with permission from Elsevier.

TJ maintenance of intestinal epithelial barrier integrity is also essential to confer protection against stress stimuli related to inflammation and infection. Alterations in TJs homeostasis, which can occur due to a variety of events, such as exposure to proinflammatory cytokines, such as Interferon (IFN)-γ and tumor necrosis factor (TNF)- α, pathogenic bacteria, lipopolysaccharides (LPS) and pathological conditions such as celiac disease and intestinal ischemia leads to intestinal barrier disruption [57, 61, 62]. In fact, TJs coordinate various signaling and trafficking molecules that regulate cell differentiation, proliferation and polarity, which are critical for epithelial and endothelial cell sheets to establish distinct compartments within the body, maintaining homeostasis. Moreover, disturbances of TJs may contribute to a variety of pathological conditions such as infections, cancers, and inflammatory bowel disease, among others [57].

The passage of orally delivered hydrophilic compounds through the intestinal epithelium is normally a rate-limiting step in the absorption process, since this transport is most likely to occur by passive diffusion through the paracellular pathway. These drugs are slowly and incompletely absorbed, since they distribute poorly into cell membranes. Tight junctions can hinder the passage of such compounds. Thus, the co-administration of absorption enhancers can be an effective way to increase the bioavailability of these compounds [63-65].

Epithelia are normally classified as “tight” or “leaky”, based on the overall electrical resistance [43]. The TJs of the small intestine tend to be leaky, while those of the large intestine tend to be tight and impermeable [66].

TJs are generated by the assembly of multiple proteins that are located near the apical end of the cells and their expression in the intestinal tract is tissue and age specific [62]. They form two functional categories: the integral transmembrane proteins, which form a network between adjacent cell membranes, and the peripheral membrane proteins. The interaction between these two categories of proteins and the arrangement of actin are paramount for the regulation of TJs integrity. Occludins, claudins, junctional adhesion molecules (JAMs) and tricellulin are integral transmembrane proteins. Zona Occludens (ZO) 1, 2 and 3 and cingulin are peripheral membrane adaptor proteins and act as bridges to connect integral membrane proteins to the actin cytoskeleton and to other signaling proteins, being vital to the maintenance of TJ structure and permiting the cytoskeletal regulation of TJ barrier integrity (Figure 1.3) [62, 67, 68].

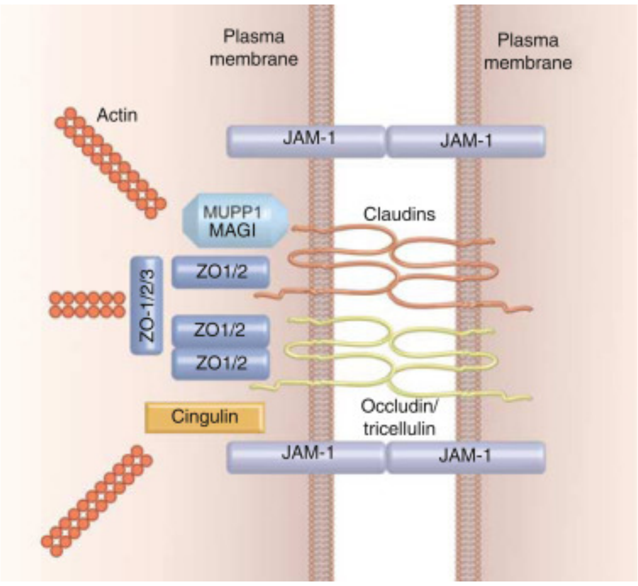

Figure 1.3 - Schematic representation of the basic structural transmembrane components of tight junctions. Reprinted from [69] with permission from Elsevier.

1.4.2.1.1.1. Zona Occludens

ZO-1, -2, and -3 are scaffolding peripheral proteins that recruit various types of proteins to the cytoplasmic surface of the junctions, contributing to the so called “junction plaque” [70]. ZO proteins interact with most of the transmembrane TJs proteins directly (Figure 1.4). However, they do not localize specifically in the TJs [71]. ZO associate with both cadherin-based AJs and with GJs, pointing towards a general role of ZO proteins in intercellular adhesion and communication [72-75]. The most important function of ZO proteins is the regulation of claudin polymerization at the junctional site in epithelial cells [76]. However, ZO proteins functions are not only related to the structural barrier mechanisms, but they also play a role in signal transduction and transcriptional modulation [70].

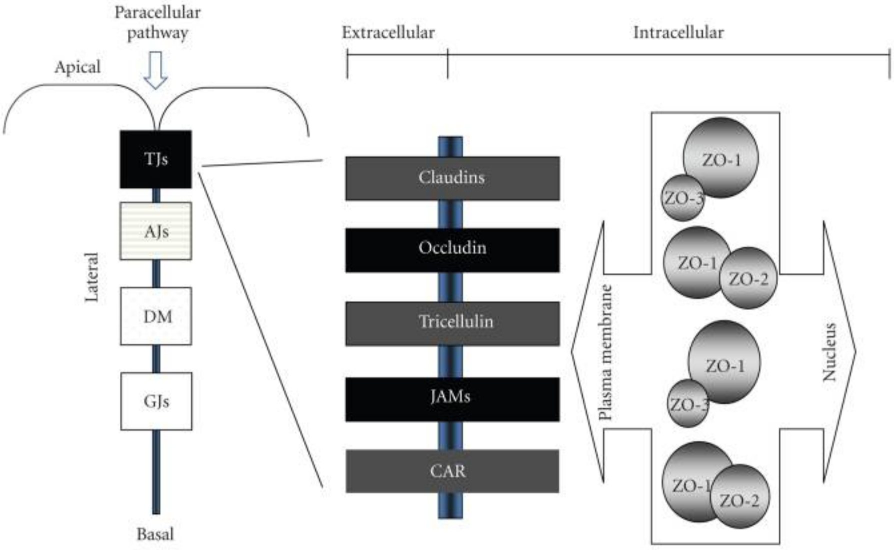

Figure 1.4 - Localization of ZO proteins at TJs. Transmembrane components of TJs interact at least with one ZO protein. Only ZO-1 and ZO-2 localize to the nucleus, while nuclear targeting of ZO-3 has not been observed so far. Interactions of ZO proteins with other types of junctions is not included here. CAR: coxsackievirus and adenovirus receptor. Reprinted from [68] under Creative Commons Attribution License.

1.4.2.1.1.2. Claudins

The discovery of claudins in 1998 was very important to advance the knowledge regarding the TJ barrier. Claudins have the ability to form strands, consisting of four transmembrane domains, two extracellular loops, a C-terminal cytoplasmic domain and conferring cell-to-cell adhesion [62, 77]. The claudin family consists of 24 members, both in humans and mice, and different expression patterns are exhibited depending of the tissue and cell type [78]. Claudins bind directly to PDZ domain-containing peripheral membrane proteins such as ZO, through a PDZ-binding motif at their C-terminus [79]. Claudins are the major determinants of the barrier function of tight junctions and define paracellular flux of small solutes, including ions and water. Intestinal claudins form two different classes: sealing and pore-forming [80]. If the expression of sealing proteins is increased, this results in a tighter barrier, which restricts the movement of luminal contents through the paracellular route. Claudins-1, -3, -4, -5, -8, -11, -14, 18, and -19 are sealing proteins. On the other hand, if pore-forming proteins have an increased expression, the selectivity for contents that can pass between the cells is reduced, which increases paracellular permeability, like it is the case of claudins-2, -10a/-10b, -15, -16, and -17 [57, 81]. Pore-forming claudins have an ionic charge specificity for cations or anions as well as ionic size selectivity, which increases the permeability for ions based on claudin-specific permeability characteristics [57]. For example, claudin-2 forms pores that are permeable to small cations and water and are size selective, while claudin-15 has two negatively charged residues whose substitution by positive ones converts this protein from cation to anion permissive [78, 82-84].

Claudins-2, -3, -4, -7, -8, -12 and -15 are richly expressed in the duodenum, jejunum, ileum and/or colon, and their expression varies throughout the different segments (Figure 1.5) [85-87]. Claudins play a critical role in the barrier formation and in the paracellular permeable selectivity. For example, it was observed that claudin-1 knockout mice died within 24 hours of birth because of increased fluid and electrolyte loss through the epidermal barrier [68, 88].

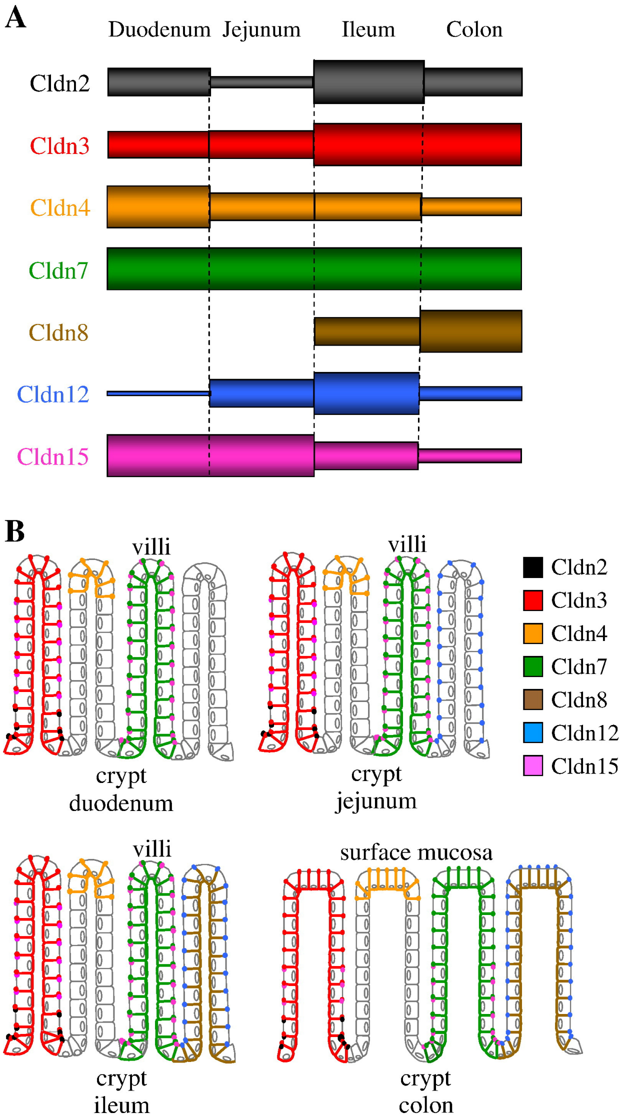

Figure 1.5 - Differential expression and subcellular localization of claudins along the mouse intestine. Relative expression levels (A) and schematic distribution (B) of Cldn2, Cldn3, Cldn4, Cldn7, Cldn8, Cldn12 and Cldn15 in the duodenum, jejunum, ileum and colon are summarized. (A) Bar height represents the expression level. (B) The colors represent the same claudins as in panel A. Colored dots and lines correspond to localization at tight

junctions and basolateral membranes, respectively. Reprinted from [76] with permission from Elsevier.

1.4.2.1.1.3. Occludins

Although there is no sequence homology between occludins and claudins, the occludin family also presents four transmembrane domains and two extracellular loops that construct TJ strands and N- and C-terminal cytoplasmic domains. ZO proteins interact with the long C-terminal domain, making the link between occludin and the actin cytoskeleton [68, 89]. It is believed that occludin is important in the assembly and maintenance of TJs, being highly expressed at cell-cell contact sites [62]. Studies have shown that that knockdown of occludin leads to an increase in the paracellular permeability to macromolecules, indicating that this protein plays an important role in the assembly and maintenance of TJs [1, 84]. Besides, occludin knockout mice showed inflammation and hyperplasia of the gastric mucosa, brain calcification, testicular atrophy, among other retardations in different organs, suggesting an unexpected role of occludin [78, 90].

1.4.2.1.1.4. JAM family

The JAM family belongs to the Ig superfamily and consists of two extracellular Ig domains, one transmembrane domain and a C-terminal cytoplasmic domain [91, 92]. This family is divided into two subgroups based on their sequence similarities. JAM-A, JAM-B and JAM-C have a class II PDZ domain-binding motif at their C-terminal ends, interacting directly with ZO-1 [93-95]. On the other hand, coxsackie and adenovirus receptor (CAR), endothelial cell-selective adhesion molecule (ESAM) and JAM-4 are members of the second subgroup and contain a class I PDZ domain-binding motif at their C-terminus [78].

JAM family members are expressed in different cell types, like epithelial, endothelial and immune cells, and exhibit different expression patterns depending on the tissue or cell. Since they are expressed in different cell types, they function as cell-cell adhesion molecules not only between the same type of cells but among different types through homophilic and heterophilic interactions [78]. In intestinal epithelial cells, JAM-A and JAM-4 are known to be expressed and involved in TJ regulation [68].

Moreover, JAM-A and coxsackie have been shown to regulate epithelial barrier function since its expression leads to a reduction in paracellular permeability, being also implicated in TJ assembly [60].

1.4.2.2. Drug transporters and the transcellular pathway

Transcellular transport involves the transfer of a solute through a cell. The transcellular pathway includes transcellular diffusion, active carrier mediated transport and transcytosis. The transcellular diffusion simply involves the movement of solutes based on a diffusion gradient moving from areas of high to low concentration. However, the cell membrane does not allow the passive diffusion of charged, hydrophilic or zwitterion molecules. Active transport involves the use of energy to transport specific substances across barriers, even against the concentration gradient [5].

Most approved drugs, which are rapidly and completely absorbed after oral administration, are transported by the passive transcellular route. They are generally lipophilic and distribute readily into the cell membranes of the intestinal epithelium [64].

Some hydrophilic drugs, whose chemical structure resembles those of nutrients, can be transported by active carrier-mediated transport, being this transport often mediated partly by the carrier and partly by passive routes [5].

Membrane transporters are, thus, considered major determinants of the pharmacokinetics, safety and efficacy profiles of drugs [96]. Transporters are considered the gatekeepers for cells and organelles, since they are able to control the uptake and efflux of very important compounds, such as amino acids, sugars, inorganic ions and drugs [97, 98]. The expression of transporters in the intestine and in the liver is very important since they affect the amount of drug that can pass and reach systemic circulation after oral delivery and influence how much drug escapes first pass metabolism in both gut and liver [97, 99]. Membrane transporters are specifically expressed in the apical and/or basolateral membrane of cells, including the intestinal enterocytes (Figure 1.6) [97].

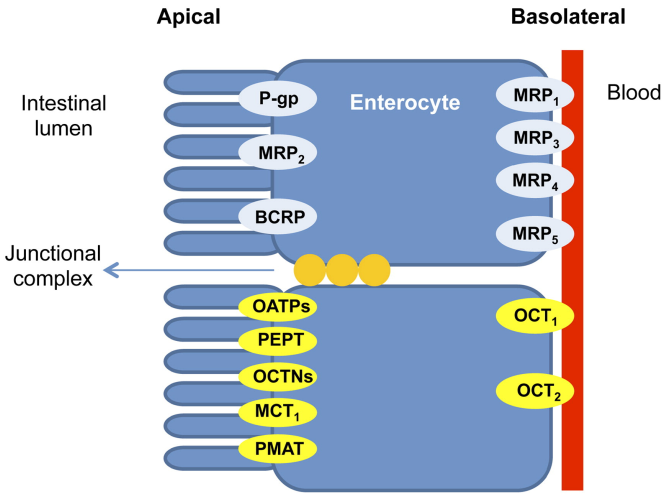

Figure 1.6 - Diagram of major drug transporters proteins expressed at the intestinal epithelia including intestinal uptake (yellow) and efflux (light blue) transporters. Multidrug

resistance protein (MDR1, P-glycoprotein), multidrug resistance associated protein (MRP), breast cancer resistance protein (BCRP), monocarboxylate transporter protein (MCT), peptide transporter protein (PEPT), organic anion transporting polypeptide (OATP), organic cation transporter (OCT), carnitine/organic cation transporter (OCTN), and plasma membrane monoamine transporter (PMAT). Reprinted from [94] with permission from Elsevier.

Different transporters have been identified in intestinal enterocytes, but not all of them are involved in the intestinal drug absorption process [97]. Transport across membrane transporters can be divided in two groups: (1) facilitated transport that uses the transporter which allows the passage of compounds across the membranes down their electrochemical gradients, without the need of energy expense and (2) active transport, which utilizes energy and is performed by active transport mechanisms that create ion/solute gradients across membranes [97].

Membrane transporters have been classified into two transporter superfamilies according to the guidelines of the Human Genome Organization (HUGO) Gene Nomenclature: group (1) are classified as solute carrier (SLC) and group (2) as adenosine triphosphate (ATP)-binding cassette (ABC) [98].

1.4.2.2.1. ABC transporters

The transporters P-glycoprotein (P-gp), multidrug resistance-associated protein 2 (MRP2) and breast cancer resistance protein (BCRP) from the ABC family are the most investigated transporters in the intestine. They are heavily expressed at the apical membrane of enterocytes, and they impair the intestinal absorption of many clinically prescribed drugs. Transporters of the ABC superfamily use ATP as energy source, which allows them to pump substrates against a concentration gradient. As they can pump compounds out of the cell, they are regarded as efflux transporters [97].

1.4.2.2.1.1. P-gp (ABCB1)

P-glycoprotein (P-gp) was the first clinically important drug transporter to be identified, in 1986 [100]. P-gp is encoded by the multidrug resistance 1 (MDR1) gene and it is the most studied efflux transporter in the intestine, possessing a broad substrate specificity, which enables the interaction with various types of molecules [97]. The apical localization of P-gp within the intestine is an ideal position to mediate the efflux of xenobiotics and toxins into the lumen. Nevertheless, this localization is also ideal to limit the oral absorption of compounds [97, 98]. Also, it contributes to the clearance of drugs that are administered intravenously by active secretion into the intestinal lumen [101].

1.4.2.2.1.2. MRP (ABCC)

Nine members of the multidrug resistance-associated protein (MRP) family have been already identified, although only MRPs 1 to 5 have demonstrated to have a well-defined role in drug transport [97]. MRP2 is present at the apical surface of enterocytes and acts as a barrier to drug absorption. On the other hand, MRP1, MRP3, MRP4 and MRP5 are expressed on the basolateral side and facilitate the entrance of compounds into circulation [102, 103].

1.4.2.2.1.2.1. MRP1 (ABCC1)

This transporter is localized at the basolateral membrane of enterocytes and is largely expressed in both small and large intestine [104]. This protein transports compounds from the cell to the interstitial fluid, acting as an absorptive transporter and preventing the accumulation of toxins in the enterocytes [105].

1.4.2.2.1.2.2. MRP2 (ABCC2)

MRP2 is localized on the apical side of enterocytes. Its expression in the rat small intestine has been shown to be mainly at the top of the villus, especially in the proximal jejunum [106]. This transporter is responsible for modulating the pharmacokinetics of many drugs. Certain compounds, toxins or disease states can alter its expression and activity [97, 107, 108]. MRP2 shows overlapping substrate specificity with P-gp, which in combination with their localization on the apical membrane of the duodenum and jejunum, proposes a combined function of the two transporters, which may act as an important barrier to the intestinal absorption of many drugs [97].

1.4.2.2.1.3. BCRP (ABCG2)

This transporter is a multidrug resistance protein expressed both at the small and large intestines, at the apical membrane [97, 109]. This protein is capable of transporting a highly diverse range of substrates, playing a major role, together with P-gp, at limiting drug absorption across the intestine. However, while P-gp generally only transports hydrophobic compounds, BCRP is able to transport hydrophobic compounds and hydrophilic conjugated organic anions [110]. There is also an overlap in the specificity of compounds between

BCRP and MRP2 that, as explained before for MPR2 and P-gp, can lead to a concerted effect of both transporters, limiting drug absorption [111].

1.4.2.2.2. SLC transporters

Members of the SLC and the solute carrier organic (SLCO) superfamilies are the major uptake transporters being involved in the transport of many substrates, such as aminoacids and peptides, vitamins, sugars, bile acids, neurotransmitters and xenobiotics [99].
Members of the SLC superfamily include proton dependent oligopeptide transporters [peptide transporter (PEPT) 1 and 2 and inorganic phosphate transporter (PHT) 1], organic anion transporters (OAT), organic cation transporters (OCT), nucleoside transporters [carbon nanotube (CNT) and equilibrative nucleoside transporter (ENT)], plasma membrane monoamine transporter (PMAT) and monocarboxylate transporters (MCT), which are considered pharmacokinetically important. The organic anion transporting polypeptides (OATP) comprise the SLCO family [97]. It is known that these uptake transporters use different porter mechanisms (uniporter, antiporter and symporter), although it has not been fully elucidated which mechanisms is used for each specific transporter. In addition, they can use chemiosmotic gradients created by translocation of ions across the membrane as energy source [97, 99].

1.4.2.2.2.1. Oligopeptide transporters (SLC15A)

Several peptide transporters are currently known, such as PEPT1 and 2 and PHT1 and 2. The human small intestine has been shown to express PEPT1, which is localized at the apical membrane of enterocytes, with increasing expression from duodenum to ileum [97, 99]. In order to be transported by PEPT1, compounds should present at least one peptide bond and a free terminal carboxyl group, which is the case of beta lactam antibiotics [97, 105]. PEPT1 has a high transport capacity but low affinity. This high transport capacity makes it very attractive as a drug target and strategies like the use of peptidomimetic drugs have been gaining popularity as therapeutic agents for the treatment of a myriad of diseases [112-114].

1.4.2.2.2.2. Organic cation transporter (SLC22A)

The organic cation/carnitine transporters 1 and 2 (OCTN1 and 2) are responsible for transporting carnitine and other organic cations and are expressed at the apical membrane of enterocytes [97].

On the other hand, OCT1 and 2 are localized in the basolateral membranes of enterocytes, mediating the basolateral uptake of relatively low molecular weight hydrophilic organic cations, into enterocytes [97, 115]. However, there are few studies describing the role of OCT transporters in the GIT, since most work regarding these transporters have been conducted in the kidney and liver [97, 115].

1.4.2.2.2.3. PMAT (SLC29)

High levels of PMAT mRNA expression at the apical membrane of polarized epithelial cells from the human intestinal tract have been identified [97]. This transporter is also expressed in other tissues like heart, pancreas, kidney, skeletal muscle and liver, but it is mostly expressed in the brain [116-118].

The PMAT transporter specifically transports monoamines and the specificity of its substrates and inhibitors broadly overlaps with that of OCTs [97, 119, 120].

1.4.2.2.2.4. MCT (SLC16A)

MCT1 is a transporter with low affinity and high capacity and it is known to play a role in intestinal drug absorption. This transporter is well characterized, being responsible for absorption of short chain fatty acids and is localized at the apical side of the small and large intestines [97, 113].

1.4.2.2.2.5. OATP (SLCO)

OATPs are mainly responsible for mediating the sodium independent transport of a diverse range of relatively high molecular weight amphiphilic organic compounds [96]. Almost all members of the OATP superfamily are localized in the apical membrane of polarized cells. While OATP1B1 and OATP1B3 are mainly expressed in the liver, OATP2B1 and OTP1A2 have been detected in the human small intestine, and have a role in drug absorption [97, 117, 121].

1.5. Predicting intestinal absorption *in vitro*

1.5.1. Two-dimensional (2D) models

The Caco-2 monolayer model is the most well-established in vitro intestinal model and is considered the “gold-standard” assay to predict intestinal absorption. Caco-2 cells were isolated from a human colon adenocarcinoma and are able to spontaneously differentiate into enterocyte-like cells at a confluent state, forming a polarized monolayer and expressing well-developed apical microvilli [122, 123]. These cells are able to express morphological and functional characteristics of absorptive intestinal cells, including the expression of enzymes such as disaccharidases and peptidases, typically expressed by enterocytes. The expression of multiple uptake and efflux transporters as also been identified in these cells [124].

However, Caco-2 cells present many differences when compared to the intestinal enterocytes, which can lead to misleading predictions of *in vivo* absorption via both the transcellular and paracellular pathways. Regarding drug transporters, expression patterns considerably differ. For example, the expression of P-gp and MRP2 in Caco-2 cells is considered to be much higher than in the human small intestine [125-127]. Maubon and colleagues [7] reported that the mRNA expression of MRP2 was higher in Caco-2 cells than in human small intestine, whereas the mRNA expression of BCRP was lower in Caco-2 cells. These results are similar to those obtained by Bruck and colleagues [25], who compared mRNA expression levels in Caco-2 with the human jejunum, and by Englund and colleagues [9], who observed 20-fold higher gene expression of BCRP in the human ileum than in Caco-2 cells. However, using two Caco-2 clones from different origins, differing mRNA expression of PEPT1 was observed by Maubon and colleagues. Relative mRNA expression was found to differ in the two analyzed Caco-2 cell clones by 4-fold [7]. Although one of the Caco-2 clones showed good correlation with the human small intestine, the other did not. Bruck and colleagues [25] observed lower mRNA expression of PEPT1 in Caco-2 clones compared to the human jejunum. Bruck and colleagues [25] also compared the protein and mRNA expression of drug transporters in Caco-2 cells and human jejunum. Importantly, the authors concluded that protein content and mRNA expression in Caco-2 cells did not correlate well. In addition, when comparing the protein expression in Caco-2 cells and human jejunal tissue, they observed that the expression of PEPT1, MRP2, and BCRP was similar in Caco-2 and human jejunum, whereas, P-gp had 2-fold higher expression in Caco-2. However, in a study by Vaessen and colleagues [26], the protein expression of MRP2 was significantly higher in Caco-2 cells than in human jejunum. On the other hand, expression of PEPT1 is considered to be lower in Caco-2 cells, and β-lactam antibiotics and ACE inhibitors, which are known substrates of dipeptide transporters, reveal poor permeability across the Caco-2 monolayers when, in turn, they are completely absorbed in vivo [128]. The Caco-2 model is capable of generating false negatives since drugs that are not absorbed in the model can be absorbed in the human small intestine [129]. The expression levels of drug-metabolizing enzymes in Caco-2 cells are very low, making it hard to predict drug-drug interactions. For example, the expression levels of cytochrome (CYP) P450 3A4, a very important drug metabolizing enzyme in the small intestine since it interacts with absorbed drugs in the enterocytes, are much lower in Caco-

2 cells, and pregnane X receptor (PXR), which is a nuclear receptor necessary for CYP3A4 induction, is expressed at very low levels in Caco-2, what makes hard to study CYP3A4 induction potency of drugs using this model [130, 131]. These cells also form tighter TJs than the ones present in human small intestine, which makes the permeability levels of hydrophilic drugs, that are absorbed via the paracellular route, considerably lower in these models [132]. In fact, the pore size of tight junctions in Caco-2 cells is estimated to be around 4.5 Å, where in the small intestine is around 8-13 Å [132, 133].

Along the years, other cell lines have been proposed as possible substitutes to be used in *in vitro* models and overcome the drawbacks posed by the Caco-2 cells. Among the alternatives, TC-7 cells, a subclone of the Caco-2 cell line, has been the second most-used cell type to predict intestinal permeability [134]. These cells are morphologically similar to Caco-2, presenting an apical brush border membrane with microvilli and forming a polarized cell monolayer with expression of TJs between adjacent cells [135]. One advantage of the TC-7 cell line is the presence of higher levels of CYP3A4 and 3A5, being useful to evaluate metabolic effects during transport. They also have greater homogeneity, ensuring more consistent results and are suitable to predict passive diffusion, like the parental cell line [135]. However, this cell line model has been shown to be unsuitable to study the intestinal absorption of poorly absorbed drugs, very lipophilic drugs and compounds in which transporter-mediated routes and/or first-pass metabolism are involved [136].

Cell lines from other origins than human have also been used to develop *in vitro* intestinal models in an attempt to overcome the disadvantages of the Caco-2 model. The Madin-Darby canine kidney (MDCK) epithelial cell line forms a superior model in terms of passive transport compared to Caco-2 because it has lower TEER values [129]. In the case of drugs that are absorbed passively this model presents a high correlation with the Caco-2 model. One advantage of these cells in relation to Caco-2 is their culture period (three days versus three weeks). However, their non-intestinal and non-human origin leads to different expression levels of some transporters, as in the case of ABC transporters, which expression is low in this cell line, as well as different metabolic activity levels [137, 138]. The intestinal epithelial cell line 2/4/A1, which originates from rat fetal intestinal epithelial cells, is ideal to test the permeability of paracellularly absorbed compounds because it has leakier pores, resembling more the human small intestine [139]. The TEER value in this cell line reached a plateau of 50 $\Omega.cm^2$, while in Caco-2 the plateau is reached at much higher values (150-400 $\Omega.cm^2$) [140]. This immortalized cell line is able to form differentiated monolayers with TJs, brush border membrane enzymes and transporter proteins [129]. However, despite the similarities with the human small intestine, these cells do not present active drug transport processes, which limits its use [141]. IEC-18 cells are also from rat small intestinal origin, derived from native ileal crypts. This cell line provides a size-selective barrier for paracellularly transported compounds [129]. These cells present similarities with the human small intestine in terms of electrical resistance, ability to differentiate into enterocyte-like cells, and permeability characteristics [142]. However, they also present some drawbacks related to the fact that they are less well differentiated than Caco-2 and as a result, some carrier-mediated transport is absent [143].

The HT29-MTX is a cell line that has its origin in human colorectal adenocarcinoma. This cell line was established by Lesuffleur and colleagues, growing the HT29 cell line in a medium containing 10^{-6} M methotrexate (MTX) [144]. This allows the cells to become mucus producing. These cells are normally combined with Caco-2 and this model better resembles the small intestine because HT29-MTX cells do not form TJs as tight as Caco-2, decreasing the overall tightness of the monolayer and leading to an increase in paracellular transport, more closely resembling the in vivo situation [145]. Moreover, HT29-MTX provides mucus to the model, which besides having the role of protecting the intestine from foreign threats, has an impact in drug absorption, acting as barrier and affecting the retention time of compounds in the intestinal epithelium, as already mentioned [146-148].

The addition of Raji B cells, a cell line originated from a human Burkitt's lymphoma, to the Caco-2 culture model has been reported to induce the M cell phenotype in these cells, by morphologically and functionally differentiate Caco-2 into cells with sparse and irregular microvilli and a high transcytotic activity [134, 149, 150]. The lymphocytes are added to the basolateral side of the Transwell® inserts 14 days after Caco-2 cells have been seeded. Although the lymphocytes are not in direct contact with the enterocytes, some epithelial cells demonstrate to develop the M-like phenotype [150]. The triple co-culture of Caco-2/HT29-MTX/Raji B has been achieved to better mimic the human intestinal epithelium, being the most complete 2D model [149, 151, 152].

1.5.2. Three dimensional (3D) models

3D models, although being a relatively recent topic, have been widely explored in the past years, since they can bring new insights and valuable knowledge when studying a specific organ. Regarding drug development, and specifically oral drug delivery, the need for an intestinal model that can better mimic the human small intestine is unquestionable, since models that are currently used to test the permeability potential of new formulations *in vitro* are very limited. In 2006 it was reported that if there was a 10% improvement in the preclinical screening methods used, this could reduce the costs of drug development by up to 100 million dollars per drug approved to reach the market [153, 154]. In fact, drug testing in 2D systems provides information that can often be misleading, since the way cells are grown in such substrates affects their pharmacological response, meaning that 3D multicellular models can help to bridge the gap between *in vitro* and *in vivo* experiments [155].

Actually, any cell cultured on a flat surface, like the Transwell® inserts membrane that are normally used for permeability assays, will never be able to fully replicate the *in vivo* situation. Cells *in vivo* are not flat, but are in a 3D configuration [153]. The components of the extracellular matrix (ECM) and the cell-to-cell and cell-to-matrix interactions are very important in cell behavior and, unfortunately, in 2D cultures these properties are lost [156]. In the case of the small intestine, its composition, functions and conditions make it a complex organ [157]. In this sense, is important to replicate a native-like 3D environment and build models that can better mimic the *in vivo* situation. Some work in this field has been developed in the last years, with promising results. Currently, there is a variety of 3D intestinal models, from the ones that are based on scaffolds or hydrogels, to decellularized tissue models, to more complex gut-on-a-chip models and organoids.

1.5.2.1. Multilayered models

Since the 3D support is so important for an accurate mimicry of the organ physiology, several researchers have been using 3D matrices to develop new intestinal models. These matrices are normally constituted by ECM components, being collagen the most widely used [126, 158-161]. The choice for collagen is justified by its low cost, the easiness in processing and the flexibility for live cell manipulation. The partial tunability of properties like pore size and stiffness is also a great advantage of this material [155]. Other materials, like alginate, Matrigel®, synthetic polymers and decellularized ECM are also used [125, 162-168]. In fact, the 3D environment that surrounds cells *in vivo* is extremely important in cell functioning. The mechanical properties of the substrate are dependent on its composition, architecture and degree of crosslinking, and these factors dictate how mechanical forces are transmitted to cells [169]. Cell adhesion and migration are also controlled by matrix composition, being that cells might be able to remodel it [169]. As so, it is important to take this into account when choosing what material to use in order to mimic an organ. The composition of the material, its mechanical characteristics and their impact on cells should be addressed and understood in order to replicate as much as possible the *in vivo* environment.

Intestinal models that consider the fact that the model should be a tridimensional structure, representing the different layers of the intestine, can be a promising strategy regarding intestinal models aimed to test the permeability of compounds.

Li *et al*. [126] developed a 3D intestinal model comprised of a collagen layer with embedded fibroblasts and immunocytes and with epithelial cells (Caco-2 and HT29-MTX) seeded on top. They were able to build a model with decreased expression of P-gp and increased expression of BCPR, which related more with *in vivo* levels, and the permeability correlation was also improved [126]. Pereira *et al.* [165] also developed a 3D intestinal model using Matrigel$^{®}$ with intestinal myofibroblasts embedded, and Caco-2 and HT29-MTX cells on top (Figure 1.7). The authors showed that fibroblasts were able to remodel the ECM by production of fibronectin, and the model allowed the efficient prediction of insulin absorption [165]. The downside of this model, in terms of reproducibility, is regarding the use of Matrigel$^{®}$, since the composition of this product is not completely defined and there is high batch-to-batch variation, which can be a problem when trying to reproduce the model, leading to results variability.

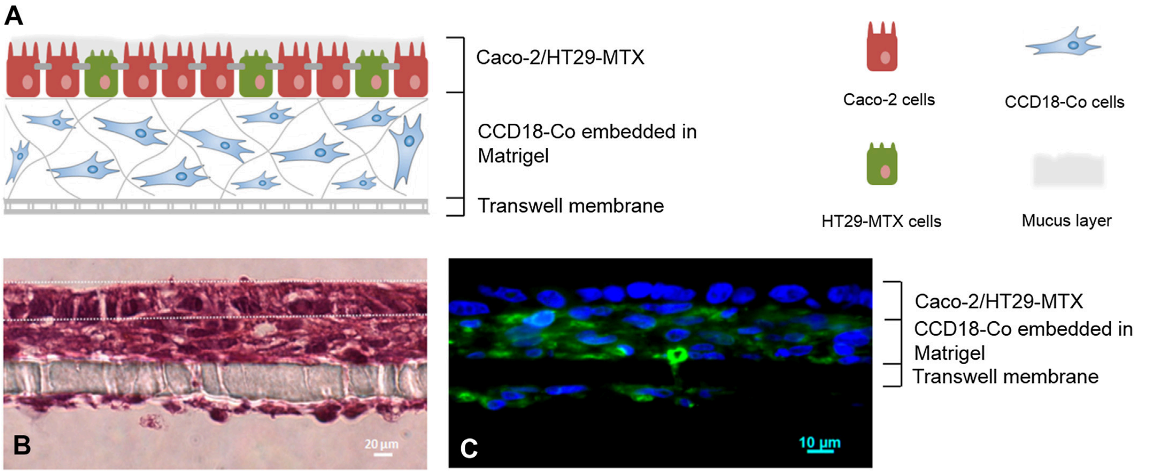

Figure 1.7 - (A) Schematic representation of the triple-culture 3D model. (B) Hematoxylin and eosin (H&E)-stained paraffin section showing myofibroblasts sustaining epithelial Caco-2 and HT29-MTX cells over them. (C) **Fibronectin** expression in a paraffin section of the triple-culture 3D model. Fibronectin was labeled with Alexa-Fluor® 488 (green) and nucleus with 4',6'-diamino-2-fenil-indol (DAPI). Reprinted from [159] with permission from Elsevier.

De Gregorio *et al.* [170] tested a collagen-based hydrogel and a cell-synthesized stromal equivalent. Authors claimed that Caco-2 cells were able to differentiate in all four types of intestinal epithelial cells and produced a higher quantity of basal lamina components like laminin, collagen type IV and hyaluronic acid when using the stromal equivalent, whereas fibroblasts were able to secrete more ECM components [170]. In a different approach, a model was developed using nanofibers, fabricated through electrospinning, to mimic the structure of the basement membrane [171]. This model presented lower TEER values, when comparing to the 2D Caco-2 model, being more similar to *ex vivo* porcine tissue. In terms of drug absorption, authors claimed this model more closely mimicked the native tissue in terms of predicting passive epithelial transport [171].

When considering the gastrointestinal tract, it is also important to understand that, in a disease state, the cellular environment can change and, consequently, this can have an impact in different processes, including absorption. Taking this into account, Leonard *et al.* [172] developed a 3D model to understand the impact of inflammation in the intestinal barrier. The model was composed by immunocytes and dendritic cells embedded in a collagen layer with Caco-2 cells seeded on top. Regarding the TEER values, authors observed that, upon stimulation of the cultures using IL-1ß, there was a decrease in the values to about 80% of the non-stimulated control values, which was similar to what was observed in the 2D Caco-2 monoculture model. It was also observed that the release of IL-8 protein into the medium in response to the stimulation was significantly higher in the 3D co-culture model in comparison to the Caco-2 2D monoculture. Regarding the 2D monoculture model, an increased permeability of the paracellularly transported dye fluorescein sodium in the state of inflammation was observed, which agrees with the decrease in the TEER values.

Beside the use of protein-based and/or synthetic hydrogels, another common practice is to use decellularized tissues to develop the *in vitro* models [125, 166]. Generally, these scaffolds are obtained using intestinal tissues from animals, normally from porcine origin. The fact that the tissues are obtained from species different from the human can be a disadvantage, because of cross-species differences. Pucsh *et al.* [166] co-cultured Caco-2 cells with primary human microvascular endothelial cells (hMECs) on decellularized porcine jejunal segments in a dynamic bioreactor. The authors concluded that Caco-2 cells resembled more the normal primary enterocytes when comparing to the static Caco-2 model. The permeability of substances that have a low permeability coefficient was also enhanced within the dynamic cultures [166]. Li and colleagues [125] also used decellularized porcine small intestine to seed Caco-2 cells, with the aim of obtaining a faster differentiation of these cells, comparing to the 21 days needed when they are seeded on Transwell® inserts. The authors verified that after 7 days, the characteristics of the cells were comparable to the 21-day Caco-2 cells, and that the permeability values of the tested compounds showed a strong correlation. However, the potential advantage is related to the time needed to obtain the model and not the model's performance itself. In another study, human small intestine microtissues were used in combination with human small intestinal epithelial cells and fibroblasts [173]. Authors were able to show that the model was capable of recapitulating the structural and physiological features of the human small intestine. In terms of permeability, the microtissues were able to discriminate between low and high permeability drugs, correlating better with human absorption data compared to Caco-2 cells and expressing drug transporters and metabolizing enzymes found on the human small intestine [173].

1.5.2.2. Models with intestinal architecture

While some authors do not give much importance to the architecture of the scaffold, using it merely as a 3D support that is more natural to the cells [126, 165], others build scaffolds with the intestinal villi and crypt architecture, claiming it has an effect on cell behavior and permeability of compounds [159, 161, 167]. It is true that *in vivo* architecture is very important when mimicking the small intestine, giving important cues for cells and altering their behavior *in vitro*, making them act more physiologically. There are several studies using scaffolds with villi architecture, where different techniques were used to obtain these structures.

A study by Sung *et al*. [167] describes a simple method to fabricate natural and synthetic hydrogels into 3D geometries with high aspect ratio and curvature. Authors were able to obtain villi structures mimicking the density and size of human intestinal villi, which is complex, without damaging them, combining laser ablation and sacrificial molding techniques that minimize the stress associated from separating the mold from the hydrogel structure [167]. After obtaining the structure, Caco-2 cells were seeded and cultured for three weeks and were able to cover the structures [167]. Later, Yi and colleagues [167] compared the absorptive and metabolic properties of Caco-2 cells cultured on the collagen villi scaffold from the previous work [167] with those in a 2D monolayer. The results obtained were quite promising, showing that the activity of the intestinal epithelial differentiation marker alkaline phosphatase (ALP) and CYP3A4 were increased. On the other hand, the activity of dipeptidase was lower than in the 2D monolayer control. The authors also tested the permeability of different compounds and observed a higher permeability in the 3D model, which correlated better to the *in vivo* situation [160]. Yu *et al*. [161] developed structures replicating the shape and size of human small intestinal villi using the method described by Sung *et al.* [167] and compared with 2D models regarding paracellular drug absorption and cell growth. In this case, the authors only cultured the cells on the scaffolds for 14 days to avoid degradation of the villi structures and multilayer formation. The permeability of atenolol, a slowly absorbed compound was higher than in the 2D model and more similar to permeability coefficients for perfused human intestine obtained by Lennernas *et al*. [174]. They were also able to observe that cell differentiation on 3D villi scaffolds varied along the villous length, where cells were more polarized and columnar at the top and less differentiated near the villous base [161].

Using villi structures has other advantages like the fact that it is easier to subject the cells to gradients of growth factors that can promote the creation of a stem/progenitor cell zone and cell migration along the crypt-villus axis [159]. This easiness to apply gradients to cells was observed by Wang and colleagues [159], who tried to recreate the intestinal microenvironment to understand the mechanisms behind the differentiation of cells. Using a collagen scaffold that was micropatterned to mimic the villi and the crypts of the small intestine using stamps, it was observed that cells plated on this scaffold were guided to form a crypt-villus architecture. Furthermore, applying a gradient of growth factors and DAPT (a gamma secretase inhibitor) to the culture resulted in cell polarization, promoting the formation of a progenitor-cell zone in the crypt and differentiated cells in the villus axis [159]. As it can be concluded from the previous study, although most authors focus on the villus, it is clear that the crypts also play an important role regarding cellular differentiation in the small intestine. Crypt influence was studied by Wang *et al.* [168], who fabricated poly(dimethylsiloxane) (PDMS) substrates with "holes" mimicking the intestinal crypts, using a mold obtained through lithography technique. The surface was coated with fibronectin and Caco-2 cells were seeded on the substrate. The authors observed that after 4-5 days in culture, cells were able to cover the entire surface, migrating from the bottom to the top of the well structures, whereas this spreading was slower comparing to flat surfaces. Nevertheless, the topography of the substrate affected cell metabolic activity and differentiation, showing an increase in mitochondrial activity and a decrease in ALP activity. These differences stress out the importance of topography, and it is important to notice that differences in cell behavior can lead to differences in results regarding permeability testing. De Gregorio et al. [175], patterned the stromal equivalent mentioned in the previous section to mimic the crypt-villus architecture. Using gelatin porous microbeads, they cultivated human intestinal subepithelial myofibroblasts (ISEMFs) and then transferred to a maturation chamber to allow their molding into a disc-shaped construct. A polymethylmethacrylate (PMMA) holed grid was used to obtain the micropatterned surface. The authors observed that the patterned stroma increased the absorbing surface area, epithelial proliferation rate and density of microvilli. In addition, it was able to induce changes in mucus production, polarization and tightness of the epithelial cells.

Costello *et al.* [163] also focused on the development of a porous poly lactic-co-glycolic acid (PLGA) 3D scaffold with villi architecture, which supported the growth of epithelial Caco-2 and HT29-MTX cell lines. In this study, authors were also able to observe that by mimicking the intestinal topography, cellular differentiation along the villous axis was enabled.

Bioprinting technology has been gaining increasing interest and it has been extensively used for tissue engineering applications. The development of intestinal models is no exception, and authors have been using cell-printing techniques to obtain more realistic models [158, 176, 177]. Kim et al. [176] developed a villus structure using a cell-laden collagen bioink cross-linked with tannic acid. In the meantime, authors developed the same villus structure and seeded the intestinal epithelial cells Caco-2 on the scaffold, instead of embedding them. It was observed that cell viability of the cell-laden model was higher than the control and that the expression of MUC17, E-cadherin and ALP was significantly higher and earlier in the cell-laden structure. Nevertheless, beside the better results of the cell-laden model, the control used in the study is more realistic and more physiologically representative, since the intestinal epithelium in vivo sits on the lamina propria.

Later, Kim et al. [158] also developed a 3D villi intestinal model using a cell-printing process. The authors used two collagen-based bioinks, one laden with Caco-2 cells for the epithelium layer and one laden with human umbilical vein endothelial cells (HUVECs) for the blood capillary structure [158]. HUVECs were able to form a capillary network inside the hydrogel, and the authors concluded that the 3D villi model containing epithelium and the capillary network demonstrated higher cell growth and expression of enzymes and MUC17, when comparing with the 3D model without capillaries or the 2D model [158]. Here, like in the previous study, but differently from all the other mentioned studies, epithelial cells were embedded in the collagen bioink. As stated before, this approach may not be so interesting because on the human small intestine epithelial cells are on top of the intestinal lamina propria, forming the epithelium, and are not entrapped in the ECM. Nevertheless, the use of HUVECs inside the hydrogel is a very interesting approach, since it mimics the capillaries inside the intestinal lamina propria, which represent the last barrier that compounds have to cross to reach systemic circulation, and can, thus, have an impact in the absorption process. More recently, Castaño et al. [162] proposed a simple and moldless fabrication technique consisting in reaction-diffusion mediated photolithography to fabricate 3D microstructures with complex geometries on poly(ethylene glycol) (PEG) hydrogels. Authors claimed that by controlling some fabrication parameters such as oxygen diffusion/depletion, distance to light source and the exposure dose, they could define the dimensions and geometry of the microstructures. Caco-2 cells were seeded on these scaffolds and they were able to form a barrier with more physiological TEER values, and the permeability of fluorescein isothiocyanate (FITC)-dextran 4kDa using this model was significantly higher than that obtained using the standard Caco-2 model, which is a good indicator, since the permeability of paracellularly absorbed compounds in Caco-2 models is underestimated.

Decellularized tissues can also be used in bioprinting to obtain microstructures. A study by Kim et. al used decellularized porcine small intestinal submucosa (SIS) together with collagen type I to obtain bioprinted villi structures laden with Caco-2 cells [178]. When comparing to a microstructured model composed only by collagen, the model containing

SIS revealed higher cellular proliferation and more relevant expression of TJs, ALP and MUC17. Besides, the SIS/collagen model presented higher permeability of FITC-Dextran 4 kDa and higher glucose uptake. However, authors did not make a comparison with physiological values [178].

Most studies use immortalized cell lines to obtain the *in vitro* models. Although using intestinal primary cells would be more representative, obtaining these cells is difficult, mainly due to donor limitation [179]. Moreover, it is hard to maintain their phenotypic characteristics and functions in culture and they have limited viability [180, 181].

1.5.2.3. Organoids

There are several definitions of organoids given by the experts in the field and all of them revolve around the use of several different stem cell-derived cell types that are capable of self-renewal and self-organization into microstructures that partially recapitulate the function of the original tissue [182, 183].

In 2009, intestinal organoids appeared and spurred research around these 3D structures. Sato et al. built, from single sorted leucine-rich repeat-containing G-protein coupled receptor 5 (Lgr5+) stem cells, a mouse intestinal organoid with differentiated cell types and self-organization capabilities in crypt-villus domains when cultured with laminin-rich Matrigel® and growth factors, a model that could be mantained for up to 8 months without losing its features [184]. The authors demonstrated the creation of an intestinal organoid with more than 40 crypts consisting of a single cell layer composed by Paneth and stem cells located at the crypt base, fully polarized enterocytes with mature brush borders, goblet cells, and enteroendocrine cells. In the same year, Ootani et al. used a different methodology through the use of an air-liquid interface exposed to a 3D culture matrix based on collagen and, using primary mouse intestinal fragments, epithelium-mesenchymal organoids were created [185]. This extremely proliferative epithelium, settled by an epithelial polarized cell layer composed by absorptive enterocytes, goblet, enteroendocrine and Paneth cells exhibited structures as microvilli, mucus granules, endocrine granules and intracellular connections of junctional complexes. In the ECM, myofibroblasts expressing α-smooth muscle actin were found. The authors found that these organoids could be cultured for up to 1 year because of the addition of growth factors that simulated Wnt signaling, which represents what happens in vivo in the intestinal crypts [185].

As already mentioned regarding the other intestinal 3D systems, the use of growth factors and ECM during in vitro culture is primordial. The organoid development and differentiation into 3D-like structures, their own self-renewal and the prolonged time in culture is only possible due to the cell source and the ECM support, as well as the use of growth factors.

Matrigel® and collagen are the preferred ECM substrates used for culturing organoids, however, other matrix components based on alginate, elastin, laminin, PEG or agarose hydrogels are also being used [184, 186-190].

The use of organoids has several advantages, such as specificity, no genetic alterations, similar structures and functions to in vivo, and possibility to culture them for long time-periods [191, 192]. However, the use of embryonic stem cells may cause ethical problems and the process is often costly and time consuming. Organoid research has evolved to combine other components of natural tissues, such as mechanical forces or fluid flow, in order to stimulate cell differentiation or to promote the influx of oxygen and nutrients [193, 194]. Gjorevski and colleagues used synthetic PEG hydrogels, with Matrigel® as control, and varied their composition and mechanical environment to create an intestinal organoid with properties similar to the ones found in vivo [193]. The authors proposed stiff and dynamic matrices based on PEG (sPEG – mechanically static PEG; dPEG – mechanical dynamic PEG) and, by varying the ratios of sPEG and dPEG they were able to control the softness of the ECM and cell differentiation and proliferation. Their results demonstrated that the 3D microenvironment, ECM constitution and mechanical stimuli have a great influence on the process of cell proliferation and self-organization during organoid formation. Thus, all these factors should be considered when testing the intestinal permeability of molecules.

Onozato et al. developed an intestinal organoid model to study drug pharmacokinetics, an important feature still scarcely studied in the organoids field. Pluripotent stem cells (PSCs) were induced to differentiate into intestinal cells to form spheroids, and these were later differentiated into intestinal organoids using small molecules [195]. Data revealed an expression of intestinal markers, and pharmacokinetic-related genes were found in the polarized lumen of the epithelium. Since these organoids expressed the functional P-gp efflux transporter, they could be used in drug development and screening, or even for mechanistic studies to assess the effect of this transporter in the intestinal permeability [195].

Techniques to study the permeability of molecules, such as microinjection or inside-to-outside approach, are commonly used in the intestinal organoids field. Bardenbacher et al. presented a method to analyze the function of the epithelial barrier in terms of permeability and molecular regulation on the 3D intestinal organoids through the use of microscopic techniques and bioinformatics analysis of 3D image data [196]. In this study, the organoids were created as previously described [184, 197], aiming for the translation from 2D to 3D cultures to better understand the IFN-γ role in barrier function. Lucifer yellow was used to study the intestinal permeability using an outside to inside approach, where Lucifer yellow fluorescence was quantified by densitometric analysis [196]. Results demonstrated that the permeability of the barrier increased when induced by IFN-γ, which promoted the cleavage of the claudins of the intestinal barrier. Hill et al. developed a real-time technique for measuring the intestinal permeability in 3D organoids using fluorescently-labeled dextran as model drug. The procedure was based on the microinjection of the model drug into the apical epithelial surface of the organoid lumen and, at the same time, it was imaged on an inverted microscope, and images were acquired at determined timepoints in order to quantify the fluorescence as mean of permeability [198].

Organoids constituted by intestinal stem cells, absorptive enterocytes, Paneth cells and secretory goblet cells presented similar morphogenic and morphometric characteristics to those found in vivo, and were used by Pearce et al. to study the heterogeneity of the TJ among different cell types [199]. This study allowed to understand that different intestinal cell types display various types and levels of TJ proteins and that this difference had a significant influence in the macromolecular permeability.

Watson and colleagues tried a different approach by creating intestinal organoids from PSCs [200, 201] and engrafted them in vivo, in mice [202]. The organoids presented columnar intestinal epithelium surrounded by supporting mesenchyme and took about 35 days to differentiate. Then, they were embedded into collagen type I and engrafted under the mice kidney, and allowed to maturate and grow along 6 weeks. The organoids highly increased their size, presented vasculature, crypt-villus architecture, submucosal layers as lamina propria, muscularis mucosa and submucosa, and smooth muscle layers, and the authors claimed to have found a mature intestinal tissue after the engrafting [202]. The epithelial barrier functionality of the engrafted organoid was tested by a permeability assay through the injection of FITC- and data revealed an increase of FITC-dextran permeability overtime, reaching 10% of permeability after 4 hours, indicating a good functioning of the epithelial barrier.

Organoids can be useful to develop targeted and personalized therapies, as they can be stored in biobanks, allowing the genetic profiling, filling the gap between genetics and diseases. However, when it comes to study permeability of compounds, they may not be the best option. As described in this section, due to their 3D polarization, they are normally formed with the apical surface towards the inner domain and the basement membranes out. This characteristic requires the injection of substrates into individual organoids so that the apical membrane is exposed to them [203]. This is probably the main reason why organoids are not routinely used to perform absorption and metabolism studies. Since their use is not straightforward for high throughput screening, there is a preferential used of 2D or 3D multilayered models for this end.

1.5.2.4. Gut-on-a-chip

Microfluidics has revealed to be a very promising strategy to mimic the human intestine. Gut-on-a-chip models can present the 3D intestinal architecture, medium flow and mimic the mechanically active microenvironment of the living intestine, which facilitates cell-cell and cell-matrix interactions [204]. Flow is useful to study drug dynamics, delivery of molecules, as well as transport and absorption mechanisms that are not present in static models [204]. The mold for the chip is typically generated from silicon, glass or plastic, and parameters such as mechanical compression or cyclic stress can be regulated and adjusted as desired in order to better mimic the intestinal environment [205]. In general, gut-on-a-chip consists in different chambers: the ones where cells can be seeded and the culture medium circulates and vacuum chambers responsible for controlling external factors, such as membrane stretch and the peristaltic motion simulation [206, 207].

A study using a gut-on-a-chip model showed that the mechanically active intestine stimulated CYP3A4 activity, glucose reuptake and mucus production, which is known to be absent in static Caco-2 models, as well as Caco-2 cells' differentiation in other intestinal cell types [208].

It as also been reported that fluidic shear stress contributes to the higher expression of Occludin and ZO-1 proteins in Caco-2 cells, which are responsible for forming TJ and, consequently, increase the TEER [209]. However, this can be a disadvantage, since the Caco-2 model already presents higher TEER values than the ones shown *in vivo*. On the other hand, another study verified that cyclic strain enhances cell differentiation, formation of 3D villi-like structures and paracellular permeability, without changing the TEER values in the monolayer, meaning that mechanical forces act directly in paracellular mechanisms [206].

Some authors chose to incorporate human intestinal organoids derived from PSCs in the gut-on-a-chip models. Besides having the four intestinal cell types of diferentiation and the characteristic crypt-villus 3D architecture, these models have shown ability of responding to exogenous stimuli [210]. On another aproach, Ingber and colleagues fabricated a gut-on-a-chip model composed by 3D organoids of epithelial cells isolated from healthy regions of intestinal biopsies. According to their transcriptomic analysis, this intestine chip was closer to the human duodenum than duodenal organoids [211]. This can be a personalized strategy for each individual, a way to understand specific mechanisms and therapies, and to get more reliable results. This system was also characterized by having human intestinal microvascular endothelium cultured in a parallel microchannel under flow. Furthermore, this model was shown to be useful for metabolism, nutrition, infection and drug pharmacokinetics studies, considering the easiness to quantify nutrient digestion, mucus secretion and to establish an intestinal barrier function [211].

Comercially available gut-on-a-chip devices have become available recently. Mimetas, a company that develops these kind of platforms, created the Organoplate® that combines microfluidics to a standard well plate. This gives the user the freedom to decide which ECM, cell types, and perfusion to use, according to its own interest [212]. Another company, Emulate, has developed the duodenum intestine chip, which combines primary human duodenal organoids and microsvascular endothelial cells of the human small intestine, providing mechanical forces and recreating the intestinal peristalsis. The company claims that this dynamic microenvironment leads cells to become well-polarized and exhibit an *in vivo*-like morphology in terms of functionality and gene expression [213].

Basically, it is possible to combine different approaches and aprimorate the intestinal models with, for example, immune cells, intestinal microbiota, organoids or mechanical forces, to approximate in the maximum possible way to an *in vivo* situation [214]. Recent studies are developing systems that enable the integration of the liver, for instance, since it is important to understand first-pass metabolism. In this sense, different organ-on-a-chip models have been developed, in order to connect them and mimic the whole system present in the body [215]. In addition, with a more complex system, it is possible to have a broader perspective of the drugs' effects, meaning that it is possible to check potential side effects in different organs [216, 217]. The future goal is to include in the whole system cells from patients. In this way, treatments can be uniquely designed for each patient or subpopulation [218, 219].

In summary, intestinal *in vitro* models have been receiving major attention in the last years, which has led to great developments in the field. A shift from 2D to 3D platforms enables the development of models that are capable of better mimicking the *in vivo* environment and, therefore, lead to more realistic outputs. Unfortunately, the use of 2D models, especially the Caco-2 models, is still widely spread. This is most likely related with the easiness to obtain this model, as well as its cost benefit. Developing more advanced models may require aditional knowledge, materials and equipments, which can prevent researchers from using such models to test their drugs. Specially when refering to models mimicking the villi or crypts found in the small intestine and guts-on-chip, which require aditional know-how in different fields, as bioprinting and microfluidics. On the other hand, the use of 3D multilayered models that do not mimic the intestinal architecture can pose as the most viable alternative to replace 2D models, as they can be simple to obtain, allowing high throughput testing without employing techniques that require a learning process.

References

1. Seeley, R., T. Stephens, and P. Tate, *Anatomy and Phisiology*. 6 ed. 2004, Boston, MA, USA: McGraw-Hill.
2. Chasin, M., *Oral Drug Absorption Prediction and Assessment* Journal of Medicinal Chemistry, 2001. **44**(3): p. 475-475.
3. Kiela, P.R. and F.K. Ghishan, *Physiology of Intestinal Absorption and Secretion.* Best Practice & Research Clinical Gastroenterology, 2016. **30**(2): p. 145-159.
4. Cheng, L.K., et al., *Gastrointestinal system.* Wiley interdisciplinary reviews: Systems biology and medicine, 2010. **2**(1): p. 65-79.
5. Margaret Smith, D.M., *The Digestive System*. 2 ed. 2010, London, UK: Elsevier Health Sciences.
6. Kobayashi, N., et al., *The Roles of Peyer's Patches and Microfold Cells in the Gut Immune System: Relevance to Autoimmune Diseases.* Frontiers in Immunology, 2019. **10**(2345).
7. Reboldi, A. and J.G. Cyster, *Peyer's patches: organizing B-cell responses at the intestinal frontier.* Immunological Reviews, 2016. **271**(1): p. 230-245.
8. Salvo Romero, E., et al., *The intestinal barrier function and its involvement in digestive disease.* Spanish Journal of Gastroenterology, 2015. **107**(11): p. 686-696.
9. Crosnier, C., D. Stamataki, and J. Lewis, *Organizing cell renewal in the intestine: stem cells, signals and combinatorial control.* Nature Reviews Genetics, 2006. **7**(5): p. 349-359.
10. Booth, C. and C.S. Potten, *Gut instincts: thoughts on intestinal epithelial stem cells.* Journal of Clinical Investigation, 2000. **105**(11): p. 1493-1499.
11. Barker, N., *Adult intestinal stem cells: critical drivers of epithelial homeostasis and regeneration.* Nature Reviews Molecular Cell Biology, 2014. **15**(1): p. 19-33.
12. Fedi, A., et al., *In vitro models replicating the human intestinal epithelium for absorption and metabolism studies: A systematic review.* Journal of Controlled Release, 2021. **335**: p. 247-268.
13. Wright, N.A., *Epithelial stem cell repertoire in the gut: clues to the origin of cell lineages, proliferative units and cancer.* International Journal of Experimental Pathology, 2000. **81**(2): p. 117-143.
14. Allaire, J.M., et al., *The Intestinal Epithelium: Central Coordinator of Mucosal Immunity.* Trends in Immunology, 2018. **39**(9): p. 677-696.
15. de Santa Barbara, P., G.R. van den Brink, and D.J. Roberts, *Development and differentiation of the intestinal epithelium.* Cellular and Molecular Life Sciences, 2003. **60**(7): p. 1322-1332.

16. Pott, J. and M. Hornef, *Innate immune signalling at the intestinal epithelium in homeostasis and disease.* EMBO Reports, 2012. **13**(8): p. 684-698.
17. Peterson, L.W. and D. Artis, *Intestinal epithelial cells: regulators of barrier function and immune homeostasis.* Nature Reviews Immunology, 2014. **14**(3): p. 141-153.
18. Herath, M., et al., *The Role of the Gastrointestinal Mucus System in Intestinal Homeostasis: Implications for Neurological Disorders.* Frontiers in Cellular and Infection Microbiology, 2020. **10**(248).
19. Ayabe, T., et al., *The role of Paneth cells and their antimicrobial peptides in innate host defense.* Trends in Microbiology, 2004. **12**(8): p. 394-398.
20. Porter, E.M., et al., *The multifaceted Paneth cell.* Cellular and Molecular Life Sciences, 2002. **59**(1): p. 156-170.
21. Engelstoft, M.S., et al., *Enteroendocrine cell types revisited.* Current Opinion in Pharmacology, 2013. **13**(6): p. 912-921.
22. Turner, J.R., *Intestinal mucosal barrier function in health and disease.* Nature Reviews Immunology, 2009. **9**(11): p. 799-809.
23. Gribble, F.M. and F. Reimann, *Enteroendocrine Cells: Chemosensors in the Intestinal Epithelium.* Annual Review of Physiology, 2016. **78**: p. 277-299.
24. Gerbe, F., et al., *Intestinal epithelial tuft cells initiate type 2 mucosal immunity to helminth parasites.* Nature, 2016. **529**(7585): p. 226-230.
25. Howitt, M.R., et al., *Tuft cells, taste-chemosensory cells, orchestrate parasite type 2 immunity in the gut.* Science, 2016. **351**(6279): p. 1329-1333.
26. von Moltke, J., et al., *Tuft-cell-derived IL-25 regulates an intestinal ILC2–epithelial response circuit.* Nature, 2016. **529**(7585): p. 221-225.
27. Zhu, P., et al., *IL-13 secreted by ILC2s promotes the self-renewal of intestinal stem cells through circular RNA circPan3.* Nature Immunology, 2019. **20**(2): p. 183-194.
28. Mabbott, N.A., et al., *Microfold (M) cells: important immunosurveillance posts in the intestinal epithelium.* Mucosal Immunology, 2013. **6**(4): p. 666-677.
29. Ohno, H., *Intestinal M cells.* The Journal of Biochemistry, 2015. **159**(2): p. 151-160.
30. Sengupta, N. and T.T. MacDonald, *The role of matrix metalloproteinases in stromal/epithelial interactions in the gut.* Physiology, 2007. **22**: p. 401-409.
31. McAnulty, R.J., *Fibroblasts and myofibroblasts: Their source, function and role in disease.* The International Journal of Biochemistry & Cell Biology, 2007. **39**(4): p. 666-671.
32. Powell, D.W., et al., *Mesenchymal cells of the intestinal lamina propria.* Annual Review of Physiology, 2011. **73**: p. 213-237.

33. Powell, D.W., et al., *Epithelial cells and their neighbors I. Role of intestinal myofibroblasts in development, repair, and cancer.* American Journal of Physiology-Gastrointestinal and Liver Physiology, 2005. **289**(1): p. G2-7.
34. Pastuła, A. and J. Marcinkiewicz, *Cellular Interactions in the Intestinal Stem Cell Niche.* Archivum Immunologiae et Therapiae Experimentalis, 2019. **67**(1): p. 19-26.
35. Darnell, M., et al., *Cytochrome P450-Dependent Metabolism in HepaRG Cells Cultured in a Dynamic Three-Dimensional Bioreactor.* Drug Metabolism and Disposition, 2011. **39**(7): p. 1131-1138.
36. Fritsch, C., et al., *Characterization of human intestinal stromal cell lines: response to cytokines and interactions with epithelial cells.* Experimental Cell Research, 1999. **248**(2): p. 391-406.
37. Justice, B.A., N.A. Badr, and R.A. Felder, *3D cell culture opens new dimensions in cell-based assays.* Drug Discovery Today, 2009. **14**(1): p. 102-107.
38. Pampaloni, F., E.G. Reynaud, and E.H. Stelzer, *The third dimension bridges the gap between cell culture and live tissue.* Nature Reviews Molecular Cell Biology, 2007. **8**(10): p. 839-345.
39. Kleinman, H.K., D. Philp, and M.P. Hoffman, *Role of the extracellular matrix in morphogenesis.* Current Opinion in Biotechnology, 2003. **14**(5): p. 526-532.
40. Bissell, M.J., et al., *The organizing principle: microenvironmental influences in the normal and malignant breast.* Differentiation, 2002. **70**(9-10): p. 537-546.
41. Madison, B.B., et al., *Epithelial hedgehog signals pattern the intestinal crypt-villus axis.* Development, 2005. **132**(2): p. 279-289.
42. Zacharias, W.J., et al., *Hedgehog is an anti-inflammatory epithelial signal for the intestinal lamina propria.* Gastroenterology, 2010. **138**(7): p. 2368-2377.
43. Ma, T.Y., P. Nighot, and R. Al-Sadi, *Chapter 25 - Tight Junctions and the Intestinal Barrier*, in *Physiology of the Gastrointestinal Tract*, H.M. Said, Editor. 2018, Academic Press: Boston, Ma, USA. p. 587-639.
44. Cone, R.A., *Barrier properties of mucus.* Advanced Drug Delivery Reviews, 2009. **61**(2): p. 75-85.
45. Cone, R.A., *Mucus*, in *Mucosal Immunology*, J. Mestecky, et al., Editors. 2005, Academic Press: San Diego, CA, USA. p. 49-72.
46. van der Waaij, L.A., et al., *Bacterial population analysis of human colon and terminal ileum biopsies with 16S rRNA-based fluorescent probes: commensal bacteria live in suspension and have no direct contact with epithelial cells.* Inflammatory Bowel Diseases, 2005. **11**(10): p. 865-871.

47. Bansil, R. and B.S. Turner, *Mucin structure, aggregation, physiological functions and biomedical applications.* Current Opinion in Colloid & Interface Science, 2006. **11**(2-3): p. 164-170.

48. Bansil, R. and B.S. Turner, *The biology of mucus: Composition, synthesis and organization.* Advanced Drug Delivery Reviews, 2018. **124**: p. 3-15.

49. Lai, S.K., et al., *Micro- and macrorheology of mucus.* Advanced Drug Delivery Reviews, 2009. **61**(2): p. 86-100.

50. Allen, A. and A. Garner, *Mucus and bicarbonate secretion in the stomach and their possible role in mucosal protection.* Gut, 1980. **21**(3): p. 249-262.

51. Sellers, L.A., et al., *Mechanical characterization and properties of gastrointestinal mucus gel.* Biorheology, 1987. **24**(6): p. 615-623.

52. Kejriwal, S., et al., *Estimation of levels of salivary mucin, amylase and total protein in gingivitis and chronic periodontitis patients.* Journal of Clinical and Diagnostic Research, 2014. **8**(10): p. ZC56-60.

53. Moran, A.P., A. Gupta, and L. Joshi, *Sweet-talk: role of host glycosylation in bacterial pathogenesis of the gastrointestinal tract.* Gut, 2011. **60**(10): p. 1412-1425.

54. Chen, D., et al., *Enhancing nanoparticle penetration through airway mucus to improve drug delivery efficacy in the lung.* Expert Opinion on Drug Delivery, 2020: p. 1-12.

55. Boegh, M. and H.M. Nielsen, *Mucus as a barrier to drug delivery - understanding and mimicking the barrier properties.* Basic & Clinical Pharmacology & Toxicology, 2014. **116**(3): p. 179-186.

56. das Neves, J., R. Sverdlov Arzi, and A. Sosnik, *Molecular and cellular cues governing nanomaterial-mucosae interactions: from nanomedicine to nanotoxicology.* Chemical Society Reviews, 2020. **49**(14): p. 5058-5100.

57. Slifer, Z.M. and A.T. Blikslager, *The Integral Role of Tight Junction Proteins in the Repair of Injured Intestinal Epithelium.* International Journal of Molecular Sciences, 2020. **21**(3).

58. Tsukita, S., M. Furuse, and M. Itoh, *Multifunctional strands in tight junctions.* Nature Reviews Molecular Cell Biology, 2001. **2**(4): p. 285-293.

59. Ichikawa-Tomikawa, N., et al., *Possible involvement of tight junctions, extracellular matrix and nuclear receptors in epithelial differentiation.* Journal of Biomedicine and Biotechnology, 2011. **2011**: p. 253048.

60. Ulluwishewa, D., et al., *Regulation of tight junction permeability by intestinal bacteria and dietary components.* Journal of Nutrition, 2011. **141**(5): p. 769-776.

61. Konig, J., et al., *Human Intestinal Barrier Function in Health and Disease.* Clinical and Translational Gastroenterology, 2016. **7**(10): p. e196.

62. Lee, B., K.M. Moon, and C.Y. Kim, *Tight Junction in the Intestinal Epithelium: Its Association with Diseases and Regulation by Phytochemicals.* Journal of Immunology Research, 2018. **2018**: p. 2645465.
63. Duizer, E., et al., *Absorption enhancement, structural changes in tight junctions and cytotoxicity caused by palmitoyl carnitine in Caco-2 and IEC-18 cells.* Journal of Pharmacology and Experimental Therapeutics, 1998. **287**(1): p. 395-402.
64. Artursson, P., K. Palm, and K. Luthman, *Caco-2 monolayers in experimental and theoretical predictions of drug transport.* Advanced Drug Delivery Reviews, 2001. **46**(1-3): p. 27-43.
65. Wu, C.Y., et al., *Differentiation of absorption and first-pass gut and hepatic metabolism in humans: studies with cyclosporine.* Clinical Pharmacology & Therapeutics, 1995. **58**(5): p. 492-497.
66. Trowers, E. and M. Tischler, *Gastrointestinal Physiology, A Clinical Approach*. 2014, Switzerland: Springer.
67. Gonzalez-Mariscal, L., et al., *Tight junction proteins.* Progress in Biophysics and Molecular Biology, 2003. **81**(1): p. 1-44.
68. Lee, S.H., *Intestinal permeability regulation by tight junction: implication on inflammatory bowel diseases.* Intestinal Research, 2015. **13**(1): p. 11-18.
69. Niessen, C.M., *Tight Junctions/Adherens Junctions: Basic Structure and Function.* Journal of Investigative Dermatology, 2007. **127**(11): p. 2525-2532.
70. Bauer, H., et al., *The dual role of zonula occludens (ZO) proteins.* Journal of Biomedicine and Biotechnology, 2010. **2010**: p. 402593.
71. Stevenson, B.R., et al., *Identification of ZO-1: a high molecular weight polypeptide associated with the tight junction (zonula occludens) in a variety of epithelia.* Journal of Cell Biology, 1986. **103**(3): p. 755-766.
72. Howarth, A.G., M.R. Hughes, and B.R. Stevenson, *Detection of the tight junction-associated protein ZO-1 in astrocytes and other nonepithelial cell types.* American Journal of Physiology-Cell Physiology, 1992. **262**(2): p. C461-C469.
73. Kausalya, P.J., M. Reichert, and W. Hunziker, *Connexin45 directly binds to ZO-1 and localizes to the tight junction region in epithelial MDCK cells.* FEBS letters, 2001. **505**(1): p. 92-96.
74. Li, X., et al., *Association of connexin36 with zonula occludens-1 in HeLa cells, βTC-3 cells, pancreas, and adrenal gland.* Histochemistry and cell biology, 2000. **122**(5): p. 485-498.
75. Singh, D., et al., *Connexin 43 interacts with zona occludens-1 and-2 proteins in a cell cycle stage-specific manner.* Journal of Biological Chemistry, 2005. **280**(34): p. 30416-30421.

76. Umeda, K., et al., *ZO-1 and ZO-2 independently determine where claudins are polymerized in tight-junction strand formation.* Cell, 2006. **126**(4): p. 741-754.
77. Furuse, M., et al., *A single gene product, claudin-1 or -2, reconstitutes tight junction strands and recruits occludin in fibroblasts.* The Journal of cell biology, 1998. **143**(2): p. 391-401.
78. Chiba, H., et al., *Transmembrane proteins of tight junctions.* Biochimica et Biophysica Acta, 2008. **1778**(3): p. 588-600.
79. Hamazaki, Y., et al., *Multi-PDZ domain protein 1 (MUPP1) is concentrated at tight junctions through its possible interaction with claudin-1 and junctional adhesion molecule.* Journal of Biological Chemistry, 2002. **277**(1): p. 455-461.
80. Shen, L., et al., *Tight junction pore and leak pathways: a dynamic duo.* Annual Review of Physiology, 2011. **73**: p. 283-309.
81. Gunzel, D. and A.S. Yu, *Claudins and the modulation of tight junction permeability.* Physiological Reviews, 2013. **93**(2): p. 525-569.
82. Rosenthal, R., et al., *Claudin-2, a component of the tight junction, forms a paracellular water channel.* Journal of Cell Science, 2010. **123**(11): p. 1913-1921.
83. Van Itallie, C.M., A.S. Fanning, and J.M. Anderson, *Reversal of charge selectivity in cation or anion-selective epithelial lines by expression of different claudins.* American Journal of Physiology - Renal Physiology, 2003. **285**(6): p. F1078-1084.
84. Van Itallie, C.M., et al., *The density of small tight junction pores varies among cell types and is increased by expression of claudin-2.* Journal of Cell Science, 2008. **121**(3): p. 298-305.
85. Satohisa, S., et al., *Behavior of tight-junction, adherens-junction and cell polarity proteins during HNF-4alpha-induced epithelial polarization.* Experimental Cell Research, 2005. **310**(1): p. 66-78.
86. Ishizaki, T., et al., *Cyclic AMP induces phosphorylation of claudin-5 immunoprecipitates and expression of claudin-5 gene in blood-brain-barrier endothelial cells via protein kinase A-dependent and -independent pathways.* Experimental Cell Research, 2003. **290**(2): p. 275-288.
87. Fujita, H., et al., *Differential expression and subcellular localization of claudin-7, -8, -12, -13, and -15 along the mouse intestine.* Journal of Histochemistry & Cytochemistry, 2006. **54**(8): p. 933-944.
88. Fujibe, M., et al., *Thr203 of claudin-1, a putative phosphorylation site for MAP kinase, is required to promote the barrier function of tight junctions.* Experimental Cell Research, 2004. **295**(1): p. 36-47.

89. Furuse, M., et al., *Direct association of occludin with ZO-1 and its possible involvement in the localization of occludin at tight junctions.* Direct association of occludin, 1994. **127**(6 Pt 1): p. 1617-1626.

90. Saitou, M., et al., *Complex phenotype of mice lacking occludin, a component of tight junction strands.* Molecular Biology of the Cell, 2000. **11**(12): p. 4131-4142.

91. Bazzoni, G., *The JAM family of junctional adhesion molecules.* Current Opinion in Cell Biology, 2003. **15**(5): p. 525-530.

92. Cunningham, S.A., et al., *A novel protein with homology to the junctional adhesion molecule. Characterization of leukocyte interactions.* Journal of Biological Chemistry, 2000. **275**(44): p. 34750-34756.

93. Ebnet, K., et al., *The cell polarity protein ASIP/PAR-3 directly associates with junctional adhesion molecule (JAM).* The EMBO Journal, 2001. **20**(14): p. 3738-3748.

94. Itoh, M., et al., *Junctional adhesion molecule (JAM) binds to PAR-3: a possible mechanism for the recruitment of PAR-3 to tight junctions.* Journal of Cell Biology, 2001. **154**(3): p. 491-497.

95. Ebnet, K., et al., *The junctional adhesion molecule (JAM) family members JAM-2 and JAM-3 associate with the cell polarity protein PAR-3: a possible role for JAMs in endothelial cell polarity.* Journal of Cell Science, 2003. **116**(19): p. 3879-3891.

96. Giacomini, K.M., et al., *Membrane transporters in drug development.* Nature Reviews Drug Discovery, 2010. **9**(3): p. 215-236.

97. Estudante, M., et al., *Intestinal drug transporters: an overview.* Advanced Drug Delivery Reviews, 2013. **65**(10): p. 1340-1356.

98. Hediger, M.A., et al., *The ABCs of solute carriers: physiological, pathological and therapeutic implications of human membrane transport proteinsIntroduction.* Pflügers Archiv: European Journal of Physiology, 2004. **447**(5): p. 465-468.

99. Shugarts, S. and L.Z. Benet, *The role of transporters in the pharmacokinetics of orally administered drugs.* Pharmaceutical Research, 2009. **26**(9): p. 2039-2054.

100. Roninson, I.B., et al., *Isolation of human mdr DNA sequences amplified in multidrug-resistant KB carcinoma cells.* Proceedings of the National Academy of Sciences, 1986. **83**(12): p. 4538-4542.

101. Muller, F. and M.F. Fromm, *Transporter-mediated drug-drug interactions.* Pharmacogenomics, 2011. **12**(7): p. 1017-1037.

102. Liu, Y.H., et al., *Multidrug resistance-associated proteins and implications in drug development.* Clinical and Experimental Pharmacology and Physiology, 2010. **37**(1): p. 115-120.

103. Yu, X.Q., et al., *Multidrug resistance associated proteins as determining factors of pharmacokinetics and pharmacodynamics of drugs.* Current Drug Metabolism, 2007. **8**(8): p. 787-802.

104. Peng, K.C., et al., *Tissue and cell distribution of the multidrug resistance-associated protein (MRP) in mouse intestine and kidney.* Journal of Histochemistry & Cytochemistry, 1999. **47**(6): p. 757-768.

105. Kunta, J.R. and P.J. Sinko, *Intestinal drug transporters: in vivo function and clinical importance.* Current Drug Metabolism, 2004. **5**(1): p. 109-124.

106. Mottino, A.D., et al., *Expression and localization of multidrug resistant protein mrp2 in rat small intestine.* Journal of Pharmacology and Experimental Therapeutics, 2000. **293**(3): p. 717-723.

107. Gerk, P.M. and M. Vore, *Regulation of expression of the multidrug resistance-associated protein 2 (MRP2) and its role in drug disposition.* Journal of Pharmacology and Experimental Therapeutics, 2002. **302**(2): p. 407-415.

108. Payen, L., et al., *The drug efflux pump MRP2: regulation of expression in physiopathological situations and by endogenous and exogenous compounds.* Cell Biology and Toxicology, 2002. **18**(4): p. 221-233.

109. Bruyere, A., et al., *Effect of variations in the amounts of P-glycoprotein (ABCB1), BCRP (ABCG2) and CYP3A4 along the human small intestine on PBPK models for predicting intestinal first pass.* Molecular Pharmaceutics, 2010. **7**(5): p. 1596-1607.

110. Ni, Z., et al., *Structure and function of the human breast cancer resistance protein (BCRP/ABCG2).* Current Drug Metabolism, 2010. **11**(7): p. 603-617.

111. Dahan, A. and G.L. Amidon, *Small intestinal efflux mediated by MRP2 and BCRP shifts sulfasalazine intestinal permeability from high to low, enabling its colonic targeting.* American Journal of Physiology-Gastrointestinal and Liver Physiology, 2009. **297**(2): p. G371-377.

112. Zhang, L., et al., *Synthesis and evaluation of a dipeptide-drug conjugate library as substrates for PEPT1.* ACS Combinatorial Science, 2012. **14**(2): p. 108-114.

113. Varma, M.V., et al., *Targeting intestinal transporters for optimizing oral drug absorption.* Current Drug Metabolism, 2010. **11**(9): p. 730-742.

114. Hellwig, M., et al., *Transport of free and peptide-bound glycated amino acids: synthesis, transepithelial flux at Caco-2 cell monolayers, and interaction with apical membrane transport proteins.* ChemBioChem, 2011. **12**(8): p. 1270-1279.

115. Shu, Y., *Research progress in the organic cation transporters.* Zhong Nan Da Xue Xue Bao Yi Xue Ban, 2011. **36**(10): p. 913-926.

116. Barnes, K., et al., *Distribution and functional characterization of equilibrative nucleoside transporter-4, a novel cardiac adenosine transporter activated at acidic pH.* Circulation Research, 2006. **99**(5): p. 510-519.

117. Okura, T., et al., *Functional characterization of rat plasma membrane monoamine transporter in the blood-brain and blood-cerebrospinal fluid barriers.* Journal of Pharmaceutical Sciences, 2011. **100**(9): p. 3924-3938.

118. Wang, J., *The plasma membrane monoamine transporter (PMAT): Structure, function, and role in organic cation disposition.* Clinical Pharmacology & Therapeutics, 2016. **100**(5): p. 489-499.

119. Engel, K. and J. Wang, *Interaction of organic cations with a newly identified plasma membrane monoamine transporter.* Molecular Pharmacology, 2005. **68**(5): p. 1397-1407.

120. Engel, K., M. Zhou, and J. Wang, *Identification and characterization of a novel monoamine transporter in the human brain.* Journal of Biological Chemistry, 2004. **279**(48): p. 50042-10049.

121. Tamai, I., *Oral drug delivery utilizing intestinal OATP transporters.* Advanced Drug Delivery Reviews, 2012. **64**(6): p. 508-514.

122. Hidalgo, I.J., *Assessing the absorption of new pharmaceuticals.* Current Topics in Medicinal Chemistry, 2001. **1**(5): p. 385-401.

123. Ozawa, T., et al., *Generation of enterocyte-like cells from human induced pluripotent stem cells for drug absorption and metabolism studies in human small intestine.* Scientific Reports, 2015. **5**: p. 16479.

124. Maubon, N., et al., *Analysis of drug transporter expression in human intestinal Caco-2 cells by real-time PCR.* Fundamental & Clinical Pharmacology, 2007. **21**(6): p. 659-663.

125. Li, N., et al., *A fast screening model for drug permeability assessment based on native small intestinal extracellular matrix.* RSC Advances, 2018. **8**: p. 34514-34524.

126. Li, N., et al., *Development of an Improved Three-Dimensional In Vitro Intestinal Mucosa Model for Drug Absorption Evaluation.* Tissue Engineering Part C: Methods, 2013. **19**(9): p. 708-719.

127. Zhang, J., J. Penny, and J.R. Lu, *Development of a novel in vitro 3D intestinal model for permeability evaluations.* International Journal of Food Sciences and Nutrition, 2020. **71**(5): p. 549-562.

128. Chong, S., et al., *In vitro permeability through caco-2 cells is not quantitatively predictive of in vivo absorption for peptide-like drugs absorbed via the dipeptide transporter system.* Pharmaceutical Research, 1996. **13**(1): p. 120-123.

129. Balimane, P.V. and S. Chong, *Cell culture-based models for intestinal permeability: a critique.* Drug Discovery Today, 2005. **10**(5): p. 335-343.

130. Nakamura, T., et al., *Real-time quantitative polymerase chain reaction for MDR1, MRP1, MRP2, and CYP3A-mRNA levels in Caco-2 cell lines, human duodenal enterocytes, normal colorectal tissues, and colorectal adenocarcinomas.* Drug Metabolism and Disposition, 2002. **30**(1): p. 4-6.

131. Kolars, J.C., et al., *First-pass metabolism of cyclosporin by the gut.* Lancet, 1991. **338**(8781): p. 1488-1490.

132. Watson, C.J., M. Rowland, and G. Warhurst, *Functional modeling of tight junctions in intestinal cell monolayers using polyethylene glycol oligomers.* American Journal of Physiology-Cell Physiology, 2001. **281**(2): p. C388-397.

133. Fine, K.D., et al., *Effect of changing intestinal flow rate on a measurement of intestinal permeability.* Gastroenterology, 1995. **108**(4): p. 983-989.

134. Pereira, C., et al., *3.3 - Cell-based in vitro models for intestinal permeability studies*, in *Concepts and Models for Drug Permeability Studies*, B. Sarmento, Editor. 2016, Woodhead Publishing. p. 57-81.

135. Grès, M.C., et al., *Correlation between oral drug absorption in humans, and apparent drug permeability in TC-7 cells, a human epithelial intestinal cell line: comparison with the parental Caco-2 cell line.* Pharmaceutical Research, 1998. **15**(5): p. 726-733.

136. Turco, L., et al., *Caco-2/TC7 cell line characterization for intestinal absorption: how reliable is this in vitro model for the prediction of the oral dose fraction absorbed in human?* Toxicology in Vitro, 2011. **25**(1): p. 13-20.

137. Avdeef, A. and K.Y. Tam, *How well can the Caco-2/Madin-Darby canine kidney models predict effective human jejunal permeability?* Journal of Medicinal Chemistry, 2010. **53**(9): p. 3566-3584.

138. Cho, M.J., et al., *The Madin Darby canine kidney (MDCK) epithelial cell monolayer as a model cellular transport barrier.* Pharmaceutical Research, 1989. **6**(1): p. 71-77.

139. Tavelin, S., et al., *A conditionally immortalized epithelial cell line for studies of intestinal drug transport.* Journal of Pharmacology and Experimental Therapeutics, 1999. **290**(3): p. 1212-1221.

140. Srinivasan, B., et al., *TEER measurement techniques for in vitro barrier model systems.* Journal of laboratory automation, 2015. **20**(2): p. 107-126.

141. Lazorova, L., et al., *Structural features determining the intestinal epithelial permeability and efflux of novel HIV-1 protease inhibitors.* Journal of Pharmaceutical Sciences, 2011. **100**(9): p. 3763-3772.

142. Ma, T.Y., et al., *IEC-18, a nontransformed small intestinal cell line for studying epithelial permeability.* Journal of Laboratory and Clinical Medicine, 1992. **120**(2): p. 329-341.

143. Marano, C.W., et al., *Phorbol ester treatment increases paracellular permeability across IEC-18 gastrointestinal epithelium in vitro.* Digestive Diseases and Sciences, 2001. **46**(7): p. 1490-1499.

144. Lesuffleur, T., et al., *Growth adaptation to methotrexate of HT-29 human colon carcinoma cells is associated with their ability to differentiate into columnar absorptive and mucus-secreting cells.* Cancer Research, 1990. **50**(19): p. 6334-6343.

145. Antunes, F., et al., *Establishment of a triple co-culture in vitro cell models to study intestinal absorption of peptide drugs.* European Journal of Pharmaceutics and Biopharmaceutics, 2013. **83**(3): p. 427-435.

146. Mahler, G.J., M.L. Shuler, and R.P. Glahn, *Characterization of Caco-2 and HT29-MTX cocultures in an in vitro digestion/cell culture model used to predict iron bioavailability.* Journal of Nutritional Biochemistry, 2009. **20**(7): p. 494-502.

147. Wikman, A., et al., *A Drug Absorption Model Based on the Mucus Layer Producing Human Intestinal Goblet Cell Line HT29-H.* Pharmaceutical Research, 1993. **10**(6): p. 843-852.

148. Behrens, I., et al., *Comparative uptake studies of bioadhesive and non-bioadhesive nanoparticles in human intestinal cell lines and rats: the effect of mucus on particle adsorption and transport.* Pharmaceutical Research, 2002. **19**(8): p. 1185-1193.

149. Araújo, F. and B. Sarmento, *Towards the characterization of an in vitro triple co-culture intestine cell model for permeability studies.* International Journal of Pharmaceutics, 2013. **458**(1): p. 128-134.

150. Gullberg, E., et al., *Expression of specific markers and particle transport in a new human intestinal M-cell model.* Biochemical and Biophysical Research Communications, 2000. **279**(3): p. 808-813.

151. Antunes, F., et al., *Establishment of a triple co-culture in vitro cell models to study intestinal absorption of peptide drugs.* European Journal of Pharmaceutics and Biopharmaceutics, 2013. **83**(3): p. 427-35.

152. Schimpel, C., et al., *Development of an advanced intestinal in vitro triple culture permeability model to study transport of nanoparticles.* Molecular Pharmaceutics, 2014. **11**(3): p. 808-818.

153. Fitzgerald, K.A., et al., *Life in 3D is never flat: 3D models to optimise drug delivery.* Journal of Controlled Release, 2015. **215**: p. 39-54.

154. Cavero, I., *Optimizing the preclinical/clinical interface: an Informa Life Sciences conference 12-13 December, 2006, London, UK.* Expert Opinion on Drug Safety, 2007. **6**(2): p. 217-224.

155. Ravi, M., et al., *3D cell culture systems: advantages and applications.* Journal of Cellular Physiology, 2015. **230**(1): p. 16-26.

156. Mazzoleni, G., D. Di Lorenzo, and N. Steimberg, *Modelling tissues in 3D: the next future of pharmaco-toxicology and food research?* Genes & Nutrition, 2009. **4**(1): p. 13-22.

157. DeWitt, R.C. and K.A. Kudsk, *The gut's role in metabolism, mucosal barrier function, and gut immunology.* Infectious Disease Clinics of North America, 1999. **13**(2): p. 465-481.

158. Kim, W. and G. Kim, *Intestinal Villi Model with Blood Capillaries Fabricated Using Collagen-Based Bioink and Dual-Cell-Printing Process.* ACS Applied Materials & Interfaces, 2018. **10**(48): p. 41185-41196.

159. Wang, Y., et al., *A microengineered collagen scaffold for generating a polarized crypt-villus architecture of human small intestinal epithelium.* Biomaterials, 2017. **128**: p. 44-55.

160. Yi, B., et al., *Three-dimensional in vitro gut model on a villi-shaped collagen scaffold.* BioChip Journal, 2017. **11**(3): p. 219-231.

161. Yu, J., et al., *In vitro 3D human small intestinal villous model for drug permeability determination.* Biotechnology and Bioengineering, 2012. **109**(9): p. 2173-2178.

162. Castano, A.G., et al., *Dynamic photopolymerization produces complex microstructures on hydrogels in a moldless approach to generate a 3D intestinal tissue model.* Biofabrication, 2019. **11**(2): p. 1-9.

163. Costello, C.M., et al., *Synthetic small intestinal scaffolds for improved studies of intestinal differentiation.* Biotechnology and Bioengineering, 2014. **111**(6): p. 1222-1232.

164. Dosh, R.H., et al., *Use of hydrogel scaffolds to develop an in vitro 3D culture model of human intestinal epithelium.* Acta Biomaterialia, 2017. **62**: p. 128-143.

165. Pereira, C., et al., *Dissecting stromal-epithelial interactions in a 3D in vitro cellularized intestinal model for permeability studies.* Biomaterials, 2015. **56**: p. 36-45.

166. Pusch, J., et al., *The physiological performance of a three-dimensional model that mimics the microenvironment of the small intestine.* Biomaterials, 2011. **32**(30): p. 7469-7478.

167. Sung, J.H., et al., *Microscale 3-D hydrogel scaffold for biomimetic gastrointestinal (GI) tract model.* Lab Chip, 2011. **11**(3): p. 389-392.

168. Wang, L., et al., *Influence of micro-well biomimetic topography on intestinal epithelial Caco-2 cell phenotype.* Biomaterials, 2009. **30**(36): p. 6825-6834.

169. Griffith, L.G. and M.A. Swartz, *Capturing complex 3D tissue physiology in vitro.* Nature Reviews Molecular Cell Biology, 2006. **7**(3): p. 211-224.

170. De Gregorio, V., et al., *3D stromal tissue equivalent affects intestinal epithelium morphogenesis in vitro.* Biotechnology and Bioengineering, 2018. **115**(4): p. 1062-1075.

171. Patient, J.D., et al., *Nanofibrous Scaffolds Support a 3D in vitro Permeability Model of the Human Intestinal Epithelium.* Frontiers in Pharmacology, 2019. **10**(456).

172. Leonard, F., E.M. Collnot, and C.M. Lehr, *A three-dimensional coculture of enterocytes, monocytes and dendritic cells to model inflamed intestinal mucosa in vitro.* Molecular Pharmaceutics, 2010. **7**(6): p. 2103-2119.

173. Ayehunie, S., et al., *Human Primary Cell-Based Organotypic Microtissues for Modeling Small Intestinal Drug Absorption.* Pharmaceutical Research, 2018. **35**(4).

174. Lennernas, H., O. Ahrenstedt, and A.L. Ungell, *Intestinal drug absorption during induced net water absorption in man; a mechanistic study using antipyrine, atenolol and enalaprilat.* British Journal of Clinical Pharmacology, 1994. **37**(6): p. 589-596.

175. De Gregorio, V., et al., *Micro-patterned endogenous stroma equivalent induces polarized crypt-villus architecture of human small intestinal epithelium.* Acta Biomaterialia, 2018. **81**: p. 43-59.

176. Kim, W. and G.H. Kim, *An innovative cell-printed microscale collagen model for mimicking intestinal villus epithelium.* Chemical Engineering Journal, 2018. **334**: p. 2308-2318.

177. Madden, L.R., et al., *Bioprinted 3D Primary Human Intestinal Tissues Model Aspects of Native Physiology and ADME/Tox Functions.* iScience, 2018. **2**: p. 156-167.

178. Kim, W. and G.H. Kim, *An intestinal model with a finger-like villus structure fabricated using a bioprinting process and collagen/SIS-based cell-laden bioink.* Theranostics, 2020. **10**(6): p. 2495-2508.

179. Kauffman, A., et al., *Alternative functional in vitro models of human intestinal epithelia.* Frontiers in Pharmacology, 2013. **4**(79).

180. Grossmann, J., et al., *New Isolation Technique to Study Apoptosis in Human Intestinal Epithelial Cells.* The American Journal of Pathology, 1998. **153**(1): p. 53-62.

181. Kabeya, T., et al., *Functional analysis of carboxylesterase in human induced pluripotent stem cell-derived enterocytes.* Biochemical and Biophysical Research Communications, 2017. **486**(1): p. 143-148.

182. Stelzner, M., et al., *A nomenclature for intestinal in vitro cultures.* American Journal of Physiology-Gastrointestinal and Liver Physiology, 2012. **302**(12): p. G1359-G1363.

183. Simian, M. and M.J. Bissell, *Organoids: a historical perspective of thinking in three dimensions.* Journal of Cell Biology, 2017. **216**(1): p. 31-40.

184. Sato, T., et al., *Single Lgr5 stem cells build crypt–villus structures in vitro without a mesenchymal niche.* Nature, 2009. **459**(7244): p. 262-265.

185. Ootani, A., et al., *Sustained in vitro intestinal epithelial culture within a Wnt-dependent stem cell niche.* Nature medicine, 2009. **15**(6): p. 701-706.

186. Capeling, M.M., et al., *Nonadhesive alginate hydrogels support growth of pluripotent stem cell-derived intestinal organoids.* Stem cell reports, 2019. **12**(2): p. 381-394.

187. Jung, P., et al., *Isolation and in vitro expansion of human colonic stem cells.* Nature medicine, 2011. **17**(10): p. 1225-1227.

188. Powell, R.H. and M.S. Behnke, *WRN conditioned media is sufficient for in vitro propagation of intestinal organoids from large farm and small companion animals.* Biology open, 2017. **6**(5): p. 698-705.

189. Rustad, K.C., et al., *Enhancement of mesenchymal stem cell angiogenic capacity and stemness by a biomimetic hydrogel scaffold.* Biomaterials, 2012. **33**(1): p. 80-90.

190. Vazin, T. and D.V. Schaffer, *Engineering strategies to emulate the stem cell niche.* Trends in biotechnology, 2010. **28**(3): p. 117-124.

191. Lou, Y.-R. and A.W. Leung, *Next generation organoids for biomedical research and applications.* Biotechnology advances, 2018. **36**(1): p. 132-149.

192. Jin, M.-Z., et al., *Organoids: An intermediate modeling platform in precision oncology.* Cancer letters, 2018. **414**: p. 174-180.

193. Gjorevski, N., et al., *Designer matrices for intestinal stem cell and organoid culture.* Nature, 2016. **539**(7630): p. 560-564.

194. Qian, X., et al., *Brain-region-specific organoids using mini-bioreactors for modeling ZIKV exposure.* Cell, 2016. **165**(5): p. 1238-1254.

195. Onozato, D., et al., *Generation of intestinal organoids suitable for pharmacokinetic studies from human induced pluripotent stem cells.* Drug Metabolism and Disposition, 2018. **46**(11): p. 1572-1580.

196. Bardenbacher, M., et al., *Permeability analyses and three dimensional imaging of interferon gamma-induced barrier disintegration in intestinal organoids.* Stem cell research, 2019. **35**: p. 101383.

197. Sato, T., et al., *Long-term expansion of epithelial organoids from human colon, adenoma, adenocarcinoma, and Barrett's epithelium.* Gastroenterology, 2011. **141**(5): p. 1762-1772.

198. Hill, D.R., et al., *Real-time measurement of epithelial barrier permeability in human intestinal organoids.* JoVE (Journal of Visualized Experiments), 2017(130): p. e56960.

199. Pearce, S.C., et al., *Marked differences in tight junction composition and macromolecular permeability among different intestinal cell types.* BMC biology, 2018. **16**(1): p. 19.

200. Spence, J.R., et al., *Directed differentiation of human pluripotent stem cells into intestinal tissue in vitro.* Nature, 2011. **470**(7332): p. 105.

201. McCracken, K.W., et al., *Generating human intestinal tissue from pluripotent stem cells in vitro.* Nature protocols, 2011. **6**(12): p. 1920.

202. Watson, C.L., et al., *An in vivo model of human small intestine using pluripotent stem cells.* Nature medicine, 2014. **20**(11): p. 1310.

203. Ogaki, S., et al., *A cost-effective system for differentiation of intestinal epithelium from human induced pluripotent stem cells.* Scientific Reports, 2015. **5**(1): p. 17297.

204. Gupta, N., et al., *Microfluidics-based 3D cell culture models: Utility in novel drug discovery and delivery research.* Bioengineering & Translational Medicine, 2016. **1**(1): p. 63-81.

205. Balijepalli, A. and V. Sivaramakrishan, *Organs-on-chips: research and commercial perspectives.* Drug Discovery Today, 2017. **22**(2): p. 397-403.

206. Kim, H.J., et al., *Human gut-on-a-chip inhabited by microbial flora that experiences intestinal peristalsis-like motions and flow.* Lab Chip, 2012. **12**(12): p. 2165-2174.

207. Bein, A., et al., *Microfluidic Organ-on-a-Chip Models of Human Intestine.* Cellular and Molecular Gastroenterology and Hepatology, 2018. **5**(4): p. 659-668.

208. Kim, H.J. and D.E. Ingber, *Gut-on-a-Chip microenvironment induces human intestinal cells to undergo villus differentiation.* Integrative Biology, 2013. **5**(9): p. 1130-1140.

209. Shim, K.Y., et al., *Microfluidic gut-on-a-chip with three-dimensional villi structure.* Biomedical Microdevices, 2017. **19**(2): p. 37.

210. Workman, M.J., et al., *Enhanced Utilization of Induced Pluripotent Stem Cell–Derived Human Intestinal Organoids Using Microengineered Chips.* Cellular and Molecular Gastroenterology and Hepatology, 2017. **5**(4): p. 669-677.

211. Kasendra, M., et al., *Development of a primary human Small Intestine-on-a-Chip using biopsy-derived organoids.* Scientific Reports, 2018. **8**(1): p. 2871.

212. Trietsch, S.J., et al., *Membrane-free culture and real-time barrier integrity assessment of perfused intestinal epithelium tubes.* Nature Communications, 2017. **8**(1): p. 262.

213. *Duedunum Intestine-Chip*. Available online on: https://emulatebio.com/duodenum-intestine-chip/ [accessed on 01/09/2021].

214. Huh, D., et al., *Microengineered physiological biomimicry: organs-on-chips.* Lab Chip, 2012. **12**(12): p. 2156-2164.

215. Maschmeyer, I., et al., *Chip-based human liver-intestine and liver-skin co-cultures--A first step toward systemic repeated dose substance testing in vitro.* European Journal of Pharmaceutics and Biopharmaceutics, 2015. **95**(Pt A): p. 77-87.

216. Esch, M.B., et al., *Body-on-a-chip simulation with gastrointestinal tract and liver tissues suggests that ingested nanoparticles have the potential to cause liver injury.* Lab on a Chip, 2014. **14**(16): p. 3081-3092.

217. Tottey, W., et al., *The human gut chip "HuGChip", an explorative phylogenetic microarray for determining gut microbiome diversity at family level.* PLoS One, 2013. **8**(5): p. e62544.

218. Bhatia, S.N. and D.E. Ingber, *Microfluidic organs-on-chips.* Nature Biotechnology, 2014. **32**: p. 760.

219. Ingber, D.E., *Reverse Engineering Human Pathophysiology with Organs-on-Chips.* Cell, 2016. **164**(6): p. 1105-1109.

CHAPTER 2 – Overview and aims

2.1. Overview

The pharmaceutical field is constantly requesting for new tools that can enable the speed-up of early screening phases of drug development. *In vitro* intestinal models are used to assess the absorption of compounds that are aimed to be delivered orally to the patients. In the past years many efforts have been made and developments have been achieved in the field of intestinal *in vitro* models, but 2D models are still the most widely used. However, these models are not able to replicate important features of the human small intestine, and may lead to erroneous results. Replicating the 3D environment that cells experience *in vivo*, as well as mimicking cell-cell and cell-matrix interactions, to obtain a physiologically relevant model is important to obtain reliable outcomes. In this thesis, different configurations of 3D *in vitro* intestinal models, mimicking the human small intestine, were developed and tested, in order to validate a credible model for drug screening.

In the framework of this thesis, a collaborative work between the Institute for Research and Innovation in Health (i3S) at the University of Porto (Portugal) and the Institute for Bioengineering of Catalonia (IBEC) at Barcelona (Spain) was established.

The Nanomedicines and Translational Drug Delivery group, led by professor Bruno Sarmento, focus mainly in two areas. (1) The development of drug delivery systems, based on nanotechnology, to obtain functionalized nanomedicines to tackle a myriad of diseases, from different types of cancer to diabetes and inflammation and (2) the establishment of 3D cellular *in vitro* models and organ-on-a-chip platforms that can faithfully replicate *in vivo* characteristics of healthy and injured tissues, with special focus on intestinal and pulmonary tissues and the tumor microenvironment. The combination of these two areas enable testing the absorption and cytotoxicity of the developed nanoformulations, as well as to identify the mechanisms of nanoparticle uptake in a reliable fashion, correlating with the *in vivo* results.

The Biomimetic Systems for Cell Engineering group, led by professor Elena Martínez, is focused on the development of artificial systems that can mimic tissue micro and nanofeatures to perform biomimetic *in vitro* assays. Currently the group's research activities focus on the development and validation of complex *in vitro* models of the small intestine and cardiac tissue and the engineering of a vessel-on-a-chip model to reproduce the tumor metastatic environment, using novel tools such as bioprinting and/or organoids.

The collaboration between these two groups enabled the development of this thesis, improving my scientific and personal skills, while establishing new 3D *in vitro* intestinal models aimed at testing the absorption of compounds.

2.2. Aims and specific objectives

The main aim of this thesis was to establish a new 3D *in vitro* intestinal model to test the absorption of compounds of pharmacological interest. It was expected that this new 3D model could better resemble the human small intestine and, in that sense, provide more reliable results when predicting permeability outcomes. The ultimate objective was that this model could be adopted as a new standard *in vitro* intestinal model for permeability screening.

The specific objectives were:

1. To establish a layer that could mimic the intestinal lamina propria, composed by type I collagen and human intestinal fibroblasts (HIF), which should maintain its integrity in culture for 21 days, sustaining the differentiation of epithelial cells on top and the further development of the model (Chapter 3);

2. To unveil the crosstalk between the different cells composing the model, disclosing key factors that can lead to collagen contraction by fibroblasts (Chapter 3);

3. To add the epithelial layer, fully characterize the models and test paracellular and transcellular absorption (Chapter 4 and 5);

4. To add the endothelial layer, mimicking the blood vessels present in the intestinal lamina propria *in vivo*, and understand its impact in terms of cellular behavior and permeability outcomes (Chapter 5);

5. To introduce the characteristic 3D architecture of the small intestine, establishing a model containing villus-like structures, and understand the impact of these structures in cellular behavior and permeability outcomes (Chapter 6).

2.3. Structure

This thesis was organized in seven chapters. Chapter 1 contains a revision of the literature, focusing on the physiology of the small intestine, the mechanisms implicated in absorption and the *in vitro* models developed to predict this process. Chapter 2 provides a general overview of the work performed, as well as the institutions involved in the work. The main aim, as well as the specific objectives of the study, are also elucidated. Chapter 3 details the procedures to obtain a collagen layer with embedded fibroblasts, which mimics the intestinal lamina propria and provides the 3D features to the model. In this chapter, the crosstalk between the different types of cells is elucidated, regarding the contraction of the matrix by fibroblasts. Chapter 4 describes the formation of the epithelial layer on top of the collagen hydrogel and the outcomes of permeability assays with a paracellular marker after 14 days in culture. Chapter 5 describes a further optimization of the collagen layer, enabling it to sustain integrity for 21 days in culture, as well as the addition of the endothelial layer underneath the lamina propria. In this chapter, a complete characterization of the model is described, as well as permeability screening with paracellular and transcellular compounds. In Chapter 6 the impact of the villi structures found in the human small intestine is disclosed, both in terms of cellular behavior as well as intestinal absorption. Lastly, Chapter 7 contains the overall conclusions of the work, as well as the future perspectives. At the end, an appendix supporting chapters 5 and 6 is provided.

CHAPTER 3 – Optimization of the collagen layer with embedded fibroblasts

The information provided in part 3.3 - The impact of the different cells on collagen contraction by fibroblasts was based in the following publication:

Macedo M.H., Barros A.S., Martínez E., Barrias C.C., Sarmento B., 2021, All layers matter: Innovative three-dimensional epithelium-stroma-endothelium intestinal model for reliable permeability outcomes, *submitted*.

In this paper I was responsible for the conception, execution and revision of the manuscript. Sofia Barros was responsible for execution of experiments and revision of the manuscript. The supervisors were responsible for reviewing and submit the manuscript. This paper was not previously included in other thesis, and it is partially reproduced in this section.

3.1. Abstract

In vitro tools are very important in the field of oral drug delivery, since they represent an easy and economical way of getting important results before moving into more sophisticated experiments, which normally involve using animals, thus implicating higher costs and ethical issues. In this sense, it is very important that these platforms are reliable and provide trustable results on intestinal absorption processes and mechanisms. Research on *in vitro* models as platforms to perform permeability studies has received much attention and new models are constantly being developed. The Caco-2 model is still the most widely used, although it is too simplistic, not representing the 3D physiology and cellular complexity of the tissue.

In the present work we aimed at establishing a 3D layer composed of collagen type I with embedded human intestinal fibroblasts (HIF). Since it is well known that fibroblasts are able to degrade and contract collagen, several optimizations, both in terms of collagen concentration and cellular density, had to be performed. At the same time, the crosstalk between the epithelial and endothelial cells with the fibroblasts was studied to uncover key players in matrix contraction events. Finally, we were able to obtain a layer that could sustain its integrity for a long time in culture.

3.2. Introduction

The development of intestinal models to study physiological processes *in vitro*, namely intestinal absorption, is a topic that receives great attention. If these platforms are capable of reliably mimicking the human tissue, they can be widely employed in different fields. To build relevant models, 3D cultures must be established, as the cells *in vivo* are in a 3D environment accounting for the proper cell-cell and cell-matrix contacts, and not onto hard 2D polymer membranes.

Different materials are used to mimic the extracellular matrix (ECM) and provide the 3D support to the cells, such as collagen, Matrigel®, alginate and different synthetic polymers [1-8]. The ECM in the body is composed of structural and functional molecules secreted by the cells that reside in the tissue and it is nature's perfect template. The most important features of the materials to be used in the 3D models are to provide the structural support and the microenvironmental niche that is able to modulate cell attachment and behavior [9]. Collagen is one of the most widely used biomaterials to mimic the ECM. This protein is abundantly present in the ECM, constituting its primary structural element, providing tensile strength, directing tissue development and regulating cell adhesion, among other functions [10]. Currently, 29 different types of collagens have been identified, falling into 4 divisions based on their primary structure and the sizes of their triple-helical domain [11]. Type I collagen is part of the fibril-forming collagens and is the most abundant in human tissues and a key player in their structural composition [11, 12]. The intestine is no exception and collagen type I is the major collagen type present in this tissue [13]. Having all the above mentioned into consideration, this biomaterial was chosen to develop the 3D layer of our model.

In a tissue, the ECM can completely surround the cells, as the interstitial matrix of connective tissues, or serve as a substrate for cells to attach, as the basal membrane of epitheliums. For the development of our 3D model, we aimed at mimicking the intestinal lamina propria using a collagen type I network laden with human intestinal fibroblasts (HIF). The behavior of fibroblasts inside collagen matrices has been widely studied and it is well known that these cells are able to contract and degrade collagen. Human fibroblasts cultured in 3D collagen matrices are subjected to a completely different environment relative to the one experienced in 2D cultures [14]. The interaction between the fibroblasts and collagen result in the formation of mechanical entanglements, inducing matrix remodeling by transmitting fibroblast forces to the surrounding matrix. This matrix remodeling depends on several factors, including growth factors and the mechanical environment [14]. For example, fibroblasts under mechanical load are able to develop actin stress fibers and organize a fibronectin-rich matrix, while in the absence of mechanical load cells can become quiescent [15]. On the other hand, factors present in the culture medium, such as fetal bovine serum (FBS), fibronectin, transforming growth factor (TGF), endothelin-1 (ET1), platelet derived growth factor (PDGF), thrombin, lysophosphatidic acid (LPA), and others, can mediate fibroblast contraction and consequent remodeling of the surrounding matrix [15-22].

In this chapter we describe the steps performed to obtain a 3D collagen layer with embedded fibroblasts. Taking all the aforementioned information into consideration, we tested different concentrations of collagen, as well as cellular densities, to obtain a layer that could sustain integrity in culture for 21 days and harbor the epithelial cells on top, as this duration is established as the standard time needed for Caco-2 cells to completely differentiate into enterocyte-like cells for most existing intestinal *in vitro* models [23]. It was observed that both collagen and cellular concentration played a role in matrix contraction, but the addition of epithelial and endothelial cells also had a role in this phenomenon.

3.3. Materials and methods

3.3.1. Cell culture conditions

Caco-2 C2BBe1 (regarded as Caco-2 cells) were purchased from American type culture collection (ATCC, USA). Mucus producing HT29-MTX cells were kindly provided by Dr. T. Lesuffleur (INSERM U178, Villejuif, France). Caco-2 and HT29-MTX cell lines were grown in Dulbecco's modified Eagle's medium (DMEM) with 4.5 g/L glucose and Ultraglutamine™ (Gibco), supplemented with 1% Non-Essential Amino Acids (NEAA) 100X (Gibco), 1% Penicillin/Streptomycin 100X (Biowest) and 10% Fetal Bovine Serum (FBS) (Biochrom).

Human intestinal fibroblasts (HIF) primary cells (passage 6) were obtained from ScienCell and were cultured in Fibroblast medium (FM) supplemented with 2% FBS, 1% of Fibroblast Growth Supplement (FGS) and 1% of penicillin/streptomycin solution (all from ScienCell).

Human pulmonary microvascular endothelial cells (HPMEC)-ST1.6R (regarded as HPMEC) cells were kindly provided by professor C. James Kirkpatrick (Institute of Pathology, Johannes Gutenberg University of Mainz, Germany). Cells were cultured (passage 39 to 45) with M-199 medium (Merck) supplemented with 20% (v/v) FBS (Biochrom), 1% (v/v) Penicillin/Streptomycin (Biowest), 25 µg/mL of Endothelial Cell Growth Supplement (ECGS) (Merck), 25 µg/mL of heparin sodium salt from porcine intestinal mucosa (Merck) and 0.1 mg/mL L-glutamine (LabClinics).

Cells were grown separately in tissue culture flasks (SPL) and maintained in an incubator (Binder) at 37ºC and 5% CO_2 in a water saturated atmosphere.

3.3.2. Collagen hydrogel with HIF embedded

To obtain the collagen hydrogels with HIF embedded, 10X Phosphate Buffered Saline (PBS), 1 N sodium hydroxide (NaOH) and FM with HIF with different initial seeding densities were added to the high concentrated rat tail collagen solution (Corning), following supplier recommendations, in order to obtain the desired collagen final concentration. The solution was placed on the 12-well Transwell® inserts (Millicell), using 110 µL to obtain a layer with approximately 1 mm in thickness. The solution was dispersed carefully, in order to cover the entire surface of the insert and then incubated at 37ºC, 5 % CO_2 in a water saturated atmosphere for 30 min to allow gelation. 0.5 mL and 1.5 mL of DMEM, supplemented as described in the previous section, was added to apical and basolateral sides of the inserts, respectively. Different attempts were performed in order to avoid collagen contraction by the fibroblasts, using either different concentrations of collagen, varying the initial seeding density of fibroblasts inside the hydrogels or changing the percentage of FBS in DMEM.

The first attempt to obtain the collagen layer with fibroblasts embedded was performed using a fixed concentration of collagen of 5 mg/mL and testing four different initial seeding densities of fibroblasts (A – 1 x 10^5; B – 2 x 10^5; C - 10 x 10^5 and D – 20 x 10^5 cells/mL) as well as a control without fibroblasts.

The second attempt was performed increasing the concentration of collagen. The initial seeding density of HIF was kept at 1 x 10^5 cells/mL and three different concentrations of collagen were used [E – 5 (same as condition A); F – 6 and G – 7 mg/mL].

In a third attempt, a decrease to the initial number of fibroblasts was performed, using 0.5 x 10^5 cells/mL and the same collagen concentrations of the previous try were used (H – 5; I – 6 and J – 7 mg/mL).

In a fourth attempt, collagen concentration and HIF initial seeding density of HIF were maintained constant at 7 mg/mL and 0.5x10^5 cells/mL, respectively, and the percentage of FBS in cell culture medium was changed [K – 0; L – 2; M – 5 and N – 10% (same as condition J)].

3.3.3. Metabolic activity of the HIF inside the collagen hydrogels

The metabolic activity of the HIF inside the collagen disks was determined at different timepoints using the resazurin assay. Collagen hydrogels with the desired concentration and cell density were obtained, dispersed in 48-well plates and allowed to gel for 30 min inside the incubator at 37ºC, 5% CO_2 in a water saturated atmosphere. After complete gelation, 2 mL of DMEM was added to each well and the plate was placed again in the incubator and the medium was changed every two-three days. The resazurin solution was obtained dissolving 50 mg of resazurin sodium salt (Sigma) into 25 mL of PBS 20X and 475 mL of dH_2O overnight, at room temperature with agitation in the dark, and then filtered. At each timepoint (collagen disks with 1, 7, 14 and 21 days in culture), a solution containing 20% resazurin in DMEM complete was prepared. The solution was pre-warmed to 37ºC and 600 µL was added to each well. The plate was incubated for 2 h at 37ºC, 5% CO_2 in a water saturated atmosphere in order to allow viable cells with active metabolism to reduce resazurin into the resorufin product, which is pink and fluorescent. After the incubation period, samples were quantified by measuring the relative fluorescence units (RFU) using a microplate reader Synergy™ Mx HM550 (Biotek) set at 530/590 (excitation/emission wavelength, respectively).

3.3.4. Visualization of HIF inside the gels

To confirm the presence of the HIF seeded in the collagen hydrogels after the time in culture, as well as the presence of fibronectin, an indicator of fibroblasts ability to secrete

ECM and remodel the matrix, immunostaining assays were performed. Samples were washed once with PBS and fixed using 2% paraformaldehyde (PFA) in PBS for 30 min at room temperature (RT). This step was followed by permeabilization with a solution of 0.2% (v/v) Triton X-100 in PBS for 10 min at RT and samples were washed thrice with PBS for 5 min. After, a blocking step was performed using a blocking solution (BS) containing 1.5% bovine serum albumin (BSA) and 5% FBS in PBS for 1h at RT. Samples were then transferred to a humidified chamber and were incubated with mouse anti-human vimentin primary antibody (1:50) (sc-6260, Santa Cruz Biotechnology) + rabbit anti-human fibronectin primary antibody (1:50) (F3648, Sigma Aldrich) overnight at 4ºC. After incubation with the primary antibodies, samples were washed three times for 5 min with a solution of 0.05% Tween-20 in PBS (PBST). This was followed by incubation with the secondary antibodies F(ab')2-Goat anti-Mouse IgG (H+L) Cross-Adsorbed, Alexa Fluor 594 (A-11020, Thermofisher Scientific) (1:500) + Goat anti-Rabbit IgG (H+L) Cross-Adsorbed, Alexa Fluor 488 (A-11008, Thermofisher Scientific) (1:500) and cell nuclei were counterstained with DAPI (Sigma Aldrich) (500 ng/mL). Finally, cells were washed twice with PBST and once with PBS for 5 min and kept in PBS in the dark until visualization by a spectral confocal laser scanning microscope TCS-SP5 AOBS (Leica).

3.3.5. Seeding of the epithelial layer

Collagen hydrogels with the desired concentration and HIF density were obtained as previously described. After the 30 min gelation process, Caco-2 or Caco-2 + HT29-MTX ($1x10^5$ cells/cm^2 at a 9:1 ratio, respectively) in 0.5 mL of DMEM, were added on top of the fibroblast-laden collagen layer. 1.5 mL of DMEM was added to the basolateral side and plates were incubated at 37ºC, 5% CO_2 in a water saturated atmosphere. The cultures were maintained during 21 and the medium of the models was changed every 2-3 days. For this part, several attempts were also performed, whereas for the first three attempts only Caco-2 cells were added on top of the collagen hydrogels and on the last attempt both Caco-2 or a combination of Caco-2 + HT29-MTX cells were used.

In the first attempt, the conditions used were the previously optimized of 7 mg/mL of collagen concentration, an initial seeding density of HIF of 0.5×10^5 cells/mL and 5% FBS in cell culture medium.

In a second attempt, the initial seeding density of fibroblast varied (O – 2×10^5; P – 3×10^5; Q – 4×10^5 and R – 5×10^5 cells/mL), while concentration of collagen used was 7 mg/mL and the percentage of FBS was increased, once again, to 10%. This percentage of FBS was maintained for the following attempts.

The third attempt consisted in maintaining the initial cell number constant at 5 x 10^5 cells/mL and varying the collagen concentration [S – 5; T – 6 and U – 7 mg/mL (same as condition R)].

In the fourth attempt a collagen concentration of 6 mg/mL and a HIF initial seeding density of 5 x 10^5 cells/mL were used, whereas the epithelial layer was changed [V – Caco-2 (same as condition T) and X – Caco-2 + HT29-MTX].

3.3.6. Seeding of the endothelial layer

HPMEC cells were seeded by inverting the 12-well Transwell® inserts on 6-well plates (SPL) and coating the basolateral side of the insert with 100 µL of 0.2% gelatin (Merck) for 1h at RT to stimulate cellular adhesion. After 1 h, excess of gelatin was removed and HPMEC cells were seeded (5 x 10^4 cells/cm^2) using a suspension volume of 100 µL. The cells were allowed to adhere for 2 h at RT and 1 mL of PBS was placed in each well to maintain humidity and prevent cells from drying. After 2 h, Transwell® inserts were moved into 12-well plates (VWR) in the normal configuration and the collagen and epithelial layers were added, as previously described.

3.3.7. Quantification of ET-1, PDGF-BB and TGF-ß1

Endothelin-1 (ET-1), Platelet-derived Growth Factor BB (PDGF-BB) and Transforming Growth Factor Beta (TGF-ß) present in the medium of different configurations of the 3D models were quantified using the enzyme linked immunosorbent assay (ELISA).

The medium samples were collected at different timepoints (7, 14 and 21 days) and immediately frozen until further analysis. For the quantification of ET-1, PDGF-BB and TGF-ß, the Endothelin-1 (ET-1) Human ELISA Kit (EIAET1, Invitrogen), Human PDGF-BB ELISA Kit (RAB0398, Merck) and Human TGF-ß1 ELISA Kit (RAB0460, Merck) were used, respectively, following manufacturer's instructions.

For the quantification of ET-1, 50 µL of prepared standards or samples were added to the wells. The plate was sealed and incubated for 60 min at RT. After incubation, solution from the wells was discarded and wells were washed 4 times with 1x wash buffer. Then, 50 µL of endothelin-1 conjugate was added to each well and incubated again for 60 min at RT and the washing step was repeated. 100 µL of 3,3',5,5'-Tetramethylbenzidine (TMB) substrate was then added and the plate was incubated for 30 min at RT. Lastly, 50 µL of stop solution was added to each well and the absorbance was immediately read at 450 nm using a microplate reader (SynergyTM Mx HM550, Biotek).

For the determination of the amounts of PDGF-BB and TGF-ß in the samples, 100 µL of each prepared standard and samples were added to each well and the plates were covered and incubated for 2.5 h at RT with gently shaking. After the incubation period, the solutions of each well were discarded and wells were washed 4 times with 1x wash solution. Then, 100 µL of prepared 1x Biotinylated Detection Antibody was added to each well and the plate was incubated for 1 h at RT with gentle shaking. The solution was then discarded and the washing step was repeated. 100 µL of prepared horseradish peroxidase (HRP)-Streptavidin solution was then added to each well and incubated for 45 min at RT with gentle shaking and, after incubation, solution was discarded and the washing step was, once again, repeated. 100 µL of ELISA colorimetric TMB reagent was added to each well and the plate was incubated in the dark for 30 min, at RT and with gently shaking. Finally, 50 µL of stop solution was added to each well and the absorbance was immediately read at 450 nm using a microplate reader.

3.3.8. Quantification of MMP-2 and MMP-9

The gelatinases Metalloproteinases 2 and 9 (MMP-2 and 9) present in the medium of different configurations of the 3D models were quantified through gelatin zymography. Medium was collected at different timepoints (7, 14 and 21 days) and immediately frozen until further analysis. The procedure was performed as previously described [23]. Briefly, protein content in the samples was determined by Dc Protein Kit (Bio-rad) and 7.5 µg of protein were mixed with sample buffer [10% sodium dodecyl sulfate (SDS), 4% sucrose and 0.03% bromophenol blue in 0.5 M Tris-HCl, pH 6.8 (all from Sigma)] and separated on a 10% polyacrylamide gel containing 1% gelatin (Sigma) as substrate. Gels were subjected to electrophoresis and then washed twice with Triton X-100 for 15 min each wash under agitation at 50 rpm. This was followed by incubation with MMP substrate buffer (50 mM Tris-HCl, pH 7.5 and 10 mM CaCl2 and NaN2) for 16h at 37ºC. Gels were stained with 0.1% Coomassie Brilliant Blue R-250 (Sigma), 7.5% acetic acid and 50% ethanol (Merck) and then a De-stained in a solution of 20% Methanol and 10% Acetic acid (Merck) until bands were clear. Gels were visualized and scanned using a GS-800 Calibrated Densitometer (Bio-rad) and the area of the bands was calculated using Image J software.

3.3.9. Statistical analysis

Statistical analysis was performed using the software GraphPad Prism 8.0 (GraphPad Software Inc.). All results are represented as mean ± standard error of the mean (SEM). Statistical differences were calculated using 2-way analysis of variance (ANOVA) multiple comparisons test. The level of significance was set at probabilities of $^{*}p < 0.05$, $^{**}p < 0.01$, $^{***}p<0.001$, $^{****}p<0.0001$.

3.4. Results and discussion

3.4.1. Optimization of the collagen layer with embedded HIF

The first attempt to obtain the collagen layer with embedded fibroblasts was performed using a fixed collagen concentration and varying the initial HIF seeding density. It is well known that fibroblasts are able to generate traction forces and lead to matrix contraction when they are cultured in 3D collagen gels [22, 25, 26]. In this sense, a high collagen concentration of 5 mg/mL was used and different HIF seeding densities were embedded in the hydrogels to assess their behavior: A – 1 x 10^5; B – 2 x 10^5; C - 10 x 10^5 and D – 20 x 10^5 cells/mL. This high concentration of collagen was based on the reference values in native tissues, which is normally above 5 mg/mL, although most of the developed 3D use lower concentrations [27].

It was possible to observe that fibroblasts were able to contract the collagen disks in all conditions, proportionally to increasing HIF concentration (Figure 3.1). The metabolic activity of the cells inside the disks was also assessed (Figure 3.2), relating with cell number, where disks with higher HIF density presented significant higher metabolic activity. The three conditions with higher concentration of cells reached a plateau in metabolic activity after 14 days, which was probably related to space constraints that prevented cells from proliferating. Condition A presented a stairway profile along the time in culture, being that by 21 days in culture, no significant differences were observed between conditions. Results indicate that, overall, fibroblasts were able to grow and proliferate inside the collagen hydrogels. To better characterize the cells phenotype and their ability to produce endogenous ECM, the presence of vimentin and fibronectin was analyzed (Figure 3.3) in condition A after 21 days, since this was the hydrogel that showed less contraction. Fibroblasts expressed vimentin, presented an elongated shape and were capable of secreting fibronectin, which assembled into a fibrous meshwork in the extracellular space.

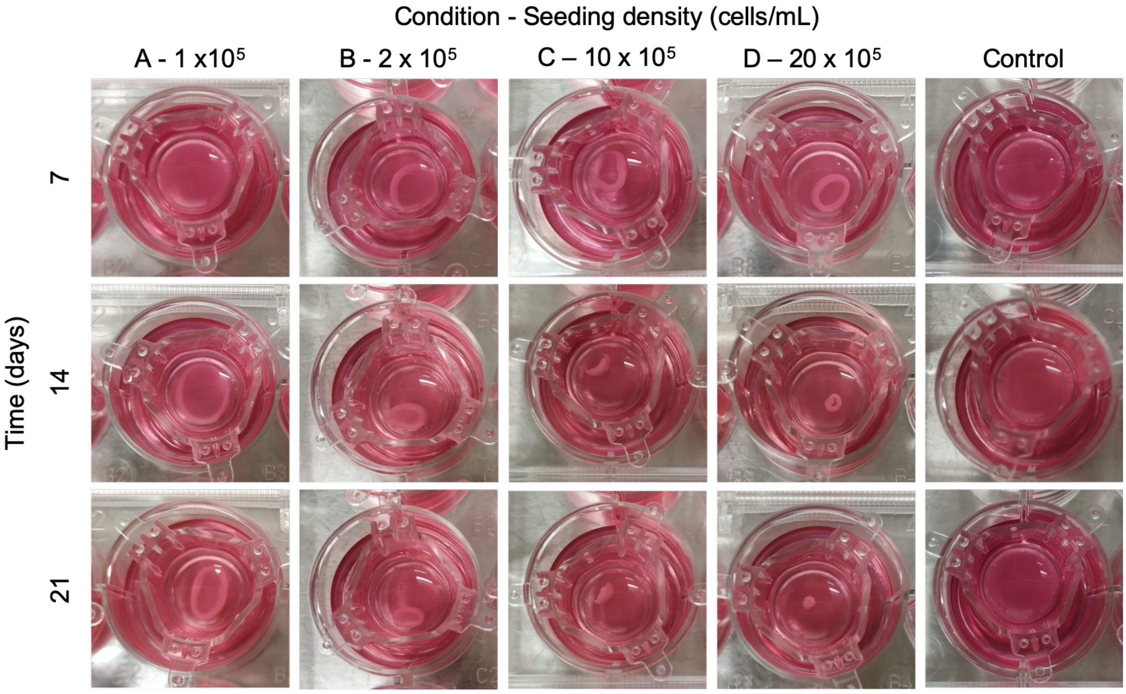

Figure 3.1 - First attempt with embedded HIF in the collagen hydrogels to determine the optimal concentration of HIF. Different HIF seeding densities (A – 1 x 10^5; B – 2 x 10^5; C - 10 x 10^5 and D – 20 x 10^5 cells/mL) were embedded in the disks with a collagen concentration of 5 mg/mL. A control without cells was used confirm if contraction was related to the presence of fibroblasts.

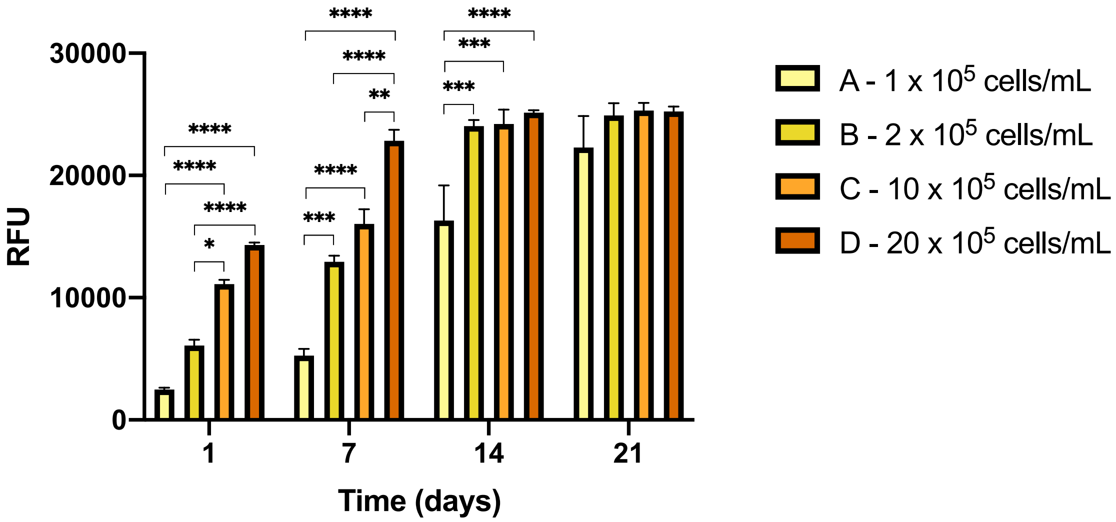

Figure 3.2 - Metabolic activity of the HIF inside the collagen hydrogels with different initial seeding densities (A – 1 x 10^5; B – 2 x 10^5; C – 10 x 10^5 and D – 20 x 10^5 cells/mL) at different timepoints (1, 7, 14 and 21 days). Results are the average of triplicates and bars represent the standard error of the mean (SEM). Statistical differences $p < 0.05$ are denoted by (*), $p < 0.01$ are denoted by (**), $p < 0.001$ are denoted by (***) and $p < 0.0001$ are denoted by (****).

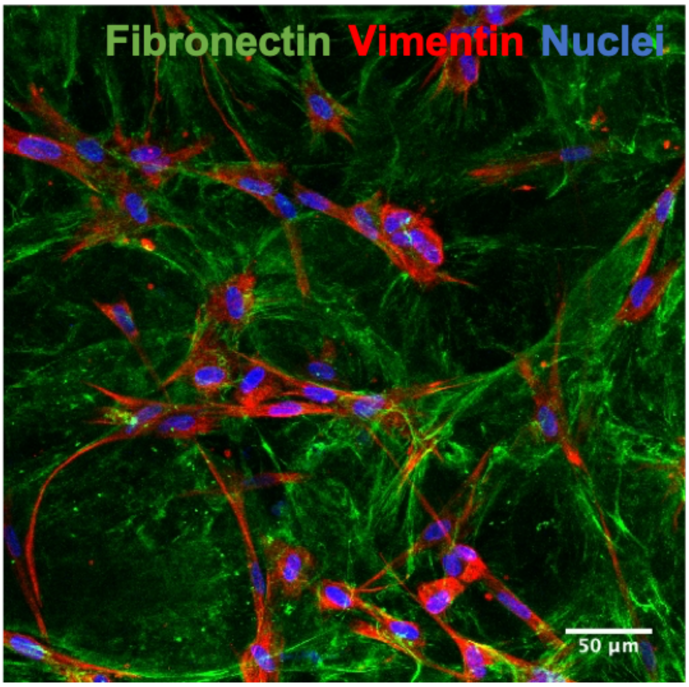

Figure 3.3 – **Vimentin** and **fibronectin** deposition by human intestinal fibroblasts in collagen hydrogels in condition A (1 x 10^5 cells/mL) after 21 days in culture. Picture depicts a maximal projection of the several stacks of the gel. Fibronectin and vimentin were labelled with Alexa-Fluor 488 and with Alexa-Fluor 594, respectively. The nuclei were counterstained with DAPI.

A second attempt was performed to limit the contraction of the collagen hydrogels by fibroblasts. A higher collagen concentration was tested, while HIF concentration was kept constant, since it is known that initial collagen concentration may regulate the degree of contraction [26]. The chosen initial seeding density was 1 x 10^5 cells/mL, considering that this was the density that led to least contraction in attempt number 1. Collagen concentration varied and three different concentrations were tested: E – 5 (same as condition A); F – 6 and G – 7 mg/mL.

It was possible to observe that an increase in collagen concentration led to a decrease in collagen contraction, as expected, but it was not able to prevent it completely (Figure 3.4). Contraction was minimal in condition G, where collagen concentration was the highest, but it was still observable. To understand if this increase in collagen concentration would impact cell metabolism, metabolic activity was assessed (Figure 3.5). The increase in collagen concentration to 7 mg/mL (Condition G) led to a lower metabolic activity of the cells. However, since this concentration was the one with the most promising results regarding collagen contraction and considering that cells were still metabolically active, this concentration was used in further attempts.

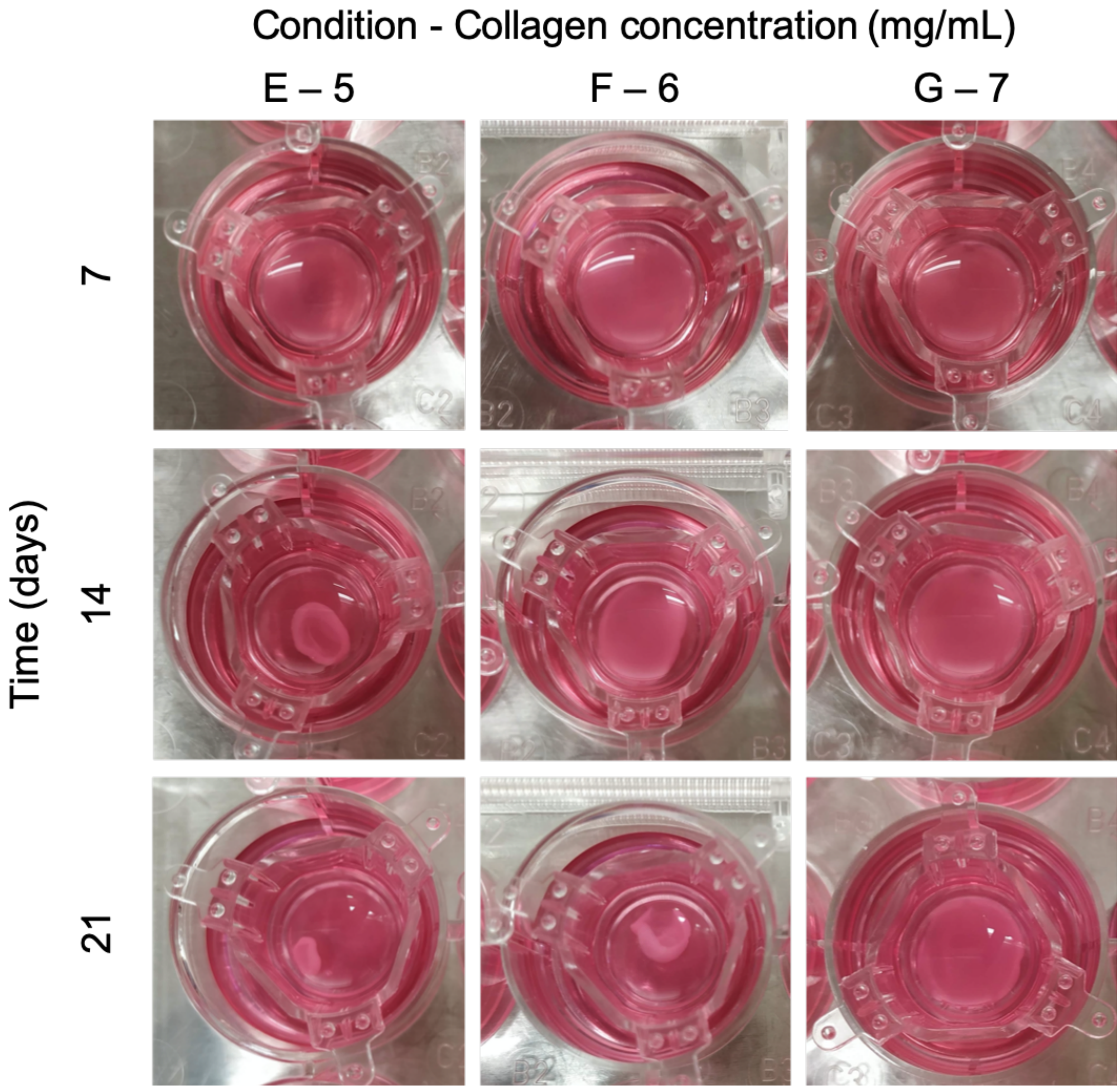

Figure 3.4 - Second attempt with HIF embedded in the collagen hydrogels to determine the optimal concentration of collagen. Different collagen concentrations (E - 5; F – 6 and G – 7 mg/mL) were used with HIF embedded in an initial seeding density of 1 x 10^5 cells/mL. The behavior of the disks was assessed during 21 days.

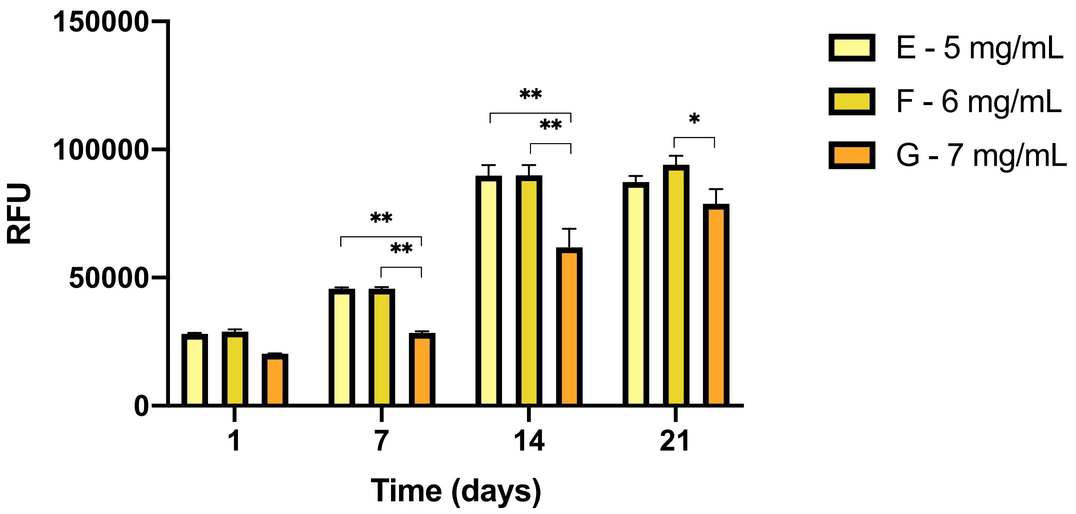

Figure 3.5 - Metabolic activity of the HIF (initial seeding density of 1 x 10^5 cells/mL) inside the collagen hydrogels with different concentrations (E – 5; F - 6 and G – 7 mg/mL) at different timepoints (1, 7, 14 and 21 days). Results are the average of triplicates and bars represent the standard error of the mean (SEM). Statistical differences were calculated using 2-way ANOVA multiple comparisons to compare between cellular viability in each condition for each timepoint ($p<0.05$ are denoted by * and $p<0.01$ are denoted by **).

In a third attempt, a lower density of HIF (0.5 x 10^5 cells/mL) was tested, while the collagen concentrations from previous attempt were maintained (H – 5; I – 6 and J – 7 mg/mL).

As for the previous attempt, it was possible to observe that an increase in the collagen concentration led to less contraction, without completely avoiding it (Figure 3.6). The level of contraction was very similar in both attempts, although the initial density of fibroblasts was lower this time. Again, contraction was minimal in the gels with a concentration of 7 mg/mL, but still occurred. Metabolic activity was evaluated (Figure 3.7) and it was significantly lower for the condition with the highest collagen concentration (condition J). These results may be due to the fact that a higher concentration of collagen leads to a hydrogel with tighter and stiffer networks that act as physical barriers for cell proliferation [28-30]. Although metabolic activity was significantly lower in the gels with a concentration of 7 mg/ml of collagen, they still showed metabolic activity, meaning they were alive by the end of time in culture. Since there had to be a compromise between cellular viability and contraction, the next attempt was performed using this high collagen concentration.

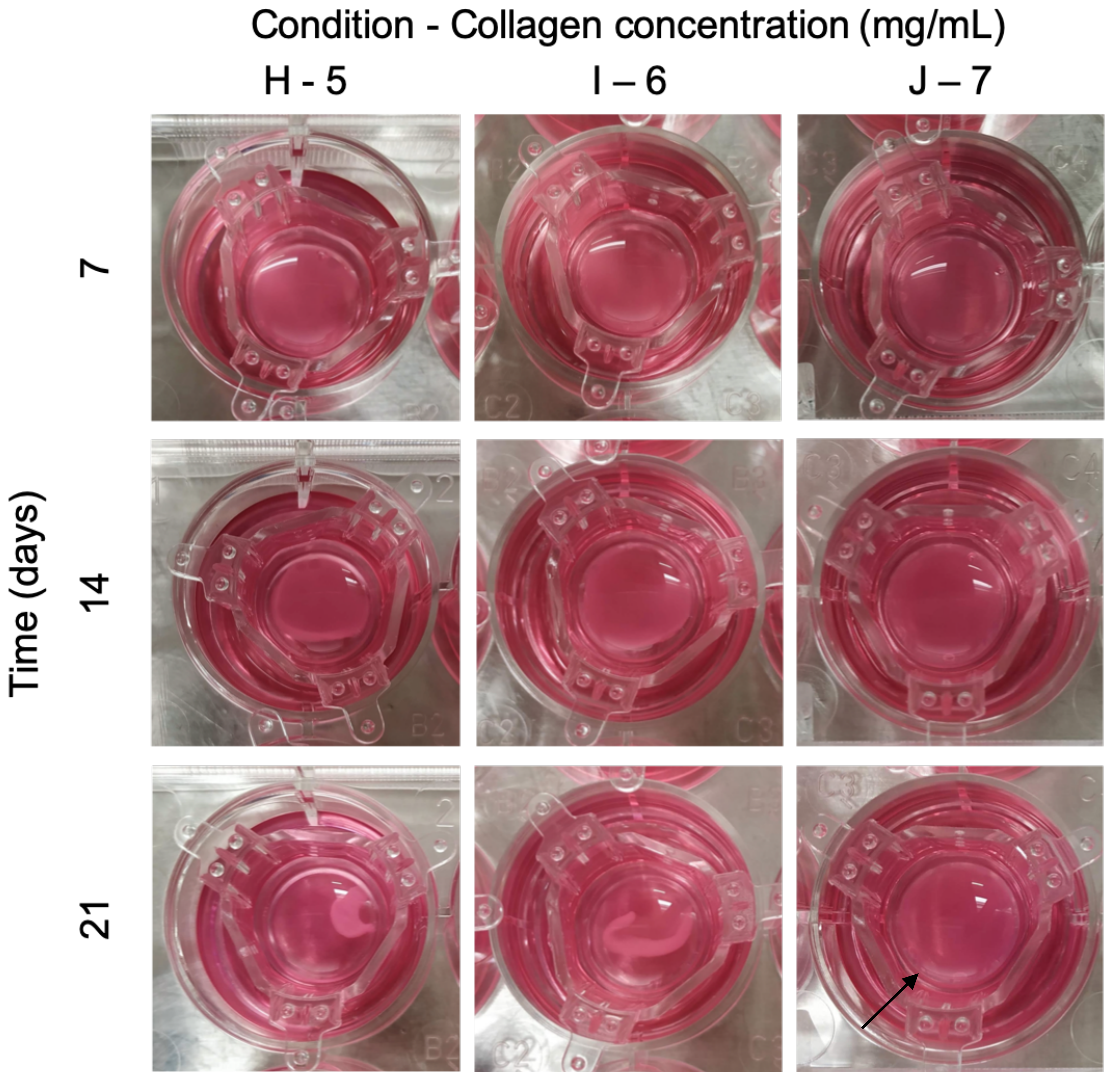

Figure 3.6 - Third attempt with HIF embedded in the collagen hydrogels to determine the optimal concentration of collagen. Different collagen concentrations (H - 5; I - 6 and J – 7 mg/mL) were used with HIF embedded in an initial seeding density of 0.5 x 10^5 cells/mL. The behavior of the disks was assessed during 21 days.

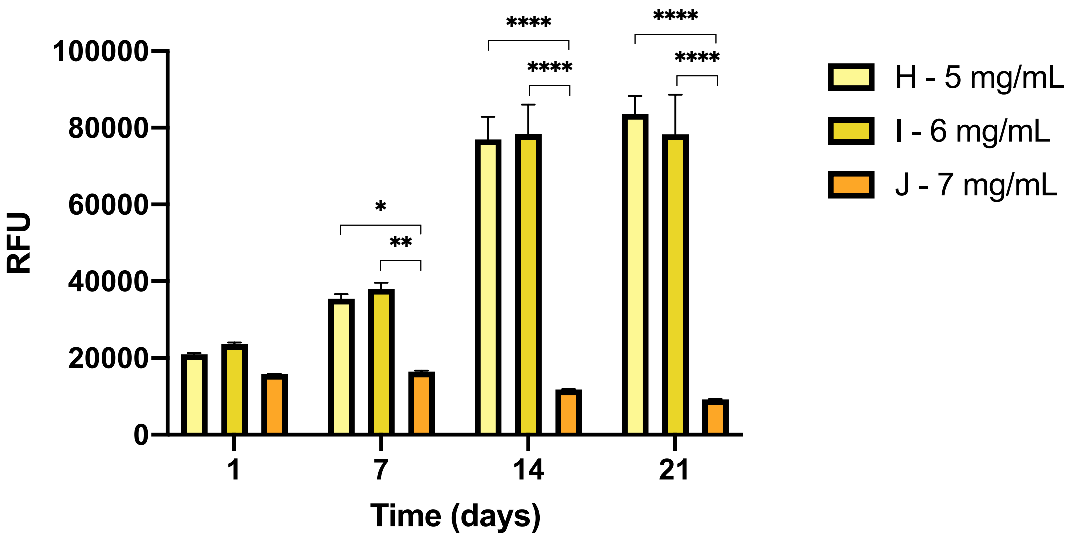

Figure 3.7 - Metabolic activity of the HIF (initial seeding density of 0.5 x 10^5 cells/mL) inside the collagen hydrogels with different concentrations (H – 5; I - 6 and J – 7 mg/mL) at different timepoints (1, 7, 14 and 21 days). Results are the average of triplicates and bars represent the standard error of the mean (SEM). Statistical differences were calculated using 2-way ANOVA multiple comparisons to compare between cellular viability in each condition for each timepoint ($p<0.05$ are denoted by *, $p<0.01$ are denoted by ** and $p<0.0001$ are denoted by ****).

More bibliographic research about the contraction of collagen by fibroblasts was performed to disclose possible players contributing to this behavior, and it was found that FBS could be an important variable in the study, as FBS can stimulate contraction by the cells [31-33]. Therefore, in the fourth attempt, a decrease of the percentage of FBS was tested. Fibroblast initial seeding density was maintained at 0.5 x 10^5 cells/mL, collagen concentration at 7 mg/mL and the percentage of FBS varied [K – 0; L – 2; M – 5 and N – 10% (same as condition J)].

A decrease in the percentage of FBS proved to be a good strategy to prevent collagen contraction (Figure 3.8). The metabolic activity was, once again, evaluated (Figure 3.9) and significant differences were observed between conditions at days 14 and 21, being the conditions with lower percentages of FBS the ones presenting lower levels of metabolic activity. This result was expected since the presence of serum in culture medium enhances cellular proliferation [34]. Condition M was the one showing a higher metabolic activity, without matrix contraction. Thus, the expression of vimentin and fibronectin was assessed in this condition to guarantee that fibroblasts were still capable of maintaining their elongated shape and secrete ECM components, as it had been previously observed. It was possible to see that some fibroblasts could be found inside the collagen gels, although the cell density was clearly lower than in the first attempt (Figure 3.10). Most of the fibroblasts presented an elongated shape and expressed vimentin. Fibronectin was also detected, showing a heterogeneous distribution inside the gel. Overall, this condition represented a good compromise and was, therefore, selected for further experiments.

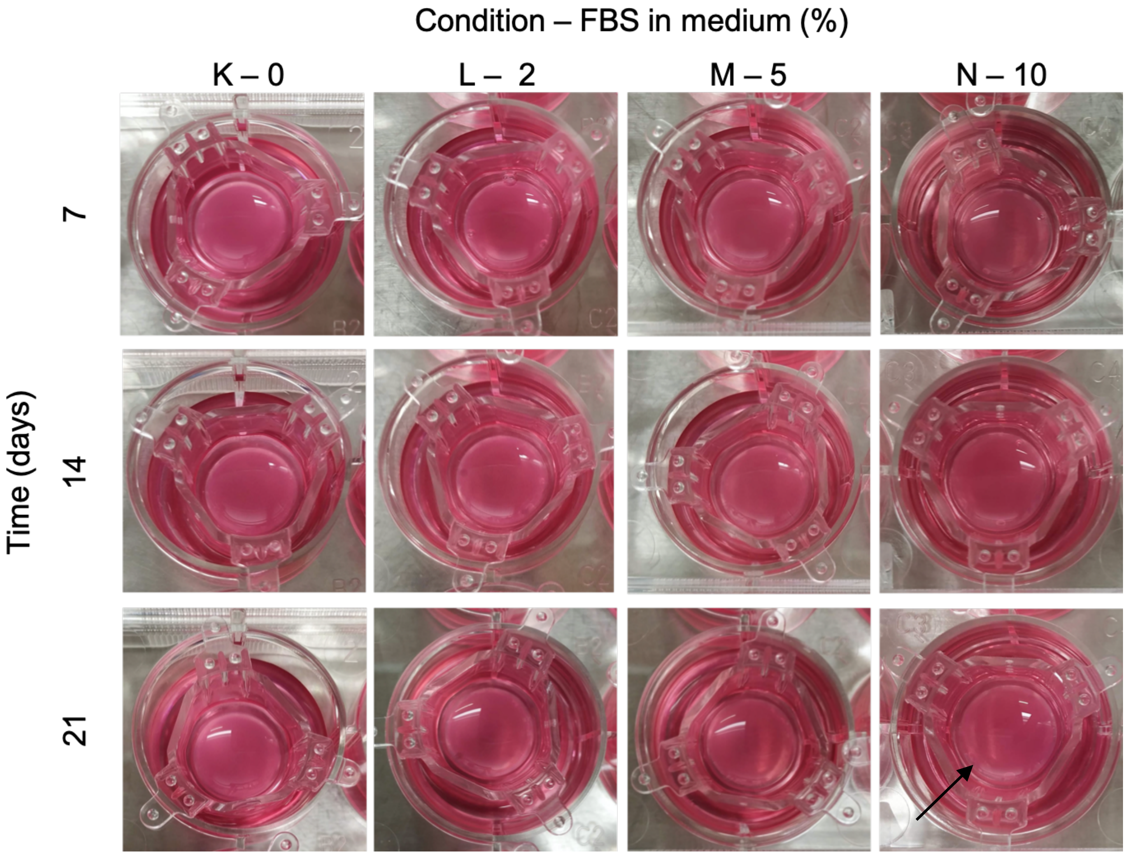

Figure 3.8 - Fourth attempt with HIF embedded in the collagen hydrogels to determine the optimal concentration of FBS in medium to prevent contraction. Different percentages of FBS in cell culture medium (K – 0; L - 2; M – 5 and N – 10%) were used in hydrogels with a collagen concentration of 7 mg/mL and a HIF initial seeding density of 0.5 x 10^5 cells/mL. (The pictures for condition N are the same as for condition J). The behavior of the disks was assessed during 21 days.

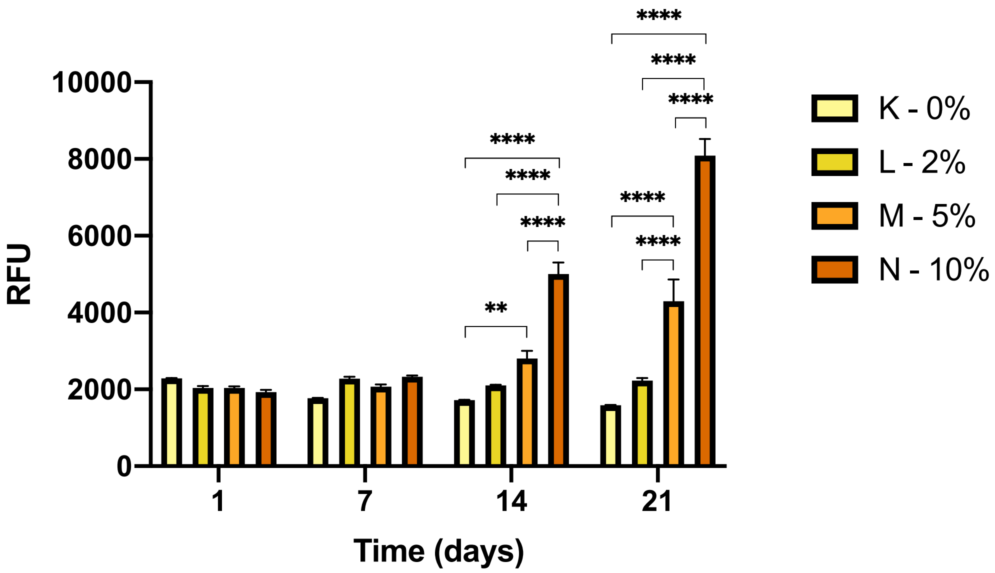

Figure 3.9 - Metabolic activity of the HIF (initial seeding density of 0.5 x 10^5 cells/mL) inside the collagen hydrogels with a collagen concentration of 7 mg/mL and different percentages of FBS in cell culture medium (K - 0; L – 2; M – 5 and N – 10%) at different timepoints (1, 7, 14 and 21 days). Results are the average of triplicates and bars represent the standard error of the mean (SEM). Statistical differences were calculated using 2-way ANOVA multiple comparisons to compare between cellular viability in each condition for each timepoint (p<0.01 are denoted by ** and p<0.0001 are denoted by ****).

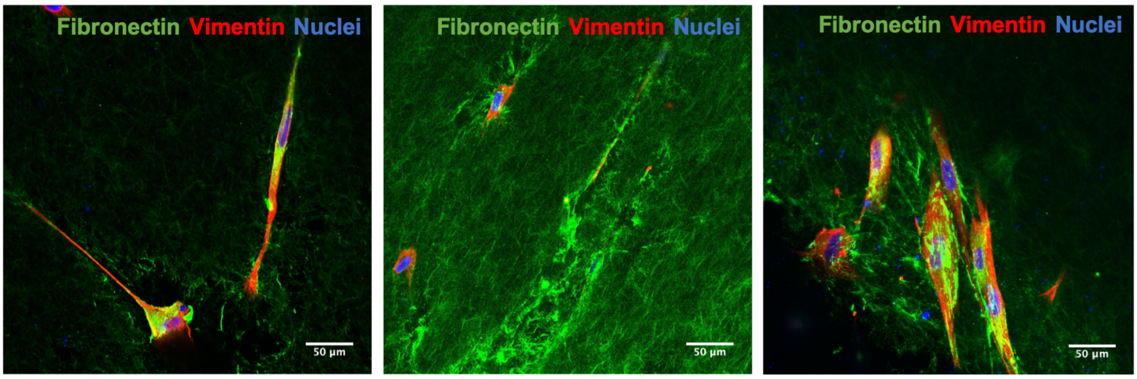

Figure 3.10 - **Vimentin** and **fibronectin** deposition by human intestinal fibroblasts in collagen hydrogels in condition M (5% FBS) after 21 days in culture. Fibronectin and vimentin were labelled with Alexa-Fluor 488 and with Alexa-Fluor 594, respectively. The nuclei were counterstained with DAPI.

3.4.2. Seeding of epithelial cells

After optimizing the conditions to obtain collagen hydrogels with embedded fibroblasts and limited contraction (collagen concentration of 7 mg/mL, HIF initial seeding density of 0.5 x

10^5 cells/mL and 5% of FBS in cell culture medium), Caco-2 cells were seeded on top of the hydrogel layer.

In the first attempt, the metabolic activity of the fibroblasts could not be measured, since epithelial cells were also in culture, so their viability inside the gels was assessed by immunocytochemistry. However, no fibroblasts were found inside the hydrogel by the end of the time in culture. Considering this, another attempt was made, increasing again the initial seeding density of fibroblasts (O – 2 x 10^5; P – 3 x 10^5; Q – 4 x 10^5 and R – 5 x 10^5 cells/mL) and returning to a concentration of 10% FBS in cell culture medium to stimulate their proliferation. Collagen concentration was maintained at 7 mg/mL.

Once more, after 21 days in culture, the presence of HIF inside the hydrogels was assessed through immunocytochemistry and, again, fibroblasts were not present, suggesting they were still not able to survive and proliferate under these conditions. Following the same reasoning as before, it was decided to decrease again collagen concentration [S – 5; T – 6 and U – 7 mg/mL (same as condition R)] and use the higher density of fibroblasts tested in the previous attempt (5 x 10^5 cells/mL) to stimulate their survival and proliferation. From this moment on, FBS percentage was always kept at 10%.

In this attempt, contraction was observed again for condition S at 14 and 21 days and for condition T at 21 days, while no contraction was observed for condition U, as expected (Figure 3.11). However, as observed in the previous attempt, there were no fibroblasts inside the 7 mg/mL hydrogels after 21 days in culture. The presence of vimentin and fibronectin was assessed for condition T, since between conditions S and T, this was the one where integrity was maintained for a longer period of time. Fibroblasts were alive in this condition, presenting their prototypical elongated shape and secreting fibronectin (Figure 3.12). As expected, more fibroblasts were observed in the hydrogels after 21 days, as compared to 14 days, as they had more time to proliferate.

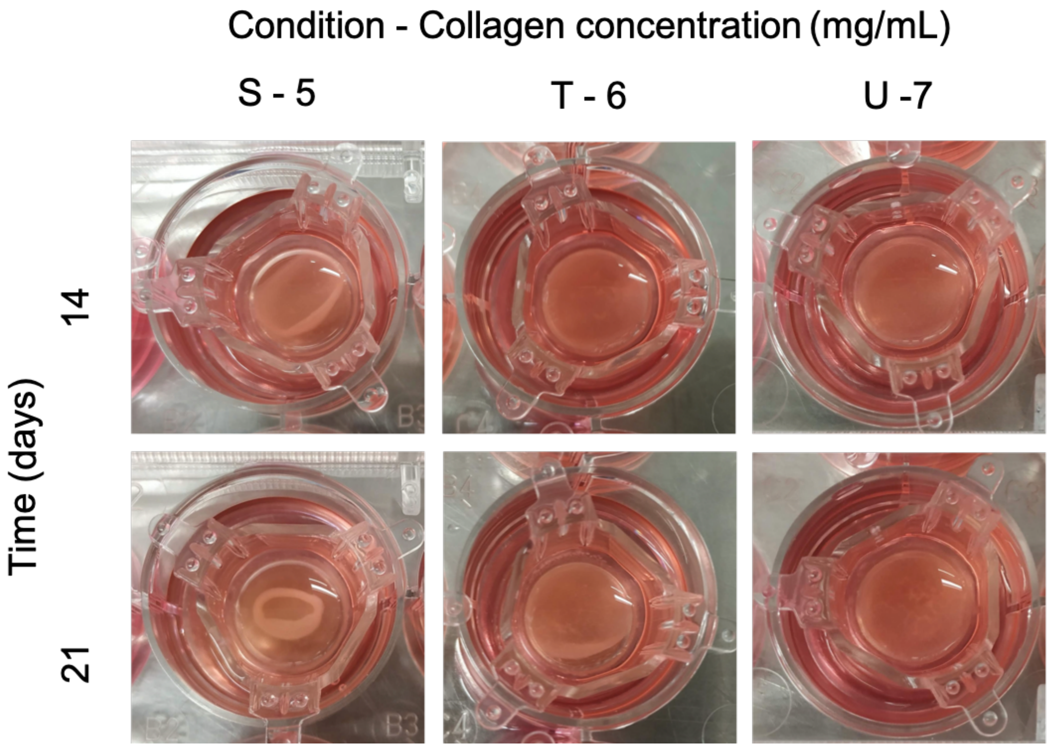

Figure 3.11 - Third attempt of the collagen hydrogels with fibroblasts embedded and Caco-2 cells on top to determine the optimal concentration of collagen to prevent contraction. Different concentrations of collagen (S – 5; T - 6 and N – 7 mg/mL) were used and the HIF initial seeding density was maintained at 5 x 10^5 cells/mL. The behavior of the disks was assessed at 14 and 21 days.

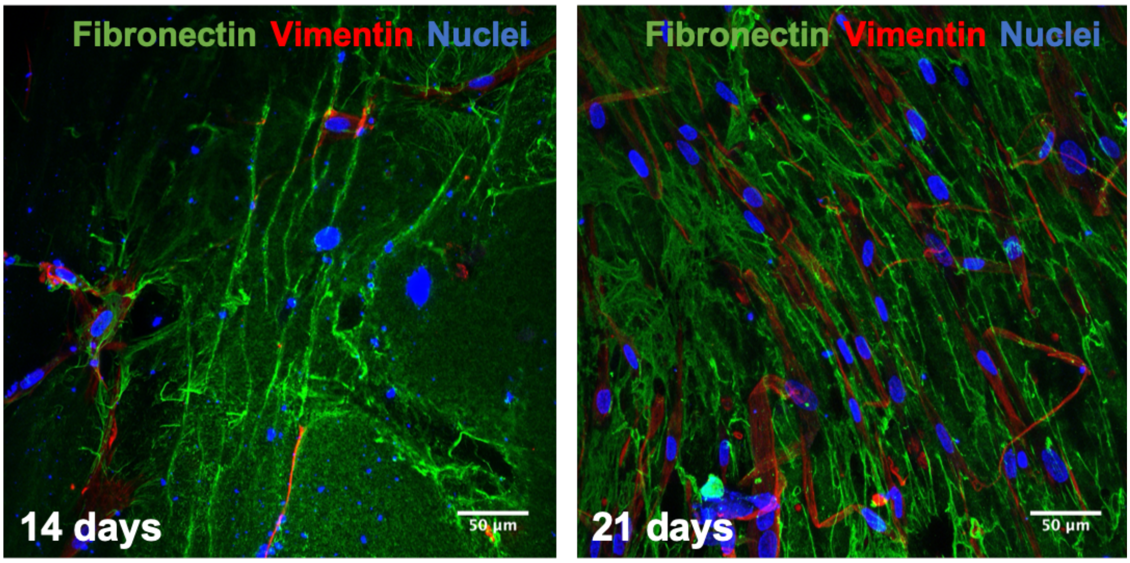

Figure 3.12 - Vimentin and fibronectin deposition by human intestinal fibroblasts in collagen hydrogels in condition T (collagen concentration 6 mg/mL) after 14 and 21 days in culture. Picture depicts a maximal projection of the several stacks of the gel. Fibronectin

and vimentin were labelled with Alexa-Fluor 488 and with Alexa-Fluor 594, respectively. The nuclei were counterstained with DAPI.

In a fourth attempt, the addition of HT29-MTX cells to the model was performed. Considering that in the final model, the intention would be to have both types of epithelial cells (Caco-2 and HT29-MTX), it was decided to test if these cells could somehow affect fibroblast behavior and ability to contract the collagen matrix. Collagen concentration was kept at 6 mg/mL and the HIF initial seeding density at 5 x 10^5 cells/mL, while the epithelial layer was changed [V – Caco-2 (same as condition T) and X – Caco-2 + HT29-MTX].
Surprisingly, this time, hydrogels from condition V contracted before day 14 (which had not occurred in the previous attempt), while hydrogels from condition X where able to maintain their integrity for a longer period of time, but still contracting after 14 days in culture. These new findings allowed to withdraw two major conclusions: (1) the presence of the epithelial layer on top of the hydrogel influences the behavior of fibroblasts, as it was hypothesized before, since contraction was different when Caco-2 or a mixture of Caco-2 + HT29-MTX cells were seeded; and (2) the concentration of the stock solution of collagen used affects the behavior of fibroblasts inside the gels. To perform these experiments, different bottles of collagen were used. Since these bottles were from different batches, the collagen concentration varied. Besides, as collagen comes from a natural source, there is an intrinsic variability from batch to batch, which can have implications on the outcomes. This change in lot number was not considered as a potential inducer of variability because, in the end, the final concentration of collagen was the same. The last attempt, where, for the same condition, results were different from the previous attempt (conditions V and T) indicates the potential effect of changing the concentration of the collagen stock solution, since this was the only variable from one attempt to another. It is likely that the concentration of the stock solution has an impact on cellular behavior because the amounts of PBS, NaOH and cell culture medium used to obtain the hydrogel varies according to the initial collagen concentration. When using a stock solution with a lower concentration, a higher amount is needed. For this reason, cells were able to survive in condition M, but not in the following attempt, where a collagen bottle with a lower concentration was used and, therefore, more collagen and less medium was required in the mixture. On the other hand, when epithelial cells were added, from attempt number 2 to attempt number 3, the opposite occurred. A bottle with a higher concentration of collagen was used, so less collagen was needed in order to obtain the same final concentration, which enabled cells to grow and proliferate more freely, leading to higher contraction.
Considering this, it was decided to keep the same batch number of collagen stock during the entire project, to avoid variability. Therefore, a new optimization of the conditions had to

be performed. Based on previous results, it was decided to use a collagen concentration of 6 mg/mL and a fibroblast initial seeding density of 1 x 10^5 cells/mL, without epithelial cells on top first. With these conditions, contraction did not occur and fibroblasts were metabolically active inside the hydrogels (Figure 3.13), presenting an elongated shape, secreting fibronectin and remodeling the surrounding matrix (Figure 3.14). Taking this into account, epithelial cells were seeded on top and further studies were performed, as depicted in the following chapter.

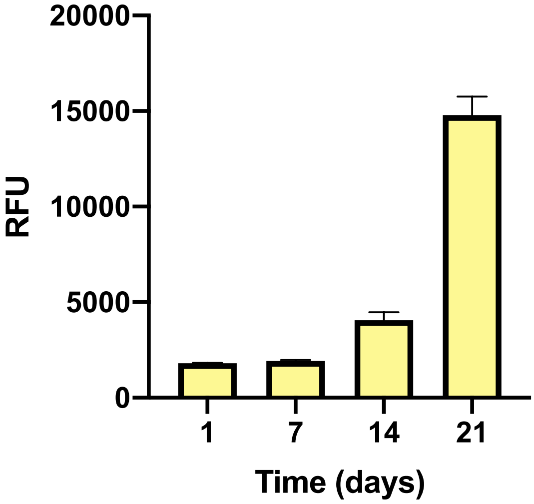

Figure 3.13 - Metabolic activity of the HIF (initial seeding density of 1 x 10^5 cells/mL) inside the collagen hydrogels with a collagen concentration of 6 mg/mL at different timepoints (1, 7, 14 and 21 days). Results are the average of triplicates and bars represent the standard error of the mean (SEM).

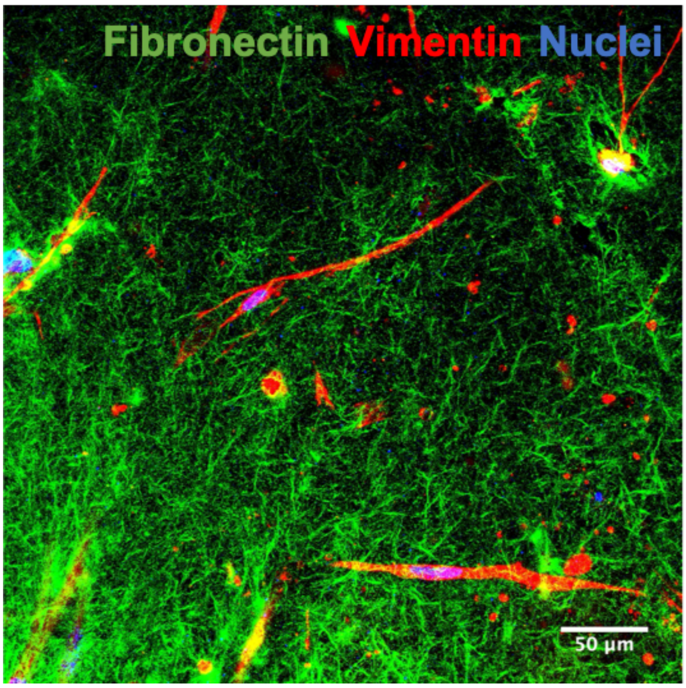

Figure 3.14 - Vimentin and fibronectin deposition by human intestinal fibroblasts in hydrogels with a collagen concentration of 6 mg/mL and a HIF initial seeding density of 1 x 10^5 cells/mL after 21 days in culture. Picture depicts a maximal projection of the several stacks of the gel. Fibronectin and vimentin were labelled with Alexa-Fluor 488 and with Alexa-Fluor 594, respectively. The nuclei were counterstained with DAPI.

3.4.3. The impact of the different cells on collagen contraction by fibroblasts

After realizing that epithelial cells could have an impact on the contraction of the collagen gels by the fibroblasts, it became clear that the addition of endothelial cells could also play a role in this phenomenon. In fact, it was observed that when only Caco-2 or HPMEC were seeded with the HIF-laden collagen gels, contraction of the disks would always occur around day 14, or even sooner, mainly for the endothelial cells. However, when HT29-MTX were added contraction would not occur. Since the number and type of fibroblasts were the same, as well as collagen concentration, this behavior could be linked to soluble factors secreted by the cells, that could eventually be modulated by the presence of HT29-MTX cells.

The extent of contraction can vary depending on fibroblast source and density, the collagen concentration and the presence of specific soluble factors [22]. Studies regarding the cellular crosstalk occurring between the different type of cells present in the model have shown that some secreted compounds can influence the behavior of fibroblasts and their contractile behavior [16-22].

To address this hypothesis, the secretion levels of soluble factors that were selected based on literature findings evidencing they could have an effect on the contractile ability of fibroblasts where analyzed, when in co-culture with epithelial and endothelial cells [16-22]. Examples of such factors are TGF- ß1, ET-1, PDGF-BB, fibronectin, thrombin, among others [16-22]. It was observed that the concentration of some of these factors in conditioned media effectively varied depending on the type of cells that were present in the model. In the case of TGF- ß1 (Figure 3.15a), concentration in the medium was significantly higher in the configurations HIF + HPMEC and HIF + Caco-2 after 21 days, when comparing to the other configurations, correlating to the contraction observed around day 14 for both of them. The ET-1 peptide (Figure 3.15b) was mainly detected when HPMEC cells were present in the model, suggesting that it was being secreted by these cells, as expected [35]. Notably, levels of ET-1 were significantly higher when only endothelial cells were seeded with the HIF-loaded collagen layer, decreasing when epithelial cells were added, which suggests that epithelial cells may have an inhibitory effect. It was also possible to observe that ET-1 levels were higher at day 14 of culture, when contraction would occur.

The presence of PDGF-BB (Figure 3.15c) was not detected in the HIF + Caco-2 configuration, which normally presented contraction. Also, both at days 14 and 21, the concentration of PDGF-BB in the medium was higher for the complete model than for the configuration containing HIF + HPMEC.

Our findings corroborate what has been previously reported, for instance, for TGF-ß, that was shown to enhance the contraction of collagen gels, being involved in the remodeling process of the matrix, inducing fibroblasts to become contractile myofibroblasts and increasing ECM protein deposition [16, 18, 19, 21]. Several studies indicate that co-culturing fibroblasts with epithelial cells leads to a significant increase in fibroblast-associated gel contraction, since these cells may secrete high amounts of this growth factor [17, 19, 22]. In a study employing Caco-2 and HT29 cells, it was confirmed that these cells produced high levels of TGF-ß [17].

In the skin, keratinocytes have been shown to be partially responsible for the induction of alpha-smooth muscle actin (alpha-SMA) in fibroblasts via TGF-ß and ET-1, which has also been shown to regulate the secretion of matrix degrading enzymes by colonic fibroblasts [20, 36]. PDGF also regulates cell division and growth, and also seems to be responsible for enhancing the contractile capability of fibroblasts [37]. Our results indicate that, indeed, TGF- ß1 and ET-1 are likely to contribute to the enhancement of fibroblast contractile capacity in the models, since both factors were present in higher levels in the configurations that showed contraction. Also, the concentration of both compounds was lower when HT29-MTX cells were present, further suggesting that these cells can exert an inhibitory effect on the secretion of these compounds by other cells. However, our results do not support the implication of PDGF-BB in the contraction process.

The cellular crosstalk has also been shown to modulate the levels of metalloproteinases 2 and 9 (MMP 2 and 9) [36]. MMPs are a family of zinc-dependent enzymes known to digest ECM components and are considered important mediators of tissue remodeling [19, 38-40]. MMP2 and MMP9 are known as gelatinases, since their preferential substrate is gelatin. Besides being able of cleaving gelatins, they can also degrade collagen, elastin, fibronectin and other ECM substrates [41, 42]. MMPs are composed of a specific domain sequence including the signal peptide, the pro-peptide domain, the catalytic domain and, present in almost all MMPs, the C-terminal hemopexin-like domain. Most MMPs are synthesized and secreted in the pro-enzyme form, also known as zymogen, which is inactive and, to become active, the cleavage of the pro-peptide domain must occur [39, 41, 42]. A study regarding the epithelial-mesenchymal crosstalk in a human bronchial tissue revealed that epithelial cells were necessary for secretion of Pro-MMP9 and active MMP-2 and that their proteolytic activity was controlled by the tissue inhibitors of metalloproteinases (TIMPs) secreted from mesenchymal fibroblasts, confirming that epithelial-mesenchymal interactions are important for ECM protein degradation and, consequently, matrix contraction [19]. In our models (Figures 13.5d and 3.15e), it was only possible to quantify the activity of the inactive form (Pro-MMP2 and Pro-MMP9), as the bands for the active forms were very subtle, especially at 21 days, and, thus, hard to quantify (Figure A.1 of Appendix). For pro-MMP9, no statistically significant differences were observed between different configurations, and similar levels were detected along the culture. Nevertheless, at day 21, the higher activity in the HIF and HIF + HMPEC configurations is clear. Regarding pro-MMP2, an increase at day 21 was observed in all configurations without HT29-MTX cells, when comparing to the ones where these cells are present. However, the difference is only statistically significant for the HIF + HPMEC configuration.

The results for MMPs levels corroborate the ones obtained for ET-1 and TGF-ß, and further strengthen the hypothesis that the crosstalk between the cells and their secreted factors is modulated by the microenvironment and the type of cells. It is also clear that these complex interactions can lead to alterations on cell behavior. In this case, changes in the cell populations present in the model can modulate the contractile ability of HIF. It seems that HT29-MTX cells have an inhibitory effect over the secretion of some factors by other cells that result in decreased HIF contraction ability, taking, therefore, a leading role in the maintenance of the model integrity.

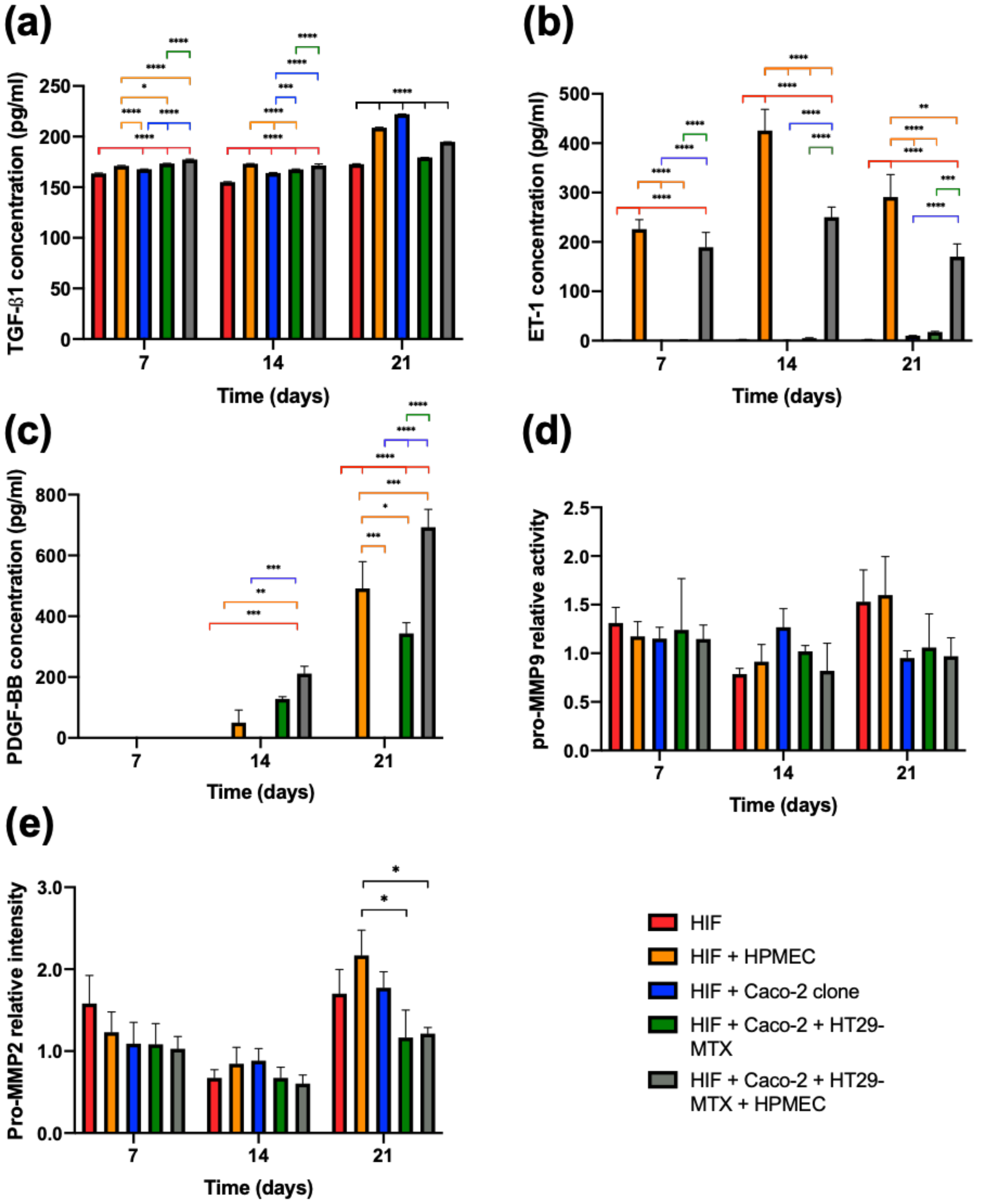

Figure 3.15 - Concentration levels of (a) TGF- ß1, (b) ET-1 and (c) PDGF-BB and relative intensity of (d) pro-MMP9 and (e) pro-MMP2 in the culture medium at different timepoints (7, 14 and 21 days) during the time in culture. Results are the average of triplicates, and bars represent the standard error of the mean (SEM). Statistical differences were calculated using 2-way ANOVA multiple comparisons to compare the levels of each compound in the different cellular configurations for each timepoint ($p<0.05$ are denoted by *, $p<0.01$ are denoted by **, $p<0.001$ are denoted by *** and $p<0.0001$ are denoted by **** and the color represents the reference for each analysis).

3.5. Conclusion

The present study aimed at establishing optimal conditions to form a collagen layer with embedded fibroblasts that could sustain integrity for 21 days in culture to be used in the development of a 3D intestinal *in vitro* model. Different collagen concentrations and initial seeding densities of cells were tested. The number of cells inside the hydrogel, as well as the concentration of collagen were shown to play a role in contraction. Moreover, the concentration of the collagen stock solution, as well as interaction with co-cultured epithelial and endothelial cells showed to have in impact in the contractile ability of fibroblast and remodeling of the surrounding matrix.

To understand the crosstalk between the different cell types present in the model and their influence on the contractibility of fibroblasts, the concentration in the medium of certain growth factors, peptides and metalloproteinases, which can be secreted by the cells, was evaluated. It was observed that Caco-2 and endothelial cells could have a role in enhancing the contractile ability of fibroblasts by secreting TGF-ß1 and ET-1, respectively, while the addition of HT29-MTX leads to a decrease of these compounds and, therefore, to less contraction. This study of cellular interaction can be very important for further studies where these types of cells are used.

Overall, in this study we were able to establish a 3D collagen layer with HIF embedded that is able to maintain its integrity for 21 days in culture, which can now be used to mimic the stromal component of the lamina propria, enabling the establishment of a more physiologically relevant *in vitro* intestinal model.

References

1. Castano, A.G., et al., *Dynamic photopolymerization produces complex microstructures on hydrogels in a moldless approach to generate a 3D intestinal tissue model.* Biofabrication, 2019. **11**(2): p. 1-9.
2. Costello, C.M., et al., *Synthetic small intestinal scaffolds for improved studies of intestinal differentiation.* Biotechnology and Bioengineering, 2014. **111**(6): p. 1222-1232.
3. Dosh, R.H., et al., *Use of hydrogel scaffolds to develop an in vitro 3D culture model of human intestinal epithelium.* Acta Biomaterialia, 2017. **62**: p. 128-143.
4. Li, N., et al., *A fast screening model for drug permeability assessment based on native small intestinal extracellular matrix.* RSC Advances, 2018. **8**: p. 34514-34524.
5. Pereira, C., et al., *Dissecting stromal-epithelial interactions in a 3D in vitro cellularized intestinal model for permeability studies.* Biomaterials, 2015. **56**: p. 36-45.
6. Pusch, J., et al., *The physiological performance of a three-dimensional model that mimics the microenvironment of the small intestine.* Biomaterials, 2011. **32**(30): p. 7469-7478.
7. Sung, J.H., et al., *Microscale 3-D hydrogel scaffold for biomimetic gastrointestinal (GI) tract model.* Lab Chip, 2011. **11**(3): p. 389-392.
8. Wang, L., et al., *Influence of micro-well biomimetic topography on intestinal epithelial Caco-2 cell phenotype.* Biomaterials, 2009. **30**(36): p. 6825-6834.
9. Hussey, G.S., M.C. Cramer, and S.F. Badylak, *Extracellular Matrix Bioscaffolds for Building Gastrointestinal Tissue.* Cellular and Molecular Gastroenterology and Hepatology, 2018. **5**(1): p. 1-13.
10. Rozario, T. and D.W. DeSimone, *The extracellular matrix in development and morphogenesis: A dynamic view.* Developmental Biology, 2010. **341**(1): p. 126-140.
11. Sorushanova, A., et al., *2.15 Collagen: Materials Analysis and Implant Uses☆*, in *Comprehensive Biomaterials II*, P. Ducheyne, Editor. 2017, Elsevier: Oxford. p. 332-350.
12. Henriksen, K. and M.A. Karsdal, *Chapter 1 - Type I Collagen*, in *Biochemistry of Collagens, Laminins and Elastin*, M.A. Karsdal, Editor. 2016, Academic Press. p. 1-11.
13. Graham, M.F., et al., *Collagen content and types in the intestinal strictures of Crohn's disease.* Gastroenterology, 1988. **94**(2): p. 257-65.
14. Rhee, S., *Fibroblasts in three dimensional matrices: cell migration and matrix remodeling.* Experimental & Molecular Medicine, 2009. **41**(12): p. 858-865.

15. Grinnell, F., *Fibroblast–collagen-matrix contraction: growth-factor signalling and mechanical loading.* Trends in Cell Biology, 2000. **10**(9): p. 362-365.
16. Montesano, R. and L. Orci, *Transforming growth factor beta stimulates collagen-matrix contraction by fibroblasts: implications for wound healing.* Proceedings of the National Academy of Sciences of the United States of America, 1988. **85**(13): p. 4894-4897.
17. Drygiannakis, I., et al., *Proinflammatory cytokines induce crosstalk between colonic epithelial cells and subepithelial myofibroblasts: implication in intestinal fibrosis.* Journal of Crohn's and Colitis, 2013. **7**(4): p. 286-300.
18. Finesmith, T.H., K.N. Broadley, and J.M. Davidson, *Fibroblasts from wounds of different stages of repair vary in their ability to contract a collagen gel in response to growth factors.* Journal of Cellular Physiology, 1990. **144**(1): p. 99-107.
19. Ishikawa, S., K. Ishimori, and S. Ito, *A 3D epithelial-mesenchymal co-culture model of human bronchial tissue recapitulates multiple features of airway tissue remodeling by TGF-beta1 treatment.* Respiratory Research, 2017. **18**(1): p. 195.
20. Knowles, J.P., et al., *Endothelin-1 stimulates colon cancer adjacent fibroblasts.* International Journal of Cancer, 2012. **130**(6): p. 1264-1272.
21. Kurosaka, H., et al., *Transforming growth factor-beta 1 promotes contraction of collagen gel by bovine corneal fibroblasts through differentiation of myofibroblasts.* Investigative Ophthalmology & Visual Science, 1998. **39**(5): p. 699-704.
22. Mio, T., et al., *Human bronchial epithelial cells modulate collagen gel contraction by fibroblasts.* American Journal of Physiology, 1998. **274**(1): p. 119-126.
23. Artursson, P. and J. Karlsson, *Correlation between oral drug absorption in humans and apparent drug permeability coefficients in human intestinal epithelial (Caco-2) cells.* Biochemical and Biophysical Research Communnications, 1991. **175**(3): p. 880-885.
24. Cardoso, A.P., et al., *Macrophages stimulate gastric and colorectal cancer invasion through EGFR Y(1086), c-Src, Erk1/2 and Akt phosphorylation and smallGTPase activity.* Oncogene, 2014. **33**(16): p. 2123-2133.
25. Branco da Cunha, C., et al., *Influence of the stiffness of three-dimensional alginate/collagen-I interpenetrating networks on fibroblast biology.* Biomaterials, 2014. **35**(32): p. 8927-8936.
26. Zhu, Y.K., et al., *Contraction of fibroblast-containing collagen gels: initial collagen concentration regulates the degree of contraction and cell survival.* In Vitro Cellular & Developmental Biology, 2001. **37**(1): p. 10-16.

27. Antoine, E.E., P.P. Vlachos, and M.N. Rylander, *Review of collagen I hydrogels for bioengineered tissue microenvironments: characterization of mechanics, structure, and transport.* Tissue Engineering Part B: Reviews, 2014. **20**(6): p. 683-696.
28. Stylianou, A., et al., *Collagen content and extracellular matrix cause cytoskeletal remodelling in pancreatic fibroblasts.* Journal of The Royal Society Interface, 2019. **16**(154): p. 20190226.
29. Roeder, B.A., et al., *Tensile mechanical properties of three-dimensional type I collagen extracellular matrices with varied microstructure.* Journal of Biomechanical Engineering, 2002. **124**(2): p. 214-222.
30. Timraz, S.B.H., et al., *Stiffness of Extracellular Matrix Components Modulates the Phenotype of Human Smooth Muscle Cells in Vitro and Allows for the Control of Properties of Engineered Tissues.* Procedia Engineering, 2015. **110**: p. 29-36.
31. Gouveia, R.M., et al., *The bioactivity of composite Fmoc-RGDS-collagen gels.* Biomaterials Science, 2014. **2**(9): p. 1222-1229.
32. Olson, A.D., *Contraction of collagen gels by intestinal epithelial cells depends on microfilament function.* Digestive Diseases and Sciences, 1993. **38**(3): p. 388-395.
33. Steinberg, B.M., et al., *Establishment and transformation diminish the ability of fibroblasts to contract a native collagen gel.* Journal of Cell Biology, 1980. **87**(1): p. 304-308.
34. Jayme, D., T. Watanabe, and T. Shimada, *Basal medium development for serum-free culture: a historical perspective.* Cytotechnology, 1997. **23**(1-3): p. 95-101.
35. Kowalczyk, A., et al., *The role of endothelin-1 and endothelin receptor antagonists in inflammatory response and sepsis.* Archivum Immunologiae et Therapiae Experimentalis, 2015. **63**(1): p. 41-52.
36. Sawicki, G., et al., *Interaction of keratinocytes and fibroblasts modulates the expression of matrix metalloproteinases-2 and -9 and their inhibitors.* Molecular and Cellular Biochemistry, 2005. **269**(1-2): p. 209-216.
37. Gullberg, D., et al., *Beta 1 integrin-mediated collagen gel contraction is stimulated by PDGF.* Experimental Cell Research, 1990. **186**(2): p. 264-272.
38. Lagente, V., et al., *Role of matrix metalloproteinases in the development of airway inflammation and remodeling.* Brazilian Journal of Medical and Biological Research, 2005. **38**(10): p. 1521-1530.
39. Nagase, H. and J.F. Woessner, Jr., *Matrix metalloproteinases.* Journal of Biological Chemistry, 1999. **274**(31): p. 21491-21494.
40. Visse, R. and H. Nagase, *Matrix metalloproteinases and tissue inhibitors of metalloproteinases: structure, function, and biochemistry.* Circulation Research, 2003. **92**(8): p. 827-839.

41. Lopez-Avila, V. and J. Spencer, *Methods for Detection of Matrix Metalloproteinases as Biomarkers in Cardiovascular Disease.* Clinical Medicine Insights: Cardiology, 2008. **2**: p. 75-87.
42. Lijnen, H.R., *Plasmin and matrix metalloproteinases in vascular remodeling.* Thrombosis and Haemostasis, 2001. **86**(1): p. 324-333.

CHAPTER 4 – Development of an improved 3D *in vitro* intestinal model to perform permeability studies of paracellular compounds

The information provided in this chapter was based in the following publication:

Macedo M.H., Martínez H., Barrias C., Sarmento B., Development of an improved 3D in vitro intestinal model to perform permeability studies of paracellular compounds, Frontiers in Bioengineering and Biotechnology, 8(524018).

In this paper, I was responsible for the conception, execution and revision of the manuscript. The supervisors were responsible for reviewing and submitting the manuscript. This paper was not previously included in another thesis, and it is partially reproduced in this section.

4.1. Abstract

The small intestine is the primary site of drug absorption following oral administration, being paramount the proper monitoring of the absorption process. *In vitro* tools to predict intestinal absorption are particularly important in preclinical drug development since they are less laborious, cost-intensive, and raise less ethical considerations compared to *in vivo* studies. The Caco-2 model is considered the gold-standard of *in vitro* intestinal models regarding the prediction of absorption of orally delivered compounds. However, this model presents several drawbacks, such as the expression of tighter tight junctions, not being suitable to perform permeability of paracellular compounds. Besides, cells are representative of only one intestinal cell type, without considering the role of non-absorptive cells on the absorption pathway of drugs. In the present chapter, we developed a new 3D intestinal model that aims to bridge the gap between *in vitro* tools and animal studies. Our 3D model comprises a collagen layer with human intestinal fibroblasts (HIF) embedded, mimicking the intestinal lamina propria and providing 3D support for the epithelium, composed of Caco-2 cells and mucus producing HT29-MTX cells, creating a model that can better resemble, both in terms of composition and regarding the outcomes of drug permeability when testing paracellular compounds, the human small intestine. HIF morphology and extracellular matrix (ECM) deposition were assessed, confirming fibroblasts presented a normal and healthy elongated shape and secreted fibronectin and laminin, remodeling the collagen matrix. Regarding the epithelial layer, transepithelial electrical resistance (TEER) values decreased when cells were in the 3D configuration, comparing with the 2D analogs (Caco-2 and co-culture of Caco-2+HT29-MTX models), becoming more similar with *in vivo* values. The permeability assay with fluorescein isothiocyanate (FITC)-Dextran 4kDa showed that absorption in the 3D models was significantly higher than in the 2D models, confirming the importance of using a more biorelevant model when testing the paracellular permeability of compounds.

4.2. Introduction

The drug development field is increasingly requesting for reliable tools that can speed up the initial phases of drug development. Indeed, evaluating the absorption of compounds at an early stage of drug discovery is extremely important. Ineffective intestinal absorption allied with undesirable metabolic stability accounts for about 50% of drug failure in clinical studies [1-3]. Understanding the absorption potential of a molecule in the beginning will allow the reduction of animal testing, besides saving time and resources.

Considering that the oral route is the most common and practical non-invasive way to administer a drug, the need for an intestinal model that can properly mimic what happens *in vivo* is unquestionable. In fact, although being the most practical route, not all drugs are suitable to be administered orally, either due to toxicity or poor absorption, and this should be determined as early as possible [4].

In vitro cell-based intestinal models have the advantage of being simple to obtain and produce consistent results and this is why they have been around since the 1980s [5]. Although there have been new developments and improvements to the intestinal *in vitro* models, trying to mimic as closer as possible the human intestine, the Caco-2 model is still considered the "gold-standard". Caco-2 cells are cultured on Transwell® inserts for 21 days in order to differentiate into enterocyte-like cells, forming a polarized monolayer with a brush border membrane, microvilli and tight junctions (TJs) [6]. Besides, these cells express some relevant influx and efflux transporters, as well as enzymes [7]. Nevertheless, this model presents several drawbacks. The fact that these cells present tighter tight junctions than what is observed *in vivo*, makes the permeability of paracellular compounds to be underestimated [8, 9]. This happens because paracellular transport refers to the transfer of substances across the epithelium through the intercellular space between the cells forming it [10]. It is a transport that is unmediated and passive down a concentration gradient. This route normally allows the permeation of hydrophilic molecules (e.g. nadolol, atenolol, terbutaline) which normally are not able to permeate through the lipid membrane and may not have affinity for membrane-bound transporters being, therefore, excluded from transcellular pathway. The TJs gating the entrance to this route restrict the paracellular pathway of transport and this is enhanced in the Caco-2 model, where the presence of TJs is higher than in the human small intestine, forming a very tight monolayer and impeding the passage of paracellular compounds [8, 11]. Besides the tightness of the monolayer, the lower permeability of paracellular compounds in the Caco-2 model may also be attributed to the lower number of pores per cm^2 that is observed in this model, comparing to the human jejunum [12].

To overcome these issues, other cell lines have been proposed to be used in *in vitro* intestinal models, such as Madin-Darby canine kidney (MDCK), Lewis lung carcinoma-porcine kidney 1 (LLC-PK1), 2/4/A1, TC-7 (a Caco-2 subclone), and IEC-18 [13-17]. Besides presenting some advantages, they all possess their own limitations, making the Caco-2 *in vitro* model the most widely accepeted until today. An enhancement of the Caco-2 model has been achieved, co-culturing these cells with HT29-MTX cells. These cells are known to be mucus producers, mimicking the goblet cells of the small intestine. Besides, these cells present looser tight juctions, decreasing the tightness of the monolayer and making it more similar to what is observed *in vivo* [18]. More recently, a triple co-culture model has been developed with the addition of Raji B monocytes, that are capable of secreting factors that make a fraction of Caco-2 cells differentiate into M-cells, that have a role in transepithelial transport [18]. Although this model is more similar to the human small intestine and provides better results regarding the permeability of compounds, it still continues to represent only one layer of the intestine – the epithelium. Besides, cells are seeded on top of the Transwell® insert membranes that do not provide biological cues to the epithelial cells and do not replicate the architecture and mechanisms occurring in the living organ. In fact, cells that are grown in 2D lack the interactions that occur on *in vivo* 3D matrixes, which are crucial for maintaining cell functions and polarity [19, 20]. The presence of a 3D matrix that can resemble the *in vivo* ECM is of paramount importance regarding cell behavior and differentiation [21-23]. Besides, regarding intestinal absorption, the epithelium represents an important role on the process, but it is not the unique anatomic barrier that conditions the permeability of drugs. The small intestine is divided into four main layers: the mucosa, the submucosa, the muscularis propria and the serosa [5]. The absorption process occurs in the mucosa, the most complex layer, which comprises the epithelium, the lamina propria and the muscularis mucosae [22]. The composition of the lamina propria can have a role in the absorption process and influence the behavior of the epithelial cells [24]. Trying to replicate the 3D intestinal environment and develop models that can better replicate the *in vivo* situation to better predict permeability outcomes is of extreme importance. Although being a relatively new topic, 3D models have been explored in the past years and different models have been developed by different groups [25-31]. Each model has its own peculiarities and there is a variety of models, from the ones that are based on scaffolds, to decellularized tissue models, to more complex gut-on-a-chip models or even organoids. In this study, we propose a model that comprises a layer composed of collagen with fibroblasts embedded, developed in the previous chapter, which mimics the intestinal lamina propria, giving support to the epithelium and having a role in the behavior of epithelial cells and in the permeability outcomes. In this study, the aim was to obtain a model that could better resemble the human small intestine, making cells feel a more physiological environment and behaving in a way that could resemble more what is observed *in vivo*. Regarding the permeability of paracellular compounds, underestimated in the Caco-2 models, our hypothesis laid on the possibility of this model providing closer biomimetic conditions, considering the aforementioned reasons.

4.3. Materials and methods

4.3.1. Cell culture conditions

Human colon adenocarcinoma Caco-2 cells (passage 26) were purchased from American type culture collection (ATCC, USA). Mucus producing HT29-MTX (passage 41) cells were kindly provided by Dr. T. Lesuffleur (INSERM U178, Villejuif, France). Caco-2 and HT29-

MTX cell lines were grown in Dulbecco's modified Eagle's medium (DMEM) with 4.5 g/L glucose and Ultraglutamine™ (Gibco), supplemented with 1% Non-Essential Amino Acids (NEAA) 100X (Gibco), 1% Penicillin/Streptomycin 100X (Biowest) and 10% Fetal Bovine Serum (FBS) (Biochrom). Human intestinal fibroblasts (HIF) primary cells (passage 6) were obtained from ScienCell and were cultured in Fibroblast medium (FM) supplemented with 2% FBS, 1% of Fibroblast Growth Supplement (FGS) and 1% of penicillin/streptomycin solution (all from ScienCell). Cells were grown separately in tissue culture flasks (SPL) and maintained in an incubator (Binder) at 37ºC and 5% CO_2 in a water saturated atmosphere.

4.3.2. Collagen hydrogel with HIF embedded

To obtain the collagen hydrogels with HIF embedded, 10X Phosphate Buffered Saline (PBS), 1N Sodium Hydroxide (NaOH) and FM with HIF with an initial seeding density of 1 x 10^5 cells/mL were added to the high concentrated rat tail collagen solution (Corning), following supplier recommendations, in order to obtain a final collagen concentration of 6 mg/mL. The solution was placed on the 12-well Transwell® inserts (Millicell), using 110 µL to obtain a layer with approximately 1 mm of thickness. The solution was dispersed carefully, in order to cover the entire surface of the insert and was incubated at 37ºC, 5% CO_2 in a water saturated atmosphere for 30 min to allow gelation and epithelial cells were then seeded on top of the hydrogels.

4.3.3. Determination of collagen hydrogels rheological properties

To determine the rheological properties of the collagen hydrogels, the rotational rheometer Kinexus Pro (Malvern Instruments) with an 8 mm parallel disc geometry was used. Frequency sweep experiments were performed at 1% strain and a frequency ranging from 0.1 to 10 Hz within the linear viscoelastic region to determine the shear elastic and viscous moduli of the samples. The experiments were performed on collagen disks obtained as previously mentioned, without fibroblasts embedded, with approximately 1 mm thickness and cut into 8 mm diameter disks.

4.3.4. Visualization of collagen hydrogels

Collagen disks with a concentration of 6 mg/mL, without HIF embedded, were obtained, as mentioned previously, to visualize the fibers through atomic force micrsocopy (AFM) and scanning electron cryomicroscopy (CryoSEM).

AFM images in collagen were obtained using a PicoPlus 5500 controller (Keysight Technologies, USA). The images were performed in Contact mode, in liquid (PBS), using a V-shaped MLCT-BIO-DC-D cantilever with a spring constant (k) in the range of 0.03 N/m

(Bruker Corporation, USA). The scan speed was set at 0.5 l/s. The scan size was 30 x 30 μm^2. The software used to obtain the images was the PicoView 1.2 (Keysight Technologies, USA).

The CryoSEM examination was performed using the high-resolution scanning electron microscope JSM 6301F (JEOL), X-Ray microanalysis using INCA Energy 350 (Oxford) and the low temperature sample observation system Alto-2500 (Gatan). The sample was rapidly cooled through immersion in slush nitrogen and transferred, in vacuum, to the sample preparation chamber with cooled platinum. The sample was fractured, sublimated for 120 s at -90ºC and coated with gold/palladium (Au/Pd) by ionic pulverization for 50 s. The sample was then transferred to the SEM chamber and visualization of the sample was performed at -150ºC.

4.3.5. Three-dimensional *in vitro* model

Collagen hydrogels with a concentration of 6 mg/mL and 1 x 10^5 HIF/mL were obtained as previously described. After the 30 min gelation process, Caco-2 cells (1 x 10^5 cells/cm^2) (3D Caco-2) or a mixture of Caco-2 and HT29-MTX (1 x 10^5 cells/cm^2 at a 9:1 ratio, respectively) (3D Co-culture) in 0.5 mL of DMEM, were added on top of the fibroblast embedded collagen layer (Figure 4.1). 1.5 mL of DMEM was added to the basolateral side and plates were incubated at 37ºC, 5% CO_2 in a water saturated atmosphere. Same cell numbers of Caco-2 (2D Caco-2) and Caco-2 + HT29-MTX (2D Co-culture) were added directly on top of inserts without collagen, with the same DMEM volume, to use as 2D controls. The cultures were maintained during 14 or 21 days and the medium of the models was changed every 2-3 days. TEER was periodically measured using an EVOM^2 equipment (World Precision Instruments).

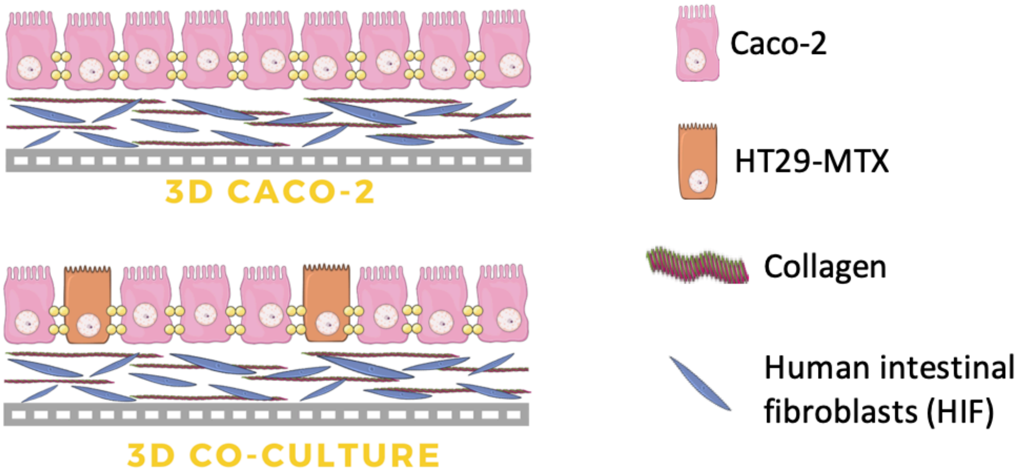

Figure 4.1 - Scheme of the configuration of the 3D intestinal model (3D Caco-2 and 3D Co-culture). The 3D model is composed of a collagen layer with human intestinal fibroblasts embedded and, on top, Caco-2 and HT29-MTX epithelial cells are added in order to mimic the intestinal enterocytes and goblet cells, respectively.

4.3.6. Assessment of HIF morphology and ECM secretion

The morphology of the HIF seeded inside the collagen hydrogels after 14 days was assessed using an antibody against vimentin and expression of fibronectin and laminin was also assessed.

Samples were washed once with PBS and fixed using 2% paraformaldehyde (PFA) in PBS for 30 min at room temperature (RT). After the fixation step, samples were washed three times for 5 min with PBS. This step was followed by permeabilization with a solution of 0.2% (v/v) Triton X-100 in PBS for 10 min at RT and samples were washed thrice with PBS for 5 min. After, a blocking step was performed using a blocking solution (BS) containing 1.5% bovine serum albumin (BSA) and 5% FBS in PBS for 1h at RT. Samples were then transferred to a humidified chamber and were incubated, either with mouse anti-human vimentin primary antibody (1:50) (sc-6260, Santa Cruz Biotechnology) + rabbit anti-human fibronectin primary antibody (1:50) (F3648, Sigma Aldrich) or with mouse anti-human vimentin primary antibody (1:50) + rabbit anti-human laminin primary antibody (1:30) (L9393, Sigma Aldrich) overnight at 4ºC. After incubation with the primary antibodies, samples were washed three times for 5 min with a solution of 0.05% Tween-20 in PBS (PBST). This was followed by incubation with the secondary antibodies F(ab')2-Goat anti-Mouse IgG (H+L) Cross-Adsorbed, Alexa Fluor 594 (A-11020, Thermofisher Scientific)

(1:500) + Goat anti-Rabbit IgG (H+L) Cross-Adsorbed, Alexa Fluor 488 (A-11008, Thermofisher Scientific) (1:500) and cell nuclei was counterstained with 4',6'-diamino-2-fenil-indol (DAPI) (Sigma Aldrich) (500 ng/mL). Finally, cells were washed twice with PBST and once with PBS for 5 min and kept in PBS until visualization by a spectral confocal laser scanning microscope TCS-SP5 AOBS (Leica).

4.3.7. Assessment cell layer formation by hematoxylin & eosin (H&E) staining

To assess cell layer formation in both 2D models at day 14 and 21 and 3D models at day 14, H&E staining was performed. For this, inserts with the cells were washed once with PBS for 5 min and fixed using 2.5% glutaraldehyde and 2% PFA in 0.1 M phosphate buffer (PB) for 1 h at RT. Then, inserts were washed thrice with PBS for 5 min and kept in PBS at 4ºC until further processing for paraffin embedding. Sections of 3 µm were obtained using a RM2255 microtome (Leica). Sections were then stained for H&E. Briefly, sections were deparaffinized and rehydrated, stained 3 min in Gil's Hematoxylin (ThermoScientific), 6 min in running water, dehydrated, stained 1 min in Eosin Y (ThermoScientific), cleared and mounted in Entellan (Merck).

4.3.8. Assessment of cell layer formation, tight junction and MUC2 expression by immunocytochemistry

The formation of an intact layer was confirmed using an antibody against EpCAM and the presence of TJs was assessed using Claudin-1 and ZO-1, which are integral transmembrane and peripheral TJ proteins, respectively. The presence of adherens junctions was evaluated using an antibody against E-chaderin. MUC2 was evaluated because is the mucin that is mostly expressed in the small intestine [32].

The models were washed with PBS and fixed with 2% PFA for 30 min. Then, cells were washed three times with PBS. The models were submersed in a solution of sucrose 15% (in PBS) for 3h and, after that, they were left overnight in a solution of 30% sucrose. Then, models were embedded in Optimal Cutting Temperature (OCT) compound (Kaltek) and frozen at -20ºC. Sections with 7 µm were obtained using a HM550 cryostat (Microm).

To stain with different antibodies, the slides with the cuts were dipped into PBS to dissolve the OCT. A permeabilization step using a solution of 0.2% (v/v) Triton X-100 in PBS for 5 min at RT was performed. After, slides were washed thrice with PBS for 5 min. A blocking step was performed using a solution containing 1.5% BSA and 5% FBS in PBS for 1 h at RT. Slides were incubated with the primary antibodies' solutions [rabbit anti-human EpCAM primary antibody (1:250) (10694-R028, Sino Biological) + mouse anti-human Vimentin primary antibody (1:100) (sc-6260, Santa Cruz Biotechnology) or rabbit anti-human Zona

Occludens 1 (ZO-1) primary antibody (1:50) (sc-10804, Santa Cruz Biotechnology) + mouse anti-human MUC2 primary antibody (1:50) (ab118964, Abcam) or rabbit anti-human Claudin-1 primary antibody (1:200) (MA5-16351, Thermofisher) or mouse anti-human E-cadherin primary antibody conjugated with Alexa Fluor 488 (1:100) (324110, Biolegend)] overnight at 4ºC. Slides where washed three times for 5 min with PBST and incubated with the secondary antibodies and DAPI to counterstain the nuclei (500 ng/mL) (Sigma). For the first two combinations, F(ab')2-Goat anti-Mouse IgG (H+L) Cross-Adsorbed, Alexa Fluor 594 (A-11020, Thermofisher Scientific) (1:500) and Goat anti-Rabbit IgG (H+L) Cross-Adsorbed, Alexa Fluor 488 (A-11008, Thermofisher Scientific) (1:500) were used and for Claudin-1, the secondary antibody against rabbit (Alexa Fluor 488) was used. Secondary antibodies were added to samples for 3h at 4ºC. For E-cadherin, no secondary antibody was needed, since the primary antibody was already conjugated to a fluorochrome. Slides were then washed twice with PBST and once with PBS, all for 5 min. Slides were mounted using fluorescent mounting medium (Dako). Samples were left to dry overnight protected from light at 4ºC and were maintained in these conditions until visualization by a spectral confocal laser scanning microscope TCS-SP5 AOBS (Leica). Since the aim was to compare the amount and localization of tight and adherens junctions between samples, laser power and gain of each laser were maintained for all samples regarding each antibody.

4.3.9. Permeability assay with FITC-Dextran

Permeability of fluorescein isothiocyanate (FITC)-Dextran 4 kDa (Sigma) was performed through the 3D and 2D intestinal models to assess the robustness of each model regarding paracellular transport. FITC-dextran with a molecular weight of 4 kDa was chosen because it represents a measure for paracellular permeability of the intestinal epithelium [33]. The permeability assays were performed at the 14th and 21st day of culture.

Culture medium was removed from both sides of the Transwell® inserts and models were washed twice with pre-warmed Hanks balanced salt solution (HBSS). After the washes, 1.5 mL and 0.5 mL of HBSS were placed on the basolateral and apical sides of the inserts, respectively, and they were allowed to equilibrate for 30 min at 37ºC and 100 rpm in a KS 4000 ic control orbital shaker (IKA). After 30 min, HBSS on the apical side was replaced by 0.5 mL of 200 µg/mL FITC-Dextran dissolved in HBSS. At pre-determined timepoints (15, 30, 45, 60, 90, 180, 240 and 300 min), TEER was measured in order to assess the monolayers integrity and a sample of 200 µL was taken from the basolateral side and replaced by the same amount of HBSS. At the end of the assay, a sample from the apical side was taken. The amount of FITC-Dextran was measured using a Synergy microplate reader (Biotek) at excitation/emission wavelengths of 490/520. The permeability results were expressed in percentage of release and apparent permeability (P_{app}), that was calculated using the following equation:

$$P_{app} = \frac{\Delta Q}{A \times C_0 \times \Delta t}§$$

Where ΔQ is the amount of compound detected in the basolateral side (mg), A is the surface area of the insert (cm^2), C_0 is the initial concentration in the apical compartment (mg/mL) and Δt is the time of the experiment (seconds).

4.3.10. Statistical analysis

To perform statistical analysis, the software GraphPad Prism 7.0 (GraphPad Software Inc.) was used. All results are represented as mean ± standard error of the mean (SEM). Differences between groups in percentage of permeability were compared using one-way analysis of variance (ANOVA) Tuckey's post hoc test. Differences in resazurin and P_{app} results were compared using T-student test. The level of significance was set at probabilities of $^*p<0.05$, $^{**}p<0.01$, $^{***}p<0.001$ and $^{****}p<0.0001$.

4.4. Results and discussion

4.4.1. Collagen hydrogels properties

Rheological assays allowed the determination of the elastic and viscous components of the shear modulus (Figure 4.2a) under test conditions. The average value of the elastic component of the shear modulus was 483 ± 106 Pa, while the viscous component was 198 ± 18 Pa, indicating the disks are soft matrices and rheological values are within normal values for the intestinal lamina propria, whose elastic modulus is between 0.5 and 1 kPa [34-36]. Nevertheless, comparisons with human values or values found in the literature are not straightforward. Using different equipments, e.g. a rheometer or a nanoindentation tester, or even using the same equipment but changing the geometry, introduces variability to the results, making it hard to compare with the existing literature.

AFM (Figure 4.2b) and CryoSEM (Figure 4.2c and d) techniques showed that hydrogels have a porous mesh, with random porous size, ranging from less than 1 to 10 μm, and random distribution. This highly porous structure was expected, since hydrogels are composed mainly by water, enabling the survival and proliferation of fibroblasts [37].

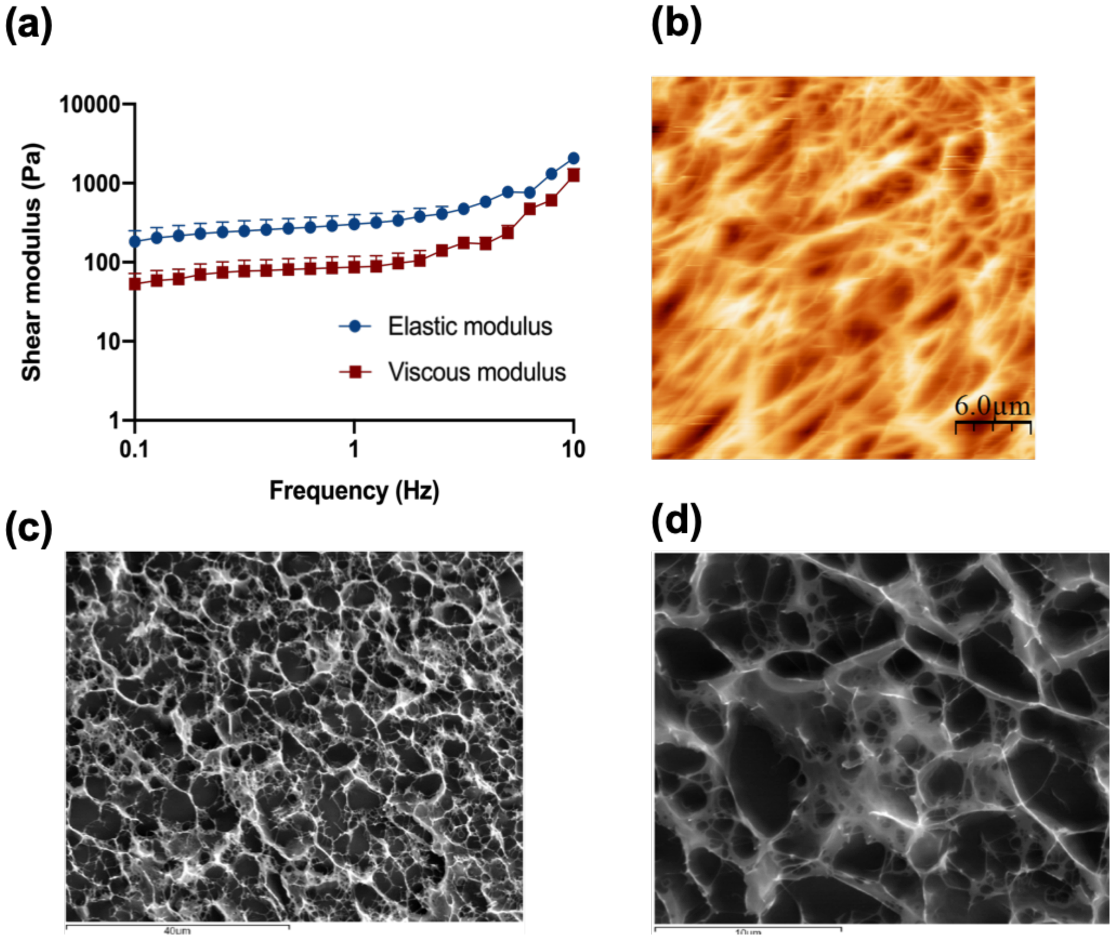

Figure 4.2 - Characterization of the collagen matrix. (a) Rheological behavior of the 6 mg/mL collagen hydrogels when subjected to frequency sweep tests (0.1 to 10 Hz) with a strain of 1%. Results are the average of triplicates and bars represent the standard error of the mean (SEM). (b) Visualization of the 6 mg/mL collagen hydrogel surface by AFM. (c) and (d) Visualization of the 6 mg/mL collagen hydrogel inner structure by CryoSEM.

4.4.2. Three-dimensional *in vitro* model

The addition of epithelial cells on top of the collagen layer with embedded fibroblasts resulted in enhanced collagen contraction. In one hand, when fibroblasts were seeded inside the collagen disks and no epithelial cells were seeded on top, disks would not contract for 20-21 days. However, when only Caco-2 cells were seeded on top of the gels, contraction of the disks occurred around day 16. Although contraction did not occur for the 3D co-culture, where HT29-MTX cells were present, in order to be coherent, both 3D models were used at 14 days in this set of experiments. This behavior had been previously observed, as reported in chapter 3, where the possible key players for this behavior were disclosed.

4.4.3. HIF morphology and fibronectin and laminin secretion inside the collagen disks

To observe the morphology of the HIF inside the collagen hydrogels and understand if they presented a normal morphology, as well as to assess the secretion of fibronectin and laminin, immunocytochemistry technique was used. Figure 4.3 depicts the elongated shape of fibroblasts in each condition. Besides, a higher cellular density and a higher amount of fibronectin and laminin (Figure 4.3a and b) was observed when Caco-2 or Caco-2+HT29-MTX cells were seeded on top of the gels, when comparing to the disks embedded with HIF without epithelial cells on top. Comparing the 3D Caco-2 with the 3D Co-culture model, it was possible to observe that there was a higher number of fibroblasts and fibronectin deposition inside the disks when only Caco-2 cells were on top comparing to the co-culture. After 14 days in culture the disks were no longer comprised of only type I collagen from rat tail, but human fibronectin and laminin, secreted by the fibroblasts. This indicates fibroblasts were able to degrade the collagen and proliferate, secreting their own matrix, remodeling their surrounding environment, which is important for cell survival [38].

It is well known that cells have the ability to communicate with each other, being this phenomenon regard as cellular crosstalk [39]. When epithelial cells were added to the cultures, a higher number of fibroblasts inside the disks was observed, which seemed to indicate epithelial cells enhanced the proliferation of stromal cells inside the collagen matrix. The secretion of ECM components, such as fibronectin and laminin, was also increased when this crosstalk occurred, which can be explained by the fact that epithelial adhesions with the ECM are most commonly mediated by integrins and the extracellular ligands that anchor these adhesions include fibronectin [39]. There was, also, a higher number of fibroblasts when only Caco-2 cells were seeded on top, being that the addition of HT29-MTX seemed to have an inhibitory effect on the crosstalk between Caco-2 and the fibroblasts, in agreement with the results obtained in the previous chapter. Besides being visible by the higher number of fibroblasts and fibronectin deposition, this was also supported by the fact that 3D Caco-2 models contracted after 16 days in culture, whether 3D Co-culture models maintained their integrity for 21 days, meaning that fibroblasts of the 3D Caco-2 models were more contractile than the ones of the 3D Co-culture model.

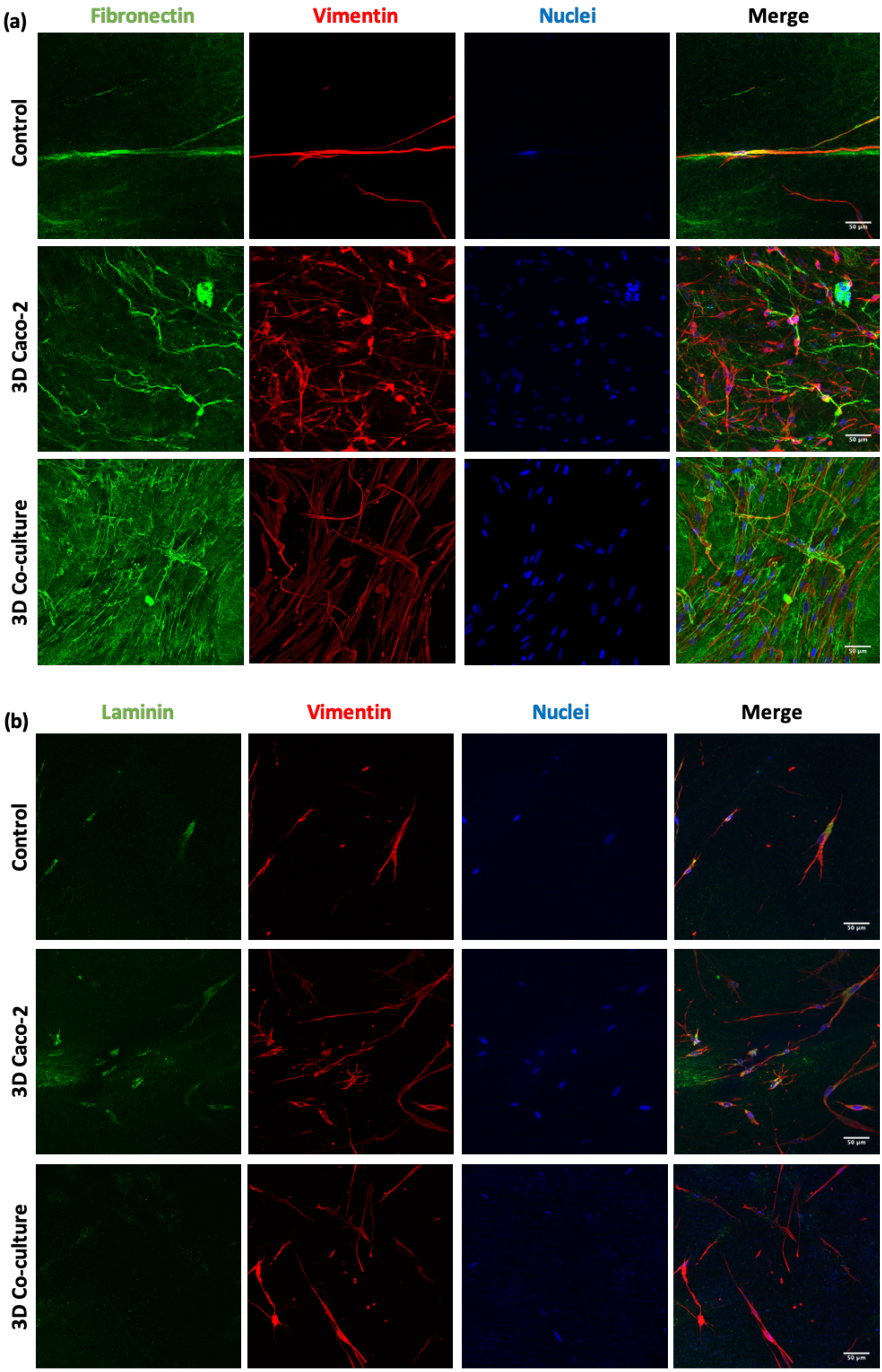

Figure 4.3 - HIF morphology was assessed through the expression of **vimentin**, while the ability to secrete ECM components was determined by the deposition of (a) **fibronectin**

and (b) **laminin**, during the time in culture, with and without epithelial cells on top. Pictures show maximal projections of the several stacks of the gels. Fibronectin and laminin were labelled with Alexa-Fluor 488 and Vimentin was labelled with Alexa-Fluor 594. The nuclei were counterstained with DAPI.

4.4.4. Cell layer formation and expression of proteins of the junctions

The cell layer formation was assessed through H&E staining and immunocytochemistry on the different timepoints to understand if there were differences regarding the epithelial layer in different days. It was observed that, in all models, the cellular layer was already formed at day 14 and no visible differences in the 2D models were observed comparing to day 21 (Figure 4.4 and 4.5a). It was also possible to observe some multilayer formation.

Regarding the expression of tight and adherens junctions and the secretion of mucins by HT29-MTX cells it was possible to see that Claudin-1 and E-cadherin were expressed in all the models at the different timepoints (Figure 4.5b and c). Comparing the 2D Caco-2 model at different days, there was a higher expression of the proteins on day 21, comparing to day 14. Nevertheless, when comparing the 2D Co-culture models, although the expression of E-cadherin seemed higher at day 21, the same did not happen with the expression of Claudin-1, that seemed lower. Regarding the 3D models, the expression of E-cadherin was in the middle of the expression of the 2D models, whether for Claudin-1, expression seemed to be similar to the 2D models at 21 days.

Regarding the expression of the tight junction protein ZO-1 (Figure 4.6) it was possible to observe that all the models had high expression of this protein and there were no visible differences between the models. Regarding the expression of MUC2 (Figure 4.6), as it was expected, this mucin was only secreted when HT29-MTX cells were present in the model, since these are mucus-secreting cells, unlike Caco-2 cells.

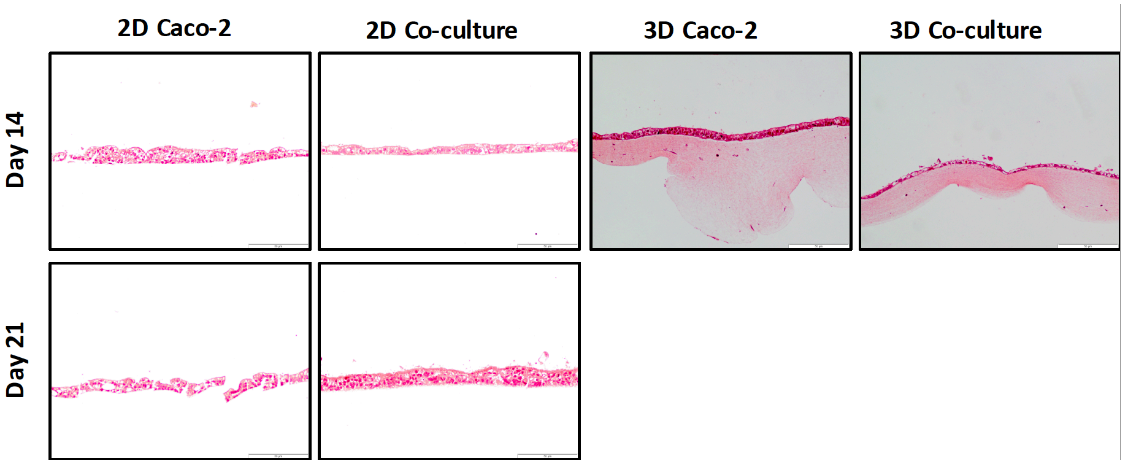

Figure 4.4 - H&E staining of the different models at 14 and 21 days.

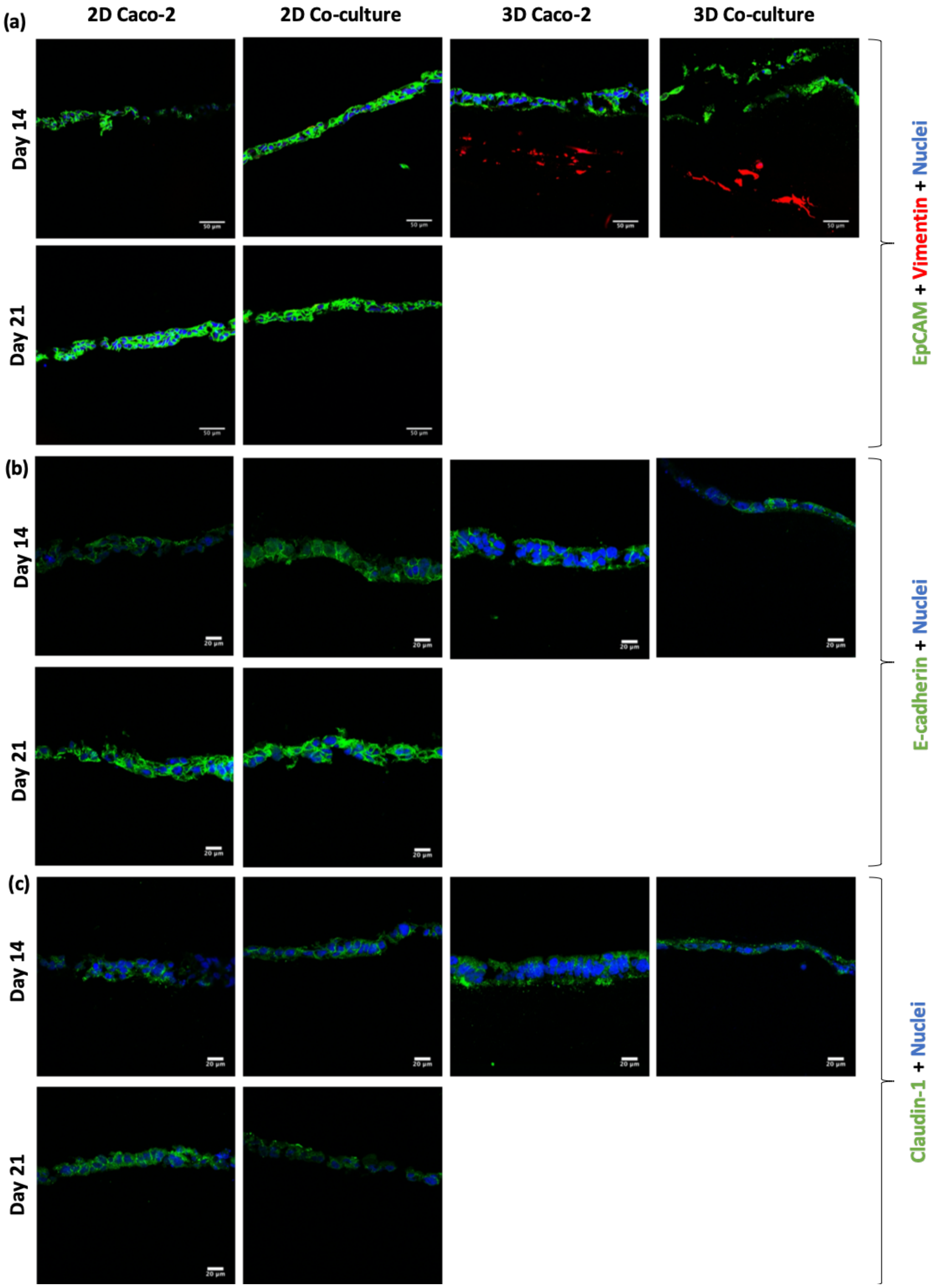

Figure 4.5 - (a) Visualization of cell layer formation by EpCAM. (b) Assessment and comparison of cellular adherens junctions in different models at different timepoints using E-cadherin. (c) Assessment and comparison of the tight junctions' protein Claudin-1 in the different models at different timepoints. EpCAM, E-cadherin and Claudin-1 were labeled with Alexa-Fluor 488 and nuclei were stained with DAPI.

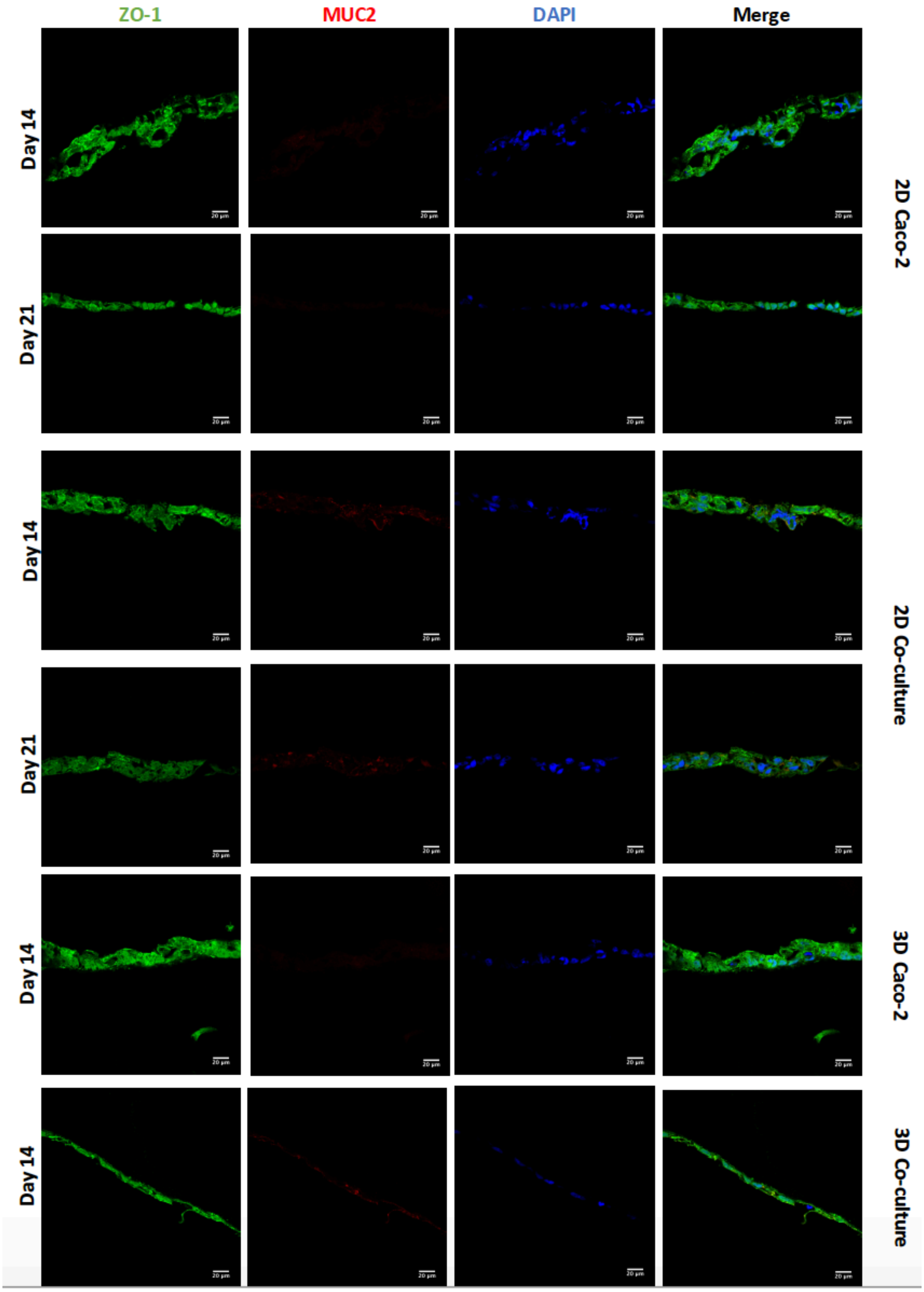

Figure 4.6 - Assessment and comparison of the tight junctions' protein **ZO-1** and the mucin **MUC2** in the different models at different timepoints. ZO-1 was labelled with Alexa-Fluor 488 and MUC2 was labelled with Alexa Fluor 594. The nuclei were counterstained with DAPI.

4.4.5. Permeability assay with FITC-Dextran 4kDa

The barrier integrity of the intestinal models was assessed by TEER measurements along the time in culture (Figure 4.7a). As expected, the 2D Caco-2 model was the one with higher TEER values, around 800 Ω.cm^2. The addition of HT29-MTX cells to the model rendered a decrease in TEER to approximately 350 Ω.cm^2. Regarding the 3D models, both models presented lower TEER values than their 2D analogues, being described in the literature that when cells are seeded on top of biological matrices, instead of artificial ones like the Transwell® membrane, the TEER decreases [40]. This decrease in TEER is usually not associated with barrier integrity, but with the tightness of the tight junctions [40, 41]. When cells are seeded on top of 3D biological matrices, they tend to show a more *in vivo* behavior, not forming such tight TJs and becoming more similar to what is observed in the intestinal epithelium, where TEER values are around 30 Ω [42]. As it happens in the 2D models, in 3D the Caco-2 model presented higher TEER values than the 3D Co-culture.

Regarding the permeability outcomes, it was observed that all models showed a similar tendency of increased permeability along time. It can be observed in Figure 4.7b and d that regarding the 2D Caco-2 model, there were significant differences between permeability values at day 14 and 21, being that permeability was higher at day 14 than 21. This can be explained by the fact that at day 14, the Caco-2 monolayer in the 2D model does not possess such tight TJs, what makes the compound pass more easily. This is actually sustained by the expression of Claudin-1, with higher expression at day 21, comparing to day 14. Since it is described that the Caco-2 model is not a suitable model to study the permeability of paracellular compounds because of the tightness of the barrier, making permeability underestimated, maybe it would be better to perform permeability assays at day 14 when using the Caco-2 model to study paracellular transport [43]. Nevertheless, it is important to say that permeability was still low on the 2D Caco-2 model at day 14 and that even with the addition of HT29-MTX cells, that are able to decrease the TEER of the barrier, values of absorption of dextran continued very low [18].

Regarding the 2D Co-culture model, the opposite occurred and it was possible to observe that permeability was higher at day 21 than at day 14. We hypothesize that this is related with the number of HT29-MTX cells, that increases with the time in culture. Since these cells do not possess such tight TJs, a higher number of these cells in the model may improve the passage of compounds paracellularly.

Considering the widely established protocols for 2D Caco-2 and Co-culture models for 21 days in culture [44, 45], the permeability of these models with the values obtained for the 3D models after 14 days was compared. In the 3D models at day 14 (Figure 4.7c and e), it was possible to observe they presented higher permeability, when comparing to their 2D analogues, being that the 3D Co-culture model was the one which presented the greatest permeability. These results are in accordance with the TEER values, since the 3D models present lower TEER values than the 2D models, which means the compounds can pass more easily between the cells. Nevertheless, when comparing the TEER values of the 3D Caco-2 model at day 14 with the values of the 2D Co-culture model at day 21, values were similar and around 300 $\Omega.cm^2$. However, when it came to permeability, the values were completely different, being that permeability on the 3D Caco-2 model was 5 times higher than in the 2D Co-culture model. This discrepancy indicates that permeability is not just merely related with the TEER values, but most likely with the cells themselves, and the fact that a 3D layer that mimics the *in vivo* environment is present, that can have a huge impact in cellular behavior, as already stated. In fact, permeability phenomenon may be regulated not only by the fact that cells are seeded on top of the collagen layer, but also by the crosstalk between the epithelial and stromal cells that we have seen to have an important role in the remodeling of the matrix [39]. It is likely that this crosstalk also influences the behavior of cells regarding permeability. This correlates with the expression of tight junctions. When comparing the expression of Claudin-1 and ZO-1, which are TJ proteins, it seems that expression in the 3D models at day 14 is similar to the expression of the 2D models at day 21. It is expected that the TEER values are not only regulated by the TJs expression, but other mechanisms may have a role. Besides, it is also a proof that the absorption of the paracellular compounds does not depend merely on TJs expression and barrier tightness, but that the fact that the cells are in a more *in vivo* state may influence their behavior at other levels, and this may affect the permeability of the compounds.

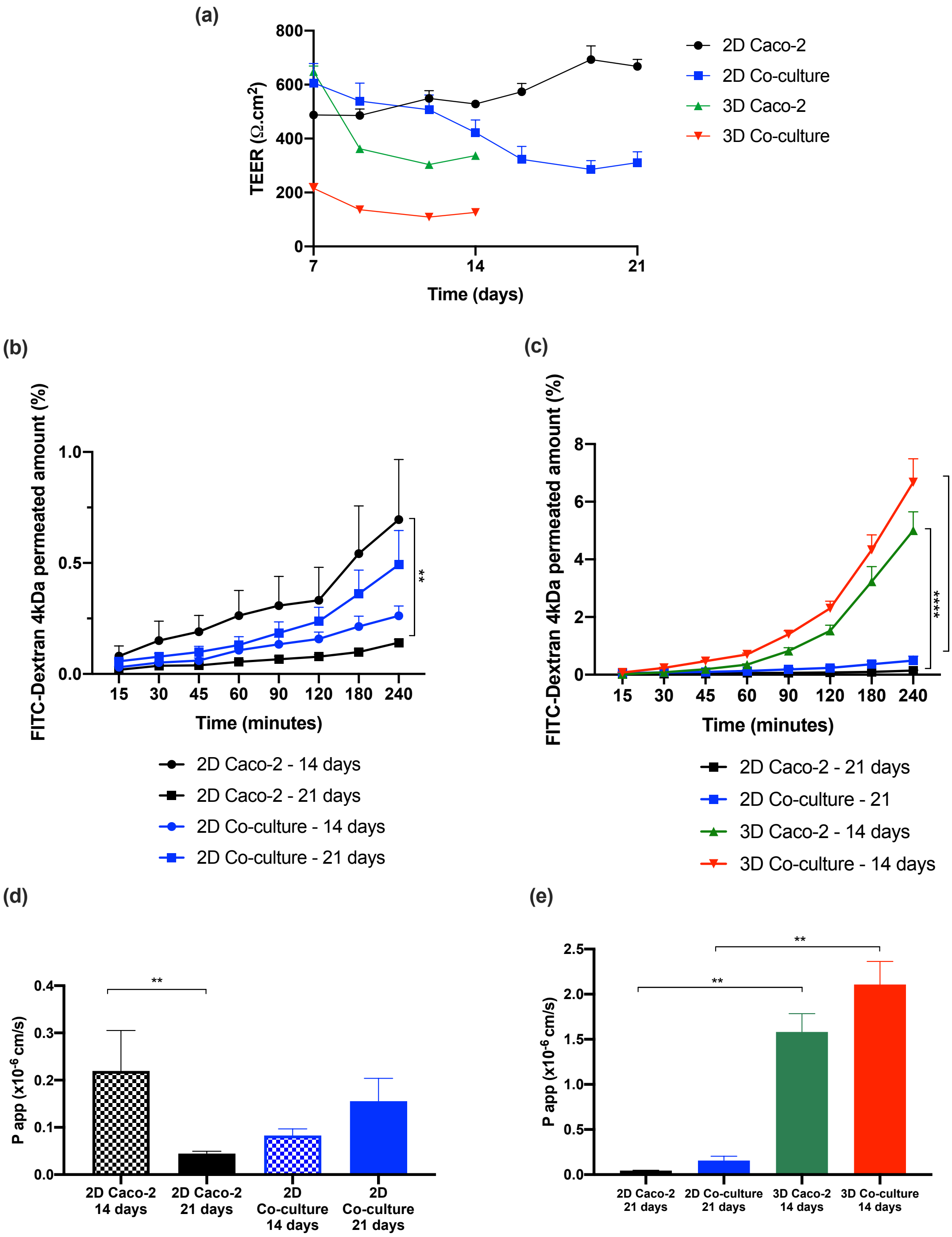

Figure 4.7 - Comparison between 2D and 3D models regarding TEER values and permeability. (a) TEER values of the models over time. Comparison of the cumulative transport of FITC-Dextran across the (b) 2D models after 14 vs. 21 days in culture and (c) 3D models after 14 days in culture vs. 2D models after 21 days in culture. Comparison of P_{app} values of (d) 2D models after 14 vs. 21 days in culture and (e) 3D models after 14 days in culture vs. 2D models after 21 days in culture. Results are the average of triplicates (except for permeability of 3D Caco-2, which n=2) and bars represent the standard error of

the mean (SEM). Statistical differences were calculated using 2-way ANOVA and Unpaired t-test ($p<0.01$ are denoted by ** and $p<0.0001$ are denoted by ****).

4.5. Conclusion

In the present chapter, a novel 3D intestinal model was established, reproducing, in a more physiological way, the architecture and composition of the human small intestine. It was confirmed that fibroblasts embedded in collagen, mimicking the intestinal lamina propria, had the capability of producing ECM components, remodeling the surrounding environment and having a pivotal role on the behavior of epithelial cells. The 3D models were used for permeability assays after 14 days of culture, since it was observed that the epithelial layer was already formed and the expression of Claudin-1 was similar to the 2D models at day 21. Besides, although TEER values presented differences between the 2D and 3D models, the expression of TJs (Claudin-1 and ZO-1) and adherens junctions was similar between them. Permeability of FITC-Dextran 4kDa, a hydrophilic compound that is known to cross the epithelium by the paracellular route, was significantly higher in the 3D models. We believe that these results are important, since it is known that paracellular permeability in the Caco-2 model is underestimated, since these cells resemble more the colonic epithelium. These results contribute to the believe that the fact that cells are in a more physiological configuration, sensing a biological 3D matrix, instead of the Transwell® insert membrane, has an effect over the epithelial layer, making cells have a behavior more similar to what is observed *in vivo*. In conclusion, a new *in vitro* intestinal model is herein proposed, to better and faster predict the permeability of paracellular compounds, helping bridging the gap between *in vitro* models and animal testing and contributing to the 3Rs policy.

References

1. Li, A.P., *Screening for human ADME/Tox drug properties in drug discovery.* Drug Discovery Today, 2001. **6**(7): p. 357-366.
2. Kennedy, T., *Managing the drug discovery/development interface.* Drug Discovery Today, 1997. **2**(10): p. 436-444.
3. Dahlgren, D. and H. Lennernas, *Intestinal Permeability and Drug Absorption: Predictive Experimental, Computational and In Vivo Approaches.* Pharmaceutics, 2019. **11**(8): p. 1-18.
4. Billat, P.A., et al., *Models for drug absorption from the small intestine: where are we and where are we going?* Drug Discovery Today, 2017. **22**(5): p. 761-775.
5. Pereira, C., et al., *Cell-based in vitro models for intestinal permeability studies*, in *Concepts and Models for Drug Permeability Studies*. 2016, Woodhead Publishing: Cambridge. p. 57-81.
6. Artursson, P. and J. Karlsson, *Correlation between oral drug absorption in humans and apparent drug permeability coefficients in human intestinal epithelial (Caco-2) cells.* Biochemical and Biophysical Research Communications, 1991. **175**(3): p. 880-885.
7. Maubon, N., et al., *Analysis of drug transporter expression in human intestinal Caco-2 cells by real-time PCR.* Fundamental & Clinical Pharmacology, 2007. **21**(6): p. 659-663.
8. Artursson, P., K. Palm, and K. Luthman, *Caco-2 monolayers in experimental and theoretical predictions of drug transport.* Advanced Drug Delivery Reviews, 2001. **46**(1-3): p. 27-43.
9. Sun, H., et al., *The Caco-2 cell monolayer: usefulness and limitations.* Expert Opinion on Drug Metabolism & Toxicology, 2008. **4**(4): p. 395-411.
10. Edelblum, K.L. and J.R. Turner, *Chapter 12 - Epithelial Cells: Structure, Transport, and Barrier Function*, in *Mucosal Immunology (Fourth Edition)*, J. Mestecky, et al., Editors. 2015, Academic Press: Boston. p. 187-210.
11. Lennernäs, H., et al., *Comparison between active and passive drug transport in human intestinal epithelial (caco-2) cells in vitro and human jejunum in vivo.* International Journal of Pharmaceutics, 1996. **127**(1): p. 103-107.
12. Linnankoski, J., et al., *Paracellular Porosity and Pore Size of the Human Intestinal Epithelium in Tissue and Cell Culture Models.* Journal of Pharmaceutical Sciences, 2010. **99**(4): p. 2166-2175.
13. Balimane, P.V. and S. Chong, *Cell culture-based models for intestinal permeability: a critique.* Drug Discovery Today, 2005. **10**(5): p. 335-343.

14. Gres, M.C., et al., *Correlation between oral drug absorption in humans, and apparent drug permeability in TC-7 cells, a human epithelial intestinal cell line: comparison with the parental Caco-2 cell line.* Pharmaceutical Research, 1998. **15**(5): p. 726-733.

15. Lazorova, L., et al., *Structural features determining the intestinal epithelial permeability and efflux of novel HIV-1 protease inhibitors.* Journal of Pharmaceutical Sciences, 2011. **100**(9): p. 3763-3772.

16. Marano, C.W., et al., *Phorbol ester treatment increases paracellular permeability across IEC-18 gastrointestinal epithelium in vitro.* Digestive Diseases and Sciences, 2001. **46**(7): p. 1490-1499.

17. Turco, L., et al., *Caco-2/TC7 cell line characterization for intestinal absorption: how reliable is this in vitro model for the prediction of the oral dose fraction absorbed in human?* Toxicology In Vitro, 2011. **25**(1): p. 13-20.

18. Antunes, F., et al., *Establishment of a triple co-culture in vitro cell models to study intestinal absorption of peptide drugs.* European Journal of Pharmaceutics and Biopharmaceutics, 2013. **83**(3): p. 427-435.

19. Darnell, M., et al., *Cytochrome P450-dependent metabolism in HepaRG cells cultured in a dynamic three-dimensional bioreactor.* Drug Metabolism and Disposition, 2011. **39**(7): p. 1131-8.

20. Desrochers, T.M., E. Palma, and D.L. Kaplan, *Tissue-engineered kidney disease models.* Advanced Drug Delivery Reviews, 2014. **69-70**: p. 67-80.

21. Justice, B.A., N.A. Badr, and R.A. Felder, *3D cell culture opens new dimensions in cell-based assays.* Drug Discovery Today, 2009. **14**(1-2): p. 102-107.

22. Pampaloni, F., E.G. Reynaud, and E.H. Stelzer, *The third dimension bridges the gap between cell culture and live tissue.* Nature Reviews Molecular Cell Biology, 2007. **8**(10): p. 839-845.

23. Chitcholtan, K., et al., *Differences in growth properties of endometrial cancer in three dimensional (3D) culture and 2D cell monolayer.* Experimental Cell Research, 2013. **319**(1): p. 75-87.

24. Shaker, A. and D.C. Rubin, *Intestinal stem cells and epithelial–mesenchymal interactions in the crypt and stem cell niche.* Translational Research, 2010. **156**(3): p. 180-187.

25. Dosh, R.H., et al., *Use of hydrogel scaffolds to develop an in vitro 3D culture model of human intestinal epithelium.* Acta Biomater, 2017. **62**: p. 128-143.

26. Yi, B., et al., *Three-dimensional in vitro gut model on a villi-shaped collagen scaffold.* BioChip Journal, 2017. **11**(3): p. 219-231.

27. Sung, J.H., et al., *Microscale 3-D hydrogel scaffold for biomimetic gastrointestinal (GI) tract model.* Lab Chip, 2011. **11**(3): p. 389-392.

28. Yu, J., et al., *In vitro 3D human small intestinal villous model for drug permeability determination.* Biotechnology and Bioengineering, 2012. **109**(9): p. 2173-2178.

29. Pereira, C., et al., *Dissecting stromal-epithelial interactions in a 3D in vitro cellularized intestinal model for permeability studies.* Biomaterials, 2015. **56**: p. 36-45.

30. Li, N., et al., *Development of an improved three-dimensional in vitro intestinal mucosa model for drug absorption evaluation.* Tissue Engineering, Part C: Methods, 2013. **19**(9): p. 708-719.

31. Madden, L.R., et al., *Bioprinted 3D Primary Human Intestinal Tissues Model Aspects of Native Physiology and ADME/Tox Functions.* iScience, 2018. **2**: p. 156-167.

32. Schneider, H., et al., *Study of mucin turnover in the small intestine by in vivo labeling.* Scientific Reports, 2018. **8**(1): p. 5760.

33. Woting, A. and M. Blaut, *Small Intestinal Permeability and Gut-Transit Time Determined with Low and High Molecular Weight Fluorescein Isothiocyanate-Dextrans in C3H Mice.* Nutrients, 2018. **10**(6): p. 685.

34. Costa, J. and A. Ahluwalia, *Advances and Current Challenges in Intestinal in vitro Model Engineering: A Digest.* Frontiers in Bioengineering and Biotechnology, 2019. **7**(144): p. 1-14.

35. Stidham, R.W., et al., *Ultrasound elasticity imaging for detecting intestinal fibrosis and inflammation in rats and humans with Crohn's disease.* Gastroenterology, 2011. **141**(3): p. 819-826.

36. Stewart, D.C., et al., *Quantitative assessment of intestinal stiffness and associations with fibrosis in human inflammatory bowel disease.* PLOS ONE, 2018. **13**(7): p. 1-16.

37. Ahmed, E.M., *Hydrogel: Preparation, characterization, and applications: A review.* Journal of Advanced Research, 2015. **6**(2): p. 105-121.

38. Roulis, M. and R.A. Flavell, *Fibroblasts and myofibroblasts of the intestinal lamina propria in physiology and disease.* Differentiation, 2016. **92**(3): p. 116-131.

39. Geiger, B., et al., *Transmembrane crosstalk between the extracellular matrix and the cytoskeleton.* Nature Reviews Molecular Cell Biology, 2001. **2**(11): p. 793-805.

40. Li, N., et al., *Development of an Improved Three-Dimensional In Vitro Intestinal Mucosa Model for Drug Absorption Evaluation.* Tissue Engineering Part C: Methods, 2013. **19**(9): p. 708-719.

41. Yi, B., et al., *Three-dimensional in vitro Gut Model on a Villi-shaped Collagen Scaffold.* Biochip Journal, 2017. **11**(3): p. 219-232.

42. Legen, I., M. Salobir, and J. Kerč, *Comparison of different intestinal epithelia as models for absorption enhancement studies.* International Journal of Pharmaceutics, 2005. **291**(1): p. 183-188.

43. Tavelin, S., et al., *Prediction of the oral absorption of low-permeability drugs using small intestine-like 2/4/A1 cell monolayers.* Pharmaceutical Research, 2003. **20**(3): p. 397-405.

44. Delie, F. and W. Rubas, *A human colonic cell line sharing similarities with enterocytes as a model to examine oral absorption: advantages and limitations of the Caco-2 model.* Critical Reviews in Therpeutic Drug Carrier Systems, 1997. **14**(3): p. 221-86.

45. Hidalgo, I.J., T.J. Raub, and R.T. Borchardt, *Characterization of the human colon carcinoma cell line (Caco-2) as a model system for intestinal epithelial permeability.* Gastroenterology, 1989. **96**(3): p. 736-749.

CHAPTER 5 – All layers matter: Innovative three-dimensional epithelium-stroma-endothelium intestinal model for reliable permeability outcomes

The information provided in this chapter was based in the following publication:

Macedo M.H., Barros A.S., Martínez E., Barrias C.C., Sarmento B., All layers matter: Innovative three-dimensional epithelium-stroma-endothelium intestinal model for reliable permeability outcomes, *submitted*.

In this paper I was responsible for the conception, execution and revision of the manuscript. Sofia Barros was responsible for execution of experiments and revision of the manuscript. The supervisors were responsible for reviewing and submit the manuscript. This paper was not previously included in other thesis, and it is partially reproduced in this section.

5.1. Abstract

Drug development is an ever-growing field, increasingly requesting reliable *in vitro* tools to speed up early screening phases, reducing the need for animal experiments. In oral delivery, understanding the absorption pattern of a new drug in the small intestine is paramount. Classical 2D *in vitro* models are generally too simplistic and do not accurately represent native tissues. The main goal of this chapter was to develop an advanced three-dimensional (3D) *in vitro* intestinal model to test absorption in a more reliable manner, by better mimicking the native environment. The 3D model is composed of a collagen-based stromal layer with embedded fibroblasts mimicking the intestinal lamina propria and providing support for the epithelium, composed of enterocytes and mucus-secreting cells. An endothelial layer, surrogating the absorptive capillary network, is also present. The developed 3D model presented lower levels of P-glycoprotein (P-gp) and Multidrug Resistance Protein 2 (MRP2) efflux transporters, which are normally overexpressed in traditional Caco-2 models, and are paramount in the absorption of many compounds. This, allied with transepithelial electrical resistance (TEER) values closer to physiological ranges, leads to improved and more reliable permeability outcomes, which are observed when comparing our results with *in vivo* values.

5.2. Introduction

The field of drug development is in constant growth, challenged by the needs of a world that is always facing new diseases and requesting for effective tools to fight them. In the case of oral delivery, which is the preferable route for drug administration, understanding the absorption potential of a drug at an early stage of its development takes a major role, since without effective absorption, the drug is not able to reach the site of action and fulfill its purpose.

Ineffective intestinal absorption and metabolic instability are responsible for 50% of drug failure in clinical studies [1-3]. This shows that *in vitro* screening platforms can take a major role in preclinical drug development and help reducing, or even replacing, animal experiments, which are more laborious, expensive and raise ethical concerns [4]. Thus, results provided by these platforms must be reliable. The gold standard of *in vitro* intestinal permeability tests remains the Caco-2 model, which presents several drawbacks, as the presence of a tighter barrier than what is observed *in vivo*, the up-regulation of P-gp and other transporters, the lack of a mucus layer, and the fact that it only represents one cell type and one layer of the intestinal mucosa [5, 6]. Although there have been some improvements in the Caco-2 model, such as the co-incorporation of HT29-MTX cells, that reduce barrier tightness and provide the mucus component, and, more recently, the development of improved 3D models, the 2D still remains the most widely used [7-15].

In 2D models, cells are seeded on top of semipermeable membranes, which are made of hard plastic and do not recapitulate the 3D environment that exists *in vivo*. This environment plays a crucial role in the maintenance of cell functions and polarity, and the presence of extracellular matrix (ECM) strongly influences cell behavior [9, 16-20]. Indeed, it has been demonstrated that ECM composition can alter intestinal epithelial proliferation and differentiation [21, 22]. While in 2D, mechanical and biochemical cues, as well as cell-cell and cell-matrix communication are lost, in 3D these interactions can be recapitulated, helping to understand key events, such as proliferation, migration and apoptosis, which are determined by the cellular context [18]. There is no doubt that reproducing the 3D environment is crucial when the goal is to mimic native tissue. In fact, the last decades of research in the field have shown that culturing cells in 3D can bridge the gap between the traditional 2D cultures and the native tissue [18].

In order to be biologically relevant, a model of the gastrointestinal tract should include, besides the epithelial layer, ECM with stromal cells to mimic the complex interactions between the cells and the surrounding tissues [23]. The endothelium, which is present in our model, also has an impact in the behavior of the surrounding cells, taking part of the cellular crosstalk that occurs.

When it comes to the development of *in vitro* models for permeability drug screening, mimicking the native environment is important, as it can affect the outcomes of absorption. In fact, some of the disadvantages of the Caco-2 model, that are observed when cells are cultured in 2D in semipermeable plastic membranes, may be surpassed when cells are cultured in 3D. The tightness of the barrier is one of them, since it has been seen that when Caco-2 cells are seeded on top of more physiological substrates, the TEER is reduced, which can be due to a lower expression of tight junctions, relating more to what is observed *in vivo*, which can greatly affect the permeability of paracellular compounds [9, 10, 12, 24, 25]. Besides, in terms of intestinal drug transporters, it has been observed that seeding the cells in more physiological matrices can lead to an expression more similar to *in vivo* levels, which can have a major impact in the permeability outcomes, especially when referring to important efflux transporters, as P-gp and MRP2 [10, 25, 26]. In fact, while 2D Caco-2 models can have some success at predicting permeability data for passively absorbed drugs, in the case of carrier-mediated compounds they have been less successful, showing significantly different correlation between *in vivo* and *in vitro* results, mainly in terms of the expression of intestinal transporters [27].

The main goal of the present chapter was to develop an advanced 3D intestinal *in vitro* model that could better mimic the native small intestine. This was achieved by providing a biological 3D support and include cells that could have an impact in cellular crosstalk and in the obtained results, by adding complexity to the model. Still, the goal was to keep it simple enough, so that it could be easily reproduced by others, in order to replace the conventional 2D models.

The model proposed in this chapter is comprised of a collagen layer with embedded human intestinal fibroblasts (HIF) representing the intestinal lamina propria and giving the 3D support to the intestinal epithelium. The latter is composed by Caco-2 and HT29-MTX cells, which mimic the enterocytes and goblet cells, respectively. An endothelial layer was added underneath the lamina propria, mimicking the barrier posed by the blood vessels. To our knowledge, this was the first attempt of addition of an endothelial layer in a 3D intestinal *in vitro* model to understand its impact in the absorption process.

In the previous chapters, we developed a 3D model composed of a collagen layer with embedded HIF and epithelial cells on top, but contraction of the collagen by the fibroblasts along cultures was observed, which limited the set of studies performed. In the current chapter, the model was optimized to avoid contraction and was characterized in terms of the expression of drug transporters, intestinal markers, tight junctions and MUC2, to understand if it would, in fact, better mimic the *in vivo* environment. Since the rationale for the development of this model laid on the hypothesis that obtaining a more physiological model would render better permeability outcomes, the absorption of different model drugs was evaluated and compared to the conventional 2D models, as well as *in vivo* data.

5.3. Materials and methods

5.3.1. Cell culture conditions

Caco-2 C2BBe1 (regarded as Caco-2 cells) were purchased from American type culture collection (ATCC, USA) and mucus producing HT29-MTX cells were kindly provided by Dr. T. Lesuffleur (INSERM U178, Villejuif, France). Caco-2 (passage 53 to 80) and HT29-MTX (passage 41 to 55) cell lines were grown in Dulbecco's modified Eagle's medium (DMEM) with 4.5 g/L glucose and Ultraglutamine™ (Gibco), supplemented with 1% Penicillin/Streptomycin 100X (Biowest) and 10% Fetal Bovine Serum (FBS) (Biochrom), regarded as DMEM complete from now on.

Human intestinal fibroblasts (HIF) primary cells (passage 6) were obtained from ScienCell and were cultured in Fibroblast medium (FM) supplemented with 2% FBS, 1% of Fibroblast Growth Supplement (FGS) and 1% of penicillin/streptomycin solution (all from ScienCell).

Human pulmonary microvascular endothelial cells (HPMEC)-ST1.6R (regarded as HPMEC) cells were kindly provided by professor C. James Kirkpatrick (Institute of Pathology, Johannes Gutenberg University of Mainz, Germany). Cells were cultured (passage 39 to 45) with M-199 medium (Merck) supplemented with 20% (v/v) FBS (Biochrom), 1% (v/v) Penicillin/Streptomycin (Biowest), 25 µg/mL of Endothelial Cell Growth Supplement (ECGS) (Merck), 25 µg/mL of heparin sodium salt from porcine intestinal mucosa (Merck) and 0.1 mg/mL L-glutamine (LabClinics).

All cells were grown separately in tissue culture flasks (SPL) and maintained in an incubator (Binder) at 37ºC and 5% CO_2, in a water saturated atmosphere.

5.3.2. Optimization of the collagen layer with HIF embedded

In the previous chapters we developed a 3D intestinal model containing a collagen layer with a concentration of 6 mg/mL and encompassing a HIF initial seeding density of 1 x 10^5 cells/mL. When epithelial cells were seeded on top, fibroblasts would contract the collagen layer after day 14 in culture, impeding the execution of permeability experiments by day 21, which is the established protocol. In order to circumvent this problem, in this chapter, the initial seeding density of HIF was decreased to half (5 x 10^4 cells/mL).

Briefly, to obtain the collagen layer with HIF, 10X Phosphate Buffered Saline (PBS), 1N Sodium Hydroxide (NaOH) and FM with HIF in a final concentration of 5 x 10^4 cells/mL were added to the high concentrated rat tail collagen solution (Corning), following supplier recommendations, in order to obtain a final concentration of 6 mg/mL of collagen. The solution was placed on the 12-well Transwell® inserts with 1 µm of pore size (Millicell), using 110 µL to obtain a layer with approximately 1 mm of thickness. The solution was dispersed carefully, in order to cover the entire surface of the insert and avoid the formation of bubbles, and was incubated at 37ºC, 5% CO_2 in a water saturated atmosphere for 30 min to allow gelation.

5.3.3. Metabolic activity of the HIF inside the collagen hydrogels

To understand if the decrease in the HIF seeding density would influence the metabolic activity of the cells inside the collagen disk, a resazurin assay was performed at different timepoints (1, 7, 14 and 21 days). Collagen hydrogels with a final concentration of 6 mg/mL and a HIF density of 5 x 10^4 and 1 x 10^5 cells/mL were obtained, as previously explained, dispersed in 48-well plates and allowed to gel for 30 min, after which 2 mL of complete DMEM was added and the plate was incubated at 37ºC, 5% CO_2, in a water saturated atmosphere and the medium was changed every 2-3 days. The resazurin solution was obtained dissolving 50 mg of resazurin sodium salt (Sigma) into 25 mL of PBS 20X and 475 mL of dH_2O overnight (ON), at room temperature (RT) with agitation in the dark, and then filtered. At each timepoint, resazurin solution was pre-warmed to 37ºC, mixed with DMEM at a final concentration of 20% and 600 µL of solution was added to each well. The plate was incubated for 2 h at 37ºC and 5% CO_2, in a water saturated atmosphere. After the incubation period, 3 samples of 150 µL from each well were collected and quantified by measuring the relative fluorescence units (RFU) using a microplate reader Synergy™ Mx HM550 (Biotek) set at 530/590 (excitation/emission wavelength, respectively) and results were normalized by subtracting the blank (collagen disk without cells).

5.3.4. Assessment of HIF morphology and ECM secretion

After 21 days in culture, disks obtained with the new HIF seeding density were washed once with PBS and fixed using 2% paraformaldehyde (PFA) (Delta Microscopies) in PBS for 30 min at RT. This step was followed by permeabilization with a solution of 0.2% (v/v) Triton X-100 (Sigma) in PBS for 10 min at RT and samples were washed thrice with PBS for 5 min. After, a blocking step was performed using a blocking solution (BS) containing 1.5% bovine serum albumin (BSA) (VWR) and 5% FBS in PBS, for 1 h at RT. Samples were then transferred to a humidified chamber and were incubated, with mouse anti-human vimentin (1:50) (sc-6260, Santa Cruz Biotechnology) + rabbit anti-human fibronectin (1:50) (F3648, Merck), ON at 4ºC. After incubation with the primary antibodies, samples were washed three times for 5 min with a solution of 0.05% Tween-20 (VWR) in PBS (PBST). This was followed by incubation with the secondary antibodies F(ab')2-Goat anti-Mouse IgG (H+L) Cross-Adsorbed, Alexa Fluor 594 (1:500) (A-11020, Invitrogen) + Goat anti-Rabbit IgG (H+L) Cross-Adsorbed, Alexa Fluor 488 (1:500) (A-11008, Invitrogen) and cell nuclei was counterstained with 4',6'-diamino-2-fenil-indol (DAPI) (500 ng/mL) (Merck). Finally, disks were washed twice with PBST and once with PBS for 5 min and kept in PBS until visualization by a spectral confocal laser scanning microscope TCS-SP5 AOBS (Leica).

5.3.5. Three-dimensional in vitro models

To obtain the 3D Complete model with the endothelial layer, the density of HPMEC cells was optimized to obtain a complete monolayer by day 21 in culture.

Different initial seeding densities (1, 5 and 10 x 10^4 cells/cm^2) were tested by inverting the 12-well Transwell® inserts on 6-well plates (SPL) and coating the basolateral side of the insert with 100 µL of 0.2% gelatin (Merck) for 1 h at RT to stimulate cellular adhesion. After 1 h, excess gelatin was removed and HPMEC cells were seeded using a suspension volume of 100 µL. The cells were allowed to adhere for 2 h at RT and 1 mL of PBS was placed in each well to maintain humidity and prevent cells from drying. After 2 h, Transwell® inserts were moved into 12-well plates (VWR) in the normal configuration and 0.5 mL and 1.5 mL of DMEM was added do the apical and basolateral compartments, respectively.

After 21 days, the formation of a monolayer was confirmed through immunohistochemistry (ICC) and hematoxylin and eosin (H&E) techniques. ICC was performed following the procedure described in the previous section, with the exception of the last step, where membranes were mounted in glass slides using fluorescent mounting medium (Dako) and left to dry overnight, protected from light at 4ºC. Mouse anti-human CD31 (1:50) (M0823) (Dako) conjugated with the secondary antibody F(ab')2-Goat anti-Mouse IgG (H+L) Cross-Adsorbed, Alexa Fluor 594 (1:500) (A-11020, Thermofisher Scientific) and DAPI (500 ng/mL) (Merck) were used. H&E was performed as described in the previous chapter. Briefly, a fixation step was performed with PFA 2% in PBS, after washing the inserts once with PBS. After fixation, cells were washed again with PBS 3 times for 5 min. The membrane of the Transwell® inserts was cut and embedded in paraffin. Sections of 3 mm were obtained using a RM2255 microtome (Leica). Sections were then deparaffinized and rehydrated, stained for 3 min in Gil's Hematoxylin (ThermoScientific), 6 min in running water, dehydrated, stained for 1 min in Eosin Y (ThermoScientific), cleared and mounted in Entellan (Merck).

After disclosing the ideal seeding density of endothelial cells, the 3D models were obtained (Figure 5.1), by seeding these cells as described. After the 2 h adhesion step, the collagen solution with HIF (6 mg/mL collagen and 5 x 10^4 HIF/mL), obtained as described in section 5.3.2, was placed on the apical side of the Transwell®. After the 30 min gelation process, inserts were moved to a new 12-well plate to prevent that HPMEC cells that might had dropped to the bottom of the well could have an impact in the culture. Then, Caco-2 and HT29-MTX cells (1 x 10^5 cells/cm^2 at a 9:1 ratio, respectively) in 0.5 mL of DMEM, were added on top of the fibroblast embedded collagen layer. 1.5 mL of DMEM was added to the basolateral side and plates were incubated at 37ºC, 5% CO_2 in a water saturated atmosphere. This configuration is regarded as “3D Complete model”. The 3D model without the endothelial layer is regarded as “3D Co-culture model”, whereas the 2D model with Caco-2 + HT29-MTX, that was used as control, is regarded as “2D Co-culture model”.

The cultures were maintained during 21 days and the medium of the models was changed every 2-3 days. TEER was periodically measured using an EVOM^2 equipment (World Precision Instruments).

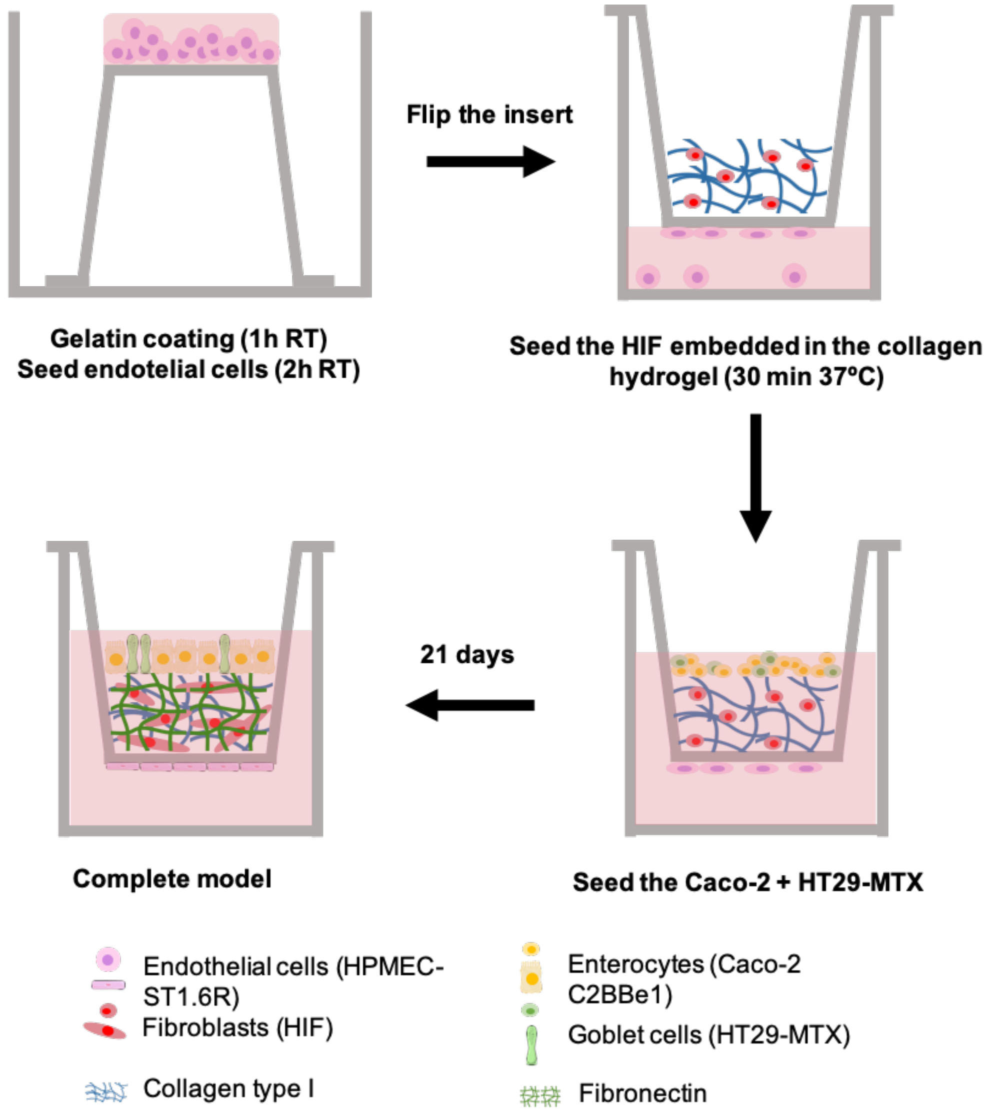

Figure 5.1 - General overview of the procedure followed to obtain the 3D complete model.

5.3.6. Quantification of markers of intestinal differentiation

Alkaline phosphatase (ALP) activity was quantified using a colorimetric alkaline phosphatase assay kit (ab83369, Abcam), as described by the manufacturer. Medium from the different models (2D Co-culture, 3D Co-culture and 3D Complete) were harvested at different timepoints (7, 14 and 21 days) and the ALP activity was immediately quantified. Briefly, the samples, the sample background control (culture medium) and p-Nitrophenyl phosphate (pNPP) standards were added to the provided plate. 20 µL of stop solution was added to the sample background control wells to terminate ALP activity in these samples. Then, 50 µL of 5 mM pNPP was added to each well containing samples and sample background controls. 10 µL of ALP enzyme were added to each standard. The plate was incubated for 60 min at 25ºC and protected from light, to allow the conversion of pNPP substrate to an equal amount of colored p-Nitrophenol (pNP). The reaction was then stopped by adding 20 µL of stop solution and absorbance was read at 405 nm using a microplate reader (SynergyTM Mx HM550, Biotek).

The intestinal markers Specific Intestine Homeobox (ISX), Sucrase Isomaltase (SI) and Villin1 (Vil1) were assessed using Real Time Polymerase Chain Reaction (qPCR).

First, 2D Caco-2 models, 2D Co-culture models, 3D Co-culture models and 3D Complete models were seeded on 12-well Transwell® inserts, as described in section 5.3.5. At day 14 and 21 RNA extraction was performed. A Quick-RNA MiniPrep kit (R1054, Zymo Research) was used according to manufacturer's instructions. First, cells were lysed by removing culture medium and adding RNA lysis buffer directly to the monolayer. Lysate was centrifuged at 10 000 g for 1 minute, the supernatant was transferred to a Spin-Away Filter in a Collection Tube and centrifuged again at 10 000 g for 1 min to remove gDNA. The flow through was then used for RNA purification. Briefly, 99% ethanol was mixed to the sample in a 1:1 proportion and mixed well. The mixture was transferred to a Zymo-Spin IIICG Column in a Collection Tube and centrifuged for 30 s. A DNase I Treatment was performed for DNA removal, washing the column with RNA Wash Buffer, centrifuging and, then, incubating the samples for 30 min at RT with DNase I Reaction Mix and centrifuging again. RNA Prep Buffer and Wash Buffer were added to the samples with centrifugations of 30 s in between. Wash Buffer was added again and centrifugation was performed for 2 min to ensure the complete removal of the buffer. Columns were carefully transferred into RNAase-free tubes and 50 µL of DNase/RNase-Free water was added directly to the column matrix and centrifuged for 30 s. The eluted RNA was stored at -80ºC until further use.

The quality and concentration of the sample's RNA was evaluated in an automated electrophoresis station (Experion Automated Electrophoresis System, Bio-rad) using Experion RNA StdSens Kit (700-7105, Bio-rad) according to manufacturer's instructions using 1 µL of RNA in a quantification range of 5-500 ng/µL of each purified total RNA sample.

To obtain cDNA from the RNA samples, iScript cDNA Synthesis Kit (1708891, Bio-rad) was used. Briefly, RNA template was mixed with 5x iScript Reaction Mix, iScript Reverse Transcriptase and Nuclease free water in a final volume of 40 µL. The samples were then placed in a thermal cycler (MyCycler™ Thermal Cycler System, Bio-rad) and the protocol was performed following the manufacturer instructions. Briefly, a priming step of 5 min at 25ºC was followed by a reverse transcription step for 20 min at 46ºC. RT inactivation was performed for 1 min at 95ºC.

The cDNA was used to perform the qPCR. A customized primePCR plate (Bio-rad) with the genes of interest mentioned above and the housekeeping genes Glyceraldehyde 3-

phosphate dehydrogenase (GADPH) and Actin Beta (ACTB) was used. 1 µL of RT control template was added to each 20 µL of cDNA synthesis reaction. The master mix was prepared adding iTaq Universal SYBR Green Supermix (10000068167, Bio-rad), cDNA template and Nuclease Free Water according to manufacturer's instructions to a final volume of 400 µL. The protocol was run using a real time PCR instrument (CFX96 Touch Real-Time PCR Detection System, Bio-rad), according to the prime PCR plate protocol, which consisted in an activation step at 95°C for 2 min, followed by 40 cycles of a denaturation step for 5 s also at 95°C and an annealing/extension step at 60°C for 30 s. The melt curve was performed between 65°C and 95°C in 0.5°C increments for 5 s/step.

5.3.7. Genetic expression of important intestinal drug transporters

The genetic expression of different drug transporters [ABCB1 - P-glycoprotein (P-gp); ABCC1 - Multidrug Resistance Protein 1 (MRP1); ABCC2 - Multidrug Resistance Protein 2 (MRP2); ABCG2 – Breast Cancer Resistance Protein (BCRP); SLC15A1 – Peptide Transporter 1 (PEPT1); SLC16A1 – Monocarboxylate Transporter 1 (MCT1); SLC22A1 – Organic Cationic Transporter 1 (OCT1)] was assessed using a two approach Reverse Transcriptase Real Time Polymerase Chain Reaction (RT-qPCR), as described in the previous section.

5.3.8. Immunostaining of tight and adherens junctions, drug transporters and MUC2

Immunocytochemistry technique was employed to confirm the integrity of the epithelial layer in the 2D and 3D Co-culture and 3D Complete models. The presence of tight junctions (TJs) was confirmed using antibodies against Claudin-1, an integral transmembrane TJ protein, and ZO-1, a TJ with a peripheral localization. The presence of E-cadherin, an adherens junction was also observed, as well as presence of MUC2. In terms of transporters, the expression of P-gp and MRP2 was evaluated.

After 14 or 21 days in culture, models were washed once with PBS and fixed using 2% PFA for 30 min, following three washes with PBS for 5 min. Before freezing the cells in Optimal Cutting Temperature (OCT) compound (Kaltec) at -20ºC, a cryopreservation step was performed submerging the cells in a solution of 15% sucrose in PBS for 3h, followed by incubation ON in a solution of 30% sucrose. Once frozen, models were sectioned into 7 mm slices onto glass slides using a HM550 cryostat (Microm). To perform the immunochemistry technique with the different antibodies, first slides were dipped into PBS to dissolve the OCT and sections were afterwards marked with a water-repellent Pen (Dako) to facilitate visualization of the localization of the samples in the slides and to help obtain a more homogenous immunocytochemical staining. Then cells were permeabilized in a solution containing 0.2% (v/v) Triton in PBS for 10 min. After permeabilization, slides were washed again with PBS three times for 5 min each. A blocking step was performed subjecting samples to a solution containing 1.5% BSA and 5% FBS in PBS for 1h. All the previous steps were performed at RT. Slides were then incubated with the primary antibodies' solutions [rabbit anti-human P-gp (1:250) (ab170904, Abcam) + mouse anti-human E-cadherin conjugated with Alexa Fluor 488 (1:100) (324110, BioLegend) or rabbit anti-human Claudin-1 (1:200) (SAB5500083, Merck) + mouse anti-human MRP2 (1:100) (MA1-26536, Invitrogen) or rabbit anti-human ZO-1 (1:50) (SC10804, SantaCruz Biotechnology) + mouse anti-human MUC2 (1:50) (ab118964, Abcam)] in a humidified chamber ON. In the following day, slides were washed thrice for 5 min with PBST. This step was followed by incubation with the secondary antibodies and DAPI (500 ng/mL; Sigma Aldrich) to counterstain the nuclei. Secondary antibodies used were anti-rabbit Alexa Fluor 488 F(ab')2 fragment of IgG (H+L) (A11070, Invitrogen), anti-mouse Alexa Fluor 594 F(ab')2 fragment of IgG (H+L) (A11020, Invitrogen) and anti-rabbit IgG H&L Alexa Fluor 594 preadsorbed (Ab150064, Abcam), accordingly to the primary antibodies' combinations. Both secondary antibodies and DAPI were added to samples for 2h at 4ºC in a humidified chamber. After incubation, slides were washed twice with PBST and once with PBS, for 5 min each. Slides were mounted using fluorescent mounting medium (Dako) and left to dry protected from light at 4ºC until visualization by a spectral confocal laser scanning microscope (TCS-SP5 AOBS (Leica). To compare the expression between samples, laser power and gain of each laser were maintained for all samples regarding each antibody combination.

5.3.9. Evaluation of P-gp activity

The activity of the drug transporter P-gp was evaluated through transport assays in both apical to basolateral and basolateral to apical directions, using Rhodamine 123 (Rho 123) (ENZ52307, Enzo Life Sciences).

The assays were performed in the 2D Co-culture, 3D Co-culture and 3D complete models after 14 and 21 days in culture.

For the assays, culture medium was removed from both sides of the Transwell® inserts and washed twice with pre-warmed HBSS. After the washes, 1.5 mL and 0.5 mL of HBSS were placed on the basolateral and apical sides of the inserts, respectively and they were allowed to equilibrate for 30 min at 37ºC and 100 rpm in an orbital shaker (KS 4000 ic control, IKA). After 30 min, HBSS on the apical or basolateral side (depending on the direction of the transport) was replaced for 0.5 mL or 1.5 mL of 5 µg/mL of Rho 123, respectively. At pre-determined timepoints (15, 30, 60, 180, 120 and 240 min), TEER was measured in order to assess the monolayers integrity and a sample of 200 µL was taken from the basolateral or apical side and replaced by the same amount of HBSS. At the end of the assay, a sample from the donor chamber side was taken. The amount of Rho 123 in the samples was measured using a microplate reader (SynergyTM Mx HM550, Biotek) at excitation/emission wavelengths of 507/529.

The permeability results were expressed in terms of apparent permeability (P_{app}), that was calculated using Equation 1.

$$P_{app} = \frac{\Delta Q}{A \times C_0 \times \Delta t} \text{ (Equation 1)}$$

Where ΔQ is the amount of compound detected in the basolateral side (mg), A is the surface area of the insert (cm^2), C_0 is the initial concentration in the donor compartment (mg/mL) and Δt is the time of the experiment (seconds).

5.3.10. Drug permeability assays

Permeability assays of colchicine (C9754, Merck), atenolol (A7655, Merck) and metoprolol (PHR1076, Merck), drugs with intrinsic low, moderate and high permeability, respectively, were performed in order to compare the permeability between the 2D Co-culture, 3D Co-culture and 3D complete models after 14 and 21 days in culture.

For the assays, culture medium was removed from both sides of the Transwell® inserts and washed twice with pre-warmed HBSS (14025050, Gibco). After the washes, 1.5 mL and 0.5 mL of HBSS were placed on the basolateral and apical sides of the inserts, respectively and they were allowed to equilibrate for 30 min at 37ºC and 100 rpm in an orbital shaker (KS 4000 ic control, IKA). After 30 min, HBSS on the apical side was replaced by 100 µM of colchicine or metoprolol or 200 µM of atenolol dissolved in HBSS. At pre-determined timepoints (15, 30, 60, 120, 180 and 240 min), TEER was measured in order to assess the monolayers integrity and a sample of 200 µL was taken from the basolateral side and replaced by the same amount of HBSS. At the end of the assay, a sample from the apical side was taken. Drugs were quantified by High Performance Liquid Chromatography (HPLC) using an Ultra-Fast Liquid Chromatograph (UFLC) Prominence System equipped with two Pumps LC-20AD, a column oven CTO-20AC, and autosampler SIL-20AC, a System Controller CBM-20A, a degasser DGU-20A5, a RF-10Axl fluorescence detector coupled to the LC System and a LC Solution, Version 1.24 SP1 (Shimadzu). Detailed methods are described in Table A.1 of Appendix.

The permeability results were expressed in percentage of release and apparent permeability (P_{app}), that was calculated using Equation 1.

5.3.11. Statistical Analysis

Statistical analysis was performed using the software GraphPad Prism 8.0 (GraphPad Software Inc.). All results are represented as mean ± standard error of the mean (SEM) or mean ± standard deviation (SD) or mean ± upper and lower limits. Statistical differences were calculated using 2-way analysis of variance (ANOVA) multiple comparisons test. The level of significance was set at probabilities of *$p<0.05$, **$p<0.01$, ***$p<0.001$, ****$p<0.0001$.

5.4. Results and Discussion

5.4.1. Optimized 3D model of the intestinal mucosa

A novel 3D *in vitro* intestinal model, combining the epithelial, stromal and endothelial barriers of the small intestine mucosa, was developed and characterized as a tool to perform more reliable permeability studies.

Regarding the optimization of the collagen layer with embedded fibroblasts, the decrease to half of the initial HIF seeding density, comparing to the previous chapters, allowed the models to maintain their integrity throughout the entire culture period (21 days), even when epithelial and endothelial cells were added, in contrast to what had been previously observed. This optimized configuration allowed to extend the culture time and compare results obtained with the different models after 14 and 21 days. A comparison between the two timepoints was performed to understand if 14 days in culture would be enough. If results between 14 and 21 days were similar, future permeability experiments could be performed sooner, decreasing the waiting time between seeding the model and performing the permeability experiments, reducing the overall experiment time.

The resazurin assay showed that cells remained metabolically active, even if at lower initial density (Figure 5.2a). The levels of metabolic activity were always lower for the lower density of cells, which was expectable. Although, this difference is only statistically significant at day 14. Regarding the evolution of the metabolic activity, both densities presented a stairway profile, as it had been previously observed, indicating that cells become more active after the first 7 days in culture. Later in time, cells seemed to reach a plateau, which indicates that probably they were not able to proliferate anymore, possible due to contact inhibition, as it had been observed before [12].

Regarding the evaluation of HIF morphology and the deposition of fibronectin, an ECM component, it was possible to observe that fibroblasts presented a prototypical elongated shape, expressed vimentin and secreted fibronectin, remodeling the collagen disk (Figure 5.2b). Thus, fibroblasts were able to secret their own ECM proteins within the original matrix, which is important for their survival and for the crosstalk with the surrounding cells. Notably, there was no contraction of the collagen matrix along culture, as observed in the previous chapter and in multiple other reports in the literature, which is a significant advantage of the present setting [28, 29]. The fact that fibroblasts are capable of producing endogenous ECM is also relevant to the subsequent establishment of the epithelial layer, since it is known that cellular interactions with the ECM are crucial for the organization of epithelial cells in forming a well polarized and cohesive tissue [29].

After establishing the lamina propria-like stromal layer, the endothelial layer was added in order to mimic permeability into blood capillaries. After crossing the epithelium and the lamina propria, compounds need to enter blood vessels to reach systemic circulation. It is described that endothelial cells provide a dynamic barrier between the tissue and the bloodstream, controlling vascular permeability [30, 31]. It was observed that an intermediate concentration of 5 x 10^4 cells/cm^2 allowed cells to form a monolayer after 21 days in culture (Figure A.2 of Appendix).

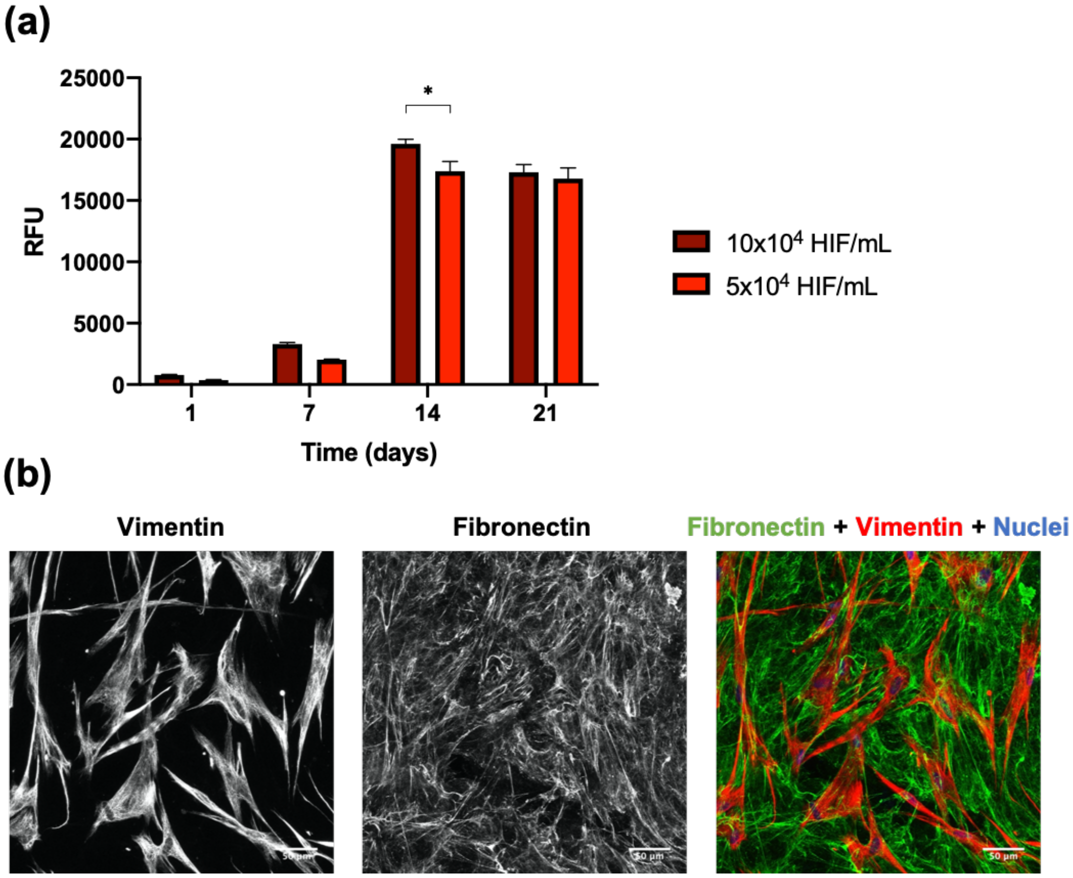

Figure 5.2 – Human intestinal fibroblasts (HIF) (a) metabolic activity along the time in culture and (b) expression of **fibronectin** and **vimentin** after 21 days, when cells are seeded inside the collagen disks. The nuclei were counterstained with DAPI. Results for (a) are the average of triplicates, and bars represent the standard error of the mean (SEM). Statistical differences were calculated using 2-way ANOVA multiple comparisons to

compare between different initial seeding densities of HIF in different days ($p<0.05$ is denoted by *).

5.4.2. Expression of intestinal markers

Intestinal ALP is a brush border protein that is exclusively expressed by differentiated enterocytes, thus serving as an enterocyte differentiation marker [32, 33]. The activity of this protein was measured to assess potential differences between the 2D and 3D models (Figure 5.3). A significant difference was only observed between the 2D and 3D models in the first week of culture, being higher in the 2D model. Nevertheless, for the other timepoints, activity was similar, mainly at the end of the culture. Thus, enterocyte differentiation does not seem to be enhanced when cells are in 3D. Notwithstanding, since it is well established that Caco-2 cells become fully differentiated enterocytes after 21 days in culture, being able to achieve similar levels of ALP activity in 3D is a good result [34].

The genetic expression of other markers that are recognized as typical intestinal markers, such as ISX, SI and Vill1, was also determined (Figure 5.4) [35-37]. ISX is a transcription factor that regulates gene expression in the intestine and shows an intestine-specific expression [38, 39]. SI is a gene specific of the enterocyte lineage and is well accepted as a marker of intestinal differentiation, as well as Vill1, which is a marker of mature epithelial cells [35-37]. Herein, we decided to first compare their expression in 2D co-culture models vs. 2D Caco-2 models, as a control (Figure 5.4a). It was possible to observe significant differences between the expression of SI in Caco-2 monoculture and the co-culture. Although for ISX, differences were not statistically significant, there was a much lower expression in the co-culture. We found no reports in the literature referring to a potential impact of HT29-MTX in Caco-2 cells differentiation into intestinal enterocytes. Given that genetic expression was evaluated globally, i.e. in the whole model, and not just in Caco-2 cells, this decrease was probably not related to a lower level of Caco-2 differentiation into enterocytes, but just due to the presence of the goblet cells in the model [6, 40, 41].

Comparing the expression of the intestinal markers between the 2D and 3D models (Figure 5.4b), and using the 2D Co-culture model at day 21 as reference, it was possible to observe a significant decrease in the levels of SI for both 3D configurations at both timepoints. Nevertheless, when analyzing the other two intestinal markers, no statistical differences were observed. This means that the fact that cells are in 3D has a negative impact in the expression of SI, but the levels of the other markers are maintained, indicating that intestinal differentiation of the model is achieved.

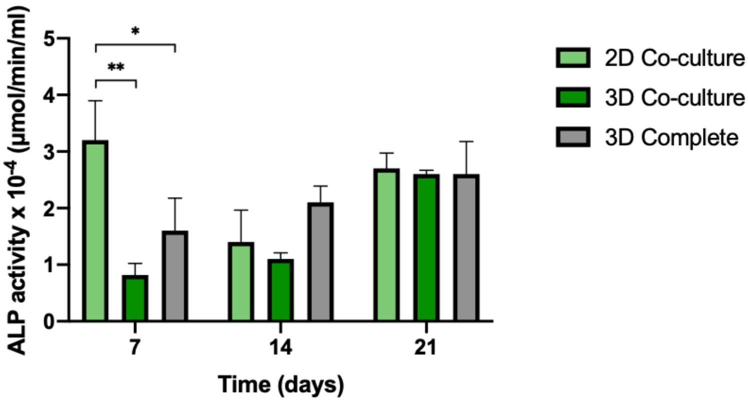

Figure 5.3 – ALP activity levels in the different configurations of the models in different timepoints (7, 14 and 21 days) during the time in culture. Results are the average of triplicates, and bars represent the standard error of the mean (SEM). Statistical differences were calculated using 2-way ANOVA multiple comparisons to compare the levels of ALP in the different configurations for each timepoint ($p<0.05$ is denoted by * and $p<0.01$ is denoted by **).

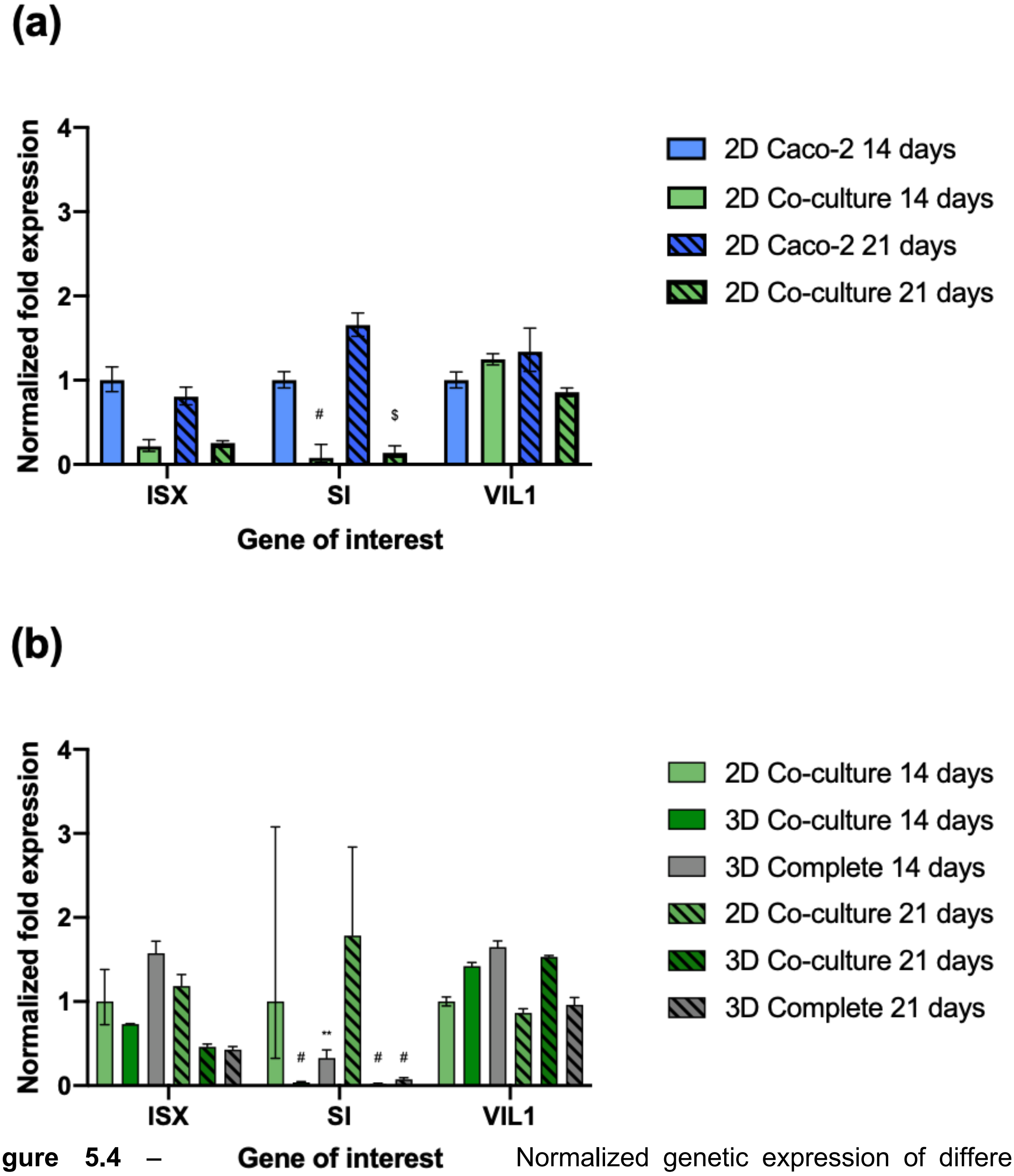

Figure 5.4 – Normalized genetic expression of different intestinal markers between (a) 2D Caco-2 and 2D Co-culture models and (b) 2D Co-culture, 3D Co-culture and 3D Complete models at 14 and 21 days. Results are the average of triplicates, and bars represent the upper and lower limits. Statistical differences were calculated using the log transformed data with 2-way ANOVA multiple comparisons in relation to (a) 2D Caco-2 21 days and (b) 3D Co-culture 21 days, used as references ($p<0.01$ is denoted by **, $p<0.001$ is denoted by $ and $p<0.0001$ are denoted by #).

5.4.3. Expression of tight and adherens junctions, drug transporters and MUC2

The expression and activity of drug transporters in intestinal models can greatly influence the absorption of drugs, playing an important role in drug disposition, targeting, toxicity and interactions, impacting the pharmacokinetics and pharmacodynamics of compounds [42, 43].

The genetic expression of different transporters in the models was evaluated (Figure 5.5). As in the previous section, a comparison between 2D models was initially performed (Figure 5.5a). The only significant difference, when comparing to the 2D Caco-2 model at day 21, was observed for PEPT1 (SLC15A1) in the 2D Co-culture at day 14.

Regarding the genetic expression of the transporters in the 3D models comparing with the 2D, differences where observed for some transporters (Figure 5.5b). In the case of efflux transporters (P-gp – ABCB1; MRP1 – ABCC1; MRP2 – ABCC2; BCRP – ABCG2), significant differences were observed for P-gp, MRP2 and BCRP. For P-gp, levels were lower in the 3D Complete model at both timepoints, and for the other two transporters, levels were lower in both 3D configurations. P-gp is the most studied intestinal efflux transporter, since it modulates the bioavailability of orally administered drugs [42]. P-gp is localized in the apical membrane of the intestinal epithelium, an ideal location to limit the oral absorption of compounds [44]. Different anthracyclines, alkaloids, peptides, steroid hormones, local anesthetics and immunosuppressive agents are pumped by P-gp [42, 45]. P-gp may also contribute to the clearance of intravenously administered drugs, like digoxin, paclitaxel, and vinblastine, among others, by actively secreting them into the intestinal lumen [46, 47]. This results from the fact that P-gp has a broad substrate specificity, being involved in the efflux of various compounds [42, 48]. Since P-gp is normally overexpressed in Caco-2 cells comparing to what is observed *in vivo*, the fact that its expression is lower in the 3D Complete model is encouraging [6, 49-51].

MRP2, like P-gp, is also located on the apical side of enterocytes, acting as a barrier to drug absorption [42]. This transporter is clinically relevant as it modulates the pharmacokinetics of multiple drugs [52]. Since MRP2 is also normally overexpressed in Caco-2 cells, our 3D models can be advantageous [49, 53]. An overlapping substrate specificity has been observed for MRP2 and P-gp, suggesting that these transporters can act together and impose a very significant barrier to intestinal absorption [42]. The fact that 3D models have a lower expression of these proteins is, thus, relevant. While MRP1 is also an efflux pump, it is localized on the basolateral side of enterocytes so, unlike P-gp and MRP2, it acts as an absorptive transporter, playing a role in protecting the enterocytes from the accumulation of toxic substances [42, 47]. For this transporter, no differences were observed between models. BCRP is also located on the apical membrane and, similarly to MRP2 and P-gp, it has a role in limiting oral bioavailability [42]. Studies suggest that this transporter is normally under expressed in Caco-2 cells compared to the small intestine [49, 53, 54]. Since the 3D models have an even lower expression compared to the 2D, they may be inadequate to screen for BCRP substrates, since false positive results may occur.

For the influx transporters (PEPT1 – SLC15A1, MCT1 – SLC16A1, OCT1 – SLC22A1), significant differences were observed for MCT1 in the 3D models, at all timepoints. However, for both PEPT1 and OCT1, the only difference was observed for the 3D complete model at day 21. Expression of PEPT1 in the small intestine, in the apical side of enterocytes, has been demonstrated in different species [55]. The presence of this transporter is important in the drug absorption process since many compounds, like the majority of beta-lactam antibiotics, are its substrates. Different studies suggest that this transporter is normally under expressed in Caco-2 cells [49, 54]. Although the expression was decreased in the 3D complete model at day 21, which can be seen as a negative result, in 2D this transporter was more expressed in the co-culture model. Comparing the 3D models with the Caco-2, it is possible to observe that the amount of PEPT1 is higher in the 3D models, even though this increase may not be significant in statistical terms. MCT1 is also implicated in intestinal drug absorption, being expressed in the apical side of the small intestine [42]. Although not as important and studied as PEPT1, overexpression in the Caco-2 cells has been shown, suggesting that the decrease of expression in the 3D models may better reflect *in vivo* values [61]. The same study also refers the overexpression of OCT1 in Caco-2 [53]. This transporter, unlike PEPT1 and MCT1, is localized on the basolateral side of the enterocytes, so it can mediate basolateral uptake [42, 56]. Although a significant decrease was only observed in the 3D Complete model at 21 days, it is possible to observe a lower expression in 3D models when comparing to the Caco-2 model.

In general, it is possible to state that regarding the expression of transporters, 3D models present levels closer to *in vivo*, except for the BCRP. Expression of key efflux transporters P-gp and MRP2 and influx transporter PEPT1 is more biologically relevant in the 3D models, which may translate in a great advantage when testing permeability.

The expression of P-gp and MRP2 was also evaluated by immunostaining (Figure 5.6a and 5.6b). Although it is difficult to evaluate the expression through this qualitative method, it seems that both transporters present higher expression in the 2D models, confirming the genetic expression results.

Tight junctions were also evaluated by staining Claudin-1 and ZO-1, integral transmembrane and peripheral junction proteins, respectively, and E-cadherin, an adherens junction protein. For E-cadherin, expression was similar between models (Figure 5.6a). Regarding the tight junctions, expression of Claudin-1 (Figure 5.6b) was slightly higher in the 2D model comparing to the 3D configurations at day 14 day, but similar at day 21, while

ZO-1 was highly expressed in all models at different timepoints (Figure 5.6c). Lower expression of tight junctions in the 3D models was expectable, as models presented a lower TEER (Figure 5.7). But probably differences are not so evident since comparison is being made with the 2D Co-culture model, which presents a leakier barrier than the Caco-2 model because of the presence of HT29-MTX cells, that do not form junctions as tight as Caco-2 cells. In fact, one of the disadvantages of the Caco-2 model is the formation of a barrier tighter than what is observed *in vivo*, because of the high expression of tight junctions [57, 58]. The expression of MUC2, the most expressed mucin in the small intestine, which is a gel-forming mucin, was also evaluated (Figure 5.6c) [59, 60]. The results allow to confirm that all configurations of the models, in 2D and 3D, secreted MUC2, which was expectable due to the presence of the mucus producing HT29-MTX cells [61].

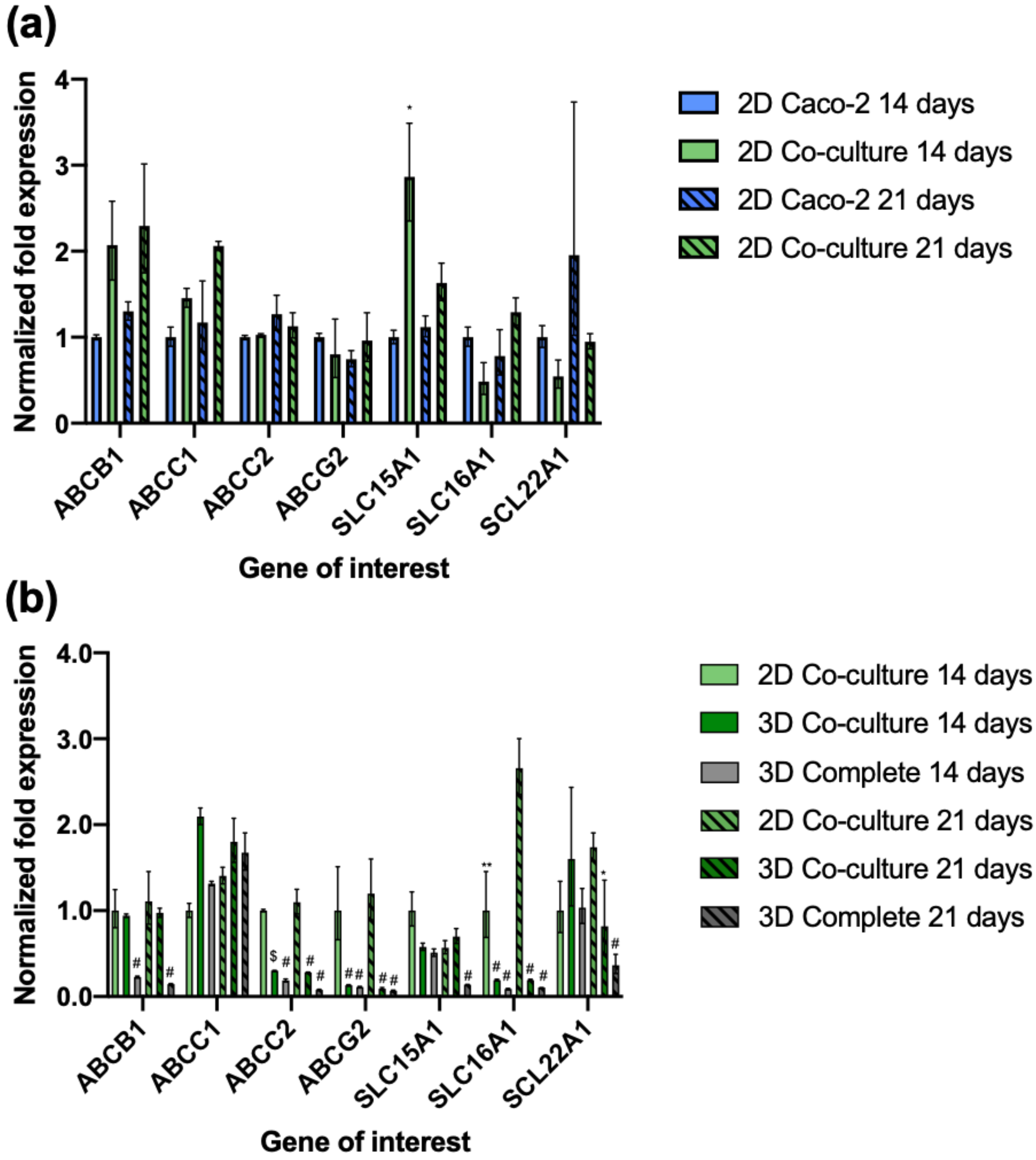

Figure 5.5 - Normalized genetic expression of different intestinal transporters between (a) 2D Caco-2 and 2D Co-culture models and (b) 2D Co-culture, 3D Co-culture and 3D Complete models at 14 and 21 days. Results are the average of triplicates, and bars represent the upper and lower limits. Statistical differences were calculated using the log transformed data with 2-way ANOVA multiple comparisons in relation to (a) 2D Caco-2 21 days and (b) 2D Co-culture 21 days, used as reference ($p<0.05$ are denoted by *, $p<0.01$ is denoted by **, $p<0.001$ is denoted by $ and $p<0.0001$ are denoted by #).

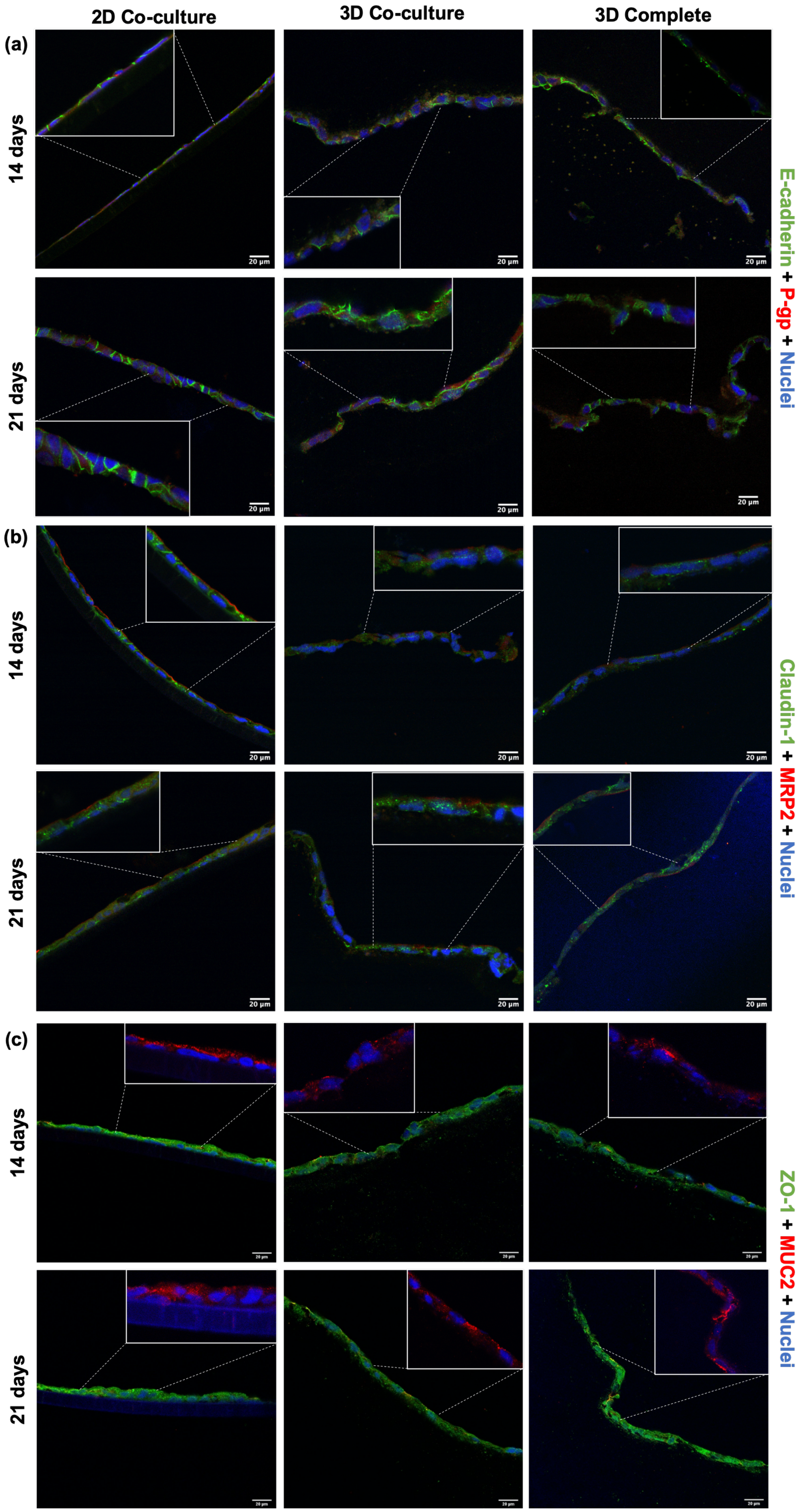
2D Co-culture
3D Co-culture
3D Complete
(a)
14 days
21 days
E-cadherin + P-gp + Nuclei
(b)
14 days
21 days
Claudin-1 + MRP2 + Nuclei
(c)
14 days
21 days
ZO-1 + MUC2 + Nuclei
20 µm

Figure 5.6 – Comparison of protein expression of (a) **E-cadherin** and **P-gp**, (b) **Claudin-1** and **MPR2** and (c) **ZO-1** and **MUC2** between the 2D Co-culture, 3D Co-culture and 3D Complete models at 14 and 21 days. The nuclei were counterstained with DAPI.

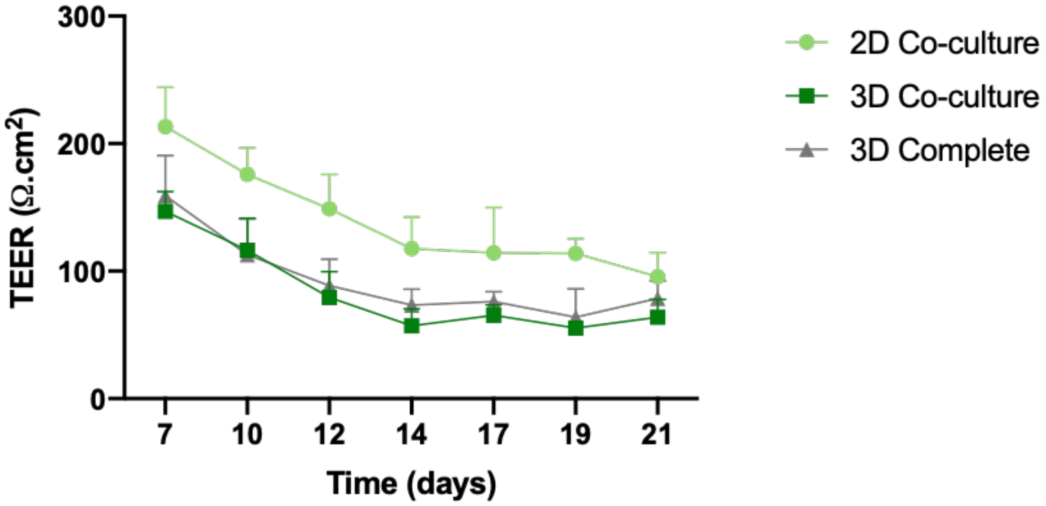

Figure 5.7 - TEER values of the 2D Co-culture, 3D Co-culture and 3D Complete models during the 21 days in culture. Results are the average of nine replicates, and bars represent the standard deviation (SD).

5.4.4. P-gp activity

Genetic expression of P-gp was higher in the 2D model, compared to the 3D configurations, and in 3D it was lower on the Complete model. Since protein expression and activity levels may differ from genetic levels [49], the activity of P-gp at protein level was evaluated using Rho 123, which is a P-gp substrate [62]. This transporter is able to decrease absorption of compounds from the apical to the basolateral compartments, but it is also able to actively pump out compounds that are on the basolateral part to the lumen, as already stated. Thus, to confirm P-gp activity the transport of Rho 123 was evaluated in both directions. Results presented in Figure 5.8 corroborate the RT-qPCR results. Regarding the results from the apical to basolateral compartment (Figure 5.8a), permeability was always higher in the 3D models, both at days 14 and 21, comparing to 2D. This difference was more pronounced and statistically significant at day 21. For both 3D models, permeability of Rho 123 was higher at day 21 than 14, being that this difference was statistically significant for the 3D complete model. This may indicate that P-gp is present in higher amounts at day 14 and its expression is decreased by day 21.

The same trend was observed in the basolateral to apical direction (Figure 5.8b). In fact, the 2D model was capable of pumping more efficiently the Rho 123 to the lumen at both timepoints. Efflux of Rho 123 was significantly lower in 3D, and at day 14 day it was significantly lower in the 3D Complete model, comparing to the 3D Co-culture. In the 3D Co-culture configuration, a significant difference was also observed between days 14 and 21. When analyzing the ratio between the basolateral to apical and the apical to basolateral transport, it is possible to see the ratio is higher in the 2D model at both time points (Figure 5.8c). This ratio is used to understand the influence of transporters in the permeability of compounds, with a lower ratio meaning a lower control of the transporter in the passage of the substrate [63]. This confirms that P-gp is less active in the 3D models, especially at day 21. Regarding the 2D model, a higher ratio is observed at day 21 than day 14, which is supported by literature findings stating that a higher activity of P-gp in Caco-2 cells is observed with longer time in culture [64]. Interestingly, the opposite is observed in the 3D models, confirming that the configuration and composition of the models can have an impact in the activity of transporters.

Collectively, these results show that activity of P-gp varies along time and is higher in 2D. When comparing both 3D configurations, it is possible to see that it is less active in the Complete configuration, which agrees with the results of genetic expression.

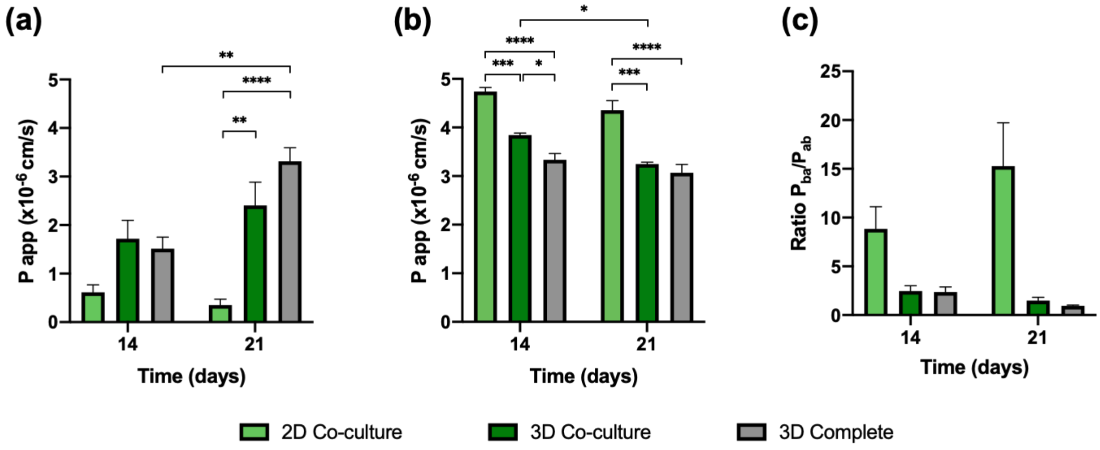

Figure 5.8 – P_{app} (x10^{-6} cm/s) values of Rhodamine 123 in the 2D Co-culture, 3D Co-culture and 3D Complete models at 14 and 21 days in the (a) apical to basolateral and (b) basolateral to apical directions and (c) ratio of the bidirectional transport. Results are the average of triplicates, and bars represent the standard error of the mean (SEM). Statistical differences were calculated using 2-way ANOVA multiple comparisons to compare P_{app} between each configuration at different time points and to compare between the same configuration at each timepoint ($p<0.05$ are denoted by *, $p<0.01$ are denoted by **, $p<0.001$ are denoted by *** and $p<0.0001$ are denoted by ****).

5.4.5. Permeability

Three model drugs with different permeability were tested. Colchicine, a low permeability drug [fraction absorbed (F_a) < 50%], is absorbed in the jejunum and ileum by the transcellular route and is considered to be a substrate of P-gp and MRP2 [42, 65-68]. Atenolol is a moderate permeability drug (50% < F_a > 84%) and was chosen because it is mainly absorbed by the paracellular route [69]. Since the permeability of paracellular markers in Caco-2 monolayers is up to 100 times lower than what is observed *in vivo* in the small intestine, a paracellular compound was used to understand if permeability outcomes would be more reliable using the 3D models [70]. Lastly, metoprolol was also used, as it is absorbed transcellularly and is considered a marker of high permeability (F_a > 85%) [71, 72]. Observing the permeability results (Figure 5.9 and Table 5.1), it is possible to see that the highest permeability was achieved for the 3D Co-culture model at day 21 for all compounds. Of note, for some compounds and models, testing the permeability at 14 or 21 days yielded different results, thus cultures were prolonged for 21 days, as normally described, and discussion will focus on that time point. As compared to values described in the literature for the P_{app} of the different compounds using the Caco-2 model (Table 5.2), results obtained herein were higher for colchicine and atenolol, and similar for metoprolol. Higher permeability comparing to the Caco-2 model was observed both for the 3D models and the 2D Co-culture model. This was expected, since the Caco-2 + HT29-MTX co-culture provides an improved model, where HT29-MTX cells decrease the tightness of the monolayer due to the lower expression of tight junctions and addition of a mucus layer to the model [6, 50]. However, it is possible to see that in the 3D Co-culture model, permeability of all compounds was significantly higher at day 21 when comparing to the 2D model (Figure 5.9 and Table 5.1). The profile of absorption was linear for all compounds in all models (Figure A.3 of Appendix).

For colchicine, this higher permeability could be explained by the fact that P-gp and MRP2, which are able to pump this drug back into the lumen, were less active in the 3D models, as observed in the previous sections.

Importantly, for the 3D Complete model, although a significantly lower expression and activity of P-gp was observed (Figure 5.5b and 5.9), this did not translate into higher permeability of colchicine, or of the other compounds. Collectively, the 3D Complete model always showed lower permeability compared to the 3D Co-culture configuration, being similar to the 2D results and even lower for metoprolol. Since the difference between the 3D Co-culture and the 3D Complete models is the presence of the endothelial layer, we believe that this additional layer may explain the results, which was expectable since it offers an additional barrier to the passage of compounds.

For atenolol, a higher permeability was also observed for the 3D Co-culture model. In this case, since atenolol is a compound that is mostly absorbed by the paracellular route, this higher permeability can be related with the decrease in the TEER values (Figure 5.7). For metoprolol, permeability was again higher for the 3D Co-culture models, but this drug is a marker of high permeability, so values are normally high even in the Caco-2 model (Table 5.2).

The ultimate goal of developing a new model to test permeability is to get as close as possible to the permeability observed in humans. However, since between the *in vitro* tests and the clinical trials in humans, there is always the need for *in vivo* testing in animals, the first objective of these *in vitro* models is to reduce animal testing. If *in vitro* results are able to give similar outcomes to what is observed *in vivo*, for examples in rats, which are normally used at a first stage and that present more similarity with humans, then the need of usage of these animals is reduced [73]. When comparing our results to a study where the P_{app} of the compounds was determined in rat small intestine, it was possible to see that our 3D Co-culture model was the one that got closer to the reported values (Table 5.2) [67]. The same is true for the effective permeability (P_{eff}) results obtained in human small intestine and rat small intestine, and also when comparing the percentage of permeability with the F_a in humans (Table 5.1 and 5.2).

The results regarding the 3D Co-culture model are quite promising. By presenting permeability profiles more similar to those observed *in vivo*, this model offers a powerful *in vitro* platform to reduce the use of animal models in an early stage of drug development, being more reliable than the 2D models used nowadays for *in vitro* testing.

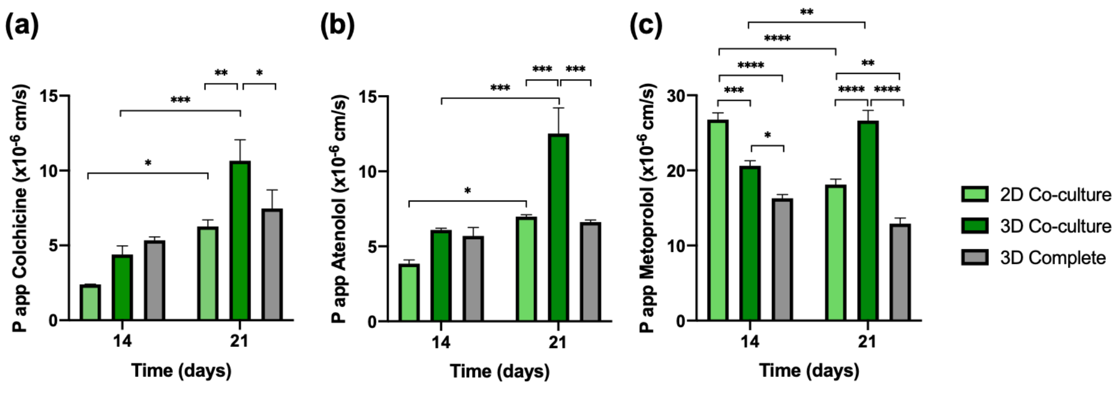

Figure 5.9 - P_{app} (x10^{-6} cm/s) values of (a) colchicine, (b) atenolol and (c) metoprolol in the 2D Co-culture, 3D Co-culture and 3D Complete models at 14 and 21 days. Results are the average of triplicates, and bars represent the standard error of the mean (SEM). Statistical differences were calculated using 2-way ANOVA multiple comparisons to compare P_{app} between each configuration at different time points and to compare between the same

configuration at each timepoint ($p<0.05$ are denoted by *, $p<0.01$ are denoted by **, $p<0.001$ are denoted by *** and $p<0.0001$ are denoted by ****).

Table 5.1 – Mean values and standard deviation (SD) of P_{app} ($x10^{-6}$ cm/s) and Permeability (%) of the different model drugs evaluated in the different configurations of the models at different time points (14 and 21 days).

		P_{app} ($x10^{-6}$ cm/s)			Permeability (%)		
	Day	**2D Co-culture**	**3D Co-culture**	**3D Complete**	**2D Co-culture**	**3D Co-culture**	**3D Complete**
Colchicine	14	2.4 ± 0.0	4.4 ± 1.0	5.3 ± 0.4	7.6 ± 0.1	13.9 ± 3.2	16.9 ± 1.3
	21	6.3 ± 0.8	10.7 ± 2.4	7.5 ± 2.1	19.9 ± 3.4	33.8 ± 7.7	23.7 ± 6.8
Atenolol	14	3.8 ± 0.4	6.1 ± 0.2	5.7 ± 1.0	12.2 ± 1.4	19.3 ± 0.6	18.0 ± 3.1
	21	7.0 ± 0.2	12.5 ± 3.0	6.6 ± 0.2	22.1 ± 0.7	39.7 ± 9.3	21.0 ± 0.8
Metoprolol	14	26.8 ± 1.6	20.6 ± 1.2	16.3 ± 0.9	84.8 ± 5.0	65.3 ± 3.8	51.6 ± 2.7
	21	18.1 ± 1.3	26.6 ± 2.4	12.9 ± 1.3	57.4 ± 4.0	84.4 ± 7.5	40.9 ± 4.1

Table 5.2 – Literature values of F_a in humans, P_{eff} ($x10^{-6}$ cm/s) in human and rat small intestine, P_{app} ($x10^{-6}$ cm/s) in Caco-2 and rat small intestine and P_{app} ($x10^{-6}$ cm/s) in the 2D Co-culture, 3D Co-culture and 3D Complete models at 21 days.

	F_a (Humans)	P_{eff} ($x10^{-6}$ cm/s) Human Small Intestine	P_{eff} ($x10^{-6}$ cm/s) Rat Small Intestine	P_{app} ($x10^{-6}$ cm/s) Caco-2	P_{app} ($x10^{-6}$ cm/s) Rat Small Intestine	P_{app} ($x10^{-6}$ cm/s) 2D Co-culture	P_{app} ($x10^{-6}$ cm/s) 3D Co-culture	P_{app} ($x10^{-6}$ cm/s) 3D Complete
Colchicine	44[72]		5[73]; 28[73]; 5-6[74]	0.9[65]; 0.93[70]	25[65];	6.3	10.7	7.5
Atenolol	50[75]	20[76, 77]	2.8[73]; 10[73]; 10.7[78]; 5.5-18[76]	1.6[65]; 3.3[79]; 1.6[80]; 0.53[81]; 1.6[70]; 1[82]	10.7[65]	7.0	12.5	6.6
Metoprolol	98[75]	134[77, 83]; 90-150[76]	36[73]; 66[73]; 62.4[78]	23[65]; 33.2[80]; 140[79]; 23.7[81]; 23[70]; 36.9[82]	62.4[65]	18.1	26.6	12.9

5.5. Conclusion

The present study establishes a novel 3D *in vitro* intestinal model composed of three different layers mimicking, in a better way, the native small intestine. To our knowledge, this study is the first where an endothelial barrier is added to a 3D model in order to study permeability of compounds.

The expression of transporters was evaluated and the 3D models revealed a lower expression of P-gp and MRP2, two very important efflux pumps which are normally overexpressed in the Caco-2 model and permeability with Rho 123 confirmed the results for P-gp. Regarding the expression of junctions' proteins, no differences were observed and the presence of MUC2 was confirmed in all models, as expected by the presence of HT29-MTX cells.

The permeability revealed that the 3D Co-culture model at day 21 was the configuration with results closer to *in vivo*, being more reliable than the other models. It was observed that for the 3D Complete model, the addition of the endothelial layer rendered a decrease in permeability outcomes. Nevertheless, this configuration can be important to understand how different molecules act with the endothelial barrier and untill what extent this barrier can pose as an important obstacle for certain compounds. Besides, since this model mimics, in a better way, the physiology of the native intestine, by replicating the layers that exist in the intestinal mucosa, it can be adapted and used for other studies.

In the present chapter, a new 3D advanced *in vitro* model showed to be capable of better mimicking the native small intestine and, in its turn, render more reliable permeability results. We believe that this model has the potential to help bridging the gap between i*n vitro* and *in vivo* testing, which could have a major impact in the drug development field and, by this, contribute to the 3Rs policy, mainly by reducing the number of animal experiments.

References

1. Kennedy, T., *Managing the drug discovery/development interface.* Drug Discovery Today, 1997. **2**(10): p. 436-444.
2. Li, A.P., *Screening for human ADME/Tox drug properties in drug discovery.* Drug Discovery Today, 2001. **6**(7): p. 357-366.
3. Dahlgren, D. and H. Lennernas, *Intestinal Permeability and Drug Absorption: Predictive Experimental, Computational and In Vivo Approaches.* Pharmaceutics, 2019. **11**(8): p. 1-18.
4. Polli, J.E., *In vitro studies are sometimes better than conventional human pharmacokinetic in vivo studies in assessing bioequivalence of immediate-release solid oral dosage forms.* AAPS Journal, 2008. **10**(2): p. 289-299.
5. Press, B. and D. Di Grandi, *Permeability for intestinal absorption: Caco-2 assay and related issues.* Current Drug Metabolism, 2008. **9**(9): p. 893-900.
6. Hilgendorf, C., et al., *Caco-2 versus Caco-2/HT29-MTX Co-cultured Cell Lines: Permeabilities Via Diffusion, Inside- and Outside-Directed Carrier-Mediated Transport.* Journal of Pharmaceutical Sciences, 2000. **89**(1): p. 63-75.
7. Chen, Y., et al., *Robust bioengineered 3D functional human intestinal epithelium.* Scientific Reports, 2015. **5**: p. 13708.
8. Fitzgerald, K.A., et al., *Life in 3D is never flat: 3D models to optimise drug delivery.* Journal of Controlled Release, 2015. **215**: p. 39-54.
9. Macedo, M.H., et al., *Development of an Improved 3D in vitro Intestinal Model to Perform Permeability Studies of Paracellular Compounds.* Frontiers in Bioengineering and Biotechnology, 2020. **8**: p. 524018.
10. Li, N., et al., *Development of an improved three-dimensional in vitro intestinal mucosa model for drug absorption evaluation.* Tissue Engineering, Part C: Methods, 2013. **19**(9): p. 708-719.
11. Madden, L.R., et al., *Bioprinted 3D Primary Human Intestinal Tissues Model Aspects of Native Physiology and ADME/Tox Functions.* iScience, 2018. **2**: p. 156-167.
12. Pereira, C., et al., *Dissecting stromal-epithelial interactions in a 3D in vitro cellularized intestinal model for permeability studies.* Biomaterials, 2015. **56**: p. 36-45.
13. Yi, B., et al., *Three-dimensional in vitro gut model on a villi-shaped collagen scaffold.* BioChip Journal, 2017. **11**(3): p. 219-231.
14. Yu, J., et al., *Three dimensional human small intestine models for ADME-Tox studies.* Drug Discovery Today, 2014. **19**(10): p. 1587-1594.

15. Yu, J., et al., *In vitro 3D human small intestinal villous model for drug permeability determination.* Biotechnology and Bioengineering, 2012. **109**(9): p. 2173-2178.
16. Darnell, M., et al., *Cytochrome P450-dependent metabolism in HepaRG cells cultured in a dynamic three-dimensional bioreactor.* Drug Metabolism and Disposition, 2011. **39**(7): p. 1131-1138.
17. Desrochers, T.M., E. Palma, and D.L. Kaplan, *Tissue-engineered kidney disease models.* Advanced Drug Delivery Reviews, 2014. **69-70**: p. 67-80.
18. Pampaloni, F., E.G. Reynaud, and E.H. Stelzer, *The third dimension bridges the gap between cell culture and live tissue.* Nature Reviews Molecular Cell Biology, 2007. **8**(10): p. 839-845.
19. Justice, B.A., N.A. Badr, and R.A. Felder, *3D cell culture opens new dimensions in cell-based assays.* Drug Discovery Today, 2009. **14**(1-2): p. 102-107.
20. Chitcholtan, K., et al., *Differences in growth properties of endometrial cancer in three dimensional (3D) culture and 2D cell monolayer.* Experimental Cell Research, 2013. **319**(1): p. 75-87.
21. Basson, M.D., G. Turowski, and N.J. Emenaker, *Regulation of human (Caco-2) intestinal epithelial cell differentiation by extracellular matrix proteins.* Experimental Cell Research, 1996. **225**(2): p. 301-305.
22. Hewes, S.A., et al., *In Vitro Models of the Small Intestine: Engineering Challenges and Engineering Solutions.* Tissue Engineering, Part B: Reviews, 2020. **26**(4): p. 313-326.
23. Snyder, J., et al., *Materials and Microenvironments for Engineering the Intestinal Epithelium.* Annals Of Biomedical Engineering, 2020. **48**(7): p. 1916-1940.
24. Castano, A.G., et al., *Dynamic photopolymerization produces complex microstructures on hydrogels in a moldless approach to generate a 3D intestinal tissue model.* Biofabrication, 2019. **11**(2): p. 025007.
25. Zhang, J., J. Penny, and J.R. Lu, *Development of a novel in vitro 3D intestinal model for permeability evaluations.* International Journal of Food Sciences and Nutrition, 2020. **71**(5): p. 549-562.
26. Li, N., et al., *A fast screening model for drug permeability assessment based on native small intestinal extracellular matrix.* RSC Advances, 2018. **8**: p. 34514-34524.
27. Sun, D., et al., *Comparison of human duodenum and Caco-2 gene expression profiles for 12,000 gene sequences tags and correlation with permeability of 26 drugs.* Pharmaceutical Research, 2002. **19**(10): p. 1400-1416.
28. Roulis, M. and R.A. Flavell, *Fibroblasts and myofibroblasts of the intestinal lamina propria in physiology and disease.* Differentiation, 2016. **92**(3): p. 116-131.

29. Olson, A.D., *Contraction of collagen gels by intestinal epithelial cells depends on microfilament function.* Digestive Diseases and Sciences, 1993. **38**(3): p. 388-395.

30. Deanfield, J.E., J.P. Halcox, and T.J. Rabelink, *Endothelial function and dysfunction: testing and clinical relevance.* Circulation, 2007. **115**(10): p. 1285-1295.

31. Szulcek, R., et al., *Transient Intervals of Hyper-Gravity Enhance Endothelial Barrier Integrity: Impact of Mechanical and Gravitational Forces Measured Electrically.* PLoS One, 2015. **10**(12): p. e0144269.

32. Hinnebusch, B.F., et al., *Enterocyte differentiation marker intestinal alkaline phosphatase is a target gene of the gut-enriched Kruppel-like factor.* American Journal of Physiology, 2004. **286**(1): p. 23-30.

33. Alpers, D.H., et al., *The secretion of intestinal alkaline phosphatase (IAP) from the enterocyte.* Journal of Gastroenterology, 1994. **29**: p. 63-67.

34. Artursson, P. and J. Karlsson, *Correlation between oral drug absorption in humans and apparent drug permeability coefficients in human intestinal epithelial (Caco-2) cells.* Biochemical and Biophysical Research Communications, 1991. **175**(3): p. 880-885.

35. Traber, P.G., et al., *Sucrase-isomaltase gene expression along crypt-villus axis of human small intestine is regulated at level of mRNA abundance.* American Journal of Physiology, 1992. **262**(1 Pt 1): p. G123-130.

36. Suh, E. and P.G. Traber, *An intestine-specific homeobox gene regulates proliferation and differentiation.* Molecular and Cellular Biology, 1996. **16**(2): p. 619-625.

37. Sato, T., et al., *Long-term expansion of epithelial organoids from human colon, adenoma, adenocarcinoma, and Barrett's epithelium.* Gastroenteroloy, 2011. **141**(5): p. 1762-1772.

38. Choi, M.Y., et al., *A dynamic expression survey identifies transcription factors relevant in mouse digestive tract development.* Development, 2006. **133**(20): p. 4119-4129.

39. Sue, S., et al., *Intestine-specific homeobox (ISX) induces intestinal metaplasia and cell proliferation to contribute to gastric carcinogenesis.* Journal of Gastroenteroloy, 2016. **51**(10): p. 949-960.

40. Wikman-Larhed, A. and P. Artursson, *Co-cultures of human intestinal goblet (HT29-H) and absorptive (Caco-2) cells for studies of drug and peptide absorption.* European Journal of Pharmaceutical Sciences, 1995. **3**(3): p. 171-183.

41. Chen, X.-M., I. Elisia, and D.D. Kitts, *Defining conditions for the co-culture of Caco-2 and HT29-MTX cells using Taguchi design.* Journal of Pharmacological and Toxicological Methods, 2010. **61**(3): p. 334-342.

42. Estudante, M., et al., *Intestinal drug transporters: an overview.* Advanced Drug Delivery Reviews, 2013. **65**(10): p. 1340-1356.
43. Liu, Z. and K. Liu, *The transporters of intestinal tract and techniques applied to evaluate interactions between drugs and transporters.* Asian Journal of Pharmaceutical Sciences, 2013. **8**(3): p. 151-158.
44. Chan, L.M., S. Lowes, and B.H. Hirst, *The ABCs of drug transport in intestine and liver: efflux proteins limiting drug absorption and bioavailability.* European Journal of Pharmaceutical Sciences, 2004. **21**(1): p. 25-51.
45. Varma, M.V., et al., *Targeting intestinal transporters for optimizing oral drug absorption.* Current Drug Metabolism, 2010. **11**(9): p. 730-742.
46. Muller, F. and M.F. Fromm, *Transporter-mediated drug-drug interactions.* Pharmacogenomics, 2011. **12**(7): p. 1017-1037.
47. Kunta, J.R. and P.J. Sinko, *Intestinal drug transporters: in vivo function and clinical importance.* Current Drug Metabolism, 2004. **5**(1): p. 109-124.
48. International Transporter, C., et al., *Membrane transporters in drug development.* Nature Reviews Drug Discovery, 2010. **9**(3): p. 215-236.
49. Bruck, S., et al., *Caco-2 cells - expression, regulation and function of drug transporters compared with human jejunal tissue.* Biopharmaceutics & Drug Disposition, 2017. **38**(2): p. 115-126.
50. Beduneau, A., et al., *A tunable Caco-2/HT29-MTX co-culture model mimicking variable permeabilities of the human intestine obtained by an original seeding procedure.* European Journal of Pharmaceutics and Biopharmaceutics, 2014. **87**(2): p. 290-298.
51. Bohets, H., et al., *Strategies for absorption screening in drug discovery and development.* Current Topics in Medicinal Chemistry, 2001. **1**(5): p. 367-383.
52. Gerk, P.M. and M. Vore, *Regulation of expression of the multidrug resistance-associated protein 2 (MRP2) and its role in drug disposition.* Journal of Pharmacology and Experimental Therapeutics, 2002. **302**(2): p. 407-415.
53. Maubon, N., et al., *Analysis of drug transporter expression in human intestinal Caco-2 cells by real-time PCR.* Fundamental & Clinical Pharmacology, 2007. **21**(6): p. 659-663.
54. Hilgendorf, C., et al., *Expression of thirty-six drug transporter genes in human intestine, liver, kidney, and organotypic cell lines.* Drug Metabolism and Disposition, 2007. **35**(8): p. 1333-1340.
55. Ogihara, H., et al., *Peptide transporter in the rat small intestine: ultrastructural localization and the effect of starvation and administration of amino acids.* Histochemical Journal, 1999. **31**(3): p. 169-174.

56. Shu, Y., *Research progress in the organic cation transporters.* Zhong Nan Da Xue Xue Bao Yi Xue Ban, 2011. **36**(10): p. 913-926.
57. Artursson, P., K. Palm, and K. Luthman, *Caco-2 monolayers in experimental and theoretical predictions of drug transport.* Advanced Drug Delivery Reviews, 2001. **46**(1-3): p. 27-43.
58. Sun, H., et al., *The Caco-2 cell monolayer: usefulness and limitations.* Expert Opinion on Drug Metabolism & Toxicology, 2008. **4**(4): p. 395-411.
59. Schneider, H., et al., *Study of mucin turnover in the small intestine by in vivo labeling.* Scientific Reports, 2018. **8**(1): p. 5760.
60. Kim, Y.S. and S.B. Ho, *Intestinal goblet cells and mucins in health and disease: recent insights and progress.* Current Gastroenterology Reports, 2010. **12**(5): p. 319-330.
61. Pontier, C., et al., *HT29-MTX and Caco-2/TC7 monolayers as predictive models for human intestinal absorption: role of the mucus layer.* Journal of Pharmaceutical Sciences, 2001. **90**(10): p. 1608-1619.
62. Wang, Y., et al., *A kinetic study of Rhodamine123 pumping by P-glycoprotein.* Biochimica et Biophysica Acta (BBA) - Biomembranes, 2006. **1758**(10): p. 1671-1676.
63. Versantvoort, C.H.M., et al., *Monolayers of IEC-18 cells as an in vitro model for screening the passive transcellular and paracellular transport across the intestinal barrier: comparison of active and passive transport with the human colon carcinoma Caco-2 cell line.* Environmental Toxicology and Pharmacology, 2002. **11**(3): p. 335-344.
64. Versantvoort, C.H., et al., *Monolayers of IEC-18 cells as an in vitro model for screening the passive transcellular and paracellular transport across the intestinal barrier: comparison of active and passive transport with the human colon carcinoma Caco-2 cell line.* Environmental Toxicology and Pharmacology, 2002. **11**(3-4): p. 335-344.
65. Ruiz, M.L., et al., *Induction of intestinal multidrug resistance-associated protein 2 (Mrp2) by spironolactone in rats.* European Journal of Pharmacology, 2009. **623**(1-3): p. 103-106.
66. Dahan, A. and G.L. Amidon, *Grapefruit juice and its constituents augment colchicine intestinal absorption: potential hazardous interaction and the role of p-glycoprotein.* Pharmaceutical Research, 2009. **26**(4): p. 883-892.
67. Lozoya-Agullo, I., et al., *In Situ Perfusion Model in Rat Colon for Drug Absorption Studies: Comparison with Small Intestine and Caco-2 Cell Model.* Journal of Pharmaceutical Sciences, 2015. **104**(9): p. 3136-3145.

68. Ben-Chetrit, E., *Colchicine.* Textbook of Autoinflammation, 2018: p. 729-749.

69. DiMarco, R.L., et al., *Improvement of paracellular transport in the Caco-2 drug screening model using protein-engineered substrates.* Biomaterials, 2017. **129**: p. 152-162.

70. Artursson, P., A.L. Ungell, and J.E. Lofroth, *Selective paracellular permeability in two models of intestinal absorption: cultured monolayers of human intestinal epithelial cells and rat intestinal segments.* Pharmaceutical Research, 1993. **10**(8): p. 1123-1129.

71. Lozoya-Agullo, I., et al., *Segmental-dependent permeability throughout the small intestine following oral drug administration: Single-pass vs. Doluisio approach to in-situ rat perfusion.* International Journal of Pharmaceutics, 2016. **515**(1-2): p. 201-208.

72. Lozoya-Agullo, I., et al., *Investigating drug absorption from the colon: Single-pass vs. Doluisio approaches to in-situ rat large-intestinal perfusion.* International Journal of Pharmaceutics, 2017. **527**(1-2): p. 135-141.

73. Youhanna, S. and V.M. Lauschke, *The Past, Present and Future of Intestinal In Vitro Cell Systems for Drug Absorption Studies.* Journal of Pharmaceutical Sciences, 2021. **110**(1): p. 50-65.

74. Skolnik, S., et al., *Towards Prediction of In Vivo Intestinal Absorption Using a 96-Well Caco-2 Assay.* Journal of Pharmaceutical Sciences, 2010. **99**(7): p. 3246-3265.

75. Lozoya-Agullo, I., et al., *In-situ intestinal rat perfusions for human Fabs prediction and BCS permeability class determination: Investigation of the single-pass vs. the Doluisio experimental approaches.* International Journal of Pharmaceutics, 2015. **480**(1-2): p. 1-7.

76. Dahan, A., H. Sabit, and G.L. Amidon, *Multiple efflux pumps are involved in the transepithelial transport of colchicine: combined effect of p-glycoprotein and multidrug resistance-associated protein 2 leads to decreased intestinal absorption throughout the entire small intestine.* Drug Metabolism and Disposition, 2009. **37**(10): p. 2028-2036.

77. Varma, M.V., et al., *pH-Dependent Solubility and Permeability Criteria for Provisional Biopharmaceutics Classification (BCS and BDDCS) in Early Drug Discovery.* Molecular Pharmaceutics, 2012. **9**(5): p. 1199-1212.

78. Dahlgren, D., et al., *Direct In Vivo Human Intestinal Permeability (Peff) Determined with Different Clinical Perfusion and Intubation Methods.* Journal of Pharmaceutical Sciences, 2015. **104**(9): p. 2702-2726.

79. Sun, L., et al., *Structure-based prediction of human intestinal membrane permeability for rapid in silico BCS classification.* Biopharmaceutics & Drug Disposition, 2013. **34**(6): p. 321-335.

80. Ruiz-Picazo, A., et al., *Comparison of segmental-dependent permeability in human and in situ perfusion model in rat.* European Journal of Pharmaceutical Sciences, 2017. **107**: p. 191-196.

81. Irvine, J.D., et al., *MDCK (Madin-Darby canine kidney) cells: A tool for membrane permeability screening.* Journal of Pharmaceutical Sciences, 1999. **88**(1): p. 28-33.

82. Cheng, L., et al., *Development of In Vitro Pharmacokinetic Screens Using Caco-2, Human Hepatocyte, and Caco-2/Human Hepatocyte Hybrid Systems for the Prediction of Oral Bioavailability in Humans.* Journal of Biomolecular Screening, 2007. **12**(8): p. 1084-1091.

83. Yazdanian, M., et al., *Correlating Partitioning and Caco-2 Cell Permeability of Structurally Diverse Small Molecular Weight Compounds.* Pharmaceutical Research, 1998. **15**(9): p. 1490-1494.

84. Yang, Y., et al., *Biopharmaceutics classification of selected beta-blockers: solubility and permeability class membership.* Molecular Pharmaceutics, 2007. **4**(4): p. 608-614.

85. Shugarts, S. and L.Z. Benet, *The role of transporters in the pharmacokinetics of orally administered drugs.* Pharmaceutical Research, 2009. **26**(9): p. 2039-2054.

CHAPTER 6 – The shape of our gut: dissecting the importance of the villi architecture in a 3D bioprinted *in vitro* intestinal model

The information provided in this chapter was based in the following publication:

Macedo M.H., Torras N., García-Díaz M., Barrias C.C., Sarmento B., Martínez E., The Shape of our gut: dissecting the importance of the villi architecture in a 3D bioprinted *in vitro* intestinal model, *under preparation*.

In this paper I was responsible for conception, execution and revision of the manuscript. Núria Torras and María García-Díaz were responsible for part of the methodology and revision of the manuscript. The supervisors were responsible for reviewing and submit the manuscript. This paper was not previously included in other thesis, and it is partially reproduced in this section.

6.1. Abstract

The small intestine is a complex organ with a characteristic architecture. Being the major site for absorption, the three-dimensional (3D) topography organized in finger-like protrusions called villi, increases remarkably the surface area, granting a more efficient absorption process. Significantly, the intestinal mucosa, where this process occurs, is a multilayered and multicell-type barrier.

In vitro intestinal models have been routinely used to study different physiological and pathological processes in the gut, such as the intestinal absorption of compounds. However, these standard models are normally two-dimensional (2D) and represent only the epithelial barrier, lacking the structural cues offered by the 3D architecture and the stromal components present *in vivo*, which can lead to inaccurate results. In this chapter, we aimed at developing a new 3D *in vitro* intestinal model with intestinal villus-like microstructures, using stereolithography-based 3D bioprinting and a hydrogel with a network of gelatin methacryloil (GelMA) and poly(ethylene glycol) diacrylate (PEGDA). Human intestinal fibroblasts were embedded within the hydrogel and enterocytes and goblet cells were seeded on top to build a surrogate of the intestinal epithelium. A comparison with a 3D flat model composed by the same hydrogel and cell types was made to understand the impact of the villi architecture in cellular behavior and permeability outcomes. The embedded fibroblasts were able to survive and proliferate inside the hydrogel, remodeling the surrounding extracellular matrix. The epithelial cells fully covered the hydrogel scaffolds and formed a uniform cell layer with barrier properties close to the *in vivo* values. The efflux activity of P-glycoprotein (P-gp), assessed by a transport assay with Rhodamine 123 (Rho 123), was significantly reduced in the villus-like scaffold compared to the flat hydrogel, as well as the genetic expression of other drugs transporters that, in general, showed a more relevant expression in this model. In terms of permeability, the villi model revealed overall increased permeability compared to the flat model. Globally, this study corroborates that the presence of the 3D architecture promotes a more physiological differentiation of the epithelial barrier and this, allied with an increased absorption area, impacts permeability outcomes.

6.2. Introduction

The small intestine is the major site of nutrient and drug absorption. It is a complex organ with a characteristic 3D architecture and composition. The intestinal tissue is organized in finger-like protrusions called villi and invaginations called crypts that greatly increase the tissue surface area and, therefore, the volume and residence time of fluids, enhancing the intestinal absorption [1-3]. Moreover, the intestinal mucosa is organized in different cell compartments [4]. Thus, in order for a molecule to reach systemic circulation, it needs to cross the intestinal epithelium and the lamina propria, before entering the blood stream through the blood capillaries. The intestinal epithelium is composed by absorptive cells – the enterocytes, goblet cells, enteroendocrine cells, Paneth cells, tuft cells and microfold cells [4-6]. The lamina propria, in its turn, contains fibroblasts, myofibroblasts, mesenchymal stem cells, endothelial and immune cells embedded in an extracellular matrix (ECM) [7, 8]. The lamina propria and its interactions with the intestinal epithelium, regarded as epithelial-mesenchymal crosstalk, are important to maintain the integrity of the intestinal mucosa [9, 10]. This crosstalk shapes the architecture of the small intestine, as well as its functions, being essential to the maintenance of cell polarity, behavior and differentiation during intestinal development into adulthood [11-13]. These cellular interactions also play a role in proliferation, migration and apoptosis, contributing to overall tissue homeostasis [14].

Although major developments and breakthroughs have been made in the field [15-20], neither the stromal compartment nor the 3D architecture of the small intestine are usually present in the standard *in vitro* intestinal models that are used to screen drug absorption, study cellular behavior or disease modelling. The gold standard for drug permeability assays is the Caco-2 model, composed of a flat polarized monolayer of enterocyte-like Caco-2 cells that only represents one compartment of the intestinal mucosa - the epithelium, and one cell type - the enterocytes [21]. Also, at the functional level, it presents some drawbacks. Compared with the human intestine, the Caco-2 model has different expression levels of drug transporters and forms a tighter barrier, which can both lead to low accuracy in predicting drug intestinal permeability [22]. Thus, the development of new *in vitro* models that can better represent the physiology of the human small intestine are of major importance to help bridging the gap between *in vitro* and *in vivo* experiments. Different works have shown that the presence of the stromal compartment in the intestinal *in vitro* models led to a more physiological behavior of the epithelial cells [10, 20, 23, 24]. For instance, our group at IBEC developed a cell-laden hydrogel co-network of poly(ethylene glycol) diacrylate (PEGDA) and gelatin methacryloil (GelMA) with fibroblasts embedded inside the scaffold as the stromal compartment and Caco-2 cells on top forming the epithelial barrier. This epithelial-stromal crosstalk promoted the epithelial barrier formation and also accelerated the barrier integrity recovery upon a temporary disruption of the epithelial tight junctions [10]. In the previous chapter of this thesis the development of an innovative 3D intestinal model was shown, composed by an epithelium of enterocytes and goblet cells that sat on top of collagen layer with human intestinal fibroblasts (HIFs) embedded, mimicking the intestinal lamina propria, and an endothelial layer underneath. The 3D configuration and the stromal-epithelial interactions that closely resembled the *in vivo* environment led to a decrease in barrier tightness to values more similar to the human intestine, to a more relevant genetic expression of most drug transporters, and to permeability values closer to the ones found *in vivo*.

The characteristic 3D topography of the small intestine has been demonstrated to have an effect on the epithelial barrier [3, 25, 26]. The finger-like protrusions of 0.2-1 mm in height and 100-200 µm in diameter have a well-defined topography and curvature that provides environmental cues to the epithelial cells growing on top. With the progress in tissue engineering and the development of novel microfabrication techniques, different microstructured *in vitro* models of the small intestine have been proposed [15, 18, 20]. Among the biofabrication techniques, the use of 3D bioprinting has gained relevance in the last years as a way to obtain engineered tissues with precise architectures [15-17, 27]. Recently, a low-cost stereolithography (SLA) 3D printer was costumized to obtain soft hydrogel scaffolds with villi-like microstructures [28]. By co-polymerizing GelMA and PEGDA it was possible to fabricate, in a robust manner, hydrogel scaffolds with the characteristic intestinal architecture that allowed the incorporation of the intestinal stromal compartment. While GelMA provides cell-adhesive and biodegradable moieties that allow for cell embedding, PEGDA provides mechanical stability to the hydrogel network, enabling the maintenance of long-term cultures [10, 28]. In the present chapter this technique was used to obtain an *in vitro* model of the small intestine that incorporates both the 3D villus-like architecture and the stromal compartment, and the same methodology presented in the last chapter was used to characterize the models and study the effect of the topography on the intestinal cell differentiation, expression of drug transporters and permeability outcomes.

6.3. Materials and Methods

6.3.1. Cell culture conditions

Caco-2 C2BBe1 (regarded as Caco-2 cells) were purchased from American type culture collection (ATCC, USA) and mucus producing HT29-MTX cells were kindly provided by Dr. T. Lesuffleur (INSERM U178, Villejuif, France). Caco-2 (passage 53 to 57) and HT29-MTX cell lines (passage 37 to 50) were grown in Dulbecco's modified Eagle's medium (DMEM) with 4.5 g/L glucose and Ultraglutamine™ (Gibco), supplemented with 1% Penicillin/Streptomycin 100X (Biowest) and 10% Fetal Bovine Serum (FBS) (Biochrom), regarded as DMEM complete from now on.

Human intestinal fibroblasts (HIF) primary cells (passage 5-6) were obtained from ScienCell and were cultured in Fibroblast medium (FM) supplemented with 2% FBS, 1% of Fibroblast Growth Supplement (FGS) and 1% of penicillin/streptomycin solution (all from ScienCell).

All cells were grown separately in T75 and T175 tissue culture flasks (Nunc) and maintained in an incubator Series II Water Jacket CO_2 incubator (ThermoScientific) at 37ºC and 5% CO_2, in a water saturated atmosphere.

6.3.2. Fabrication of the cell-laden scaffolds

A low-cost digital light processing stereolithography (DLP-SLA) system based on a commercially available SOLUS 3D printer (Junction3D) was employed for the fabrication of the cell-laden scaffolds using visible-light photopolymerization an a bioink composed of 5 % w/v GelMA, 3 % w/v PEGDA, 0.4 % w/v LAP and 0.025 % w/v tartrazine dissolved in HBSS supplemented with 1% v/v Penicillin/Streptomycin, as described in [28]. This bottom-up approach allows for the fabrication of soft and highly transparent microstructured scaffolds in a layer-by-layer manner, by projecting series of black and white patterns onto the prepolymer solution containing the cell suspension, through a transparent window. A customized printing support and a cuvette that contains the prepolymer solution were designed in aluminum, allowing for printing with reduced sample volumes while keeping the bioink at 37ºC, preserving it in liquid form, and thus providing a proper environment for the fabrication of the cell-laden scaffolds. The optical power density applied for printing was set to 12.3 $mW·cm^2$ within the spectral range from 320 to 640 nm wavelength. To avoid cell damage due to infrared (IR) radiation exposure, a KG3 SCHOTT short pass heat protection filter (ITOS, Edmund Optics) was added. Computer-aided design (CAD) designs featuring villus-like structures of 750 µm in height and 300 µm in diameter spaced by 750 µm; or flat disc-like hydrogels of 300 µm in height were printed using the following parameters: 13 µm layer thickness, 5 s exposure time including 2 burn-in layers, which were exposed 15 s to guarantee proper scaffold attachment to the printing support. To ease the later handling of the 3D printed scaffolds, a 10 mm in diameter silanized polyethylene terephthalate (PET) membrane (SABEU) was attached to the bottom part of the printing support. Once printed, scaffolds were rinsed in warm phosphate buffer saline (PBS) containing 1% v/v of Penicillin/Streptomycin and assembled in Transwell® inserts by means of two pressure sensitive adhesive (PSA) rings as described in [10].

6.3.3. HIF viability inside the scaffolds

To determine the viability of the fibroblasts inside the scaffolds along the time in culture, a live/dead (L/D) assay was performed at different timepoints (7, 14 and 21 days). Flat scaffolds with two different HIF initial densities (2.5 and 5 x 10^6 cells/mL) were obtained, as described in section 6.3.2, and kept in DMEM supplemented with Normocin (1:500, Ibian Technologies) for 21 days. At each time point the assay was performed using the calcein-

AM/ethidium homodimer Live/Dead kit (Invitrogen). Samples were washed three times with PBS for 5 min each, after which the L/D solution was added and scaffolds were incubated at 37ºC in the dark for 20-30 min. Then, samples were washed again three times for 5 min and mounted for microscope visualization. A confocal laser scanning microscope (LSM 800, Zeiss) was used, and ImageJ software was employed for image processing.

6.3.4. HIF morphology and extracellular matrix secretion inside the scaffolds

After 21 days in culture, the scaffolds with the HIF embedded were washed (all washing steps were performed thrice with PBS for 5 min in shaking conditions) and fixed using 500 µL formalin solution, neutral buffered, 10% (Sigma) for 30 min under shaking conditions at room temperature (RT). After fixation, scaffolds were washed and permeabilized using a solution of 0.5% (v/v) Triton X-100 (Sigma) in PBS and incubated for 2 h at 4°C in shaking conditions. After permeabilization, samples were washed again and then a blocking step was performed using a blocking solution (BS) containing 1% bovine serum albumin (BSA) (Life technologies), 3% donkey serum (Merck) and 0.3% Triton-X-100 in PBS, for 2 h at 4°C in shaking conditions. Samples were washed and then incubated with the primary antibodies' solutions. Mouse anti-human vimentin (1:50) (sc-6260, Santa Cruz Biotechnology) + rabbit anti-human fibronectin (1:100) (F3648, Sigma) or mouse anti-human alpha smooth muscle actin (alpha-SMA) (1:200) (ab7817, Abcam) + goat anti-human collagen type IV (1:250) (134001, Biorad) were diluted in the primary working buffer (PWB) containing 0.1% BSA, 0.3% donkey serum and 0.2% Triton X-100 in PBS and incubated with the samples overnight (ON), at 4°C in shaking conditions. The next day, samples were washed once again and were incubated in the secondary working buffer (SWB) containing 0.1% BSA and 0.3% donkey serum in PBS and the secondary antibodies donkey anti-mouse IgG (H+L) highly cross-adsorbed secondary antibody, Alexa Fluor 488 (1:500) (Invitrogen A-21202), donkey anti-rabbit IgG (H+L) highly cross-adsorbed Secondary Antibody, Alexa Fluor 568 (1:500) (Invitrogen A-10042) and donkey anti-goat IgG (H+L) cross-adsorbed secondary antibody, Alexa Fluor 647 (1:500) (Invitrogen A-21447), accordingly to the primary antibodies' combinations. DAPI (1:1000) (Fisher Scientific) and Rhodamine Phalloidin (1:140) (Cytoskeleton) were incubated together with the secondary antibodies for 2 h at 4°C under shaking conditions, protected from light. After incubation, samples were washed one last time and were kept in PBS until visualization using a confocal laser scanning microscope LSM 800 (Zeiss). ImageJ software was employed for image processing.

6.3.5. Epithelial cell seeding

The day after printing the scaffolds, both flat and villus-like hydrogels with embedded HIF were mounted in the inserts and epithelial cells were seeded on top. Caco-2 and HT29-MTX cells (7.5 x 10^5 cells/cm^2 at a 9:1 ratio, respectively) in 0.2 mL of DMEM complete supplemented with Normocin were added on top of the scaffolds and models were incubated at 37°C, 5% CO_2 in a water saturated atmosphere. Scaffolds with fibroblasts embedded and epithelial cells on top will be from now on regarded as “flat” (disc-like shaped) and “villi” (with villus-like microstructures).

The cultures were maintained during 21 days and the medium of the models was changed every 2-3 days. Before changing the medium, transepithelial electrical resistance (TEER) was measured using EVOM^3 and EndOhm-6G equipments (World Precision Instruments). Pictures were taken along the time in culture to assess cell growth and layer formation on top of the scaffolds, using an Eclipse Ts2 microscope (Nikon). The process to obtain the bioprinted models is depicted in Figure 6.1.

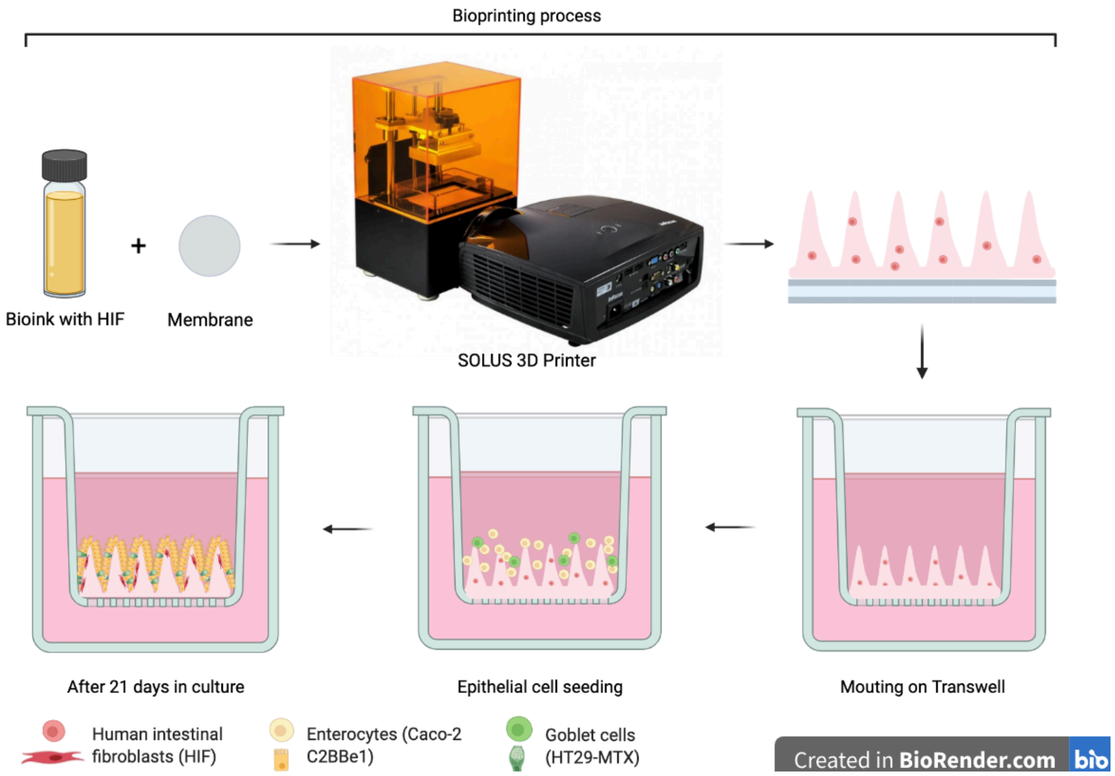

Figure 6.1 - General overview of the procedure followed to obtain the bioprinted models.

6.3.6. Quantification of intestinal differentiation markers

As in the previous chapter, different intestinal markers were quantified. The alkaline phosphatase (ALP) activity was quantified in the models using a colorimetric alkaline phosphatase assay kit (ab83369, Abcam), as described by the manufacturer. Briefly, medium from the apical side of the models was retrieved at different timepoints (7, 14 and 21 days). Immediately after collecting the medium, ALP activity was measured. For this, medium samples from the models in culture, sample background control (culture medium) and p-nitrophenyl phosphate (pNPP) standards were added to a 96-well plate (ThermoScientific). 20 µL of Stop Solution was added to the sample background control wells. Then, 50 µL of 5 mM pNPP was added to each well containing the samples and the sample background control. Finally, 10 µL of ALP enzyme were added to each standard. The plate was incubated, protected from light, for 60 min at RT. Reaction was then stopped by addition of 20 µL of Stop Solution to the samples and standard wells, as for the sample background control this solution had already been added. The plate was carefully shaken, and absorbance was read at 405 nm using an Infinite M200 PRO multimode microplate reader (Tecan).

The genetic expression of the intestinal markers Specific Intestine Homeobox (ISX), Sucrase Isomaltase (SI) and Villin1 (Vil1) were assessed using Real Time Polymerase Chain Reaction (qPCR). At day 21 in culture, RNA extraction of both flat and villi models was performed using a Quick-RNA MiniPrep kit (Zymo Research), accordingly to manufacturer's instructions. Briefly, models were lysed by removing the culture medium from the inserts, adding RNA lysis buffer directly on top of the scaffolds and pipetting up and down to completely dissolve it. The solution was centrifuged (all centrifugation steps mentioned were performed at 13000 g for 30 s, otherwise noted) and the supernatant was transferred to a Spin-Away filter in a collection tube and centrifuged again. The flow through was then used for RNA purification. For this, 96% ethanol was mixed to the samples in a 1:1 proportion and thoroughly mixed. The resulting solution was transferred to a ZymoSpin IIICG column in a collection tube and centrifuged. A treatment with DNAse I was performed to remove trace DNA. The column was firstly washed with RNA wash buffer, followed by centrifugation and incubation with DNAse I reaction mix for 30 min at RT. Samples were once again centrifuged and RNA Prep Buffer was added, followed by another centrifugation. To ensure complete washing of the samples, RNA wash buffer was added to the samples twice and in the last wash the centrifugation was performed for 1 minute to ensure complete removal of the buffer. The columns were carefully transferred into RNAse-free tubes and 50 µL of DNAse/RNAse-Free water was added directly to the column and centrifuged. The eluted RNA was stored at -80°C until further use.

The quality and concentration of the sample's RNA was evaluated in an automated electrophoresis station (Experion Automated Electrophoresis System, Bio-rad) using Experion RNA StdSens Kit (700-7105, Bio-rad) according to manufacturer's instructions, using 1 μL of RNA in a quantification range of 5-500 ng/μL of each purified total RNA sample.

Reverse transcriptase was performed to obtain cDNA from the RNA samples. For this, an iScript cDNA Synthesis Kit (1708891, Bio-rad) was used following manufacturer's instructions. Briefly, RNA template was mixed with 5x iScript Reaction Mix, iScript Reverse Transcriptase and Nuclease free water. Samples were placed in a thermal cycler (T100 Thermal Cycler, Bio-rad) and the protocol was initiated, which consisted in a priming step of 5 min at 25°C followed by a reverse transcription step at 46°C for 20 min and an inactivation step for 1 min at 95°C.

qPCR was performed using the obtained cDNA. A primePCR plate (Biorad) customized with the genes of interest and the housekeeping genes Glyceraldehyde 3-phosphate dehydrogenase (GADPH) and Actin Beta (ACTB) was used (Bio-rad). First, 1 μL of RT control template was added to each 20 μL of cDNA synthesis reaction. The master mixes were prepared adding iTaq Universal SYBR Green Supermix (Bio-rad), cDNA template and Nuclease Free Water according to manufacturer's instructions. The protocol was run using a real time PCR instrument (CFX96 Touch Real-Time PCR Detection System, Bio-rad), according to the prime PCR plate protocol, which consisted in activation step at 95°C for 2 min, followed by 40 cycles of a denaturation step for 5 s also at 95°C and an annealing/extension step at 60°C for 30 s The melt curve was performed between 65°C and 95°C in 0.5°C increments for 5 s/step.

6.3.7. Quantification of intestinal drug transporters

The genetic expression of different drug transporters [ABCB1 - P-glycoprotein (P-gp); ABCC1 - Multidrug Resistance Protein 1 (MRP1); ABCC2 - Multidrug Resistance Protein 2 (MRP2); ABCG2 – Breast Cancer Resistance Protein (BCRP); SLC15A1 – Peptide Transporter 1 (PEPT1); SLC16A1 – Monocarboxylate Transporter 1 (MCT1); SLC22A1 – Organic Cationic Transporter 1 (OCT1)] was again assessed using two step Reverse Transcriptase Real Time Polymerase Chain Reaction (RT-qPCR), exactly as described in the previous section.

6.3.8. Immunostaining

To confirm the integrity of the epithelial layer in both configurations and to compare the expression of different proteins, immunocytochemistry was performed. The presence and expression of junctions was assessed with Claudin-1, a tight junction, E-cadherin, an adherens junction and with ß-catenin, which is involved in cellular adhesion. The presence of fibronectin and vimentin in the scaffolds was also assessed.

To preserve the morphology of the hydrogels, samples were first embedded in a PEGDA solution based on a protocol developed by Altay et al. [25]. Briefly, after a fixation step with 10% formalin solution for 30 min under shaking conditions at RT, samples were submerged in a pre-polymer solution containing 10% w/v PEGDA 575 kDa (Sigma) and 1% w/v Irgacure D-2959 photoinitiator (Sigma) in PBS and kept overnight at 4ºC. Samples were then placed in polydimethylsiloxane (PDMS) round pools of 12 mm diameter and 2 mm thickness attached to a plastic support, and PEGDA 575 kDa pre-polymer solution was used to fill the pools. Constructs were irradiated using ultraviolet (UV) light at 365 nm in a MJBA mask aligner (SÜSS MicroTech). First, a 40 s at 25 $mW\cdot cm^{-2}$ of power density exposure was performed to form a support base to keep the constructs in place. Samples were irradiated twice for 100 s, first from the top and then from the bottom, to ensure the formation of a homogeneous block surrounding them. After UV exposure, unreacted polymer and photoinitiator solutions were washed out using PBS. Then, samples were incubated overnight with 30% sucrose (Sigma) and then embedded in optimal cutting temperature (OCT) compound (Sakura® Finetek). Samples were cut in order to obtain histological cross-sections of around 7 µm thickness, attached onto glass slides, air dried and stored at -20ºC until use.

Slides were carefully washed, using a Pasteur pipette, with PBS at room temperature in order to dissolve the OCT. A solution containing 0.5% (v/v) Triton-X100 in PBS was used for cellular permeabilization. Slides were incubated with this solution in a humidified chamber for 1 h at 4°C under gentle shaking. After the permeabilization, samples were washed again with PBS and a blocking step was performed to avoid unspecific binding of the antibodies. The BS was added to the samples in the humified chamber and kept for 2 h at 4°C under gentle shaking. Samples were washed and incubated with the primary antibodies' [Mouse anti-human vimentin (1:50) (sc-6260, Santa Cruz Biotechnology) + rabbit anti-human claudin-1 (1:200) (SAB5500083, Merck) or rabbit anti-human fibronectin (1:100) (Sigma F3648) + mouse anti-human e-cadherin conjugated with Alexa Fluor 488 (1:100) (324110, BioLegend) or rabbit anti-human ß-catenin (1:100) (ab2365, Abcam)] diluted in PWB in the humidified chamber at 4°C under gentle shaking ON.

The next day samples were, once again, washed with PBS and incubation with the secondary antibodies diluted in SWB was performed. Secondary antibodies used were donkey anti-rabbit IgG (H+L) highly cross-adsorbed secondary antibody, Alexa Fluor 647 (A-31573, Invitrogen), donkey anti-rabbit IgG (H+L) highly cross-adsorbed secondary antibody, Alexa Fluor 488 (A-21206, Invitrogen) and donkey anti-mouse IgG (H+L) highly cross-adsorbed secondary antibody, Alexa Fluor 647 (1:500) (A-31571, Invitrogen), accordingly to the primary antibodies' combinations. DAPI (1:100) and Rhodamine Phalloidin (1:140) were incubated together with the secondary antibodies for 2 h at 4°C under shaking conditions, protected from light. Finally, samples were washed with PBS and mounted using Fluoromount-G (SouthernBiotech) and kept at 4°C, protected from light until visualization using a confocal laser scanning microscope LSM 800 (Zeiss). Laser power and gain for each laser were the same between samples for each antibody combination in order to be able to compare protein expression. ImageJ software was employed for image processing.

3.6.9. Activity of P-gp

The activity of P-gp was assessed, once again, with a transport assay using Rhodamine 123 (Rho 123) (Enzo Life Sciences), which is a P-gp substrate. The transport was determined in both apical to basolateral and basolateral to apical directions.

After 21 days of culture, medium was first removed from both sides of the Transwell® inserts and models were washed two times with pre-warmed Hanks balanced salt solution (HBSS) (Gibco). After washing, 0.2 mL and 0.6 mL of HBSS were placed on the apical and basolateral sides of the inserts, respectively. Samples were incubated at 37°C, 5% CO_2 and 100 rpm for 30 min in a CO_2 Resistant Shaker (Thermo Scientific). After the 30 min, samples were placed on the apical or basolateral side (0.2 or 0.6 mL of 5 μg/mL of Rho 123, respectively). Samples were incubated for 4 h at 37°C and 100 rpm and by the end, a sample of 100 μL was retrieved from the apical and basolateral compartment of each model. The amount of Rho 123 in the samples was measured using an Infinite M200 PRO multimode microplate reader (Tecan) at excitation/emission wavelengths of 507/529.

The permeability results were expressed in terms of apparent permeability (P_{app}), that was calculated using Equation 1.

$$P_{app} = \frac{\Delta Q}{A \times C_0 \times \Delta t} \text{ (Equation 1)}$$

Where ΔQ is the amount of compound detected in the basolateral side (mg), A is the surface area of the insert (cm^2), C_0 is the initial concentration in the donor compartment (mg/mL) and Δt is the time of the experiment (s).

6.3.10. Permeability assays

Permeability assays were performed with the same three model drugs used in the previous chapter: colchicine, atenolol and metoprolol (all from Merck), which are drugs with low, moderate and high intrinsic permeability, respectively.

Culture medium was removed and models were washed twice with pre-warmed HBSS. Then, 0.2 and 0.6 mL of HBSS were placed on the apical and basolateral compartments, respectively, and the plate was incubated for 30 min at 37°C, 5% CO_2 and 100 rpm in the shaker. HBSS on the apical side was then replaced for 0.2 mL of the model drug solutions (100 µM of colchicine or metoprolol or 200 µM of atenolol in HBSS). At pre-determined time-points (60, 120, 180 and 240 min), a sample of 50 µL was taken from the basolateral compartment and replaced by the same volume of HBSS. Drugs were quantified by High Performance Liquid Chromatography (HPLC) using an Ultra-Fast Liquid Chromatograph (UFLC) Prominence System equipped with two Pumps LC-20AD, a column oven CTO-20AC, and autosampler SIL-20AC, a System Controller CBM-20A, a degasser DGU-20A5, a RF-10Axl fluorescence detector coupled to the LC System and a LC Solution, Version 1.24 SP1 (Shimadzu). Detailed methods are described in table A.1 of Appendix.

The permeability results were expressed in percentage of permeated amount and P_{app}, that was calculated using Equation 1.

6.3.11. Statistical Analysis

Statistical analysis was performed using the software GraphPad Prism 8.0 (GraphPad Software Inc.). All results are represented as mean ± standard error of the mean (SEM) or mean ± standard deviation (SD) or mean ± upper and lower limits. Statistical differences were calculated using 2-way analysis of variance (ANOVA) multiple comparisons test and Unpaired T-test. The level of significance was set at probabilities of *p<0.05, **p<0.01, ***p<0.001, ****p<0.0001.

6.4. Results and Discussion

6.4.1. The stromal compartment: How do fibroblasts behave inside the scaffolds?

The intestinal fibroblasts were embedded inside the scaffolds and their viability, morphology and ability to secrete ECM components were evaluated. First, flat disc-like scaffolds were bioprinted using two different initial HIF seeding densities, and cell viability was measured along culture. It was observed that there were no significant differences in cell viability for scaffolds with 2.5 and 5 x 10^6 cells/mL, which showed viability close to 100% at all time points (Figure 6.2a).

Within the first days in culture, some fibroblasts started to acquire an elongated shape (Figure 6.2b). Along the time, the number of cells showing a stretched morphology increased, being typically located closer to the top of the scaffold, while more roundish cells were found closer to the bottom (data not shown).

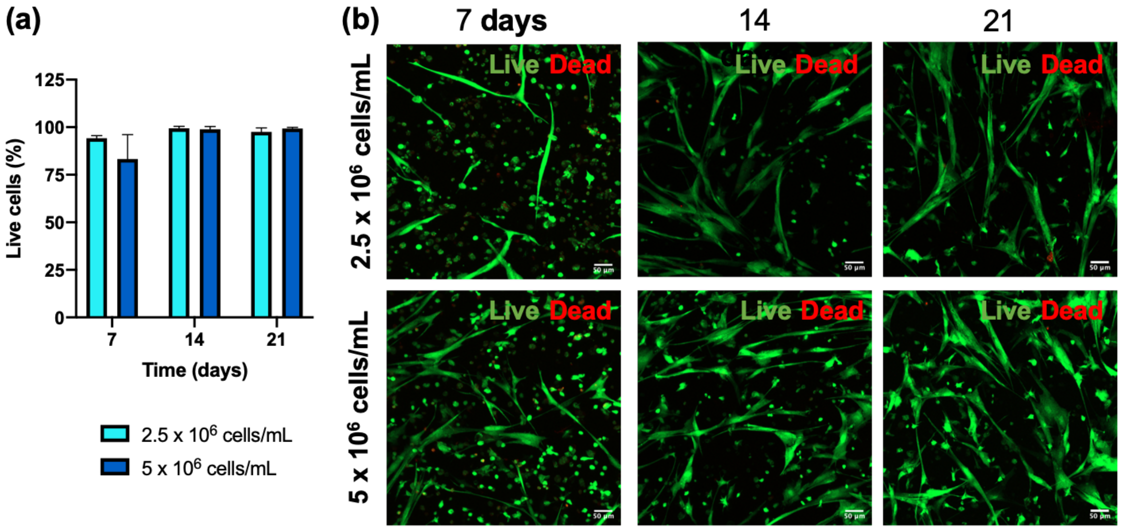

Figure 6.2 – Live and Dead assay performed on the HIF embedded in the scaffolds with two different initial seeding densities. (a) Percentage of live cells and (b) maximum intensity projection of the hydrogels showing the live and dead fibroblasts.

We also evaluated the cellular morphology and deposition of ECM components by immunocytochemistry. After 21 days in culture, the embedded HIFs showed the prototypical elongated shape and expressed both vimentin and alpha-SMA, which may indicate that they acquired a contractile phenotype (Figure 6.3) [29]. The embedded HIFs were able to secrete their own ECM components when entrapped inside the scaffold, remodeling the surrounding matrix by laying down endogenous fibronectin and collagen type IV (Figure 6.3). This ECM secretion is crucial, not only for the survival and migration of the embedded cells, but also to support the epithelial layer, since it is known that the interactions with the ECM play a key role in epithelial polarization, organization and cohesiveness [9, 30].

Since no differences in cellular viability, cell morphology or ECM secretion were observed between conditions, the initial seeding density of 2.5 x 10^6 cells/mL was chosen for practical reasons.

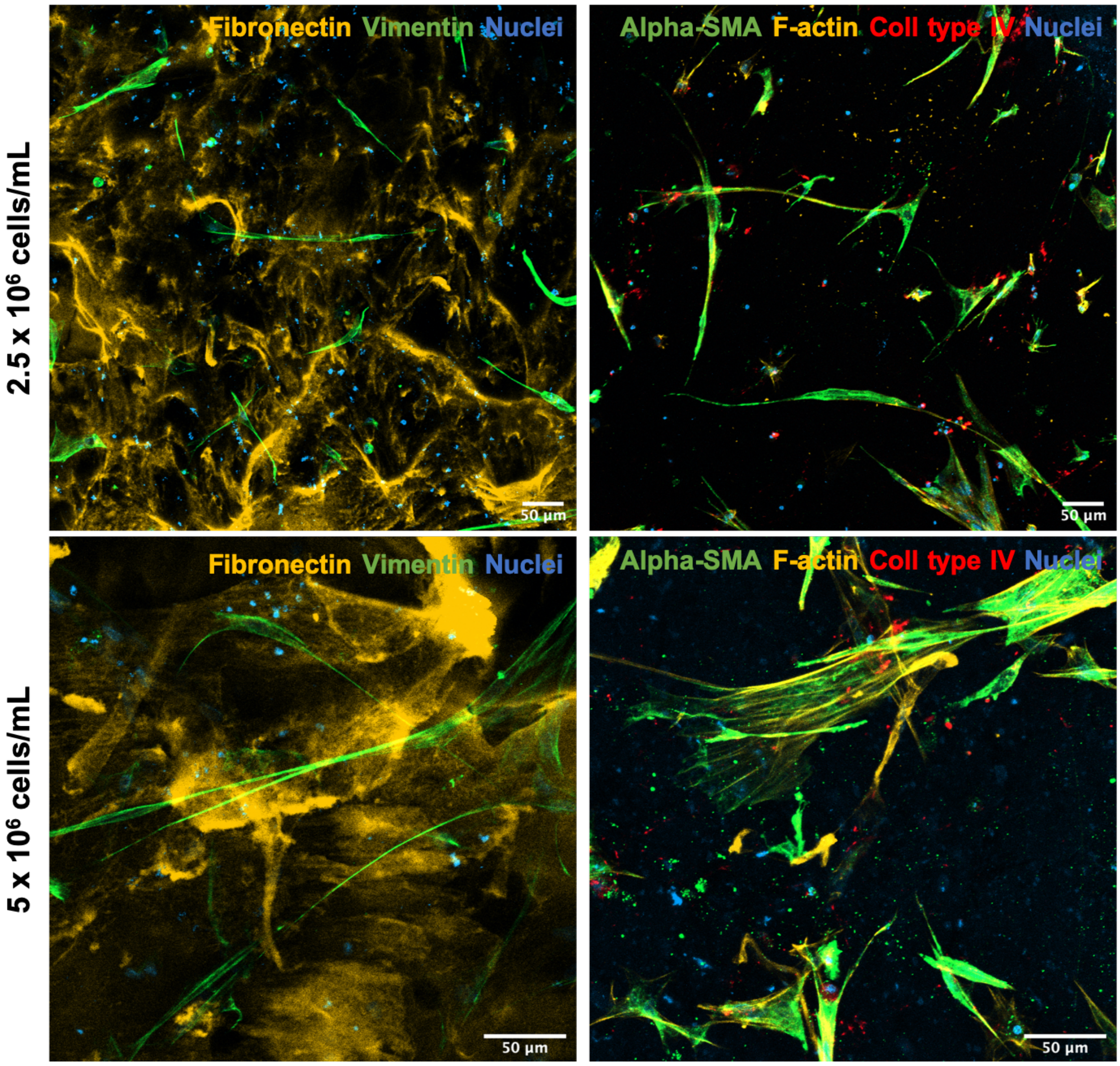

Figure 6.3 – Fibronectin, vimentin, alpha-SMA and collagen type IV deposition by HIF in hydrogels with two different initial seeding densities after 21 days in culture. Pictures depict a maximum intensity projection. Vimentin and alpha-SMA were labelled with Alexa-Fluor 488, collagen type IV was labelled with Alexa-Fluor 594 and fibronectin was labelled with Alexa-Fluor 568. The nucleus was counterstained with DAPI and f-actin was stained with Phalloidin Rhodamine.

6.4.2. The epithelial layer

Once the stromal compartment was optimized and characterized, the cell differentiation and barrier integrity of the epithelial monolayer was studied both in flat and microstructured scaffolds with embedded HIF (Figure 6.4). Along culture, the epithelial cells were able to attach, proliferate and colonize the surface of the scaffolds (Figure 6.4a). The epithelial layer formation was further confirmed by immunostaining of F-actin (Figure 6.4b). The epithelial cells showed a fully polarized morphology with accumulation of F-actin in the apical side. The villus-like microstructures were fully covered. We could observe some regions where cell multilayers were formed and this behavior has already been observed in the previous chapters and in other studies where intestinal models are developed using the same cell types [31-35].

In terms of barrier integrity, TEER values (Figure 6.4d) were close to 100 Ω.cm^2 for the flat configuration. These values were notably lower than what is normally observed in the 2D standard models [35], and close to the values depicted in chapters 4 and 5 of this thesis, suggesting that the stromal compartment contributed to a more physiological representation of the epithelial barrier. These TEER values were even lower in the case of the villus-like model, around 30 Ω.cm^2. Those TEER values were very close to the *in vivo* values, reported to be around 30 Ω.cm^2 for the rat ileum-jejunum and human jejunum [36, 37]. A decrease in the TEER in the 3D cultures has been previously observed in different works and in the previous chapters and is considered an advantage of these models [10, 24, 35].

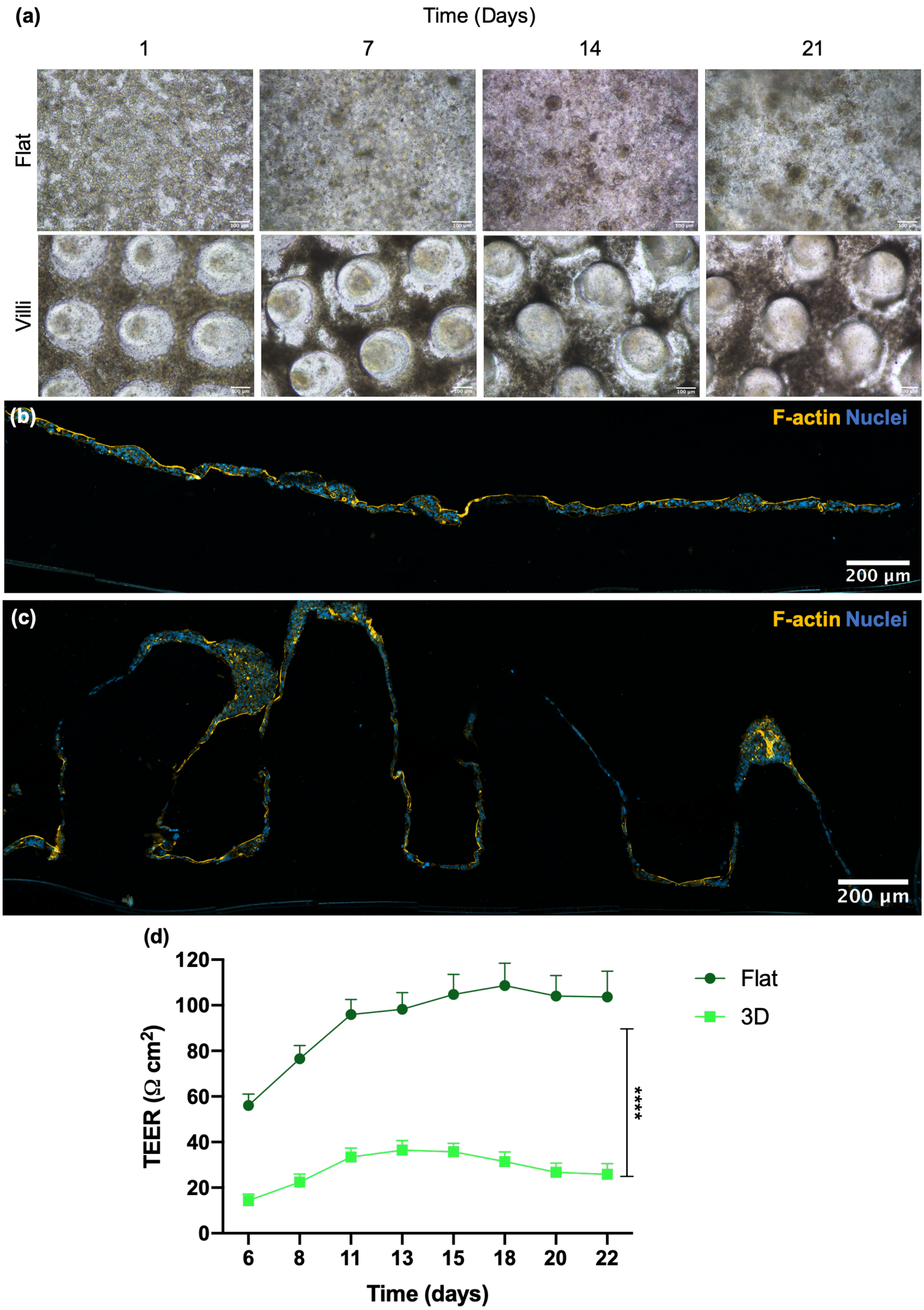

Figure 6.4 – Visualization of epithelial layer formation of top of the scaffolds. (a) Top view of the epithelial cells on top of flat and villus scaffolds at different timepoints (1, 7, 14 and 21 days) and monolayer visualization by staining of nuclei and f-actin in transversal cuts of (b) flat and (c) villus scaffolds after 21 days in culture. (d) TEER values along the 21 days

in culture, where results are the average 18 samples and bars represent the standard error of the mean (SEM). Statistical difference $p<0.0001$ are denoted by ****.

6.4.3. Quantification of intestinal markers

As already stated, intestinal ALP is considered an enterocyte differentiation marker because it is exclusively expressed by differentiated enterocytes [38, 39]. The ALP activity was measured in the flat and microstructured models, in order to evaluate the effect of the scaffold architecture in enterocyte differentiation (Figure 6.5a). In general, the ALP activity was higher in the villi scaffold, but only statistically significantly at 7 days, which may indicate that the villi architecture does not have an impact in ALP activity.

The genetic expression of ISX, SI and Vill1 was determined after 21 days in culture (Figure 6.5b). No significant differences were observed in the expression of these markers between the flat and villi configurations. Nevertheless, a tendency of lower expression of ISX in the villi model was observed, which can be related with the higher number of HT29-MTX cells present in this model. In the previous chapter it was observed that when Caco-2 were co-cultured with HT29-MTX, the expression of some intestinal markers was decreased. In combination to what was observed for ALP, results suggest that the 3D architecture does not have a noticeable impact in the expression of these markers.

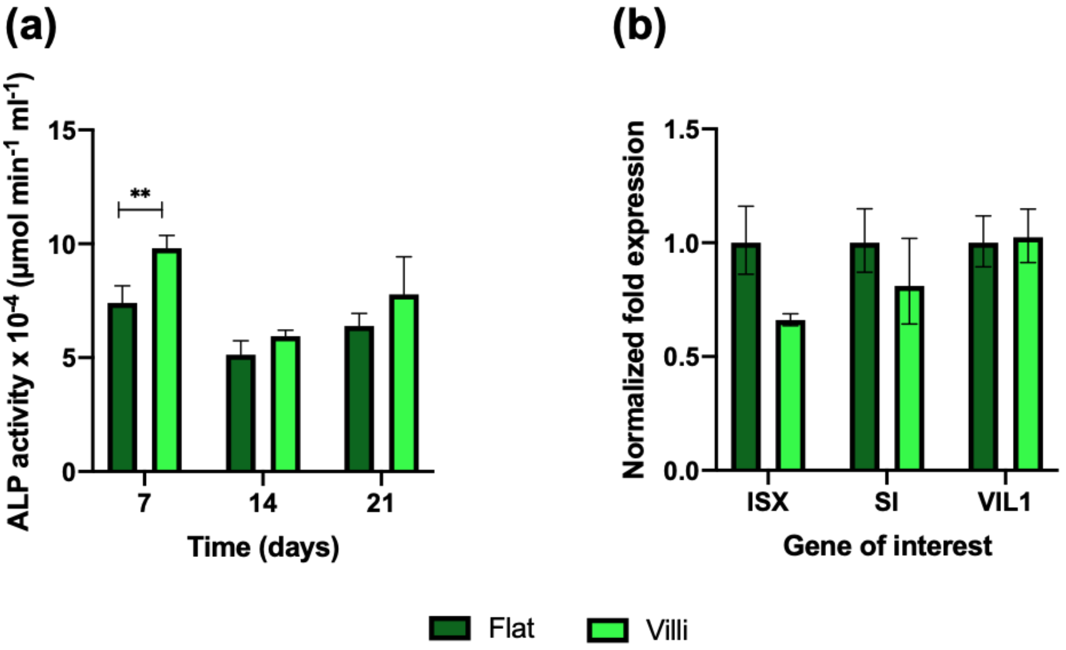

Figure 6.5 – Activity and expression of intestinal markers. (a) ALP activity levels in flat and villus configurations of the models at different timepoints (7, 14 and 21 days) during the time in culture and (b) genetic expression of ISX, SI and VIL1 after 21 days in culture. For (a) results are the average of triplicates, bars represent the standard error of the mean (SEM)

and statistical differences were calculated using 2-way ANOVA multiple comparisons to compare the levels of ALP in the different configurations for each timepoint ($p<0.01$ is denoted by **). For (b) results are the average of triplicates, bars represent upper and lower limits and statistical differences were calculated using the log transformed data with 2-way ANOVA multiple comparisons to compare expression of each gene between configurations.

6.4.4. Genetic expression of drug transporters

As already stated, drug transporters play a major role in the absorption of many compounds and, therefore, can have a great influence in drug absorption outcomes. The expression and activity of intestinal transporters can impact the pharmacokinetics and pharmacodynamics of drugs, influencing drugs disposition and interactions [40, 41].

As in the previous chapter, the genetic expression of different intestinal transporters involved in the influx and efflux of compounds was evaluated in the bioprinted models, as compared to the conventional 2D co-culture model composed by Caco-2 and HT29-MTX and the 3D Co-culture model from the previous chapters (Figure 6.6). When looking at the expression of the influx transporters PEPT1 (SLC15A1), MCT1 (SLC16A1) and OCT (SLC22A1), the 3D models showed a significant decrease compared with the 2D model. When comparing to the 3D collagen model, the expression of PEPT1 was significantly lower for both bioprinted models. On the other hand, the expression of MCT1 was higher in the flat bioprinted model, whereas the OCT expression was significantly lower in the villi model. Comparing the two bioprinted models, the only significant difference was observed for PEPT1 (SLC15A1), being lower in the villi model. Nevertheless, it is worth to mention that the villus-like model presents an overall tendency of decreased expression for all evaluated transporters. PEPT1 is expressed in the apical side of enterocytes and has a role in the absorption process of many compounds, as previously stated [42, 43]. Lower expression of PEPT1 in Caco-2 cells compared to the human small intestine has been previously reported [42, 43]. When looking at the spatial expression of this transporter in the human intestine, data indicate a high expression in the duodenum and negligible expression in the jejunum and ileum, although no qualitative comparison to the standard Caco-2 cell model was made [44]. The lower expression of this transporter in the villi configuration may indicate that the microstructured model can mimic the intestinal mucosal barrier of the jejunum and ileum, whereas the flat model would be more suitable to test the permeability of drugs that are substrates of PEPT1 in the duodenum. Notwithstanding, a higher expression was found both in the 2D and the 3D collagen model, suggesting that these models could be more suitable for mimicking PEPT1 expression in the duodenum.

MCT1 (SLC16A1) is another influx transporter that was found to be overexpressed in 2D conventional Caco-2 models [45]. The lower expression detected in the bioprinted models, especially in the villi configuration, suggest that they better represent the intestinal barrier than the conventional 2D models. On the other hand, OCT1 (SLC22A1) is localized on the basolateral side of enterocytes [40, 46]. Compared to the 2D and 3D collagen models, this transporter was significantly less expressed in the bioprinted models. Since literature data points to a higher expression of this transporter in Caco-2 models compared to *in vivo*, the lower expression of this transporter should be seen as advantageous, as it seems to be more physiologically relevant [45].

For the efflux transporters different expression profiles were observed for the different transporters. When comparing to the 2D model, P-gp (ABCB1), MRP2 (ABCC2) and BCRP (ABCG2) expressions were significantly lower in the 3D bioprinted models, whereas the expression of MRP1 (ABCC1) was slightly higher. When comparing to the 3D collagen co-culture model, expression was lower for P-gp and higher of BCRP. Since it is described that P-gp and MRP2 are tipically overexpressed in 2D standard models, as previously stated, a lower expression of these transporters in the 3D bioprinted models is important [42, 45, 47-49]. Both P-gp and MRP2 are localized in the apical surface of intestinal enterocytes and act as an important barrier to drug absorption, being able to pump compounds back into the lumen [40, 50]. A myriad of compounds are substrates of these transporters and their overexpression in the *in vitro* models can lead to false negative results. Besides, there are substrates with specificity for both transporters and, acting together, they contribute as a significant barrier to absorption [40].

BCRP is another efflux pump that is localized on the apical side of enterocytes [40]. BCRP, contrary to P-gp and MPR2, is normally underexpressed on the Caco-2 model [42, 43, 45, 51]. Although expression is lower than in the 2D model, it is higher compared to the collagen configuration, suggesting that these models are more relevant in terms of BCRP expression than the previously developed 3D model.

Overall, the expression of transporters in the 3D bioprinted models indicates that these models better mimic the carrier-mediated transporters of the small intestine, as compared to the standard 2D co-culture model. Although being mostly similar to the 3D collagen model, expression of P-gp, BCRP and OCT1 seems to be even more physiologically relevant in the bioprinted models.

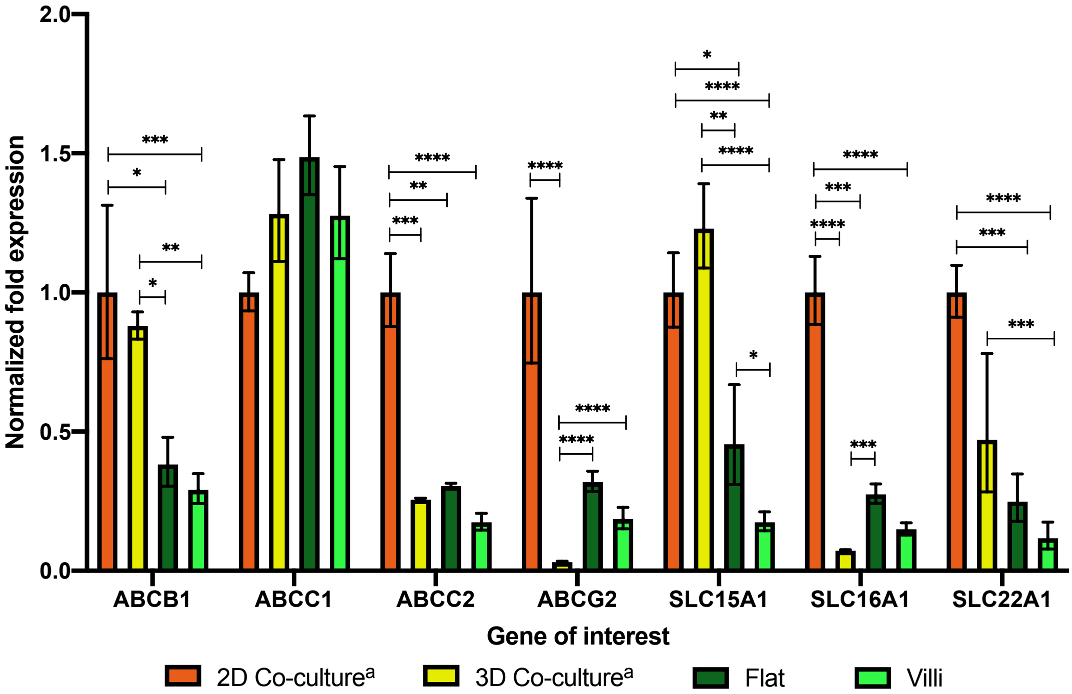

Figure 6.6 - Normalized genetic expression of different intestinal transporters between the 2D and 3D Co-cultures and the bioprinted models (flat and villi) after 21 days in culture. Results are the average of triplicates, and bars represent the upper and lower limits. Statistical differences were calculated using the log transformed data with 2-way ANOVA multiple comparisons ($p<0.05$ is denoted by *, $p<0.01$ is denoted by **, $p<0.001$ is denoted by *** and $p<0.0001$ are denoted by ****). (a) Data taken from the previous chapter.

6.4.5. Expression of junctions' proteins and ECM components

The expression of tight junctions was evaluated by immunostaining with Claudin-1, while E-cadherin was used to evaluate adherens junctions. The expression of ß-catenin, a multifunctional protein that has a role in cell-cell adhesion, being an essential component of intercellular junctions, was also evaluated [52], along with the presence of fibronectin and vimentin in the scaffolds.

E-cadherin and ß-catenin were clearly expressed in both models, demonstrating that epithelial functional polarization was achieved after 21 days of culture (Figure 6.7a, b, c and d**)**. In the case of ß -catenin, expression seems to be better defined when cells are in the villus-like topography, which can indicate a higher degree of cellular differentiation and polarization, as it had been previously observed [25]. Claudin-1 was also expressed in the epithelial monolayer (Figure 6.7e and f**)**. Images do not show a higher expression of Claudin-1 in the flat model, as it could be expected considering the higher TEER values achieved in this model (Figure 6.4d). Nevertheless, the last chapter demonstrated that expression of Claudin-1 was similar in 3D and 2D models, although TEER values were higher for the 2D [35].

It was possible to confirm that fibroblasts were able to remodel the scaffolds by secreting fibronectin (Figure 6.7a and b) and that this protein was mostly located in the upper part of the scaffold, which relates to what was observed in the L/D assay, where the majority of fibroblasts with elongated shape were located near the surface. When looking at the expression of vimentin (Figure 6.7e and f), a similar localization was observed, again indicating that elongated cells accommodate just below the epithelial layer. This behavior of stromal cells had already been observed in [28] and relates to *in vivo* behavior, where stromal cells in the lamina propria are mostly located near the epithelial layer [8].

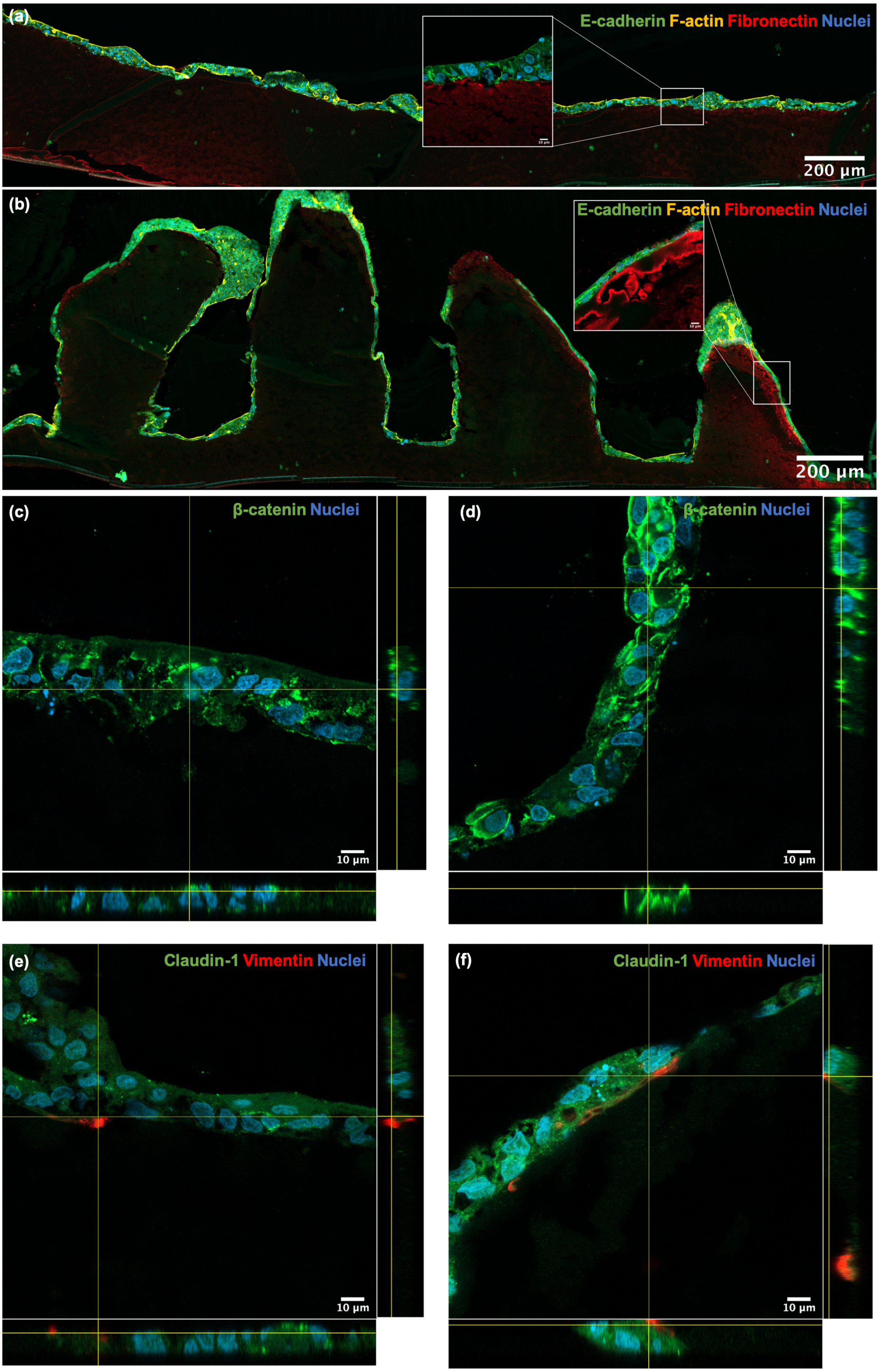

Figure 6.7 - Comparison of protein expression of (a, b) **E-cadherin** and **fibronectin**, (c, d) **ß-catenin** and (e, f) **claudin-1** and **vimentin** in (a, c, e) flat and (b, d, f) villi configuration

after 21 days in culture. E-cadherin, Claudin-1 and ß-catenin were labelled with Alexa-Fluor 488 and fibronectin and vimentin were labelled with Alexa-Fluor 594. The nuclei were counterstained with DAPI and (a, b) pictures depicts a maximal projection of the several stacks of the cut, where f-actin was counterstained with rhodamine phalloidin.

6.4.6. P-gp activity

Besides its genetic expression, the activity of the P-gp was evaluated using Rho 123, as in the previous chapter [53]. As an efflux pump, P-gp is able to decrease the permeability of compounds, preventing them from entering the cell by actively pumping them back to the lumen. This transporter is also capable of actively pumping out of the cell compounds that are on the basolateral side [40, 54].

As previously mentioned, the efflux ratio of basolateral to apical (BL-AP) and apical to basolateral (AP-BL) transport is used to understand the influence of transporters in the permeability of compounds [55]. A similar transport in both directions (ratio close to 1) is expected when the permeability of a drug is dominated by the passive diffusion. When an efflux transporter is involved pumping out the compound back to the lumen, the AP-BL transport is reduced and then the ratio is >>1. For the bioprinted models, the permeability of Rho 123 was almost 6-fold higher in the villi scaffold in the AP-BL direction (Figure 6.8a). This difference can be due to the higher surface area of the microstructured model, compared to the flat configuration, but also to a decrease in the P-gp activity. When analyzing the results from BL-AP direction (Figure 6.8b), the Papp value obtained for the microstructured model was very similar in both directions meaning that the efflux ratio was close to 1 (Figure 6.8c). In the flat model the transport of Rho 123 was significantly faster in the BL-AP direction and, thus, the efflux ratio was four times higher (Figure 6.8c). These results suggest a significant reduction in the activity of the P-gp transporter in the 3D villi model, in agreement with the difference in genetic expression, that although not significant, showed a tendency to be lower in the villi configuration (Figure 6.6). The effect of the 3D villi architecture on the expression of P-gp was previously shown by Yi et al. [23]. In that work, Caco-2 cells grown onto a collagen 3D villi scaffold expressed significantly less P-gp protein than the conventional Caco-2 model. However, they assumed that the reduced expression resulted from the collagen matrix signaling. Our results showed that, in fact, the topography of the epithelial barrier had an important contribution in the levels of expression of the efflux transporter. This correlates with the expression gradient of P-gp in the human intestine, being low in the proximal region where the surface is covered with intestinal villi, and increasingly expressed in the distal region [56].

As we have seen, this efflux transporter has been shown to be overexpressed in the standard Caco-2 *in vitro* model [42, 48, 49]. In the previous chapter, we demonstrated that when cells were in a more physiological environment, in presence of the stromal compartment, the genetic expression of P-gp as well as its activity was lower than in the conventional 2D models. Results from the current study suggest that having cells in a more relevant architecture, closely resembling the *in vivo* intestinal villi, may lead to an even lower expression of P-gp, thus increasing the predictive power of these 3D microstructured models.

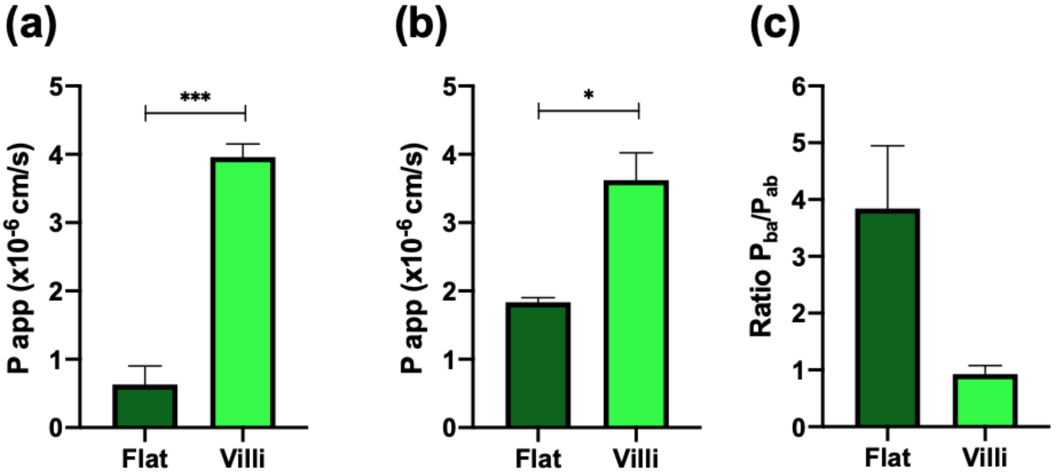

Figure 6.8 - P_{app} ($x10^{-6}$ cm/s) values of Rho 123 in the flat and villi models after 21 days in the (a) apical to basolateral and (b) basolateral to apical directions and (c) ratio of the bidirectional transport. Results are the average of triplicates, and bars represent the standard error of the mean (SEM). Statistical differences were calculated using 2-way ANOVA multiple comparisons to compare P_{app} between each configuration ($p<0.05$ are denoted by * and $p<0.001$ are denoted by ***).

6.4.7. Permeability

The permeability of three model drugs with different degrees of intestinal permeability was assessed. As previously mentioned, metoprolol is a highly permeable compound [fraction absorbed (F_a) > 85%], crossing the intestinal epithelium by the passive transcellular route [57, 58]. Atenolol, on the other hand, is transported by the paracellular pathway and has a moderate permeability (50% < F_a < 84%) [59]. Lastly, colchicine has low permeability (F_a < 50%) and is absorbed by the transcellular route, mainly on the jejunum and ileum and P-gp and MPR2 are believed to be involved in the transport of this drug [40, 60-64].

Metoprolol showed a similar apparent permeability in both bioprinted models (Figure 6.9a), indicating that the passive transcellular pathway was not affected by the 3D architecture of the model. In the case of atenolol, the amount of drug present in the basolateral side was below the limit of detection during the first time points of the assay (Figure 6.9b). We could only detect the drug after 4 h of incubation, and at that time point, there was more permeated drug in the 3D villus-like model than in the flat model. This can be due to the significantly lower TEER values of the microstructured model. Since the main transport mechanism of atenolol is through the paracellular route, the drug would permeate more in a model with a looser barrier tightness.

Colchicine showed the biggest difference in permeability between the two configurations (Figure 6.9c). The permeability of this drug was demonstrated to be highly affected by the efflux transporters P-gp and MRP2 [64]. We found that genetic expression of these transporters tended to be lower in the 3D villus-like model, and a lower activity of P-gp in this model was confirmed by the transport of Rho 123. This lower activity of the efflux pumps would allow for colchicine to permeate more than in the case of the flat model. Thus, these permeability results are consistent with the previous results.

A higher permeability for the villus-like model was expected, as reports in the literature point to higher permeability values in models that mimic the 3D villus topography [20, 23]. However, when comparing the Papp results with the results described in the last chapter, lower Papp values were generally obtained in the bioprinted models. The direct comparison, however, is not straightforward. Besides the changes in surface area in the case of the 3D microstructured model, other factors such as the different materials are likely to play a role in the diffusion of the drugs from the apical to the basolateral compartments. The different types of hydrogel used in both works (collagen vs PEGDA-GelMA) have different pore sizes (in the scale of nanometers for the PEGDA-GelMA hydrogel and in the scale of micrometers for the collagen) thus affecting the time for the molecules to diffuse through the hydrogel [35].

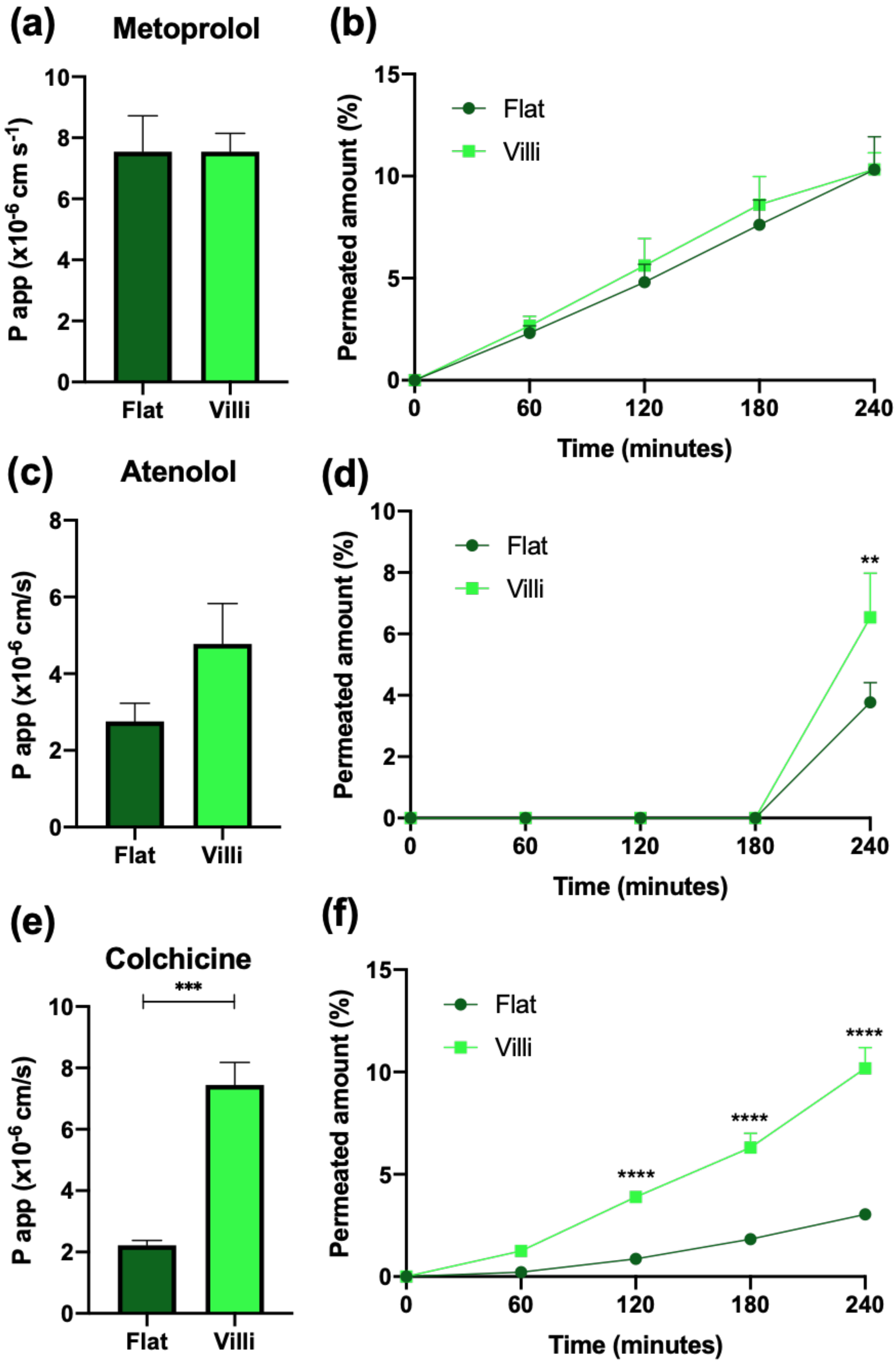

Figure 6.9 - P_{app} (x10^{-6} cm/s) values and percentage of permeated amount of (a, b) metoprolol, (c, d) atenolol and (e, f) colchicine in the flat and villus bioprinted models after 21 days. Results are the average of quadruplicates, and bars represent the standard error of the mean (SEM). Statistical differences were calculated using 2-way ANOVA multiple

comparisons to compare P_{app} between each configuration and to compare percentage of permeated amount between each timepoint ($p<0.01$ is denoted by **, $p<0.001$ is denoted by *** and $p<0.0001$ are denoted by ****).

6.5. Conclusion

A novel hydrogel-based 3D intestinal model with microstructures resembling the villi found in the human small intestine was developed. This model was built using an innovative microfabrication method based on SLA 3D bioprinting, and it comprised a stromal compartment with human intestinal fibroblasts and an epithelial compartment, surrogating intestinal enterocytes and goblet cells. The effect of the 3D villus-like architecture was evaluated in terms of intestinal markers, drug transporters expression and activity, and permeability of model drugs, and compared with a flat model containing also the stromal and epithelial compartments, but without the villi microstructures.

Although the expression of intestinal markers showed no differences between the bioprinted models, the intestinal transporters showed interesting results. The presence of a stromal compartment significantly decreased the expression of the studied influx and efflux transporters, except for the MRP1. These findings agreed with our previous results, where we found significant differences in several transporter expressions when epithelial cells were co-cultured with stromal fibroblasts in a collagen scaffold. The 3D architecture reduced the expression of these transporters even further. In fact, we showed a significant effect of the topography when measuring the activity of the P-gp efflux transporter. Using the transport assay with Rho 123, epithelial cells grown onto villus-like scaffolds showed a much lower activity of this transporter. The permeability of colchicine corroborated these results, showing an enhanced absorption in the villi configuration compared with the flat model, again indicating a lower activity of P-gp and probably of MRP2, both involved in the transport of this drug.

The villi model also showed a tendency for higher permeability with atenolol, whereas for metoprolol permeability was similar in both configurations. The higher permeability observed for the 3D collagen model described in the previous chapter, may be attributed to hydrogel properties such as pore size, which can influence the permeability of compounds. The fact that permeability results obtained with the bioprinted models developed herein are lower, may indicate that these bioprinted models are not the best option when the goal is to obtain approximate values for permeability *in vivo*. Nevertheless, they seem to be accurate when predicting the absorption profile. In addition, the presence of villi seems to lead to a higher degree of differentiation of the cells. This can be very important for other applications besides permeability, since cells may adopt a more physiological behavior when seeded on structures that mimic the intestinal architecture. In summary, in this work we described a novel 3D intestinal model with a villus topography, resembling the intestinal architecture. Differences in the expression of different proteins, as well as in permeability outcomes were observed in the microstructured model, confirming that 3D architecture has an impact in the behavior of cells and this should be considered when studying different processes within the small intestine.

References

1. Marsh, M.N. and J.A. Swift, *A study of the small intestinal mucosa using the scanning electron microscope.* Gut, 1969. **10**(11): p. 940-949.
2. Kelly, P., et al., *Responses of small intestinal architecture and function over time to environmental factors in a tropical population.* American Journal of Tropical Medicine and Hygiene, 2004. **70**(4): p. 412-419.
3. Castano, A.G., et al., *Dynamic photopolymerization produces complex microstructures on hydrogels in a moldless approach to generate a 3D intestinal tissue model.* Biofabrication, 2019. **11**(2): p. 025007.
4. Seeley, R., T. Stephens, and P. Tate, *Anatomy and Phisiology*. 6 ed. 2004, Boston, MA, USA: McGraw-Hill.
5. Gerbe, F., et al., *Intestinal epithelial tuft cells initiate type 2 mucosal immunity to helminth parasites.* Nature, 2016. **529**(7585): p. 226-230.
6. Mabbott, N.A., et al., *Microfold (M) cells: important immunosurveillance posts in the intestinal epithelium.* Mucosal Immunology, 2013. **6**(4): p. 666-677.
7. Hunyady, B., E. Mezey, and M. Palkovits, *Gastrointestinal immunology: cell types in the lamina propria--a morphological review.* Acta Physiologica Hungarica, 2000. **87**(4): p. 305-328.
8. Powell, D.W., et al., *Mesenchymal cells of the intestinal lamina propria.* Annual Review of Physiology, 2011. **73**: p. 213-237.
9. Basson, M.D., G. Turowski, and N.J. Emenaker, *Regulation of human (Caco-2) intestinal epithelial cell differentiation by extracellular matrix proteins.* Experimental Cell Research, 1996. **225**(2): p. 301-305.
10. Vila, A., et al., *Hydrogel co-networks of gelatine methacrylate and poly(ethylene glycol) diacrylate sustain 3D functional in vitro models of intestinal mucosa.* Biofabrication, 2020. **12**(2): p. 025008.
11. Fritsch, C., et al., *Characterization of human intestinal stromal cell lines: response to cytokines and interactions with epithelial cells.* Experimental Cell Research, 1999. **248**(2): p. 391-406.
12. Pampaloni, F., E.G. Reynaud, and E.H. Stelzer, *The third dimension bridges the gap between cell culture and live tissue.* Nature Reviews Molecular Cell Biology, 2007. **8**(10): p. 839-945.
13. Justice, B.A., N.A. Badr, and R.A. Felder, *3D cell culture opens new dimensions in cell-based assays.* Drug Discovery Today, 2009. **14**(1): p. 102-107.
14. Bissell, M.J., et al., *The organizing principle: microenvironmental influences in the normal and malignant breast.* Differentiation, 2002. **70**(9-10): p. 537-546.

15. Kim, W. and G. Kim, *Intestinal Villi Model with Blood Capillaries Fabricated Using Collagen-Based Bioink and Dual-Cell-Printing Process.* ACS Applied Materials & Interfaces, 2018. **10**(48): p. 41185-41196.
16. Kim, W. and G.H. Kim, *An innovative cell-printed microscale collagen model for mimicking intestinal villus epithelium.* Chemical Engineering Journal, 2018. **334**: p. 2308-2318.
17. Madden, L.R., et al., *Bioprinted 3D Primary Human Intestinal Tissues Model Aspects of Native Physiology and ADME/Tox Functions.* iScience, 2018. **2**: p. 156-167.
18. Sung, J.H., et al., *Microscale 3-D hydrogel scaffold for biomimetic gastrointestinal (GI) tract model.* Lab Chip, 2011. **11**(3): p. 389-392.
19. Wang, Y., et al., *A microengineered collagen scaffold for generating a polarized crypt-villus architecture of human small intestinal epithelium.* Biomaterials, 2017. **128**: p. 44-55.
20. Yu, J., et al., *In vitro 3D human small intestinal villous model for drug permeability determination.* Biotechnology and Bioengineering, 2012. **109**(9): p. 2173-2178.
21. Hidalgo, I.J., T.J. Raub, and R.T. Borchardt, *Characterization of the Human Colon Carcinoma Cell Line (Caco-2) as a Model System for Intestinal Epithelial Permeability.* Gastroenterology, 1989. **96**(2): p. 736-749.
22. Balimane, P.V. and S. Chong, *Cell culture-based models for intestinal permeability: A critique.* Drug Discovery Today, 2005. **10**(5): p. 335-343.
23. Yi, B., et al., *Three-dimensional in vitro gut model on a villi-shaped collagen scaffold.* BioChip Journal, 2017. **11**(3): p. 219-231.
24. Li, N., et al., *Development of an Improved Three-Dimensional In Vitro Intestinal Mucosa Model for Drug Absorption Evaluation.* Tissue Engineering Part C: Methods, 2013. **19**(9): p. 708-719.
25. Altay, G., et al., *Imaging the Cell Morphological Response to 3D Topography and Curvature in Engineered Intestinal Tissues.* Frontiers in Bioengineering and Biotechnology, 2020. **8**(294).
26. Kim, S.H., et al., *Three-dimensional intestinal villi epithelium enhances protection of human intestinal cells from bacterial infection by inducing mucin expression.* Integrative Biology, 2014. **6**(12): p. 1122-1131.
27. Almeida, A., et al., *Chapter 13 - 3D intestinal models towards a more realistic permeability screening*, in *Nanotechnology for Oral Drug Delivery*, J.P. Martins and H.A. Santos, Editors. 2020, Academic Press. p. 389-417.
28. Torras, N., et al., *Visible-light DLP-based 3D Bioprinting System for engineering complex, soft-hydrogel networks, under preparation.*

29. Shinde, A.V., C. Humeres, and N.G. Frangogiannis, *The role of α-smooth muscle actin in fibroblast-mediated matrix contraction and remodeling.* Biochimica et Biophysica Acta (BBA) - Molecular Basis of Disease, 2017. **1863**(1): p. 298-309.
30. Hewes, S.A., et al., *In Vitro Models of the Small Intestine: Engineering Challenges and Engineering Solutions.* Tissue Engineering Part B: Reviews, 2020. **26**(4): p. 313-326.
31. Allaire, J.M., et al., *The Intestinal Epithelium: Central Coordinator of Mucosal Immunity.* Trends in Immunology, 2018. **39**(9): p. 677-696.
32. Pusch, J., et al., *The physiological performance of a three-dimensional model that mimics the microenvironment of the small intestine.* Biomaterials, 2011. **32**(30): p. 7469-7478.
33. Dosh, R.H., et al., *Use of hydrogel scaffolds to develop an in vitro 3D culture model of human intestinal epithelium.* Acta Biomaterialia, 2017. **62**: p. 128-143.
34. De Gregorio, V., et al., *3D stromal tissue equivalent affects intestinal epithelium morphogenesis in vitro.* Biotechnology and Bioengineering, 2018. **115**(4): p. 1062-1075.
35. Macedo, M.H., et al., *Development of an Improved 3D in vitro Intestinal Model to Perform Permeability Studies of Paracellular Compounds.* Frontiers in Bioengineering and Biotechnology, 2020. **8**(1076).
36. Legen, I., M. Salobir, and J. Kerc, *Comparison of different intestinal epithelia as models for absorption enhancement studies.* International Journal of Pharmaceutics, 2005. **291**(1-2): p. 183-8.
37. Söderholm, J.D., et al., *Integrity and metabolism of human ileal mucosa in vitro in the Ussing chamber.* Acta Physiologica Hungarica, 1998. **162**(1): p. 47-56.
38. Alpers, D.H., et al., *The secretion of intestinal alkaline phosphatase (IAP) from the enterocyte.* Journal of Gastroenterology, 1994. **29 Suppl 7**: p. 63-67.
39. Hinnebusch, B.F., et al., *Enterocyte differentiation marker intestinal alkaline phosphatase is a target gene of the gut-enriched Kruppel-like factor.* American Journal of Physiology-Gastrointestinal and Liver Physiology, 2004. **286**(1): p. G23-30.
40. Estudante, M., et al., *Intestinal drug transporters: an overview.* Advanced Drug Delivery Reviews, 2013. **65**(10): p. 1340-1356.
41. Liu, Z. and K. Liu, *The transporters of intestinal tract and techniques applied to evaluate interactions between drugs and transporters.* Asian Journal of Pharmaceutical Sciences, 2013. **8**(3): p. 151-158.

42. Brück, S., et al., *Caco-2 cells - expression, regulation and function of drug transporters compared with human jejunal tissue.* Biopharmaceutics & Drug Disposition, 2017. **38**(2): p. 115-126.

43. Hilgendorf, C., et al., *Expression of thirty-six drug transporter genes in human intestine, liver, kidney, and organotypic cell lines.* Drug Metabolism and Disposition, 2007. **35**(8): p. 1333-1340.

44. Herrera-Ruiz, D., et al., *Spatial expression patterns of peptide transporters in the human and rat gastrointestinal tracts, Caco-2 in vitro cell culture model, and multiple human tissues.* American Association of Pharmaceutical Scientists, 2001. **3**(1): p. E9.

45. Maubon, N., et al., *Analysis of drug transporter expression in human intestinal Caco-2 cells by real-time PCR.* Fundamental & Clinical Pharmacology, 2007. **21**(6): p. 659-663.

46. Shu, Y., *Research progress in the organic cation transporters.* Zhong Nan Da Xue Xue Bao Yi Xue Ban, 2011. **36**(10): p. 913-926.

47. Beduneau, A., et al., *A tunable Caco-2/HT29-MTX co-culture model mimicking variable permeabilities of the human intestine obtained by an original seeding procedure.* European Journal of Pharmaceutics and Biopharmaceutics, 2014. **87**(2): p. 290-298.

48. Bohets, H., et al., *Strategies for absorption screening in drug discovery and development.* Current Topics in Medicinal Chemistry, 2001. **1**(5): p. 367-383.

49. Hilgendorf, C., et al., *Caco-2 versus Caco-2/HT29-MTX co-cultured cell lines: permeabilities via diffusion, inside- and outside-directed carrier-mediated transport.* Journal of Pharmaceutical Sciences, 2000. **89**(1): p. 63-75.

50. Chan, L.M., S. Lowes, and B.H. Hirst, *The ABCs of drug transport in intestine and liver: efflux proteins limiting drug absorption and bioavailability.* European Journal of Pharmaceutical Sciences, 2004. **21**(1): p. 25-51.

51. Taipalensuu, J., et al., *Correlation of gene expression of ten drug efflux proteins of the ATP-binding cassette transporter family in normal human jejunum and in human intestinal epithelial Caco-2 cell monolayers.* Journal of Pharmacology and Experimental Therapeutics, 2001. **299**(1): p. 164-70.

52. Bathaie, S.Z., et al., *Chapter One - How Phytochemicals Prevent Chemical Carcinogens and/or Suppress Tumor Growth?*, in *The Enzymes*, S.Z. Bathaie and F. Tamanoi, Editors. 2015, Academic Press. p. 1-42.

53. Wang, Y., et al., *A kinetic study of Rhodamine123 pumping by P-glycoprotein.* Biochimica et Biophysica Acta, 2006. **1758**(10): p. 1671-1676.

54. Kunta, J.R. and P.J. Sinko, *Intestinal drug transporters: in vivo function and clinical importance.* Current Drug Metabolism, 2004. **5**(1): p. 109-124.

55. Versantvoort, C.H.M., et al., *Monolayers of IEC-18 cells as an in vitro model for screening the passive transcellular and paracellular transport across the intestinal barrier: comparison of active and passive transport with the human colon carcinoma Caco-2 cell line.* Environmental Toxicology and Pharmacology, 2002. **11**(3): p. 335-344.

56. Mouly, S. and M.F. Paine, *P-glycoprotein increases from proximal to distal regions of human small intestine.* Pharmaceutical Research, 2003. **20**(10): p. 1595-1599.

57. Lozoya-Agullo, I., et al., *Segmental-dependent permeability throughout the small intestine following oral drug administration: Single-pass vs. Doluisio approach to in-situ rat perfusion.* International Journal of Pharmaceutics, 2016. **515**(1-2): p. 201-208.

58. Lozoya-Agullo, I., et al., *Investigating drug absorption from the colon: Single-pass vs. Doluisio approaches to in-situ rat large-intestinal perfusion.* International Journal of Pharmaceutics, 2017. **527**(1-2): p. 135-141.

59. DiMarco, R.L., et al., *Improvement of paracellular transport in the Caco-2 drug screening model using protein-engineered substrates.* Biomaterials, 2017. **129**: p. 152-162.

60. Ruiz, M.L., et al., *Induction of intestinal multidrug resistance-associated protein 2 (Mrp2) by spironolactone in rats.* European Journal of Pharmacology, 2009. **623**(1-3): p. 103-106.

61. Dahan, A. and G.L. Amidon, *Grapefruit juice and its constituents augment colchicine intestinal absorption: potential hazardous interaction and the role of p-glycoprotein.* Pharmaceutical Research, 2009. **26**(4): p. 883-892.

62. Lozoya-Agullo, I., et al., *In Situ Perfusion Model in Rat Colon for Drug Absorption Studies: Comparison with Small Intestine and Caco-2 Cell Model.* Journal of Pharmaceutical Sciences, 2015. **104**(9): p. 3136-3145.

63. Ben-Chetrit, E., *Colchicine.* Textbook of Autoinflammation, 2018: p. 729-749.

64. Dahan, A., H. Sabit, and G.L. Amidon, *Multiple Efflux Pumps Are Involved in the Transepithelial Transport of Colchicine: Combined Effect of P-Glycoprotein and Multidrug Resistance-Associated Protein 2 Leads to Decreased Intestinal Absorption Throughout the Entire Small Intestine.* Drug Metabolism and Disposition, 2009. **37**(10): p. 2028-2036.

CHAPTER 7 – Conclusions and future perspectives

7.1. Conclusions

The pharmaceutical field is constantly demanding new tools that can help accelerate the drug development roadmap. *In vitro* models can serve as a crucial platform to screen ADME properties of the compounds in an early stage. A correct screening in an initial phase of drug development can prevent significant costs downstream. To predict absorption of orally delivered drugs, intestinal *in vitro* models are widely used, which should mimic the absorption process that will occur *in vivo*. In order to reliably envisage the absorption in the human intestine, these platforms should resemble the organ in the best possible way. Unfortunately, while 2D models are still the most widely used, they do not recapitulate key features of the intestinal absorption process.

In this thesis, different configurations of innovative 3D intestinal models were explored. Our ultimate goal was to develop a new and improved model that could be more accurate in predicting the permeability of compounds, but at the same time be simple enough so it could be reproducible and used for drug molecules and nanomedicines screening, by our group and other researchers in the pharmaceutical field.

We started by optimizing the collagen layer with the fibroblasts embedded. This part was crucial for obtaining the model, since it mimicked the lamina propria and gave the 3D support to the epithelium. The first optimization was achieved with a collagen concentration of 6 mg/mL and a HIF initial seeding density of 1 x 10^5 cells/mL. Nevertheless, when epithelial and endothelial cells were added to the model, they stimulated the contractibility of the fibroblasts and the models were no longer able to maintain integrity for the 21 days. Considering these results, different compounds in the culture medium were quantified and it was observed that levels of ET-1, secreted primarily by endothelial cells, and TGF- ß1 were mainly increased when HT29-MTX cells were absent. This led us to believe that HT29-MTX may exert some inhibitory effect on the secretion of these and, probably, other factors that increase fibroblast ability to contract. In fact, we observed that when these cells were present, pro-MMP2 and pro-MMP9, were decreased. These findings are important as they point to a crucial role of HT29-MTX cells in the model.

Although in this first attempt the models could not hold for 21 days without contraction, it was observed that after 14 days the epithelial layer was already formed and permeability assays with a paracellular compound were performed. These preliminary results showed a higher permeability in the 3D models. Since paracellular transport in Caco-2 model is usually underestimated due to the tighter barrier that is established by these cells, this higher permeability of the 3D models was promising. In terms of TEER, a decrease in the 3D models was observed, correlating with the permeability outcomes and being more similar to reported values of the human small intestine.

Since the goal was to obtain a model that could be used to test both paracellular and transcellular permeability, and because we were aware that differences could be observed in the results in models with 14 and 21 days in culture, a further optimization of the lamina propria was made. A decrease in HIF initial density to 0.5 x 10^5 cells/mL was enough to prevent collagen contraction without compromising cellular viability and the ability of the fibroblasts to secrete fibronectin, remodeling the surrounding matrix. At this point, the endothelial layer was seeded in the basolateral side of the Transwell® membrane to mimic the blood vessels. After having the model optimized, it was fully characterized. The characterization was performed at 14 and 21 days and models with and without the endothelial layer were used. In terms of intestinal markers, no differences were observed between timepoints, whether a significant decrease was observed for SI in the 3D intestinal models both at 14 and 21 days. A higher expression of intestinal markers in the 3D models was expected because of the more physiologic environment sensed by the cells, but this did not occur. For drug transporters, 3D models presented a more relevant expression by showing a decreased presence of P-gp, MRP2 and MCT1. The lower activity of P-gp in the 3D models was confirmed with a transport assay with Rho 123. This assay revealed a higher activity of P-gp after 21 days in the 2D model, while for the 3D models, this activity was reduced at this timepoint when compared to 14 days. Lastly, permeability assays confirmed that, in fact, results were different at 14 and 21 days, especially for the 2D and the 3D Co-culture models, being that 21 days in culture led to outcomes more similar to reported *in vivo* data. When comparing the performance of the models, the 3D model without the endothelial layer after 21 days in culture was the best at predicting permeability results. The addition of the endothelial layer rendered a decrease in the values, which should be expected, as an additional layer is present hindering the passage of compounds. Surprisingly, unlike the other models, no significant differences in permeability were observed between timepoints for the 3D Complete model. Although the addition of the endothelium did not translate in a more reliable model for permeability screening, we concluded that this model could be helpful when studying interactions of drugs with the blood vessels.

The presence of villi was also dissected in this thesis. For this, bioprinted models with and without villus-like structures were obtained and the same characterization was performed on these models. In terms of intestinal markers, no differences were observed. Once again, we were expecting a higher expression of the markers in the microstructured model, as this model mimics better the intestinal architecture, but this was not observed. On the other hand, the expression of drug transporters was generally more relevant in the villi model. An even lower expression and activity of P-gp was observed in this model, when compared to the collagen model previously developed. Unfortunately, the permeability outcomes were not so promising. Although permeability was higher in the villi model, as expected, values were lower than the ones observed for the collagen model and, therefore, contrasting the reported *in vivo* data. We believe this lower absorption is related to the GelMA + PEGDA hydrogel, that is formed by a tighter network than the collagen hydrogel, hindering the passage of compounds.

Overall, the 3D Co-culture model was the one that showed more promising results regarding drug absorption. This model holds an enormous potential to become a widely used *in vitro* tool to test absorption, due to its simplicity and accuracy of results. Using a more relevant model that grants more reliable results is very important in the scientific field, contributing to the 3Rs policy.

7.2. Future perspectives

As future perspectives, different studies could be carried out to better characterize the models. For instance, a more detailed characterization of the endothelial layer may be performed, as in our studies cells would detach from the membrane during the processing, so this should be improved. The presence and expression of other intestinal transporters that were mentioned in the introduction could also be assessed. Transport studies with other compounds that are substrates of specific transporters, as Rho 123 for P-gp, would give more information about the activity of important transporters. The activity of CYP3A4 could also be measured since a low expression of this important metabolizing enzyme is described in the Caco-2 models. The presence of other mucins should be investigated, as well as the formation of the mucus layer on top of the epithelial cells. More importantly, a validation of the 3D Co-culture model should be performed using an array of model drugs to more exhaustively assess the ability of the model to predict the permeability outcomes, making a correlation with the 2D models and *in vivo* values.

As discussed previously, the small intestine is a complex organ and, therefore, the potential for improving the *in vitro* models to make them more *in vivo*-like is almost unlimited. Since our aim was to obtain a simple model, these improvements were not considered. Notwithstanding, they can be performed as proofs of concept and also to use the models for other types of studies, besides permeability. The addition of flow to the model could be considered as this would mimic the circulation of food and drugs in the lumen and the blood flow on the basolateral side. As discussed in the introduction, the addition of flow and, therefore, mechanical cues, has a huge impact on cellular behavior. Other improvement in the model could be achieved by adding more cell types. In the epithelium, the addition of Paneth and M cells (that can be achieved by using Raji B cells), and in the lamina propria the addition of immune cells. The embedding of endothelial cells inside the collagen hydrogel, instead of adding the cells underneath the insert, allowing the creation of vessels within the matrix would be more physiological. Regarding the matrix, other materials could be used together with collagen, as fibronectin, laminin, and other components of the ECM to better mimic the *in vivo* environment.

In the case of the bioprinted models, the addition of crypt structures would make the 3D architecture even more similar to what is observed *in vivo*. In this case, stem cells could be added to form the stem cell niche and gradients could be applied. In terms of using the bioprinted models for permeability, different improvements must be performed. First, as it was observed, it is likely that the hydrogel used in these models is preventing the passage of drugs, so a further optimization to obtain a mesh with larger pore size should be performed. On the other hand, the process to mount the membranes with the bioprinted hydrogels in the Transwell® membrane is not straightforward and, because of this, leakage was observed many times. This decreases the number of inserts that can be used to perform the permeability assays, leading to loss of time and resources. Besides, since the bioprinting is performed in unsterile conditions and the mounting of the membranes in the inserts requires significant manual work, the system is more susceptible to contamination.

In terms of applicability, the 3D Co-culture and Complete models developed in this work allowed us to establish collaborations with pharmaceutical companies to test intestinal permeability of drug compounds and use that data for bioequivalence regulatory requirements. Based on these proofs of interest, we believe these models can be of interest for the pharmaceutical industry in general, since they are more physiological, rendering more reliable results. Furthermore, if the above-mentioned experiments are performed to better characterize and completely validate the models, confirming their advantage over the 2D alternatives, a drug screening collaborative platform, exploring the work developed in this PhD for commercial purposes, can be established.

APPENDIX – Supplementary information for Chapter 5 and 6

Table A.2 - Summary of HPLC conditions for the compounds tested in the permeability assays. Analytical methods were carried out using a LiChrospher 100 RP-18 Column (125 mm x 4 mm, 5 μm) (1.50943, Merck Millipore) and a LiChrospher 100 RP-18 guard column (4 mm x 4 mm, 5 μm) (1.50957, Merck Millipore), with a flow rate of 1 mL/min at room temperature and were validated in terms of specificity, selectivity and linearity for each compound.

	Detection	**Mobile phase (aqueous:organic)**	**λ (nm) (excitation/emission)**	**Retention time (min)**
Colchicine	Ultraviolet	0.1% TFA in water:Acetonitrile (70:30)	245	3.45
Atenolol	Fluorescence	20 mM Ammonium Acetate:Methanol (75:25)	231/307	2.91
Metoprolol	Fluorescence	0.1% TFA in water:Acetonitrile	231/307	2.33

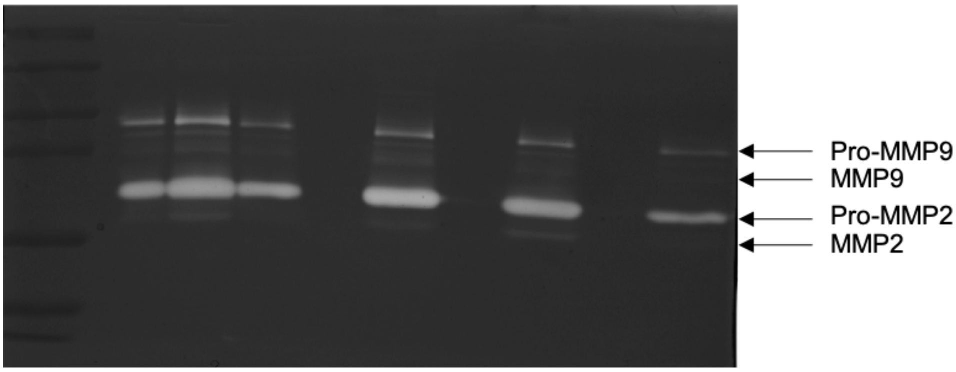

Figure A.1 - Example of a zymography obtained using the medium samples of day 21. It is possible to see the appearance of MMP9 and MMP2 bands right underneath Pro-MMP9 and Pro-MMP2, respectively, but so tenuous that makes quantification impossible.

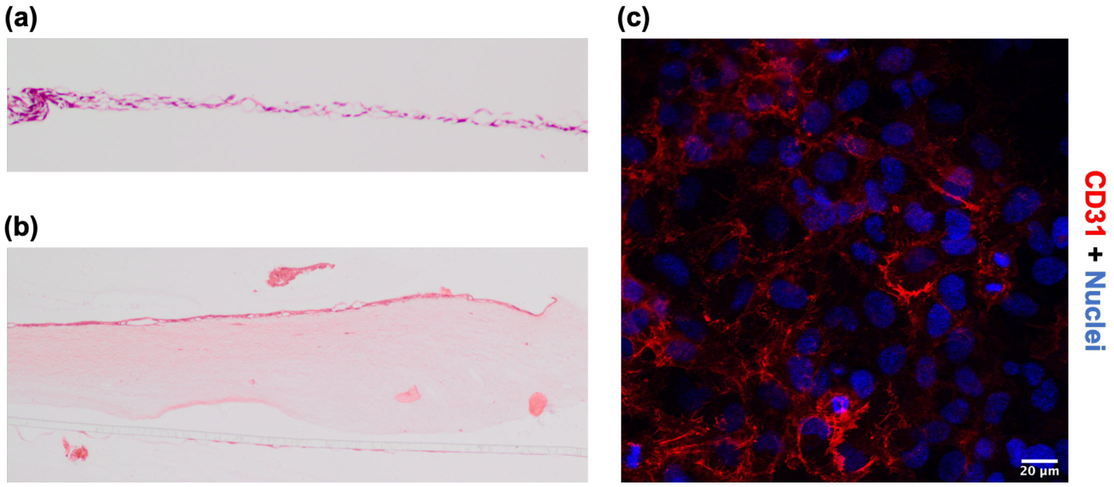

Figure A.2 – Visualization of the endothelial cell monolayer formation after 21 days on (a) histological transversal cuts with H&E staining of HPMEC cells seeded alone on the basolateral side of the insert, (b) histological transversal cuts with H&E staining of HPMEC cells seeded in combination with the epithelial cells and the collagen layer with fibroblast and (c) top view of endothelial cells on the basolateral side of the insert in the 3D Complete model immunoassayed for **CD31**, which is an endothelial cell adhesion molecule. Nuclei were counterstained with DAPI.

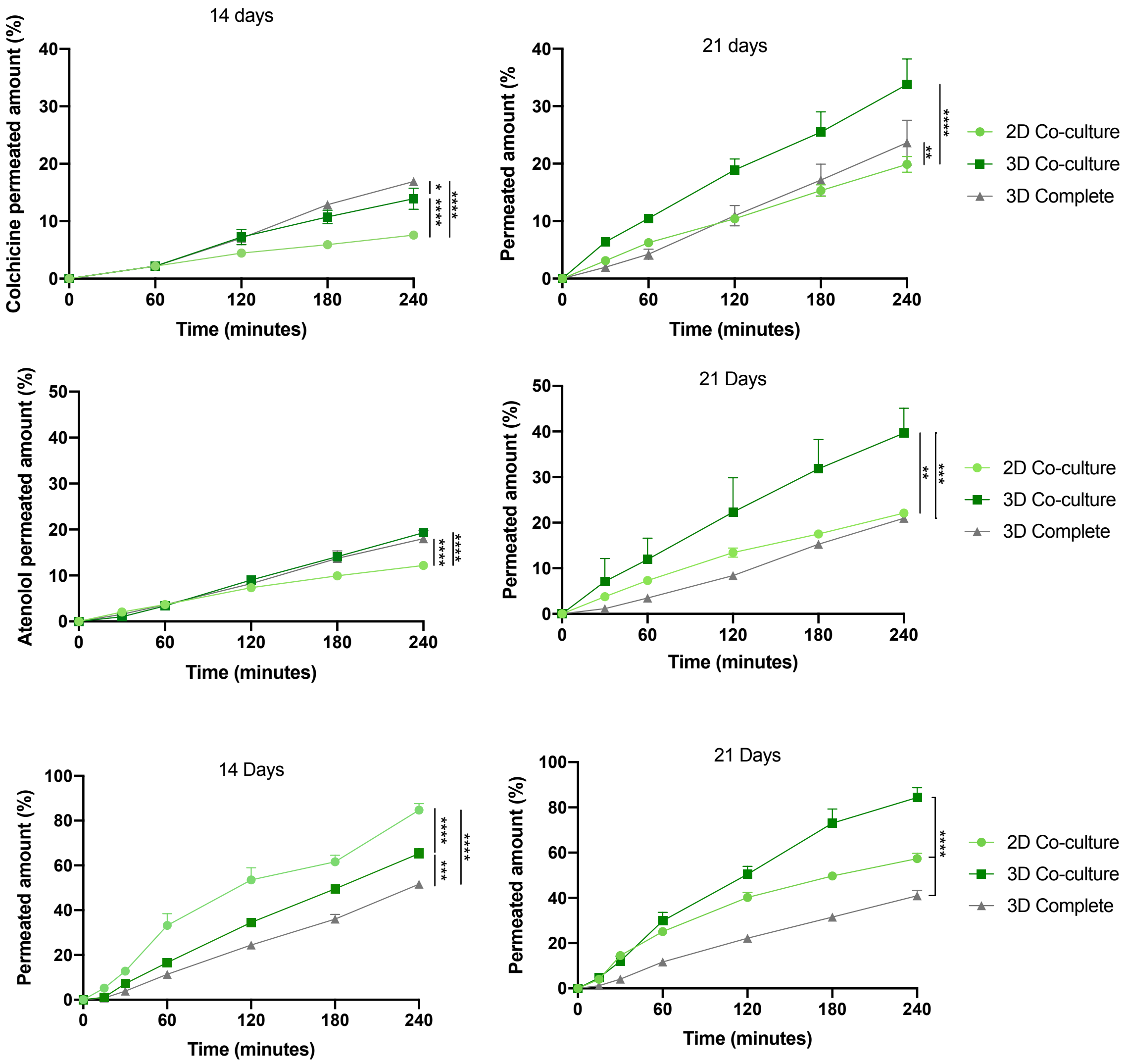

Figure A.3 - Percentage of permeated amount of colchicine, atenolol and metoprolol in the different models after 14 and 21 days. Results are the average of triplicates, and bars represent the standard error of the mean (SEM). Statistical differences were calculated using 2-way ANOVA multiple comparisons to compare the percentage of permeated amount between each configuration (p<0.05 are denoted by *, p<0.01 is denoted by **, p<0.001 are denoted by *** and p<0.0001 are denoted by ****).

BIBLIOGRAPHIC NOTE

Maria Helena Macedo was born on May 21, 1993 in Joane, Vila Nova de Famalicão, Portugal. She obtained her integrated master degree in Biomedical Engineering in 2016 in Universidade do Minho, Braga, Portugal. Since 2017 she has been developing her PhD thesis in Biomedical Sciences, PhD program from Instituto de Ciências Biomédicas Abel Salazar (ICBAS), at Instituto de Investigação e Inovação em Saúde (i3S) / Instituto Nacional de Engenharia Biomédica (INEB), Porto, Portugal. Her research mainly focused in developing *in vitro* intestinal models for determining the absorption of compounds. Her current interests focus on new technologies to obtain *in vitro* platforms, as bioprinting and microfluidics and on tissue engineering. She has developed many skills in the development and characterization of *in vitro* models, which involved cell culture techniques and cell-based assays, as well as histology, confocal microscopy and 3D bioprinting. Her research resulted in 4 peer-reviewed original articles (three published and one under preparation), 2 peer-reviewed revision articles, 9 peer-reviewed publications and 2 book chapters as a result of collaborative work, 12 poster and 8 oral presentations in international and national meetings and conferences.

During the PhD, Helena was able to improve her soft skills in innovation, creativity, entrepreneurship and technology transfer by participating in several contest for start-ups with a business idea using the 3D intestinal model developed in the PhD. Additionally, she was involved in the organization of different events as the first PhDay at i3S, the Young Scientists Seminars, and the first Pint of Science in Portugal and she is a member of the Transdermal and Mucosal Delivery Focus Group of the Controlled Release Society (CRS) as student's representative. Helena also participated in the Spin Your Thesis! Program from the European Space Agency (ESA) in Belgium and Netherlands. Moreover, Helena collaborated with the IBEC research institute in Barcelona (Spain), where she spent several months. Helena has also participated in several courses, workshops and training schools to deepen her knowledge in the scientific field.

As results of her work, Helena was awarded with several prizes as the "Norte Empreendedor" by Associação Empresarial de Portugal (AEP), four ICT conference/training schools grants from COST, two prizes from CRS (best mind-map and best video), best oral presentation in an international conference and best poster in a national meeting.